Czech Technical University in Prague

Faculty of Electrical Engineering
Department of Physics

FABRICATION AND CHARACTERIZATION OF DIAMOND PHOTONIC STRUCTURES

Doctoral Thesis

Jan Fait

Prague, July 2020

Ph.D. Programme: Electrical Engineering and Information Technology (P2612)
Branch of study: Electrotechnology and Materials (2602V009)

Supervisor: ***prof. RNDr. Bohuslav Rezek, Ph.D.***
Supervisor-Specialist: ***RNDr. Lukáš Ondič, Ph.D.***

Acknowledgements

I would like to express my deep gratitude to my supervisor Bohuslav Rezek for his guidance and support during my PhD studies. I am also grateful to my supervisor-specialist Lukáš Ondič for his guidance, willingness to help me with many aspects of my research, and all the fruitful discussions.

I would like to thank to my colleagues from the Institute of Physics of the Czech Academy of Sciences: Alexander Kromka and Marián Varga for managing the diamond depositions and fabrication of photonic structures and many fruitful discussions about that topic, Jan Čermák and Štěpán Stehlík for their help with AFM measurements and many helpful discussions, Pavla Bauerová for her kind assistance with SEM measurements, Jiří Stuchlík for amorphous Si depositions, Zdeněk Remeš for PDS measurements, and Anna Artemenko for XPS analysis. I also thank my fellow PhD students Matěj Hývl, Daria Miliaieva, and Petra Matunová for many inspiring discussions.

I also want to express my thanks and gratitude to Michael Trupke, who supervised my work at the University of Vienna, and members of his team Stefan Putz, Georg Wachter, Sarah Riesenbauer, and Rui Vasconcelos for their support.

Last but not least I would like to thank to my family and friends for their support. My special thanks go to my wife Eliška.

Declaration

I, Jan Fait, hereby declare that the work in this dissertation titled “Fabrication and characterization of diamond photonic structures” has been carried out by me in cooperation with other team-members from the Institute of Physics of the Czech Academy of Sciences and Faculty of Electrical Engineering of the Czech Technical University in Prague. My contribution is specified in the “Own contribution of the author” part. I declare that I have written my dissertation thesis independently and consistently quoted the sources in the submitted work. I agree with the publication of the dissertation thesis.

Abstract (EN)

Diamond as a wide band gap semiconductor material features many interesting optical and electronic properties, including photoluminescent color centers. The color centers are highly sensitive to the surface chemistry and surrounding environment and can be thus utilized for nanoscale detection of weak magnetic fields, temperature, or molecules. Isolated color centers can be used as the sources of non-classical states of light such as single photons or entangled photons. Yet many practical uses of diamond color centers are hindered by the high refractive index trapping the light inside diamond. Therefore, we focus here on effective generation and collection of light originating from thin synthetic diamond layers by using photonic crystals. Photonic crystals, which are periodically ordered structures with a period comparable to the wavelength of light, enable to locally modify density of photon states and control propagation of light. We introduce new methods for the fabrication of photonic crystal slabs and photonic crystal cavities that allow to achieve spectral overlap between the photonic modes of the structure and the narrow spectral line of the silicon vacancy (SiV) centers in diamond. Both the top down approach, when the patterns are created directly into a diamond layer, and the bottom-up approach, when the substrate is patterned first and the diamond layer is grown on top copying the pattern, were used. We compute, fabricate and characterize various structures by angle-resolved photoluminescence and transmission spectroscopy, micro-photoluminescence measurements as well as scanning electron and atomic force microscopy. In particular, we show that the resonant coupling of the excitation beam into the photonic crystal slabs leads to more than 100x enhancement of the outcoupled photoluminescence intensity compared to an original diamond layer. In addition, Si micro-mirrors can be used to assemble open Fabry-Perot microcavities with high quality factor and small mode volume exceeding performance of all open-access optical microcavities to date. We also show that a micropatterned thin layer of amorphous Si can be used to suppress diamond nucleation and leads to the growth of photoluminescent diamond patterns. The method can be further downsized by nanostructuring amorphous Si using local application of electric field in atomic force microscopy. Various applications from biosensors and quantum information processing to photovoltaic energy harvesting may benefit from these results.

Key words: diamond, color centers, nanostructuring, photonic crystals, optical resonators, photoluminescence, light extraction, microscopy, spectroscopy, optical simulations

Abstrakt (CZ)

Diamant je polovodič se širokým zakázaným pásem, který se vyznačuje mnoha zajímavými optickými a elektronickými vlastnostmi, mezi které se řadí přítomnost tzv. barevných center. Barevná centra jsou citlivá na chemické vlastnosti povrchu a okolního prostředí, díky čemuž je lze využít pro detekci slabých magnetických polí, teploty nebo přítomnosti molekul. Jednotlivá barevná centra lze dále využít jako zdroj kvantových stavů světla tvořených izolovanými fotony anebo kvantově provázanými fotony. Nicméně praktické využití diamantu s barevnými centry je negativně ovlivňováno vysokým indexem lomu, kvůli kterému zůstává emitované světlo zachyceno uvnitř materiálu. V této práci se proto zaměřujeme na účinnou generaci a sběr světla z tenkých, synteticky připravených diamantových vrstev za využití fotonických krystalů. Fotonické krystaly, periodicky uspořádané struktury s periodou srovnatelnou s vlnovou délkou světla, umožňují lokálně měnit hustotu optických stavů a usměrňovat šíření světla. V práci představujeme nové metody pro přípravu planárních fotonických krystalů a rezonátorů založených na fotonických krystalech, které umožňují dosáhnout spektrálního překryvu mezi optickými módy a emisní čarou křemíkových vakancí (SiV center) v diamantu. Pro vytváření fotonických struktur byly využity postupy shora dolů (top-down), při kterém jsou vzory vytvářeny přímo v tenké diamantové vrstvě, a ze spodu nahoru (bottom-up), při kterém jsou vzory vytvořené již na substrátu a růst diamantu je řízen těmito vzory. V práci modelujeme, vytváříme a charakterizujeme různé fotonické struktury pomocí měření úhlově rozlišené fotoluminiscence a transmise, mikro-fotoluminiscence, rastrovací elektronové mikroskopie a mikroskopie atomárních sil. Konkrétně ukazujeme, že rezonanční navázání excitačního záření do planárního fotonického krystalu umožňuje více než stonásobné zesílení fotoluminiscence ve srovnání s nestrukturovanou vrstvou. Dále ukazujeme, že pomocí zrcadel vytvořených v křemíku lze sestavit otevřené mikro-rezonátory Fabry-Perotova typu s největším dosud pozorovaným poměrem faktoru kvality ku objemu optických módů ve srovnání s ostatními typy otevřených rezonátorů. V práci rovněž ukazujeme, že amorfní křemík efektivně potlačuje nukleaci diamantu a lze ho tak využít jako masky pro selektivní růst diamantových vzorů s barevnými centry. Velikost diamantových vzorů lze dále zmenšit jejich vytvářením za využití lokální aplikace elektrického pole pomocí mikroskopu atomárních sil. Dosažené výsledky jsou přínosné v mnoha oborech od biosenzorů přes kvantové zpracování informace až po fotovoltaické zdroje energie.

Klíčová slova: diamant, barevná centra, nanostrukturování, fotonické krystaly, optické rezonátory, fotoluminiscence, vyvazování světla, mikroskopie, spektroskopie, optické simulace

Table of Contents

List of abbreviations

a-Si:H – hydrogenated amorphous Si
AFM – atomic force microscopy/microscope
AR – anti-reflection (coating)
BOE – buffered oxide etchant
CVD – chemical vapor deposition
DOS – density of photon states
EBL – electron beam lithography
FDP – fumed diamond powder
FDTD – finite-difference time-domain (method)
FE-MISPC – field-enhanced metal-induced solid phase crystallization
FIB – focused ion-beam
FP (cavity) – Fabry-Perot (cavity)
FWHM – full width at half maximum
GeV – germanium-vacancy (color center)
HPHT – high-pressure high-temperature
HR – high reflectivity (coating)
IR – infra-red
LDOS – local density of states
LED – light emitting diodes
MBE – molecular beam epitaxy
MPB – MIT Photonic Bands software
MEEP – MIT Electromagnetic Equation Propagation software
MOSFET – metal oxide semiconductor field-effect transistor
MOVPE – metal-organic vapor phase epitaxy
MW – microwave
NA – numerical aperture
NCD – nanocrystalline diamond
NV – nitrogen-vacancy (color center)
ODMR – optically detected magnetic resonance
PDS – photothermal deflection spectroscopy
PhC – photonic crystal
PL – photoluminescence
PMMA – Poly(methyl-methacrylate)
Q-factor – quality factor
RCWA – rigorous coupled-wave analysis
RIE – reactive ion etching
ROC – radius of curvature
SEM – scanning electron microscopy/microscope
SiC – silicon carbide
SiV – silicon-vacancy (color center)
SRIM – stopping and range of ions in matter
TE – transversal electric (polarization)
TM – transversal magnetic (polarization)
UV – ultraviolet
XPS – X-ray photoelectron spectroscopy
ZPL – zero-phonon line

Aims of the thesis

In this thesis we aim to investigate fabrication and properties of diamond photonic structures by experimental methods and theoretical simulations. The main goal is to use the photonic structures for improving the extraction efficiency of light emitted by color centers (SiV centers in particular) in polycrystalline diamond. We study various types of photonic structures (photonic crystal slabs, photonic crystal cavities, and Fabry-Perot micro-cavities) fabricated by top-down or bottom-up approach and their combination. In particular, we aim to obtain spectral overlap of photonic modes with narrow emission lines of color centers, to maximize the intensity of extracted light, to efficiently excite the emitters inside material, and to analyze the effect of structural and material imperfections on light extraction.

Introduction

This work is devoted to photonic structures in diamond that allow to control emission and propagation of light. The basic instruments, such as lenses and mirrors, for controlling light propagation are known from antiquity. These basic instruments are based on the geometrical optics, where only reflections and refractions on material boundaries are applied. Nevertheless, the geometrical optics can correctly describe the propagation of light solely for objects with dimensions significantly larger than the wavelength of light. To describe properties of light when interacting with objects of small dimensions that are comparable with the wavelength of light, the wave optics must be used. The wave optics allows to treat more phenomena such as diffraction or scattering of light and also to understand the physical fundamentals of ray optics. Nevertheless, it is not capable of describing the interaction of light with electric charges and thus cannot explain processes such as emission or absorption of light. For this, the light must be treated as the electromagnetic wave, whose behavior is described by Maxwell’s equations.

The areas of optics mentioned above are based on the classical physics. However, some optical phenomena, such as emission of light from elementary sources or light with special behavior, such as sub-Poissonian statistics or entanglement between photons, cannot be explained without the introduction of quantum physics. Currently, the quantum physics provides the most complex description of the optical phenomena. Within this work the quantum description is limited to the range of photon optics, which is based on the classical optics with the addition of some quantum properties of light, namely the corpuscular nature, localization, and fluctuation of quantum fields and energy. The light is treated as consisting of photons that are localized particles, on one hand, but simultaneously extended in the space due to their wave character. The restriction to photon optics does not allow to describe all quantum properties of light, which is beyond the scope of this work. However, it allows us to describe, for example, the interaction of light with individual emitters or to describe relevant statistical properties of light.

In the line with the theoretical advances in understanding the physics of light, new technological procedures for material processing have been invented throughout centuries. In the end of the 20th century, the methods for fabrication and direct characterization of sub-micron sized structures became accessible (scanning electron microscopy, atomic force microscopy, electron beam lithography). This progress allowed to realize experiments that were already known from microwave region of electromagnetic radiation and theoretically predicted in the region of visible light with much shorter wavelengths. One of the most important achievements was the fabrication of photonic crystals, i.e. periodic structures with period comparable with the wavelength of visible light.

The power of the photonic crystals consists in their ability to locally alter the density of photon states and thus directly and controllably affect the propagation and emission of light. Thanks to this property, photonic structures based on photonic crystals can be used to create qualitatively new devices or to enhance the performance of already existing devices by controlling the light propagation at the nanoscale.

One particular issue that the photonic structures might resolve is the enhancement of light generation, and extraction of light from materials with high refractive index. The high refractive index causes that light is trapped inside the material, which significantly decreases the performance of devices such as light emitting diodes or solid-state single photon sources. On the other hand, it offers an opportunity to fabricate efficient photonic structures, for which high refractive index contrast is essential. Subsequently, light may not only be completely extracted from the material but also the performance of individual emitters can be improved.

In this work, we use photonic structures – photonic crystal slabs and photonic crystal cavities – to enhance the emission rate of photons emitted inside a thin polycrystalline diamond layer and to efficiently extract the light from the layer. Diamond is very attractive material due to its unique physical properties such as the well-known hardness, high thermal conductivity, chemical inertness, or biocompatibility. Besides, diamond has also very interesting optical properties. This is mainly the ability to host isolated photoluminescent defect centers (called color centers), which are capable of emitting single photons, that have attracted wide interest in recent years. The color centers have many potential applications including single photon sources for quantum communication, or light sources for biomarkers in medicine or biosensors.

The photonic structures may enhance the performance of such devices by various contributions. Firstly, they may increase the light extraction from diamond layers either by suppressing the emission into some directions or by diffracting light that would be otherwise trapped in diamond into specific direction. Secondly, the structures may increase the spontaneous radiation rate of color centers as they change the local optical properties. This increases the (single) photon count rate, which is of crucial importance for quantum-based communication systems. Finally, they can also increase the intensity of electric field in some places and thus enhance the interaction of light with matter. This may be particularly interesting for quantum information processing as well as for energy harvesting or sensing.

We were especially interested in the extraction of photoluminescence from silicon vacancy (SiV) centers in diamond. Particularly we used photonic crystal slabs to redirect the light emitted by ensembles of SiV centers by Bragg diffraction. The photonic crystal slabs serve as highly directional light sources with narrow spectral lines, which can be used in applications such as bio-sensing or light generation. The more complex structures that we studied, namely the photonic crystal cavities, can be also used for sensing applications. Our experiments that were demonstrated on these structures fabricated in polycrystalline diamond and with ensembles of color centers may be expanded to monocrystalline diamond with single photon emitters in future. Structures capable of hosting single photon sources (nitrogen vacancy, NV, centers in diamond) were studied during my stay at the University of Vienna.

Another possibility of increasing the light extraction, which we also studied, is the usage of diamond nanoparticles. This approach is based on the fact that light cannot be confined in particles, which are smaller than the wavelength of light. The extraction efficiency is thus significantly increased when compared to the bulk diamond. For sensing applications, which additionally takes advantage of the large surface to volume ratio of nanoparticles, the precise placement of diamond nanoparticles on substrate might be important for efficient light collection. Therefore, we studied bottom-up fabrication techniques for the localized growth of diamond with optically active SiV centers.

This thesis is divided into the first part describing state of the art and theoretical background (4 chapters), and the second part with chapters describing our own experimental procedures and achieved results. The thesis is then complemented with reprints of selected journal articles, where the results were published.

In the first part, the motivation, concepts, and theory relevant for our experiments are explained. In the first chapter, we introduce the basic principles for light extraction and photoluminescence enhancement as well as the methods for measuring the performance of photonic structures for these purposes. The most important effects that we discuss are the extraction of light from modes guided in thin layers of materials with high refractive index and the enhancement of radiative decay rate via the increased density of photon states. We also point out the directionality of light source and its effect on light collection. The limiting factors for light extraction and photoluminescence enhancement, namely the absorption and scattering of light are also discussed.

In the second chapter, the principles of photonic crystals function are outlined and their use for light extraction is reviewed in detail. We particularly focus on two types of photonic structures: the weak photonic crystal slabs, which are usually used for efficient light extraction from large areas of the samples, and photonic crystal cavities, which are especially important for radiative count rate enhancement for emitters spatially localized in a small volume of material inside the cavity. The simulation methods that we use to design photonic structures are also briefly summarized.

Chapter three is devoted to diamond as optical and semiconductor material. After summarizing its material properties, the methods for growth of synthetic diamonds are described with the focus on the chemical vapor deposition (CVD) technique. The next section deals with photoluminescent “color” centers in diamond. The properties of NV and SiV centers, as well as the methods for fabrication of the color centers are summarized.

In the end of the first part, the possibilities of fabrication of photonic structures in diamond are described. Instead of giving details about the particular methods, the approaches (bottom-up and top-down) and their advantages are sketched. Besides the well-established methods, such as photolithography, focused ion-beam milling, or electron beam lithography, the modification of hydrogenated amorphous silicon by conductive atomic force microscope is presented as an alternative method.

Subsequently, our specific experimental methods used for sample fabrication, and optical and material characterization are shortly described in the fifth chapter. More detailed description of the experimental methods can be found in the attached articles.

In the sixth chapter, the most important results of our work are outlined, and main achievements are emphasized. The first part describes our work on weak photonic crystals for light extraction from diamond. The second and third parts are devoted to photonic crystal cavities and Fabry-Perot cavities for interaction with diamond color centers. The final part summarizes our work on the micro-structuring of hydrogenated amorphous silicon and on the selective diamond growth achieved by patterning the hydrogenated amorphous silicon layer. The related journal articles that show more details to the performed research and contain more extensive discussions are attached at the end of the thesis. In the conclusion, we summarize the results and their impact, and present ideas for further research activities.

1. Efficient light generation

There are two main types of solid light sources that can be used for light generation. The first type is a thermal source, which is any object with a non-zero temperature, and the emission of light is denoted as incandescence. For sufficiently dense objects, such as solids, liquids, or dense gases, the thermal spectrum is continuous and may be approximated by the black-body radiation. The spectral distribution of the black body radiation follows the Planck's law [1,2]. Both the total power output (described by the Stefan-Boltzmann law) and the wavelength for which the emission intensity is highest (described by the Wien's displacement law, Fig. 1), are functions of temperature. An example of a thermal source that may be well approximated by black body source is the Sun. Generally, the radiation from dense thermal sources deviates from the radiation of black body due to its dependence on the material composition and the surface properties (such as shape or roughness [3]) in the case of solids. The deviation is quantified by the property of the surface called emissivity. Nevertheless, the character of the radiation depends primarily on the temperature of the object.

The advantage of the solid thermal sources is that no extraction of light from the inside of the material is necessary because the reabsorbed light is converted back to heat. Thus, light can be considered as emitted by the surface of the solid thermal source. Nevertheless, thermal sources have several drawbacks that limit their usage and efficiency for practical applications. Firstly, light is emitted in the broad spectral region. Secondly, the temperature of the object to emit significant fraction of radiation in the visible part of spectra must be higher than 2000K, which is the minimal temperature usually achieved with incandescent light bulbs. The highest achievable temperature of a solid is, on the other hand, limited by the material properties (melting point, evaporation) to approximately 3500 K. Fig. 1 shows that the maximum power is emitted in infra-red (IR) region for this temperature range, and the process of lighting (i.e. emitting visible light) is inefficient. Thirdly, light is not directed into any particular direction. Both effects, high temperature and random propagation of light, prohibit the miniaturization of devices based on the thermal sources. Finally, solid thermal sources cannot be used for applications that utilizes non-classical properties of light.

The second mechanism for light generation is luminescence, where light is emitted during a radiative transition of excited electrons (or other excited atomic or molecular states) to a lower energy level. Due to the given energy of individual electronic states or bands, it is possible to achieve emission at narrow spectral lines (Fig. 1) from solid state sources [4,5]. Thus, the spectral characteristic is primarily not influenced by material temperature. Instead, the emission properties depend on the type of material being used and can be tuned over large spectral regions by mixing materials together [4,6], introducing material impurities or mechanical stress [7], changing dimensions (quantum wells, wires, dots) [8,9], or by placing the emitters into specific environment (e.g. into optical cavity for lasing [5]). The usage of sources based on luminescence instead of incandescence enables not-only to increase the efficiency of lighting, but also to bring new devices that are not achievable with thermal sources. Examples of such devices are lasers or applications based on single photon emitters that are currently under development.

Luminescence can be further divided based on the mechanism of electron excitation [10]. In the case of electroluminescence, which is the process mostly used in technological applications, the electrons are excited by the electric field or directly injected by the electric current. In

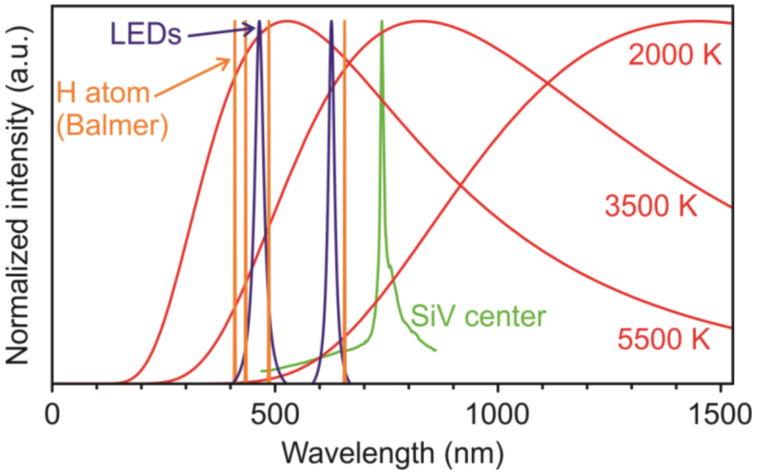

Figure 1: Illustration of spectra of different light sources. **Red**: black body radiation with temperature 5500K (~Sun), and 2000K and 3500K (~incandescent light bulbs); **Orange**: Balmer series of spectral lines from hydrogen atoms; **Blue**: electroluminescence spectra of a blue (GaInN/GaN, 470 nm) and a red (AlGaInP/GaAs, 625 nm) light emitting diode [14]. The electronic levels in crystals forms continuous bands, which causes the broadening of spectral lines. **Green**: room temperature photoluminescence spectra of ensemble of SiV centers in polycrystalline diamond with continuous background luminescence from random defects in diamond crystal (measured only for 460 nm – 850 nm range).

contrast, luminescence as a result of absorption of non-ionizing radiation is denoted as photoluminescence. Photoluminescence is often used for dynamic characterization of light sources due to the ability to control the excitation process by using very short optical pulses for excitation [11]. Despite electroluminescence was already observed on diamond color centers [12,13], the realization is technologically more complicated, expensive and time consuming. Therefore, we are mainly interested in the photoluminescence process in our experiments. Other types of luminescence (such as cathodoluminescence, chemiluminescence or bioluminescence) are not discussed in this work.

The emission of photons can be either spontaneous or stimulated by the incoming photon [15]. In common cases (including the processes in this work), most electrons stay in the lower energy states and the absorption of photons dominates over the stimulated emission. Therefore, the processes studied in this work are spontaneous and the rest of this chapter is devoted solely to the effects related to spontaneous emission.

The average time that the electron stays in the excited state before it spontaneously decays to the lower energy state is called luminescence lifetime τ. Apart from the radiative transitions, in which the photons are produced, also non-radiative transitions can occur. During the non-radiative transition, the energy may be carried away by some other means, e.g. the excitation of collective oscillations of crystal lattice (phonons) or excitation of other electrons (Auger effect). The majority of non-radiative transitions ends up producing heat. The efficiency η_r of photon emission is given by ratio of radiative decay rate Γ_r (count rate) to total decay rate Γ_{tot}:

$$\eta_r = \frac{\Gamma_r}{\Gamma_{tot}}; \; \Gamma_{tot} = \Gamma_r + \Gamma_{nr} = \frac{1}{\tau_r} + \frac{1}{\tau_{nr}} = \frac{1}{\tau} \tag{1.1}$$

where Γ_{nr}, and τ_r and τ_{nr} are non-radiative decay rate, and radiative and non-radiative lifetime, respectively. The radiative decay rate is often called count-rate. The efficiency η_r quantifies the fraction of all excitations that result in the emission of photon. Processes with short lifetime (typically < 100 ns) are denoted as fluorescence and they correspond to dipole transitions allowed by selection rules for change of quantum numbers [16,17]. The forbidden transitions, which must decay via higher order multipoles and have lifetime longer by few orders of magnitude (> 10 μs), are denoted as phosphorescence.

In many cases, there are multiple possible radiative transitions, and only one of them is of interest. An example is the emission of photons from color centers in diamond, where the transition may occur without interaction with the crystal lattice, or at a lower energy (longer wavelength) with simultaneous phonon excitation (phonon sideband), or non-radiatively via intermediate levels. Moreover, the energy levels may be split due to external or residual magnetic and electric field. The total branching ratio η_{tot} quantifies the fraction of all excitations that lead to the emission via the chosen transition, while radiative branching ratio η_i quantifies the fraction of photons emitted by the chosen transition:

$$\eta_{tot} = \frac{\Gamma_i}{\Gamma_{tot}}; \ \eta_i = \frac{\Gamma_i}{\Gamma_r} \tag{1.2}$$

where Γ_i is the decay rate of the chosen transition (e.g. emission of photon without interaction with crystal lattice for color centers in diamond).

In this work we are mainly focusing on the photoluminescence originating from diamond color centers that are localized in thin diamond layers (i.e. in material with high refractive index). Particularly, we study photonic structures as a way to maximize the optical signal coming from the color centers. Photonic structures help to enhance the collected optical signal in two fundamental ways: (i) light is efficiently extracted from diamond and ideally also redirected to some significant (vertical) direction, where it is collected (section 1.1), and (ii) the photon count-rate from individual emitters is enhanced (section 1.2). A practical difference in these two approaches is that light re-direction can be used for light extraction from large sample area (> mm^2), whereas significant photon count-rate enhancement in photonic cavities requires confinement of emitters into small volume (~μm^3). Both approaches must be considered for maximizing the light collection efficiency from any photonic structure.

1.1 Light extraction

When luminescence occurs inside a solid material, light propagates through the material before, eventually, reaching a boundary with surrounding medium (usually with smaller refractive index, most often air). On the boundary, part of light is refracted into the surrounding medium in accordance with Snell's law and other part is reflected back into the high refractive index material (Fig. 2). Only rays that hit the boundary under angle smaller than critical angle

$$\theta_c = \arcsin\left(\frac{n_2}{n_1}\right) \tag{1.3}$$

can escape from the material with the refractive index n_1 into the medium with refractive index $n_2 < n_1$. The critical angle for propagation from diamond ($n_1 = 2.41$) to air ($n_2 = 1$) is ~24.5° (Fig. 2a). When immersion oil ($n_2 = 1.55$) is applied to improve extraction, the critical angle increases to ~40°. The area limited by the critical angle is denoted as an escape cone. The escape cone occupies only 9% of the surface of the half-sphere for the diamond/air boundary. Even light that propagates within the escape cone is partially reflected with the reflectance given by Fresnel equations (Fig. 2b) [18]. The total light extraction efficiency into upper direction

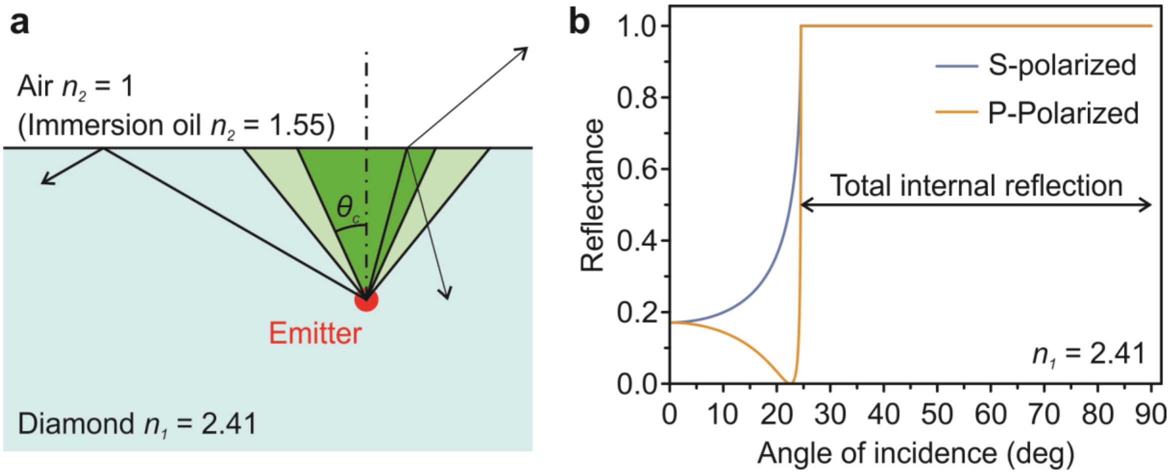

Figure 2: **(a)** Point emitter in a high-index medium (diamond): only small part of light can escape from diamond into air (green cone). The apex angle of the escape cone (θ_c) may be increased by using immersion oil (light green). **(b)** Reflectance as a function of the angle of incidence for light propagating from diamond into air.

(without considering any scattering and without multiple reflections) is thus less than 4.5%. Most of the light is reflected back into the material or propagates directly into the other half of the space (towards substrate).

During propagation in the material, light can be re-absorbed. The absorption probability increases with the distance travelled inside the material (*l*) and the loss of intensity in homogeneous material is described by the Beer-Lambert law

$$I(\lambda, l) = I_0(\lambda)e^{-\alpha_a(\lambda)l} \tag{1.4}$$

where α_a is the absorption coefficient (dependent on wavelength λ) and I_0 the initial intensity of light. Light that is re-absorbed in material is mostly transformed to heat, which decreases the total external quantum efficiency and may limit the lifetime of some high-power lighting devices due to overheating. The absorbed power can be reduced by improving the material properties (decreasing the absorption coefficient) or by reducing the path length travelled by light inside material, which is the aim of efficient light extraction.

Beside absorption, light may be scattered on the inhomogeneities inside material, such as boundaries between individual grains inside polycrystalline materials. The Rayleigh scattering applies for particles significantly smaller than the wavelength of light. The power scattered by one scattering particle P_s is quantified by the scattering cross section σ_s

$$P_s = \sigma_s I_0 \tag{1.5}$$

In the case of a dielectric sphere with diameter d_s and relative permittivity ε_s placed in a medium with permittivity ε the scattering cross-section is

$$\sigma_s = \frac{2\pi^5}{3}\frac{d_s^6}{\lambda^4}\left|\frac{\varepsilon_s - \varepsilon}{3\varepsilon}\right|^2 \tag{1.6}$$

where λ is wavelength. The Rayleigh scattering cross-section is almost independent on the shape of the particle and formula (1.6) may be used to estimate the scattering of various objects within the Rayleigh limit (dimensions smaller than ~50 nm for visible light). The main characteristics of Rayleigh scattering is its strong dependence on the wavelength of light and on the size of the scattering particle.

Scattering cross-section of larger objects (larger than ~50 nm) denoted as Mie scattering can be solved analytically only for special shapes of scattering particles (e.g. ellipsoids). Generally, the Mie scattering cross-section is roughly constant for the wavelengths in the visible region. Instead, it is more influenced by the shape of scattering particles.

In analogy to absorption the decrease of the intensity of the transmitted light due to scattering is exponential and it may be expressed in the terms of scattering coefficient α_s

$$I(l) = I_0 e^{-\alpha_s l}; \ \alpha_s = N_s \sigma_s \tag{1.7}$$

where N_s is the concentration of scattering particles (identical scattering particles with scattering cross-section σ_s are considered for simplicity). In contrast to absorption, the scattering of light may improve the extraction of light from material because light initially propagating outside the escape cone can be redirected into the escape cone due to scattering, or scattered on the rough surface and leave the material despite being incident outside the escape cone.

1.1.1 Extraction efficiency

In order to quantify the light extraction, we define extraction efficiency as the ratio between the intensity of light that is emitted by the sources in the material I_0 and the intensity that is extracted from the structure into the upper half space (air) I_{extr}

$$\eta_{extr}(\lambda) = \frac{I_{extr}(\lambda)}{I_0(\lambda)} \tag{1.8}$$

The extraction efficiency usually depends on the wavelength λ. It was already mentioned that the extraction efficiency is less than 4.5% for emitters located in bulk diamond. The extraction efficiency is important for theoretical considerations and comparison of individual systems used for light extraction. However, not all the light that leaves the material can be really exploited for the intended application (e.g. spectral measurement, information transfer, or imaging).

In this work, we are mainly interested in collection of the extracted light by simple optics – microscope objectives and optical fibers. In order to quantify the part of light that is actually collected by the collection optics, the collection efficiency can be defined as

$$\eta_{col}(\lambda) = \frac{I_{col}(\lambda)}{I_0(\lambda)} \tag{1.9}$$

where I_{col} is the intensity of collected light. The collection efficiency depends on the system that is used for the extraction and on the collection optics. An important parameter of the collection optics is the numerical aperture (NA) that characterizes the range of angles over which the detection system can accept light. Equally important for collection efficiency is the area of the surface from which the light is emitted, because high NA objectives cannot be used to collect all the light emitted/extracted from large sample areas.

The theoretical limit for collection efficiency is the extraction efficiency, which is achieved for a point source and collection optics with NA = 1. In real systems, the collection efficiency is lower due to the limited NA of the collection optics and large area of the sources. Moreover, the collection optics with high NA is expensive and must be placed very close to the light source, which is not possible for some applications. An alternative way to capture the extracted light is the use of an integration sphere [19]. Although the light can be collected by integration sphere, it cannot be further utilized (e.g. for transmitting information). Moreover, the integration spheres are expensive, and the sample design and dimensions are limited by the dimensions of the sphere. Another, more convenient, way to increase the collection efficiency is directing the light into some preferential direction, where it can be collected even with optics with small NA. This approach will be further elaborated in the next sections.

The collection efficiency cannot be directly measured, because the total intensity of light emitted by the sources is usually not known. The quantity that can be measured is the enhancement factor that compares the intensity obtained from a modified source I_{col}^{mod} with the intensity measured for a reference source I_{col}^{ref}

$$EF = \frac{I_{col}^{mod}}{I_{col}^{ref}}. \tag{1.10}$$

In this work, the intensity of the samples with photonic structures for light extraction is compared with the reference intensity of the unprocessed sample.

The value of the enhancement factor depends not only on the properties of the photonic structure but also on the parameters of the collection optics. For highly directional beams the use of collection optics with high NA may lead to decrease of the enhancement factor. The reason is that more light is captured from the reference while there is not much light coming under larger angles for directional beams. Note that the use of the same optics for measurement of I_{col}^{mod} and I_{col}^{ref} is assumed in Eq. 1.10.

Besides, the modified and reference sources may differ in other physical properties that affect the enhancement factor. For instance, the total volume of the luminescent material and the surface area differ in the case of planar layer and layer equipped with photonic crystal (PhC) slabs [20,21]. During the fabrication of photonic structures, new defects can be created in the material, which may change the optical properties. The performance of individual emitters is often (deliberately) altered. Finally, the structures used for light extraction may also lead to coupling of excitation beam into the sample that leads to more efficient excitation efficiency. All these effects are projected into the measured enhancement factor and the enhancement factor must be properly analyzed to extract the required information.

A typical application, for which the extraction of light from material with high refractive index is of critical importance, is in light emitting diodes (LEDs) [22–24]. Light is emitted from the p-n junction, which is typically located inside the semiconductor. Traditional ways to increase the extraction efficiency of LEDs are based on the limitation of the total internal reflection by closing the LED into a dome-shaped package [25]. Subsequently, the emitted light hits the surface almost perpendicularly on the whole half-sphere. Another approach is roughening of the LED surface that increase the randomness of the light propagation in material and increase the probability of light to hit the surface within the escape cone, and also improves the light extraction due to scattering [26,27]. The surface of LED diode can also be provided with anti-reflection coating to limit the Fresnel reflections [28]. A combination of these methods is often used. These methods can be employed for other types of samples as well.

Nevertheless, a common drawback for some applications is that these methods extract light without directing it into any significant direction. On the other hand, structuring the surface in a periodic manner may increase both the extraction of light and its directionality.

1.1.2 Etendue

An important characteristic of light sources is the radiation pattern that describes the variation of the power radiated by a light source as a function of the direction. The most common is the Lambertian radiation pattern, for which the angular intensity distribution follows the cosine law

$$I(\theta) = I_n(\cos\theta)^m; m = 1 \tag{1.11}$$

with θ the viewing angle and I_n the radiant flux on the normal to the surface. The Lambertian radiation pattern is followed by thermal sources and by luminescent solid material sources with flat and/or highly scattering surfaces. The luminous intensity of light travelling in a given direction per unit area of the source (luminance) is constant for all angles. For $m > 1$ in (1.11), the luminance is higher for the angles close to normal and light becomes more directional as is clearly seen on Fig. 3a.

The directionality of the light source can be described by the quantity called etendue, which describes how the light is extended in space and spread in angles [29]. Etendue of an optical system is defined as [30,31]

$$\mathrm{d}E = n^2 \cos\theta \, \mathrm{d}\Omega \mathrm{d}A \tag{1.12}$$

with dA the infinitesimal surface element, dΩ the infinitesimal solid angle at an angle θ from the normal to dA, and n the refractive index of the surrounding medium (see Fig. 3b). The lower the etendue of the optical system, the more directional is the light. The important property of etendue is that it can be never decreased by passing through an optical system, in which the optical power is conserved [32]. It is thus necessary for the applications, in which the light directionality is crucial, such as imaging or projective techniques, to use sources that produce directional light beams. Otherwise the light can be made more directional only in the expense of undesired losses of optical power or extension of the beam in the lateral direction.

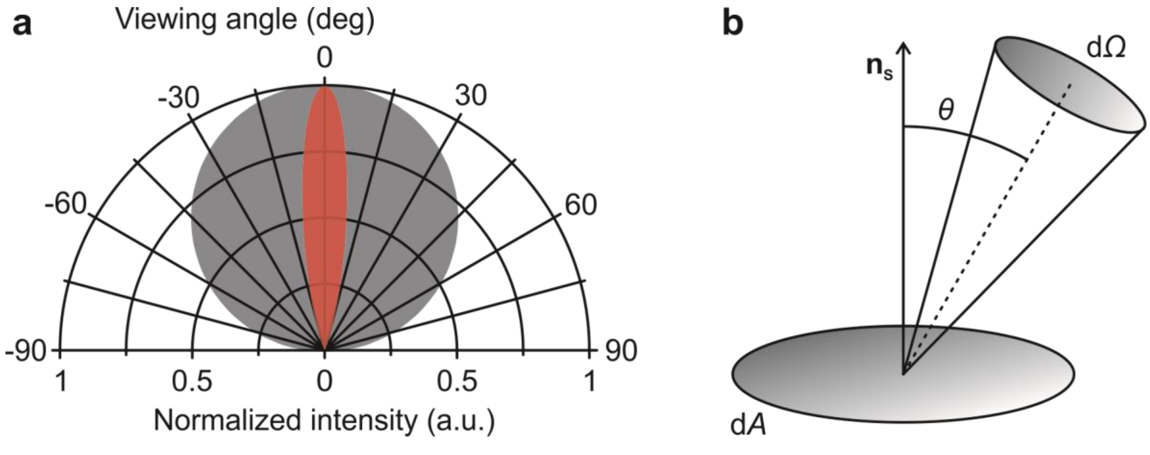

Figure 3: **(a)** Lambertian radiation pattern (grey) and radiation pattern with high directionality (red): m = 50 in Eq. 1.11; **(b)** Etendue of the optical system is defined by Eq. 1.12, where dA is the infinitesimal surface element, dΩ the infinitesimal solid angle at an angle θ from the $\mathbf{n_S}$ (normal to dA).

The directionality of light is important also when the collection optics is placed far away from the light source. This may be the case of light sources used for sensing in an aggressive environment where the collection optics cannot be placed. Collection optics with high numerical aperture (NA) and long working distance in the same time is difficult to fabricate and costly. By directing the light into a significant direction, the emitted light can be collected with affordable low NA collection optics, such as optical fibers placed far away from the source.

1.1.3 Thin layers

In many cases, the emitters are localized in a thin layer of material deposited by one of the methods for thin film deposition (e.g. chemical vapor deposition CVD, metal organic vapor phase epitaxy MOVPE, molecular beam epitaxy MBE). This is the case of some light emitting diodes [33] as well as of diamond [34]. We will further analyze situation when the refractive index of the thin layer is larger than refractive index of the substrate. In such case, the layer forms asymmetric planar dielectric waveguide.

Planar dielectric waveguide, e.g. diamond deposited on quartz glass, supports guided optical modes that are trapped inside the layer (Fig. 4; simulated by online mode solver [35]). The modes propagate in arbitrary direction within the plane because of the rotational symmetry of the waveguide. There are two groups of modes, TE (transversal electric) and TM (transversal magnetic), distinguished by the polarization of the field. For the modes propagating in x-direction, the TE modes have one non-zero component of electric field (E_y) and two non-zero components of magnetic field (H_x and H_z), while the TM mode has one non-zero component of magnetic field (H_y) and two non-zero components of electric field (E_x and E_z). Only electric field is shown in Fig. 4 since we are interested in the emission of light by electric dipoles. The electromagnetic field is not completely confined inside the layer, but its evanescent tails are extended into the surrounding material. Therefore, changes in the surrounding medium can be detected by observing the properties of the modes [36–38].

Sufficiently thin layers (with respect to wavelength) support only fundamental modes [18]. Symmetric structures (i.e. same medium is below and above the waveguide) support solely the fundamental modes when the thickness d of the layer fulfills the condition

$$d < \frac{\lambda_0}{2\sqrt{n_s^2 - n_a^2}} \tag{1.13}$$

where λ_0 is the vacuum wavelength, and n_s and n_a is the refractive index of the layer and of the surrounding medium (air), respectively. Thicker layers then support also higher order modes. The fundamental TE mode (TE_0) is supported by an arbitrarily thin waveguide. Symmetric structures always support also the fundamental TM mode (TM_0). This is not the case for asymmetric structures, where the TM_0 mode is supported only by a waveguide with sufficient thickness. For the asymmetric structures, the modes themselves become asymmetric and the condition (1.13) is not valid anymore. Nonetheless, when the refractive index of a substrate is taken as n_a, the thickness of the structure supporting only the fundamental modes is larger than the obtained value d, which can be used as the lowest estimate.

Fig. 5 shows the dispersion diagram, which is the dependence of the angular frequency ω on the component of the wave-vector parallel to the slab $|\mathbf{k}_{||}|$, of the dielectric slab waveguide. Both ω and $|\mathbf{k}_{||}|$ are given in units normalized to the slab thickness d. The slab behaves identically for

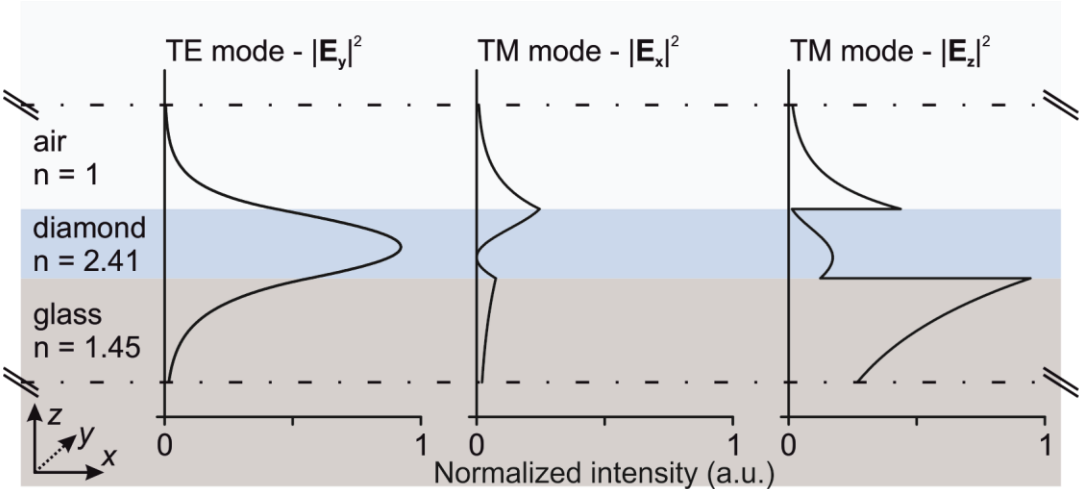

Figure 4: Profile of the intensity of the fundamental TE and TM modes (vacuum wavelength 650 nm; moving towards positive x direction) supported by thin (100 nm) diamond layer deposited on glass. TE mode has one non-zero component (E_y), while TM mode has two non-zero components (E_x and E_z) for the modes propagating in x-direction. The modes were simulated using online mode solver in dielectric waveguides OMS [35]. Dash-and-dot lines show the edge of the simulation domain.

the identical ratio between the slab thickness and frequency (wavelength) of light, when the material dispersion is neglected. The dispersion diagram is usually used to analyze photonic structures.

There are three parts of the dispersion diagram of a dielectric slab. The blue part is the escape cone where light can propagate freely through the slab and into air. The area of escape cone is limited by the light line in air $|\mathbf{k}_{||}| = k_0 = \omega/c$, which corresponds to light propagating under the critical angle for the total internal reflection inside the slab. The white part is the region of guided modes. Only a discrete set of frequencies is allowed for a given $k_{||}$. A modal effective refractive index N_{eff} can be defined for each mode as

$$N_{eff} = \frac{|\mathbf{k}_{||}|}{k_0} < n_s \tag{1.14}$$

The modal effective refractive index is the weighted average of the refractive indices of the slab and the surrounding with the contribution of individual materials based on the ratio of energy of the mode that is spreading in the respective material. In the last part of the dispersion diagram (yellow) no light can exist because this part lies below the light line in the dielectric medium (diamond) given by $|\mathbf{k}_{||}| = n_s\omega/c$.

The number of modes is increasing with the growing thickness of the slab or alternatively with the shorter wavelength of light. Dashed area in Fig. 5a denotes the part of the diagram with only fundamental modes. The structures that we use in this work belong mostly in this area. Nevertheless, very thin structures have modes with the majority of the field localized outside of the dielectric slab (Fig. 5b, red curve). The fraction of energy that is localized in the structure is very small, which weakens the effects of the photonic structures on the mode and also decrease the fraction of light being emitted into such mode. Therefore, we were mainly interested in structures with thickness slightly below the multimode regime.

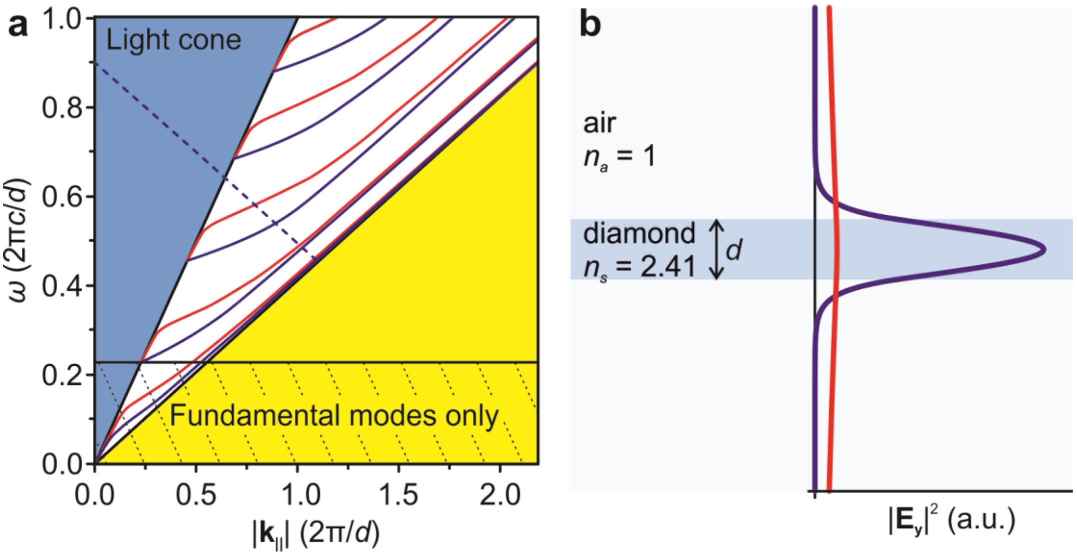

Figure 5: **(a)** Dispersion diagram, dependence of angular frequency (*ω*) on the magnitude of in-plane part of k-vector (|$\mathbf{k}_{||}$|), for symmetric slab waveguide with thickness *d* – diamond layer in air. The blue area is the escape cone. White area corresponds to the region with guided modes: TE and TM mode are denoted with blue and red color, respectively. Blue dashed line illustrates the band-folding of the TE_0 mode caused by Bragg diffraction grating. The yellow area lies below the light line in diamond. **(b)** Illustration of a symmetric structure. Profile of the fundamental TE mode for weak guiding (red; d/λ_0 ratio 1/40; bottom of the "Fundamental modes only" dashed area in (a)) and strong guiding (blue; d/λ_0 ratio 1/4.4 – top of the "Fundamental modes only" area). The modes were simulated using the online mode solver in dielectric waveguides OMS [35].

The emitters that are localized inside the layer may emit light via two output channels: into the radiative modes, which means that the light is radiated directly to the space (air/substrate), and into the guided modes. Since, the substrate has higher index of refraction than air, part of the radiative modes can be radiated only into the substrate. These modes are sometimes referred to as substrate modes. Commonly, only the light emitted directly into air is used for detection/imaging. The radiative modes emitted towards the substrate may be reflected back into air by placing a reflector at the back side of the substrate. The light coupled to the guided modes may be eventually collected at the edges of the device. Nevertheless, it must travel a long distance inside the medium and the probability of reabsorption is increased.

The distribution of light between the radiative and guided modes depends on the orientation of emitters, on the thickness of the layer (with regard to the wavelength), and on the position of the emitter inside the layer. The coupling to the individual modes depends on the local density of photon states (LDOS), which is the density of states (DOS) in the position of the emitter (see the section *1.2.1 Fermi's golden rule*), and which is continuous in $\mathbf{k}_{||}$ for radiative modes while only discrete set of $\mathbf{k}_{||}$ is allowed for guided modes for a given frequency (Fig. 5a). The LDOS of guided modes in the place of emitter is proportional to the distribution of the electric field of the modes (Fig. 4) and is also polarization dependent. For instance, light emitted by vertically oriented dipole source cannot be coupled to the TE modes, or light emitted by the horizontally oriented dipole in the middle of the layer (for symmetric structure) cannot couple to the fundamental TM mode that has a zero field in that place. There is an optimal thickness (normalized to wavelength) of the layer for maximized coupling to the TE_0 mode, which roughly corresponds to the top of the "Fundamental modes only" area in Fig. 5a. In a thinner waveguide, the energy of the TE_0 mode is localized mostly out of the waveguide (Fig. 5b, red) and the DOS is decreased. This decreases the probability of the emission into the guided modes

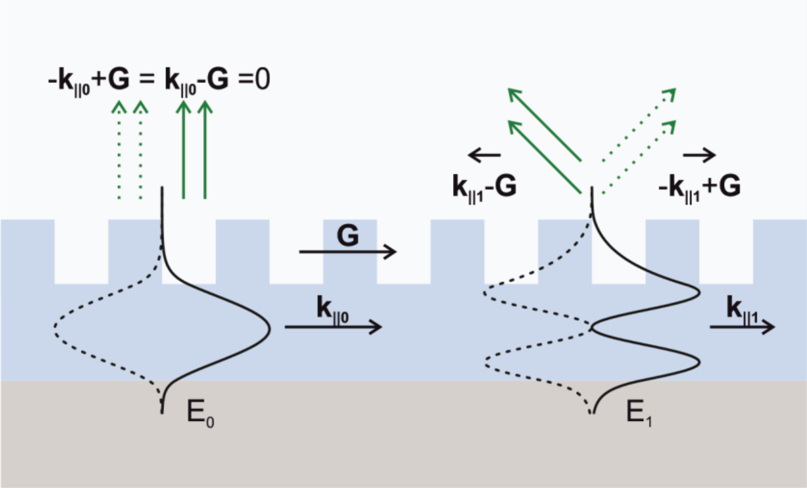

Figure 6: Schematic of the Bragg diffraction of fundamental (E_0) and first order (E_1) TE modes on a patterned dielectric layer with reciprocal lattice vector **G**. Spatial profile of modes propagating in opposite direction are denoted with black dashed lines. The modes are extracted into angles defined by the Bragg diffraction condition (green arrows; dashed for contribution from counter-propagating modes). For the particular case of diffraction into vertical direction the counter-propagating modes are extracted into the same direction.

and light is preferentially emitted into radiative modes. On the other hand, the mode is more spatially spread out also for thicker waveguides, because the waveguides themselves are extended over larger space, and the LDOS is decreased again. Moreover, light can be coupled also to higher order modes in thick structures. Note, that the TM_0 mode is usually present in the structure with the optimal thickness for the TE_0 mode [18].

There are two approaches how to redirect the light, initially coupled to the guided modes, into air. The first approach is to make the surface of the layer rough as was already discussed. The second method lies in the introduction of periodic diffractive elements. The basic example is a 1-D grating fabricated on the surface of the waveguide. The light emitted in the layer is diffracted on each period of the grating out of the structure and the propagation direction is given by the constructive interference between waves diffracted on each period (Fig. 6) – Bragg diffraction. Note, that the Bragg diffraction efficiency of the individual guided modes depends on the overlap between the modes and the diffracting structure, respectively. Light coupled to different modes is thus diffracted with different efficiency.

The direction of propagation of the diffracted light depends on the relation between the wavelength (wave-vector) of light and the reciprocal lattice vector (given by the lattice constant) of the grating. The in-plane wave-vector $\mathbf{k}_{||}$ of the radiative modes fulfills the condition

$$|\mathbf{k}_{||}| < k_0 = \frac{2\pi}{\lambda_0} \tag{1.15}$$

On the other hand, the in-plane wave-vector of guided modes is larger than this limit and the light is trapped inside the layer (Fig. 5a). The Bragg diffraction on the grating causes that the in-plane wave-vector of guided modes is changed by integral multiple of the reciprocal lattice vector ***G*** of the grating:

$$\mathbf{k}_{\mathbf{d}||} = \mathbf{k}_{\mathbf{i}||} + m\mathbf{G} \tag{1.16}$$

where $\mathbf{k}_{\mathbf{i}||}$ and $\mathbf{k}_{\mathbf{d}||}$ are the in-plane wave-vectors before and after diffraction, respectively, and m is an integer. If the condition (1.15) is fulfilled for the wave-vector after diffraction, light is diffracted out of the layer into space (Fig. 6).

The angle of Bragg diffraction for a given grating depends on the wavelength of light. Thus, the grating may be used to separate individual wavelengths. Nevertheless, for a spectrally narrow light sources (such as SiV centers in diamond), the structure may be optimized to diffract the light into a selected direction (or a set of directions). The preferred angle of Bragg diffraction for applications is the vertical direction, which occurs for $|\mathbf{k}_{\mathbf{d}||}| = 0$. At the vertical direction, the extracted light can be easily collected via simple optics. Furthermore, the vertically extracted mode is two-fold degenerate due to the fact that two counter-propagating modes contribute to the extraction into the vertical direction as sketched in Fig. 6.

The Bragg diffraction corresponds to folding of the guided modes at some point of the dispersion diagram (as schematically illustrated in Fig. 5a for the fundamental TE mode) and their subsequent intersection with the escape cone. The simple case of the 1-D grating was introduced here to present the basic idea of light extraction from thin layers. For practical realization of light extraction, structures with 2-D periodicity over the surface are more efficient. These structures will be described in the second chapter devoted to the PhCs.

1.2 Radiative rate enhancement

The second method for enhancing the light intensity collected from the light source is to directly enhance the number of photons emitted from individual emitters, and ideally to force the emitters to emit photons into some preferred direction for their easy collection in the same time. The simplest elemental light source has the form of oscillating electric dipole, which has toroidal radiation pattern in the far-field (Fig. 7). Higher multipoles (magnetic dipole, electric quadrupole etc.) have significantly lower transition rates and are not considered here. In typical light sources, there are many elemental dipoles with random orientation and the resulting radiation pattern is Lambertian. Nevertheless, the dipoles may be also oriented along one or more significant directions (for example in crystals) and their ordered orientation may influence the resulting radiation pattern. Another specific case is a light source consisting of only one elemental source that can be used for generation of single photons.

1.2.1 Fermi's golden rule

The interaction of light with matter on the scale of individual emitters cannot be treated classically, and quantum approach must be used. The time-dependent perturbation theory can be used to derive the radiative rates, where the quantum system is perturbed by the presence of electromagnetic radiation [39]. The probability of the radiative transition of electron between the initial and final state is given by Fermi's golden rule [39,15]

$$\Gamma_{i\to f} = \frac{(2\pi)^2}{h} \overbrace{|\langle f|V_s|i\rangle|^2}^{A} \overbrace{g(h\nu)}^{B} \tag{1.17}$$

where V_s is the perturbed Hamiltonian of the system, i, f denotes the initial and final state, $g(h\nu)$ is the local density of final photon states in the place of the emitter for light with frequency ν,

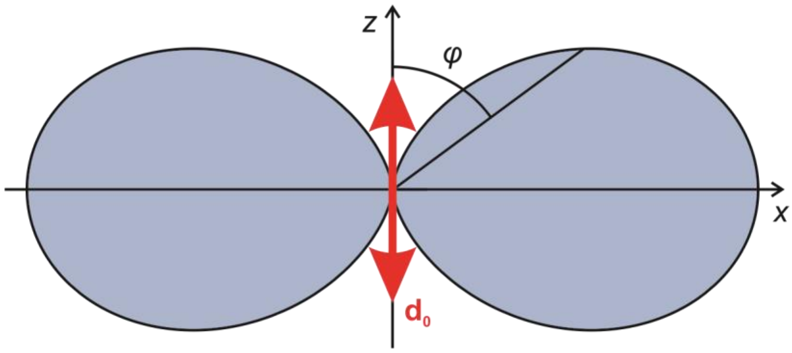

Figure 7: Cross-section (x-z plane) of the far-field radiation pattern of a dipole source with electric dipole moment $\mathbf{d_0}$. The intensity is proportional to $\sin^2\varphi$, with φ being the angle with respect to the axis of the dipole moment, and rotationally symmetric around the axis of dipole (z axis).

and h is the Planck constant. The factor A quantifies the perturbation of the quantum system by electromagnetic field, and it is proportional to the electric dipole moment of the transition $\mathbf{d_{if}}$ for fluorescence. The transition dipole moment describes the strength of transition between the two states. Transition dipole moment is specific for each quantum system and equals zero for the transitions forbidden by the selection rules. In such case the system is forced to transit via higher multipoles and the decay rate is slower by few orders of magnitude (resulting in phosphorescence). Factor A may be influenced by the neighborhood of the system, e.g. by defects in the crystalline material. Material stress (e.g. in nanoparticles) may lift some of the bulk material symmetries and allow the transitions that are forbidden in bulk material with low stress, which leads to a significant reduction of lifetime. For instance, the transition from a shelving state in SiV centers is allowed for nanodiamonds due to stress [40]. Nevertheless, we have not attempted to influence the factor A in this work. Our effort was to use material with optimal optical properties, which involves reduced stress (where possible) and limited concentration of undesired impurities.

We focus on the factor B (density of photon states) in Eq. 1.17 and its use to enhance or attenuate the count-rate and to improve the directionality of the optical emission. In free space, the DOS is proportional to the square of frequency ν^2 and the emission is not directed into any specific direction and follows the dipole radiation pattern (Fig. 7). Usually, more transitions exist, by which the electron can transit from the higher to lower energy state, and which differs in the energy of emitted photons $h\nu$. By selectively increasing the DOS for one of the radiative transitions, the count-rate of such transition may be enhanced at the expense of the count-rates (decay rates) of the other radiative or non-radiative transitions. Both quantum efficiency and radiative branching ratio (fraction of photons emitted via the chosen transition) are increased in such case. Even in the case of only one possible transition, the count-rate is increased due to the reduced lifetime that the electron spends in the excited state. The DOS may also be increased/decreased only for some directions. The radiation pattern then deviates from the dipole radiation pattern. This can be used to improve collection efficiency.

A placement of emitters into thin dielectric slab, which was already discussed, may alter the LDOS and improve/reduce the coupling into the guided modes of the slab and the total radiation rate. However, it is not possible to significantly enhance selected transitions with such simple structure. The significant enhancement of a DOS for a narrow energy (frequency) bandwidth may be achieved by confining the emitter into an optical cavity.

1.2.2 Purcell effect in cavities

The simplest type of cavity is a Fabry-Perot resonator that is composed of two mirrors (Fig. 8a). Such a cavity supports a set of optical modes (resonances) in the form of standing waves with frequencies given by the optical distance between the mirrors (cavity length). The frequency distance between the individual modes is denoted as a free spectral range and depends directly on the cavity length. The mode bandwidth, usually characterized by its full width at half maximum (FWHM), depends on the optical losses in the cavity. The higher the optical losses in the cavity are, the broader are the modes of the cavity (Fig. 8b).

There are two parameters that describe the performance of the cavity. The first one is the finesse F that compares the mode linewidth $\varDelta\nu_r$ with the free spectral range $\varDelta\nu_{FSR}$

$$F = \frac{\varDelta\nu_{FSR}}{\varDelta\nu_r} = \frac{\pi}{2\arcsin\left(\frac{1-\sqrt{1-l_{rt}}}{2\sqrt[4]{1-l_{rt}}}\right)} \approx \frac{2\pi}{l_{rt}} \tag{1.18}$$

The finesse is directly related to the total round-trip losses l_{rt} of the cavity where the approximation is valid for cavities with low losses ($l_{rt} < 10\%$). The finesse expresses the average number of photon roundtrips before a photon leaves the cavity or is lost via dissipation. Therefore, the finesse does not explicitly depend on the cavity length (the loss occurs usually on cavity mirrors in Fabry-Perot cavities). Nevertheless, the optical losses may depend on the cavity length, e.g. when the beam diameter on the mirrors is changed with the length of the cavity or when the medium inside the cavity is absorbing or scattering. The losses usually depend on the frequency of light, and the maximal finesse is achieved only for one cavity mode.

The second parameter describing the cavity performance is the quality factor (Q-factor) that compares the mode linewidth with the frequency of the cavity mode ν_r and also quantifies the losses of the cavity in one (optical) cycle

$$Q = \frac{\nu_r}{\varDelta\nu_r} = 2\pi\frac{E}{\Delta E} \tag{1.19}$$

where ΔE is the energy lost in one optical cycle when there is total energy E stored in the resonator. The Q-factor describe the temporal confinement of the light inside cavity, and it thus grows with the increasing cavity length, because most of the light is lost on the mirrors in the case of FP cavities. The Q-factor is the number of optical cycles (in radians) before the energy in resonator drops to 1/e of the initial value or equivalently the average number of optical cycles after which a single photon is lost from the cavity. It is advantageous in some cases to separate the total Q-factor into more contributions based on the mechanism of optical losses. For instance, cavity losses may be caused by losses on the cavity mirrors, and absorption and scattering in a material. The total Q-factor is then

$$\frac{1}{Q} = \frac{1}{Q_{mir}} + \frac{1}{Q_{abs}} + \frac{1}{Q_{scat}} \tag{1.20}$$

where Q_{mir}, Q_{abs}, and Q_{stat} is the Q-factor with only mirror losses, absorption losses, and scattering losses considered, respectively. This approach is often used for design of PhC cavities.

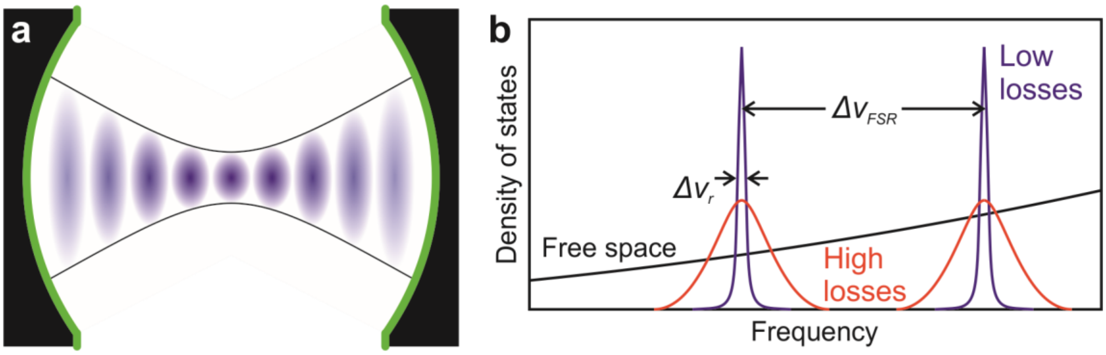

Figure 8: **(a)** Schematic picture of Fabry-Perot cavity and the field of a mode (blue). **(b)** Schematic dependence of the DOS on frequency of light. The DOS is proportional to the square of frequency ν^2 in free space, whereas the LDOS is significantly increased for narrow frequency ranges inside cavities. The lower are the round-trip losses inside cavity, the narrower is the spectral linewidth $\Delta\nu_r$ of modes and the higher is the LDOS. The free spectral range $\Delta\nu_{FSR}$ remains constant.

The LDOS inside the cavity is increased (Fig. 8b) in comparison with a free space, which may be used for radiative rate enhancement. The effect of the cavity on the emitter count-rate is described by the Purcell factor [41]

$$F_P = \frac{3}{4\pi^2}\left(\frac{\lambda_0}{n}\right)^3\left(\frac{Q}{V_{eff}}\right) \tag{1.21}$$

where λ_0 is the wavelength of light in vacuum, n refractive index of the medium, and V_{eff} the effective volume of the cavity mode. The effective cavity volume quantifies the spatial confinement of the cavity mode and is defined by the formula [42]

$$V_{eff} = \int_V \frac{\varepsilon(\mathbf{r})|\mathbf{E}(\mathbf{r})|^2}{\varepsilon(\mathbf{r_c})|\mathbf{E}(\mathbf{r_c})|^2}\,d\mathbf{r} \tag{1.21}$$

where ε is the relative permittivity, $\mathbf{E}$ electric field strength, and $\mathbf{r}_\mathbf{c}$ is the position with maximum electric field strength (antinode). The Purcell factor is the maximal achievable ratio of the decay rate of the emitter placed inside the cavity with regard to the emitter placed in a homogeneous medium. Nevertheless, the actual enhancement of the emitter decay rate depends on the exact position and orientation of the emitter inside cavity. Moreover, there must be spectral overlap between cavity mode and the transition that is being enhanced. The total decay rate for an individual emitter inside cavity can be thus written as [43]

$$\Gamma_c = F_P \overbrace{\left(\frac{\mathbf{E}(\mathbf{r_e})\cdot\mathbf{d}_{ij}}{|\mathbf{E}(\mathbf{r_c})||\mathbf{d}_{ij}|}\right)^2}^{A} \overbrace{\frac{\varepsilon(\mathbf{r_e})|\mathbf{E}(\mathbf{r_e})|^2}{\varepsilon(\mathbf{r_c})|\mathbf{E}(\mathbf{r_c})|^2}}^{B} \overbrace{\frac{\nu^2\Delta\nu_r^2}{\nu^2\Delta\nu_r^2 + 4(\nu_r^2 - \nu\nu_r)^2}}^{C}\Gamma_0 \tag{1.23}$$

where $\mathbf{d}_{\mathbf{ij}}$ is the emitter dipole moment for the radiative transition, $\mathbf{r}_\mathbf{e}$ the emitter position, ν the emitter frequency, ν_r and $\Delta\nu_r$ the frequency of mode and its bandwidth, and Γ_0 the decay rate of the emitter in a homogeneous medium. We suppose in (1.23) that the transition linewidth is much smaller than the cavity mode linewidth ($\Delta\nu << \Delta\nu_r$). The factors *A*, *B*, and *C* quantify the effects of alignment of the emitter dipole moment with regard to the electric field of the cavity mode, of the electric field strength in the place of the emitter with regard to a place with maximum electric field, and the spectral detuning from the cavity resonance, respectively. In order to maximize the decay rate, following conditions must be fulfilled: (1) the cavity *Q*-factor must be maximized (reduced optical losses), (2) V_{eff} must be minimized, (3) frequency of the cavity mode must overlap with the frequency of the transition, and (4) emitter must be in the position of largest electric field of the cavity (e.g. beam waist or Fabry-Perot cavities; center of the cavity in Fig. 8) and oriented parallel to that field.

The volume of the cavity may be decreased by decreasing the distance of mirrors in standard Fabry-Perot cavity configuration [44]. Nevertheless, the radius of curvature of mirrors must be decreased accordingly to reduce the transversal extent of the mode. The fabrication of mirrors with small radius of curvature and low optical losses is not trivial [45–49].

In order to further reduce the cavity volume, other cavity configurations [50,51], such as micro-pillar [52,53], micro-disk [54,55], micro-sphere [56,57], nano-beam [43,58,59], or PhC cavities [60–63] were designed and fabricated (even in diamond). Despite having smaller volume than Fabry-Perot cavities, the different configurations bring new problems such as higher cavity losses, difficult tuneability, or the introduction of material strain, which changes the emitter properties.

Tab. 1 compares some key features of Fabry-Perot cavities and PhC cavities. The main advantages of Fabry-Perot cavities are easy configuration and spectral tunability by length modulation (e.g. by a piezo actuator), which may be used for cavity locking [64]. It is also an open system, and a thin slab or a nanoparticle may be inserted without the need of fabrication in the material itself. This might be important as fabrication may introduce defects and cause stress inside material that negatively affects the emitter properties. On the other hand, PhC cavities allow larger spatial confinement of the modes and low mechanical noise thanks to their monolithic architecture. A photonic band gap of the PhC cavity can be used to suppress undesired radiative transitions (e.g. in color centers phonon sideband). The properties of PhC cavities are further discussed in Section *2.2.3 Photonic crystal cavities*.

Tab. 1: Advantages of Fabry-Perot and PhC cavities

Fabry-Perot cavities	**2-D PhC cavities**
Open cavity	Very small volume
No material fabrication	No interface inside cavity
Easy tuning	Low mechanical noise
Directed emission	2-D Band gap

1.3 Single photon sources

The generation of single photons is of high importance for applications such as quantum communication or quantum information processing [65–68]. The ideal single photon source emits exactly one photon in one excitation cycle [69]. To differentiate the single photon source from other sources, the autocorrelation measurement can be performed. Whereas light with super-Poissonian distribution (photon bunching) is generated by thermal sources and light with Poissonian distribution (coherent light) by common lasers, the light with sub-Poissonian distribution (photon anti-bunching) is generated by single-photon sources (Fig. 9). The autocorrelation function can be measured by Hanbury Brown-Twiss interferometer consisting

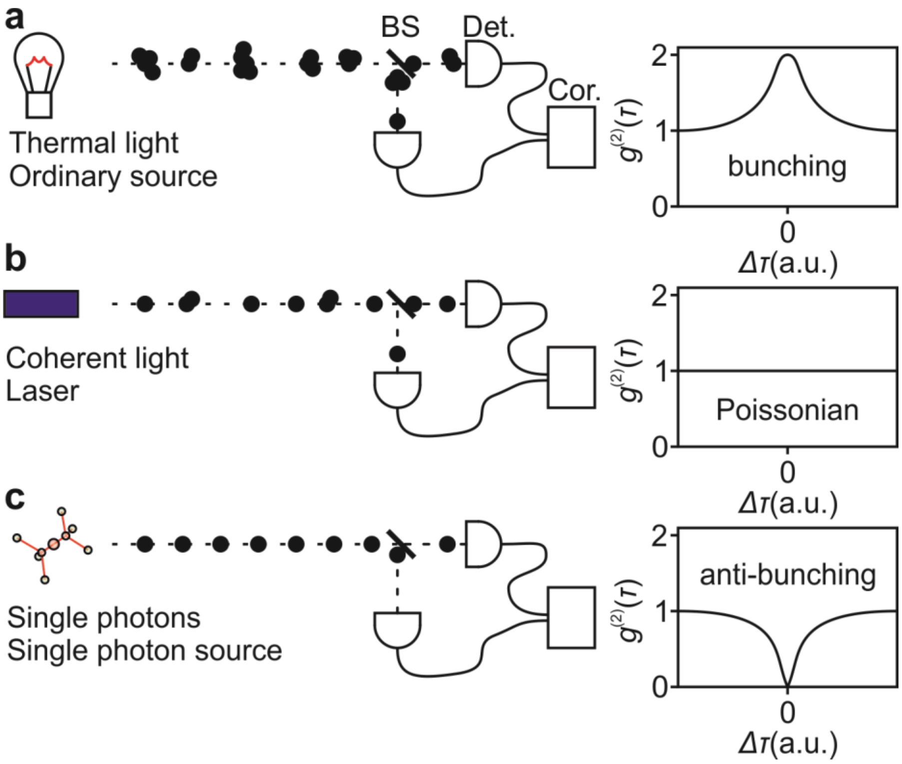

Figure 9: Schematic picture of light sources with different photon statistics: **(a)** super-Poissonian distribution of thermal source – bunching; **(b)** Poissonian distribution of ideal laser – coherent light; **(c)** sub-Poissonian distribution of single photon source – anti-bunching. BS – beam-splitter, Det. – detector, Cor. – time correlator that measures time between subsequent detections on the detectors. The right part shows the second order autocorrelation function ($g^{(2)}(\tau)$) as a function of the time delay ($\Delta\tau$) for the respective source.

of a beam-splitter and two detectors as illustrated in Fig. 9. The time interval between individual detections is measured. In the case of a pure single-photon source the probability of simultaneous detection by the two detectors is zero, which is manifested by a dip reaching zero in the autocorrelation function for zero time-delay (photon anti-bunching) [70].

Single isolated atoms or ions may be used as single photon emitters. Nevertheless, it is challenging (but not impossible [71]) to localize the isolated atoms/ions at a particular place with a given polarization of an atomic dipole in a cavity, so that the photons can be collected via cavity modes. The use of artificial atoms, such as isolated point defects in crystals (e.g. color centers in diamond) or quantum dots, is a more reliable way of generating single photons. These artificial atoms create spatially isolated and localized electronic states usually in the electronic band gap of the surrounding dielectric or semiconductor material. They can thus work as single-photon emitters with a given position in the solid material. The advantage of quantum dots lies in the possibility of tuning the emission wavelength by controlling the size of the quantum dots. On the other hand, it is challenging to fabricate quantum dots with identical properties, which hinders their use in quantum networks. In contrast, isolated point defects of the same type in chemically pure crystals are indistinguishable from each other. Moreover, various defect centers, e.g. in diamond [72] or silicon carbide [73,74], emit light in different regions of the visible and near infra-red spectra, and suitable sources can be found for a given application.

Collecting photons emitted by single photon sources localized in a solid material is non-trivial for the reasons described above, i.e. the photons are not directed into any significant direction and there are reflections on the materials boundary. There are multiple ways to increase the collection efficiency.

Firstly, by preparing the centers in nanoparticles smaller than the wavelength of light the Fresnel reflections at the boundary may be prevented [72,75]. This approach is based on the fact that light cannot be confined in particles that are smaller than its wavelength. The extraction efficiency is thus significantly increased over the bulk diamond. Placement of nanoparticles into given locations may simplify efficient light collection. The disadvantage of this method lies in the localization of single photon emitters near the surface of the nanoparticle. This may cause the enhanced count-rate on one hand, but can also lead to higher non-radiative transition probability, emission line broadening, coherence times reduction, and causes deviations between individual emitters placed in different nanocrystals [69].

Secondly, the emitted light may be re-directed into some preferred direction. For this purpose, diffraction gratings for thin layers or solid immersion lenses [76] for bulk material can be used. The collection efficiency is, however, smaller in comparison with the other approaches.

Thirdly, optical cavities may be used to improve the collection efficiency of single photons. The optical cavities not-only force the emitter to emit light into the cavity mode, but also enhance the photon count-rate and improve the quantum efficiency as discussed in the previous chapter. A special property of the optical cavities is that they enhance the interaction between light and matter at single-photon level [65]. Cavities can be thus used also to excite defects by single photons. The probability of such excitation without the use of cavity is negligible because the interaction cross-section of photons with single emitters is very low. Cavities with embedded single photon emitters are thus considered as building blocks for the quantum networks.

2. Photonic crystals

In analogy to solid state physics, where a periodic arrangement of atoms or molecules in a crystal lattice affects the motion of electrons, the photonic crystals (PhCs) have periodically modulated index of refraction which affects the propagation of photons [77]. In order to interact with light, the characteristic length scale of PhC unit cell must be of the order of the wavelength inside the material. Analogously to solid state physics, the periodic modulation of refractive index alters the local density of photon states (LDOS) inside the PhCs due to diffraction of light on individual periods. This leads to various interesting phenomena such as formation of photonic band gaps (frequency regions with no photonic states), or inversely increased LDOS for some frequencies. PhCs have several applications such as light guiding, spontaneous emission rate attenuation/enhancement in accordance with Fermi's golden rule, or Bragg diffraction of light into defined direction.

2.1 Basic properties and dimensionality

The propagation of light in PhCs may be derived from Maxwell's equations [78]. The derivation, which is described in Ref. [77] in detail, leads to the master equation for propagation of light in heterogeneous dielectric medium

$$\nabla \times \left(\frac{1}{\varepsilon(\mathbf{r})} \nabla \times \mathbf{H}(\mathbf{r}) \right) = \left(\frac{\omega}{c} \right)^2 \mathbf{H}(\mathbf{r}) \tag{2.1}$$

where **r** is the spatial coordinate, ε heterogeneous dielectric function, **H** macroscopic magnetic field (which is used to describe the complete electromagnetic field), ω angular frequency and c speed of light. The macroscopic electric field **E** can be found from the **H** field

$$\mathbf{E}(\mathbf{r}) = \frac{i}{\omega \varepsilon_0 \varepsilon(\mathbf{r})} \nabla \times \mathbf{H}(\mathbf{r}) \tag{2.2}$$

As well as Maxwell's equations, the master equation (2.1) is scale invariant. This means that when all distances in PhC are expanded or contracted by the same amount the PhC properties remain unchanged – only the mode profile and frequency (wavelength) of light will be rescaled appropriately

$$\epsilon'(\mathbf{r}) = \epsilon(\mathbf{r}/s) \; \rightarrow \; \mathbf{H}'(\mathbf{r}) = \mathbf{H}(\mathbf{r}/s) \text{ and } \omega' = \omega/s \tag{2.3}$$

where s is the scaling parameter, and **r** the position vector. This has important consequences for designing or simulating PhC structures. Structures with ideal properties, e.g. largest photonic band gap, may be found first for an arbitrary frequency (frequency normalized with regard to the period of PhC) and subsequently the band gap can be shifted to desired spectral position by simple rescaling of the physical dimensions. Similarly, there is no fundamental value of the dielectric constant and scaling of the dielectric constant leads to the scaling of frequencies while the field patterns remains unchanged:

$$\epsilon'(\mathbf{r}) = \epsilon(\mathbf{r})/s^2 \; \rightarrow \; \mathbf{H}'(\mathbf{r}) = \mathbf{H}(\mathbf{r}) \text{ and } \omega' = s\omega \tag{2.4}$$

Note, that the relation between **E** and **H** field Eq. 2.2 is changed in this case since it depends explicitly on ε. Also note that Eq. 2.4 requires the change of dielectric constant in the whole structure, which may not be possible in many practical cases, where air is used as one of the mediums and its dielectric constant cannot be altered.

By solving the master equation (2.1), its eigenvalues (frequencies ω) and eigenvectors (spatial profiles of the electromagnetic modes $\mathbf{H}(\mathbf{r})$ corresponding to the frequencies ω) can be found. The solution of the master equation in a medium with discrete translational symmetry, which can be described by the equation $\varepsilon(\mathbf{r}) = \varepsilon(\mathbf{r} + \mathbf{R})$ (i.e. PhC with lattice vectors $\mathbf{R}$), are Bloch states:

$$\mathbf{H}_{\mathbf{k}}(\mathbf{r}) = e^{i\mathbf{k}\cdot\mathbf{r}}\mathbf{u}_{\mathbf{k}}(\mathbf{r}) \tag{2.5}$$

where $\mathbf{k}$ is the wave-vector and $\mathbf{u}_{\mathbf{k}}(\mathbf{r}) = \mathbf{u}_{\mathbf{k}}(\mathbf{r} + \mathbf{R})$ is a periodic function with the same periodicity as is the periodicity of the PhC. The solution has a form of a plane wave multiplied by periodic function with the periodicity $\mathbf{R}$.

2.1.1 One-dimensional photonic crystals

The simplest case of PhC is similar to a Bragg mirror (distributed Bragg reflector) – periodic arrangement of dielectric layers with different dielectric constant (refractive index, see Fig. 10). Such structures are known for more than one hundred years, when they were studied by Lord Rayleigh [79]. This simple structure is ideal for demonstration of the basic concepts of PhCs. Nevertheless, it is also of practical importance for fabrication of highly reflective mirrors, e.g. for assembling Fabry-Perot cavities (as in one part of this work).

The light incident on the material with 1-D periodicity is partially reflected on each boundary between the two materials. There is a constructive interference between the light waves reflected from individual boundaries for certain frequencies, and the intensity of the transmitted light decreases exponentially with each period in such case. The total transmittivity reaches hypothetically zero for an endless structure. The periodic arrangement of layers thus suppresses the propagation of light within certain frequency range through the structure in the near to perpendicular direction with respect to the orientation of the layers. The frequency range is referred to as a photonic band gap in analogy to solid state physics.

A point-of-view analogous to solid state physics can be also used to derive the properties of the periodic structures. The propagation of light in 1-D PhC may be represented using dispersion diagram (Fig. 11). The dispersion diagram in a homogeneous medium consists of straight lines (when material dispersion is neglected for simplicity, blue line in Fig. 11a). When an artificial periodicity is introduced into the structure, i.e. the structure is considered as periodic, but every layer has the same refractive index so far, the dispersion diagram become periodic in k-space (Fig. 11a, red dashed lines). This property arises from Eq. 2.4, which implies that the electromagnetic field follows the periodicity of the structure. Subsequently, all information about the light propagation is already contained in one period of the dispersion diagram, which is duplicated for larger wave-vectors. Usually the period around zero wave-vector, which is called (first) Brillouin zone, is shown. The dispersion diagram of periodic structures is often called a photonic band diagram in analogy to solid states physics.

Finally, if a sufficiently large refractive index change is introduced and propagation of light in normal direction with respect to the orientation of layers is considered, the dispersion bands are bent, and the photonic band gap opens at the edge of the Brillouin zone (Fig. 11b) [77]. The band gap arises due to the periodic distribution of electric field in the periodic medium in

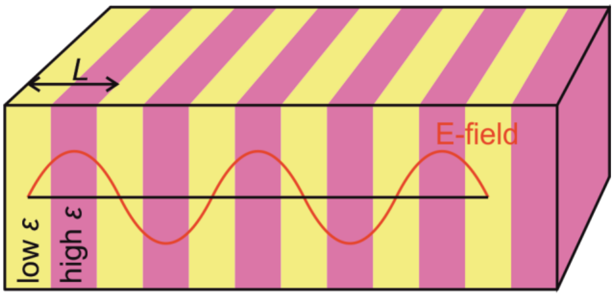

Figure 10: Schematic picture of 1-D PhC composed of stacked uniform layers with different dielectric constants *ε*. Red line shows the electric field profile of the dielectric band at the edge of the first Brillouin zone.

accordance with Eq. 2.4. The bands at the edge of Brillouin zone have the same periodicity but they differ in the localization of the electric field. The electric field of the band below the band gap is localized primarily in the dielectric medium with higher index of refraction (see Fig. 10), which decreases its frequency. This band is therefore referred to as dielectric band. On the other hand, the band above the band gap has larger fraction of the electric field (in comparison with dielectric band) localized in the dielectric medium with lower refractive index and its frequency is higher. Since the medium with lower index of refraction is mostly air (especially in the case of PhCs with higher dimensionality), this band is called air band. Additional band gaps may open at higher frequencies at the crossings of bands.

Inside the photonic band gaps, the LDOS is zero for the direction normal to the planes of the PhC. Light with the frequency lying in the band-gap cannot propagate into the structure and the structure thus works as a perfect reflector. However, the evanescent tail of the incident wave

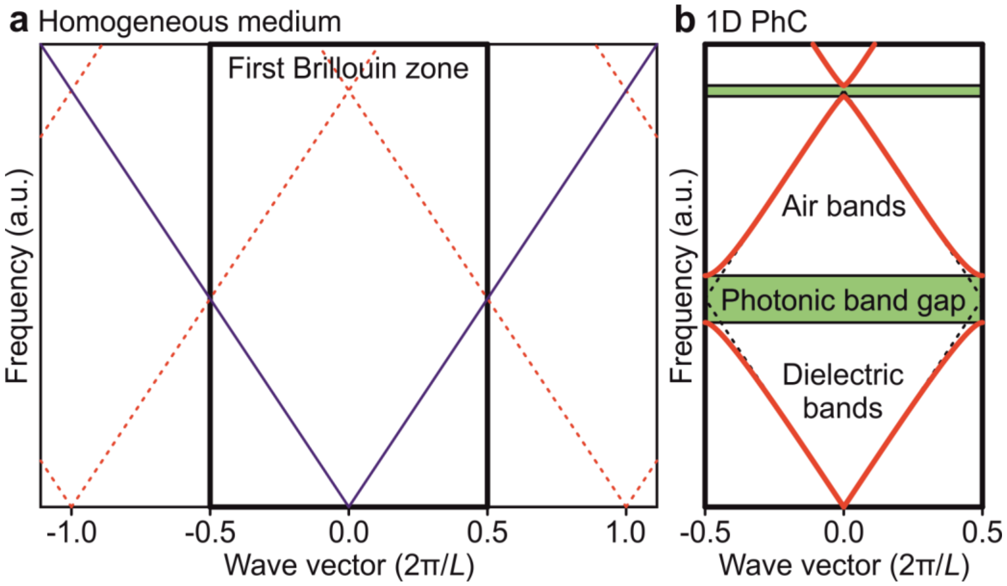

Figure 11: **(a)** Schematic dispersion diagram for homogeneous medium (blue line, material dispersion is neglected). In periodic medium and propagation in the direction of the periodicity, the dispersion diagram becomes periodic in k-space (with period 2π/*L*, where *L* is the lattice constant in real-space) and all relevant information is contained in the first period – the Brillouin zone. The bands (red dashed line) are folded on the edge of the Brillouin zone. **(b)** When the refractive index change is introduced the bands are bent and the band gap opens at the edge of Brillouin zone and at the band crossings.

extends into the structure, and when we limit the number of layers, a small part of the energy may be transferred. An emitter that emits light inside the photonic band gap and that is placed into the 1-D PhC is forced not to radiate light in the direction normal to the planes. However, the DOS in other directions is not significantly altered and thus this simple structure is not suitable for directing light or enhancing the count-rate. There are two ways how to modify the 1-D structure in order to achieve such properties. The first way consists in the introduction of a defect in the 1-D PhC, which may be achieved for example by extending the width of one layer or changing the refractive index of one material in one period. Subsequently, the defect states appear inside the band gap [77]. Due to the very narrow frequency bandwidth of these states, the LDOS inside the defect can be significantly higher than the DOS of free space. In fact, these structures are nothing else than Fabry-Perot cavities that were already described in Section 1.2.2. The other possibility how to obtain more useful properties is to extend the periodicity into more dimensions. Subsequently, the DOS is altered for a plane or even for a whole space and the emission and propagation of light may be controlled.

2.1.2 Multi-dimensional photonic crystals

The idea of extending the dimensionality of periodic structures was first proposed by Yablonovitch [80] and John [81] in 1987. 2-D PhCs are periodic along two axes and homogeneous along the third axis (Fig. 12). 3-D PhCs are then periodic along all three axes. Originally, the structures were proposed to suppress spontaneous emission into unwanted directions in laser resonators and thus to increase the efficiency of lasers. Nevertheless, the application spectrum was soon expanded into many other areas with PhCs being currently used or proposed as parts of light sources [24,29], spectral filters and couplers [82], waveguides [83] or solar cells [84–86].

We will not discuss the properties of the 3-D PhCs here (the reader is referred to the Ref. [77]). Although they allow to confine light in all three directions, they are challenging to fabricate, and they were not studied in this work. Strictly speaking, neither 2-D PhCs, which are homogeneous in z direction (Fig. 12) and endlessly tall (i.e. much taller than their lattice constant in real applications) were studied in this thesis. Nevertheless, structures studied in this thesis have many similarities with the 2-D PhCs and therefore we will briefly discuss their properties.

The physics of PhCs with the 2-D dimensionality can be also described by the master equation (2.1) and the modes have a form of Bloch waves (2.4). However, the results are much more complex than in the 1-D case for several reasons:

Firstly, the propagation of light in the 2-D PhC depends on its polarization. The modes that propagate in the plane of periodicity (x-y plane in Fig. 12) can be separated into the TE and TM modes, which have the magnetic field and the electric field oriented perpendicularly to the plane of periodicity, respectively. The frequency of bands differs for TE and TM modes. Although some 2-D PhCs have a photonic band gap for both polarizations at some frequency range, usually band gaps exist only for one polarization in the given PhC structure.

Secondly, various lattice symmetries exist in 2-D. The most common lattice symmetries, which we also use in our work, are square and hexagonal (Fig. 12). Moreover, the columns may be formed either by material with high refractive index (mostly dielectric rods in air, Fig. 12a,b)

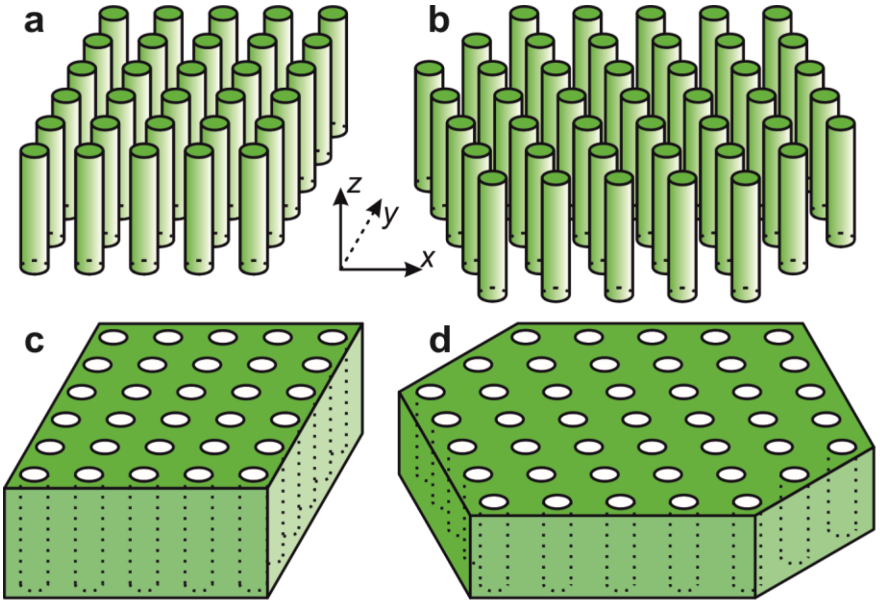

Figure 12: 2-D photonic crystals with various geometries. **(a)** and **(b)** PhCs composed of columns with high index of refraction, with square and hexagonal symmetry, respectively. **(c)** and **(d)** PhCs composed of cylindrical inclusions in a medium with higher index of refraction, with square and hexagonal symmetry, respectively. Note that the dimensions of 2-D PhCs extend to infinity in all directions.

or material with low refractive index (mostly air holes in dielectric, Fig. 12c,d). Note, that the cross-section of the columns does not have to be circular in principle.

Thirdly, the Brillouin zone is two dimensional for 2-D PhCs, which makes the illustration of the whole band diagram difficult. The 2-D PhCs have usually some other symmetries (rotation, mirror) in addition to the discrete translational symmetry. These symmetries are replicated in the Brillouin zone and as a result there are regions in the Brillouin zone related to each other. The part of the Brillouin zone reduced by the symmetries of PhC lattice is called irreducible Brillouin zone (see, e.g. the inset in Fig. 14b in the next section). The global minima and maxima of photonic bands almost always occur at the edges of the irreducible Brillouin zone. Hence the band diagram is usually visualized only for wave-vectors at the edges of the irreducible Brillouin zone (along the high-symmetry directions) where the band gap size may be easily seen.

2.1.3 2-D PhC slabs

The 2-D and 3-D PhCs offer better control over the propagation of light when compared to 1-D PhC structures. Nevertheless, the complexity of such structures makes their fabrication very challenging and expensive. On the other hand, PhC slabs represents relatively easy-to-fabricate structures, which retain many interesting properties of 2-D PhCs [87]. The fundamental difference from 2-D PhCs is the limited size in the direction perpendicular to the plane of the periodicity, which is usually in the range from dozens of nanometers to few micrometers. Thin dielectric layers can be deposited on a substrate by various methods such as CVD, MBE or MOVPE. Similarly, there are various methods for subsequent structuring of the thin layers: photolithography, electron beam lithography (EBL) [88], nanosphere lithography [89], and others [90–93], which will be discussed in chapter 4.

)

PhC slabs are often referred to as 2-D+1 structures because they consist of a dielectric or semiconductor slab with high refractive index (higher than the surrounding) and the 2-D periodic structure fabricated on the layer. The layer without PhC acts as a planar waveguide, where light propagates in the form of electromagnetic modes, which are confined in the layer due to the total internal reflection (see Section 1.1.3). The addition of the 2-D periodic structure allows (i) to change the LDOS in the layer, (ii) to manipulate the light propagation, and (iii) to efficiently diffract light from the layer.

There are three basic types of planar photonic structures that may be used to increase the count-rate and/or light extraction from sources in thin dielectric layers (Fig. 13): weak PhC slabs, strong PhC slabs, and PhC cavities, which will be discussed in the following sections in detail. The structures are composed of periodic patterns (mostly square or hexagonal) of dielectric or semiconductor columns, or air holes placed on top or etched into the planar slab. The use of other material than air is possible in principle. For example, the air can be substituted by water or other liquids, when the photonic structures are used for bio-sensing [94–96]. Nevertheless, the refractive index contrast is reduced in such case and the photonic effects are weakened.

In contrast to standard 2-D PhCs, the polarization of modes is generally not maintained for the PhC slabs due to the presence of a substrate. In vertically asymmetric structures, the TE and TM modes are coupled to each other and the energy can slowly leak from one type to the other. Note that all structures that are placed on a substrate are asymmetric because the field extends into the surrounding material (see Fig. 4 in Chapter 1). The modes can be still denoted as TE-like (even symmetry with respect to the plane in the middle of the structure) and TM-like (odd symmetry), because the energy leakage is slow. However, the losses caused by the leakage may be detrimental for some applications (like PhC waveguides or cavities).

The coupling between TE and TM modes can be completely suppressed by restoring the mirror symmetry in the vertical direction. This is usually done by etching of the substrate after the PhC slab fabrication, which leads to the formation of a suspended membrane (details in Chapter *4. Fabrication of photonic structures in diamond*). Other, less common way of making the structure symmetric is to place a material similar to the substrate on top of the structure [97]. It should be noted that the symmetry in the theoretically symmetric structures can be broken due to defects originating in the fabrication process, which also leads to the coupling between the TE and TM modes.

The PhC slabs, where the periodic layer does not extend through the whole layer (Fig. 13a), does not have any photonic band gap. These structures are denoted as weak PhC slabs and they can be used to diffract light out of the layer as the DOS is not significantly affected. The light is out-coupled into air utilizing the same mechanism (Bragg diffraction) as gratings that were already described in section 1.1.3. The advantage over the 1-D structures is that light propagating in more directions is extracted and the degeneracy at vertical direction (that corresponds to the Γ-point in band diagram) is higher (Fig. 14a). However, when the perturbation is increased over a certain level, the bands are bent and the degeneracy at the Γ-point is lifted.

PhC slabs may be also used to prevent the propagation of light within some frequency range (band gap) inside the slab (Fig. 14b). These structures are denoted as strong PhC slabs, because they have large modulation of refractive index, which significantly alters the DOS. Note that

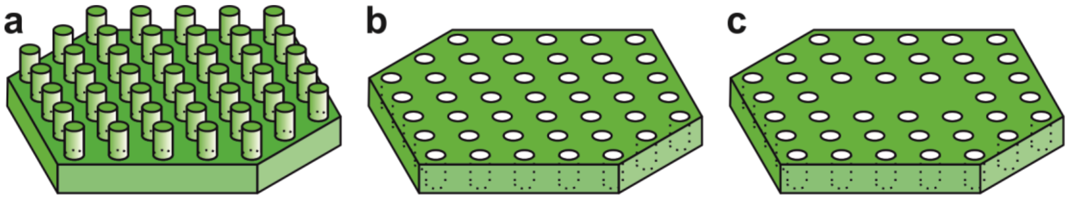

Figure 13: Three basic types of planar photonic structures that can be used for light extraction: **(a)** weak PhC slab; **(b)** strong PhC slab; and **(c)** PhC cavity.

the band gap is not complete which means that it only suppresses the propagation of guided modes, while the radiative modes are still supported (due to the existence of the escape cone, Fig. 14b). Moreover, the propagation is usually suppressed only for one polarization of modes (TE for structures with air holes in a slab) in a given frequency range. For asymmetric structures, the modes can couple to the other polarization and the band gap is lost in such case. The strong PhC slabs may be used to create resonators by introducing localized defects into the periodicity (Fig. 13c). These structures allow to confine light in all three directions similarly to the 3-D PhCs. Localized photonic states with high DOS are introduced into the band gap due to this defect, which increases the spontaneous emission rate from emitters placed inside such PhC cavity. The weak and strong PhC slabs are described in the next sections in more detail.

2.2 Weak PhC slabs

2-D PhC slabs in a weak regime are characterized by low perturbation, which results in negligible band bending, and therefore they don’t possess any band gap (Fig. 14a). The low perturbation may be achieved by choosing two materials with similar refractive indices. Nevertheless, weak PhC slabs are usually composed of a waveguide layer and a periodic photonic structure fabricated on the top of the layer (Fig. 13a). This arrangement effectively reduces the refractive index contrast.

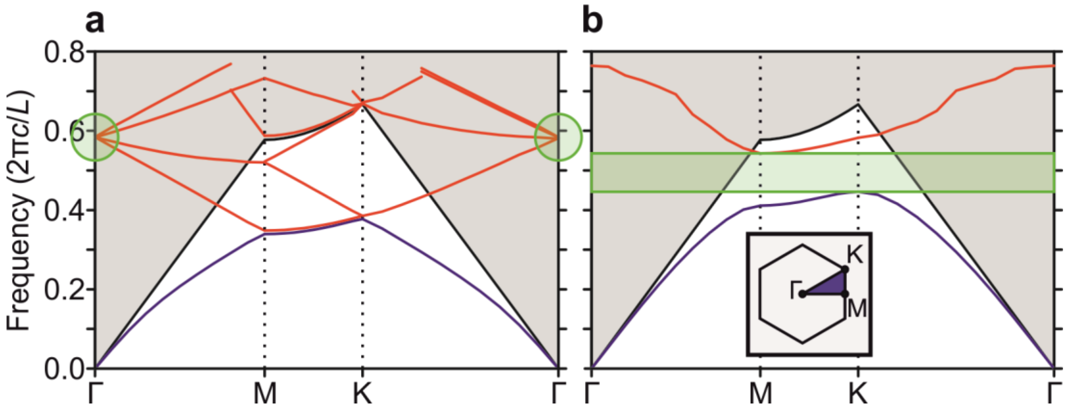

Figure 14: Photonic band structure of PhC slabs for TE polarized modes (simulated by MPB, see subchapter “2.3 Computer simulations”). The PhC slabs are formed by dielectric layer (n_S = 2.41) with air holes with hexagonal lattice symmetry (such as in Fig. 13b). The thickness of the layer is $w = 0.4L$, where L is the lattice constant. The grey shaded area with black boundary line denotes the escape cone. **(a)** Weak PhC slab with holes depth h_{PhC} = w/8. The interesting regions for Bragg diffraction with high degeneracy are located at Γ-point (green circles). **(b)** Strong PhC slab with holes throughout the whole slab. Only two lowest lying bands with band gap in between are plotted. The inset shows the Brillouin zone of hexagonal lattice with highlighted irreducible Brillouin zone and highlighted high-symmetry points.

Despite the absence of the band gap, the weak PhC slabs can be still used for light manipulation, namely for Bragg diffraction of light out of the thin dielectric/semiconductor layers. Since the diffracted light is not confined inside the layer anymore, the modes are called leaky modes. Sometimes, leaky modes are referred to as guided resonances, due to their narrow bandwidth for a given angle of diffraction. Due to the reciprocity of light propagation, the light incident on the structure from air can be coupled into the leaky modes. This effect can be used to map the spectral position of leaky modes and to enhance the excitation efficiency (resonant excitation).

2.2.1 Leaky modes mapping

The diffraction angles of leaky modes can be mapped by measuring the angle-resolved transmission efficiency of light through the PhC slab (Fig. 15a square lattice, vertical direction). When a spectrally broad, collimated beam passes through the PhC slab under a specific angle of incidence, light with wavelength, for which the coupling condition is fulfilled, couples to leaky modes and minima are observed in transmission. Each minimum corresponds to coupling of light to one of the leaky modes of the structure. The minima in transmission are observed because there is a half-wavelength phase difference and thus destructive interference between the straight propagating light and light that is firstly coupled to leaky modes and then out-coupled again. The measurement is possible only in the case that the slabs are placed on a transparent substrate. An alternative is to measure the angle-resolved reflection efficiency. The reflection efficiency is complementary to the transmission efficiency for long wavelength ($\lambda > n_s L$ for the normal incidence). For shorter wavelengths however, the light may be also Bragg diffracted on the PhC lattice to the real diffraction orders, which causes differences between reflection and transmission spectra.

Angle-resolved transmission efficiency of a given PhC can be simulated by using rigorous coupled-wave analysis technique (RCWA; see Section 2.3). An example of such simulation for the Γ-X direction of a square lattice PhC is shown in Fig. 15b. The square lattice, and the Γ-X direction especially, enables to distinguish modes propagating in different directions in the real space based on their polarization (Fig. 15c). For the complete understanding of the leaky mode distribution, the Bragg diffraction into other directions must be also considered. This can be done by plotting the modes in the k-space for one wavelength (Fig. 16).

Fig. 16a shows the k-space for a structure without PhC. The TE_0 mode (green cone/circle) lies outside the escape cone (black cone/circle) and is guided inside the material. Reciprocally, no light from air can be coupled to the mode. Note that the TM_0 mode is ignored for this analysis. The introduction of translational periodicity with a lattice constant L into the structure creates the periodicity in k-space with period $2\pi/L$ (Fig. 16b). Each black point corresponds to the node of the reciprocal lattice and all of them are equivalent to the point at $k_x = k_y = 0$ (Γ-point). The whole k-space is filled with cells that are copies of the cell centered at $k_x = k_y = 0$, which is the Brillouin zone. The Brillouin zone can be further reduced by the rotational symmetry of the square lattice to irreducible Brillouin zone (grey area), which contains all relevant information about the photonic modes of the structure.

Simultaneously with the Brillouin zone, the modes and the escape cone are also replicated within the k-space. Fig. 16c shows the effect of periodicity on the TE_0 mode for the wavelength 653 nm, where light impacting from the vertical direction is coupled to the structure (point 1, see also Fig. 15 where the coupling at 653 nm is clearly visible in the measured and simulated

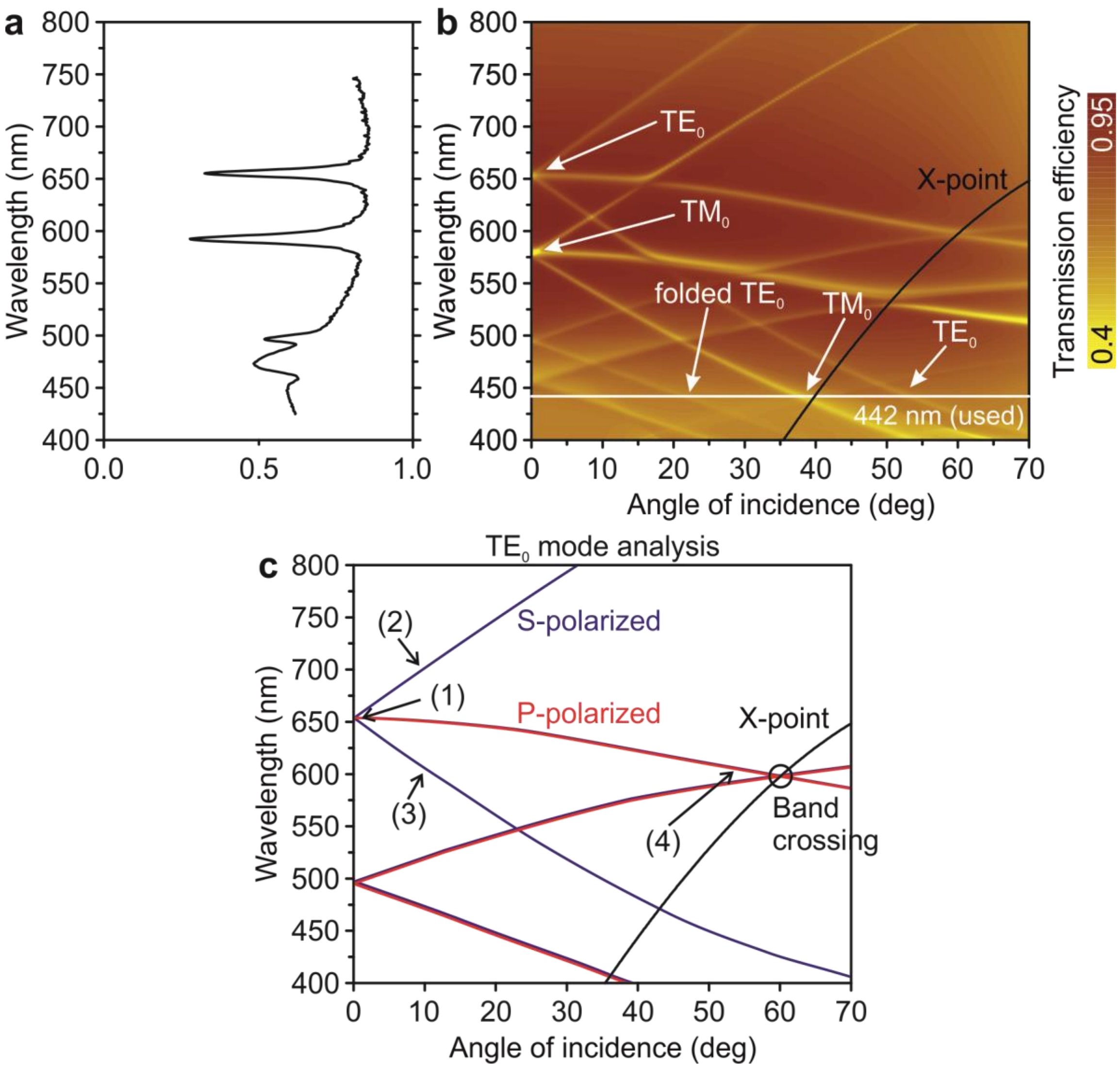

Figure 15: **(a)** Measured transmission efficiency for light incident at vertical direction (0 deg) for PhC slab with square geometry and lattice constant $L = 345$ nm. **(b)** Angle-resolved transmission efficiency for incident beam impacting under the given angle of incidence along Γ-X direction. Simulation for the same PhC slab as in (a). Picture taken from [21], where complete description of the simulation details can be found. **(c)** Polarization of the individual branches of the TE_0 mode: s-polarized (blue) and p-polarized (red). The points (1-4) correspond to points indicated in Fig. 16.

transmission efficiency). The modes from neighboring reciprocal lattice points intersect with the Brillouin zone and the escape cone and the coupling to these modes from space is thus allowed. The light impacting from vertical direction can be coupled to the TE_0 mode that propagate in four possible directions. The light polarized in the x direction is coupled to the modes propagating in $+k_y$ and $-k_y$ directions (red circles in Fig. 15c) because only the transversal component of TE_0 mode is non-zero. Similarly, light polarized in the y direction (blue circles in Fig. 15c) is coupled to the modes propagating in $+k_x$ or $-k_x$. Unpolarized light is then divided to s- and p-polarized components, which are then coupled to the respective modes. The area inside escape cone circle may be measured or simulated by the RCWA method (Fig. 17). The dashed line (Γ-X direction) corresponds to the horizontal cut in Fig. 15 for the respective wavelength of 653 nm.

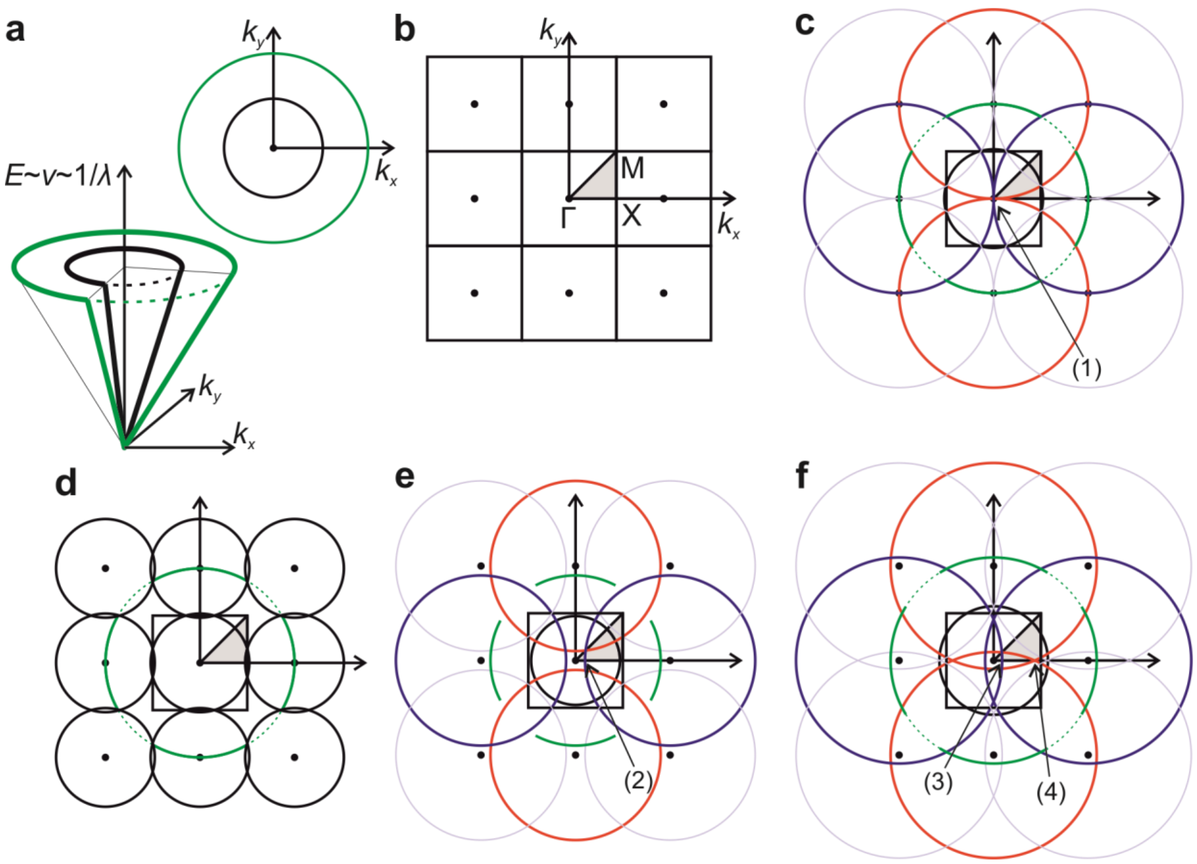

Figure 16: **(a)** Light line (black circle/cone) and TE_0 mode (green circle/cone) in k-space as a function of energy/frequency/wavelength (bottom) and for one frequency (top). Material and waveguide dispersion are neglected for simplicity. **(b)** The reciprocal lattice is composed of equivalent cells with the Brillouin zone centered at $k_x = k_y = 0$. The irreducible Brillouin zone is shown in grey color. **(c)** Bragg diffraction represented in the k-space. Part of the TE_0 mode is in-/out-coupled during first order diffraction process (solid green) and part in second order diffraction process (dotted green). The light impacting from the vertical direction that is polarized in x direction is coupled to the modes propagating in $+k_y$ or $-k_y$ direction (red circles) because only the transversal component of TE_0 mode is non-zero. Similarly, light polarized in y direction is coupled to the modes propagating in $+k_x$ or $-k_x$ (blue circles). Faint blue circles centered at $k_x = k_y = \pm 2\pi/L$ denote TE_0 mode formed by second order diffraction process. **(d)** Alternative way of illustration of Bragg diffraction in k-space – the extraction cone is replicated instead of the TE_0 mode. **(e)** Same as (c) for longer wavelength. **(f)** Same as (c) for shorter wavelength. The points (1-4) in **(c)**, **(e)**, and **(f)** correspond to the respective points indicated in Figs. 15b and 17a,b.

An alternative visualization is shown in Fig. 16d, where the escape cone is drawn periodically instead of the mode. This visualization is more convenient for reasoning about the extraction efficiency. Due to the fact that whole mode circle (green circle) lies within the escape cones, regardless of the in-plane propagation direction within the slab, the light from the TE_0 mode can be extracted from the slab into air. The parts that are drawn as the solid line are extracted during first order diffraction process. The dotted parts correspond to the contributions of the cells centered at $k_x = \pm 2\pi/L$ and $k_y = \pm 2\pi/L$, and higher order diffraction processes are needed for extraction of these parts [29]. The consequence of this is that the diffraction length is much longer for these directions, which will be discussed in the section about the extraction length.

When the wavelength is increased, the diameter of the circles corresponding to both the modes and the light line is decreased (Fig. 16a). Note that the change of the wavelength is

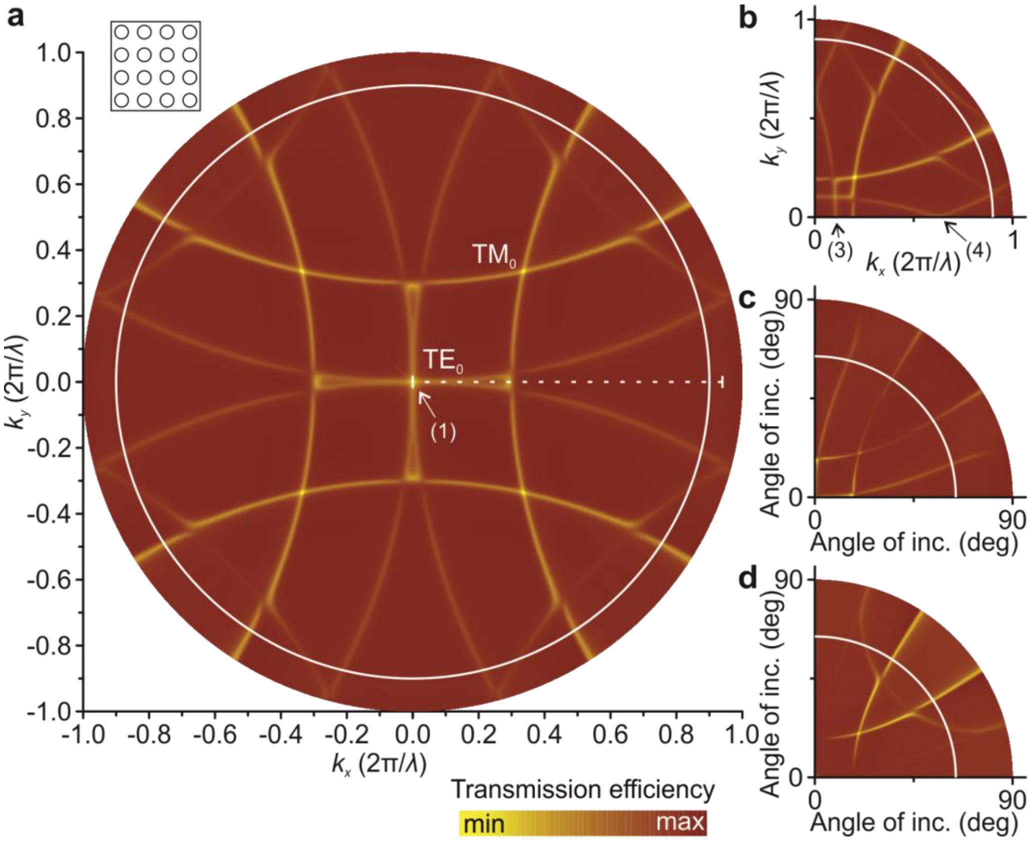

Figure 17: **(a)** The leaky modes in escape cone simulated by RCWA method for wavelength 653 nm (the same structure as in Fig. 15). Inset shows the top view of the PhC in real space (structure similar to Fig. 13a). **(b)** Same as (a) for wavelength 625 nm. Labeled points in (a) and (b) corresponds to the respective points in Figs. 15 and 16. **(c)** Angle-resolved transmission efficiency for p-polarized light for wavelength 653 nm. **(d)** Angle-resolved transmission efficiency for s-polarized light for wavelength 653 nm. The collection circle for objective with 0.9 NA is shown by white circle. The wave-vector in the units of 2π/λ is equal to the sine of the angle of incidence.

considered small and the material dispersion and dispersion caused by different fraction of mode propagating in high refractive index material is neglected. Thus, the diameter of the circles corresponding to TE$_0$ mode and to the light line are decreased by the same amount. Three things happen in the k-space (Fig. 16e) after the increase of the wavelength (the lattice constant remains unchanged). Firstly, there is no circle that intersects the Γ-point, so the modes cannot be coupled to light propagating in the vertical direction. Secondly, the circles from zones with $k_y = 2\pi/L$ intersect no longer with the Γ-X line in x direction. Therefore, there is only one intersection with Γ-X line – point (2) in the band diagram in Fig. 15, which corresponds to the contribution from cell centered at $k_x = 2\pi/L$. The light incident along the Γ-X direction must be polarized in y direction otherwise it cannot be coupled into the structure. The y direction corresponds to the s-polarized incident beam (Fig. 15b). The p-polarized beam propagating in the same direction transmits through the structure with reflectance given by Fresnel equations. Therefore, the structure can be used also as a polarization filter. Thirdly, the light from cells centered at $k_x = \pm 2\pi/L$ and $k_y = \pm 2\pi/L$ is located outside the light line circle all the time. Thus, the light for this wavelength cannot be completely diffracted from the slab (missing parts in the green circle in Fig. 16e remain guided in the slab).

Fig. 16f show the situation for a wavelength shorter than in Fig. 16c. Again, there is no mode for the vertical direction. Nevertheless, there are two modes on the Γ-X line. The point (3) corresponds to the contribution from the cell centered at $k_x = -2\pi/L$. This mode is again purely s-polarized. The point (4), which was missing for longer wavelengths, corresponds to the contribution from cells centered at $k_y = \pm 2\pi/L$. This mode is propagating parallel to neither axis of the square lattice within the PhC. Nevertheless, it propagates close to the y-axis and can be, thus, considered as mostly p-polarized regarding the incident beam. The fraction of s-polarized contribution increases for shorter wavelengths.

When the wavelength is further shortened, the point (4) reaches the X-point. At this point the circle intersects with the circles from cells centered at $k_x = 2\pi/L$ and $k_y = \pm 2\pi/L$. This corresponds to the band crossing highlighted in Fig. 15c. After that, the original circle from $k_y = \pm 2\pi/L$ leaves the light line circle and the first order diffraction stops contributing to the coupling between guided and radiative modes. The coupling is happening via second (or even higher) order diffraction processes that moves back to the Γ-point with shorter wavelengths, and eventually reaching the Γ-point for wavelength slightly below 500 nm (Fig. 15).

2.2.2 Extraction and collection efficiency

The band diagram and the k-space representation that were discussed in connection with light in-coupling in the previous section (Figs. 15 and 16) can be used also for considerations about the extraction and collection efficiency of light outcoupled from the structure via leaky modes. Nevertheless, there are some important differences between in-coupling and out-coupling of light into and from the photonic structure. When a collimated beam is incident on the PhC, it can couple to the TE_0 mode that propagates in one direction. Only at the points of high symmetry (e.g. the Γ-point) with the degeneracy, the in-coupled light can propagate into more than one in-plane direction as discussed in detail in the previous sections. This corresponds to a set of discrete points in the k-space. However, the light that is emitted by sources in the layer is coupled to modes that propagate in all possible directions within the PhC plane, which for a single wavelength corresponds to the whole circle in Fig. 16d.

In order to extract light from the layer completely, all parts of the circle must lie inside the light line circle of some reciprocal lattice cell (Fig. 16d). When this happens, the extraction efficiency reaches 100% for a material with no absorption (50% into one half of the space). The rate of extraction is quantified by the extraction length, which is the distance that the mode travels inside PhC structure before its energy drops to 1/e due to Bragg diffraction. When absorption is present, the extraction length must be reduced as much as possible to achieve high extraction efficiency. The extraction length of Bragg diffraction from the layer increases (exponentially in the first approximation) with the number of diffraction processes that are needed. There is already a large difference between the first-order Bragg diffraction process originating from the four neighboring cells in the k-space and the second-order Bragg diffraction process originating from the cells centered at $k_x = \pm 2\pi/L$, $k_y = \pm 2\pi/L$. This is explicitly shown in Fig. 18a where the angle-resolved photoluminescence from thin polycrystalline diamond layer with a PhC on its surface is plotted [21]. The folded TE_0 band originating from the second order diffraction process is significantly less intensive than the unfolded band for the same wavelength.

The highest extraction efficiency for a desired wavelength is obtained when the reciprocal lattice vector **G** has similar length as the in-plane wavevector of the mode $k_{||}$ (Fig. 16c). Then, the arc length of the modes that lies inside the light line circle is maximized. This is also very convenient for high collection efficiency. The collection efficiency can be estimated from the

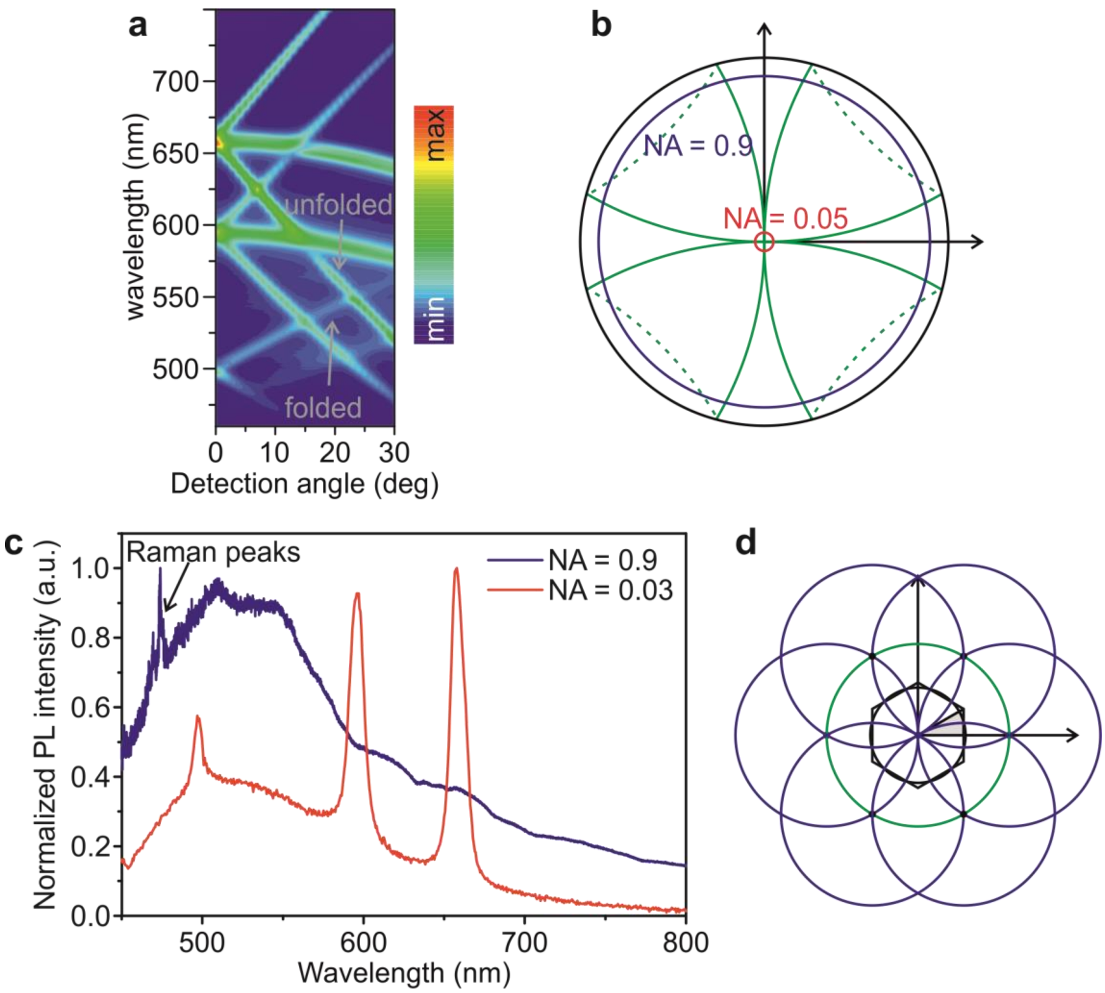

Figure 18: **(a)** Angle-resolved PL intensity along Γ-X direction: The intensity of the folded TE_0 band (second-order diffraction process) is much lower than the intensity of the unfolded TE_0 band (first-order diffraction process). Picture taken from Ref. [21]. **(b)** Detail of the extraction cone from Fig. 16c. The red and blue circle corresponds to the part of the k-space that is collected with low NA = 0.05 and high NA = 0.9 collection optics, respectively. **(c)** PL intensity measured with low NA = 0.03 (red) and high NA = 0.9 (blue) collection optics. Whereas narrow spectral peaks appear in the spectra measured with low NA optics, the enhancement is similar for the whole spectra for the measurement with high NA optics. **(d)** Bragg diffraction represented in the k-space for the weak PhC with the hexagonal lattice symmetry. The whole TE_0 circle is in-/out-coupled via first-order diffraction processes, which improves the extraction efficiency in comparison with square lattice.

k-space using the collection circle. The collection circle is centered at Γ-point when the collection optics is placed parallel to the normal of the sample. There are two limiting cases of the collection optics (Fig. 18b): high NA collection optics that collects light over large area of angles (microscope objective) and small NA collection optics that collects only small fraction of angles but can probe larger area of the sample (optical fiber, camera). The $|\mathbf{G}| \approx k_{||}$ condition is advantageous in both cases. Moreover, low NA collection optics allows to capture only leaky modes that lie in very narrow spectral range. The leaky modes thus form very narrow spectral lines (resonances) in the spectra as can be seen in Fig. 18c. This may be utilized for sensing applications, where the spectral shift of these resonances (caused e.g. by changes of refractive index in the surrounding environment) may be used as one of the detection channels [96].

So far, the considerations were made for the square lattice, which allows relatively easy analysis of the results. In order to extract light more efficiently from the layer, the lattice with hexagonal symmetry can be used. There are contributions from six neighboring cells for the hexagonal lattice (Fig. 18d) in contrast with four neighboring cells of the square lattice. Subsequently, all light is extracted via first-order diffraction process, which leads to higher extraction efficiency. Note, that this is not true for material with larger refractive index than diamond, where the diameter of light line circle is relatively smaller when compared to the diameter of the guided modes in the k-space. In such case, higher order diffraction processes or lattice with even higher symmetry are required [98]. The hexagonal symmetry is also advantageous for low NA collection optics because it increases the degeneracy at the Γ-point and improves the collection efficiency.

2.2.3 Extinction length

In non-absorbing materials, the extraction length does not have any effect on the extraction efficiency. In order to quantify the speed of extraction efficiency, the modal extraction coefficient μ_d can be defined as

$$I(l) = I_0 e^{-\mu_d l} \tag{2.7}$$

where l is the distance travelled in a PhC slab, which is supposed to be larger than the lattice constant of the PhC L, and I_0 and I the initial and final intensity of light coupled to some mode after travelling the distance l, respectively. Generally, the modal extraction coefficient depends on the propagation direction and is zero for the directions that are not extracted (e.g. missing parts of the green circle in Fig. 16e). An inverse of the modal extraction coefficient is the effective extraction length $l_d = 1/\mu_d$, which is the distance after which the intensity of light in the mode decreases to 1/e due to the Bragg diffraction.

In reality, the extraction length must be reduced as much as possible to maximize the extraction efficiency, because it competes with absorption and scattering. The total decrease of intensity can be thus written as

$$I(l) = I_0 e^{-\mu l}, \mu = \mu_d + \mu_a + \mu_s \tag{2.7}$$

where μ is the total modal extinction coefficient, which includes losses caused by Bragg diffraction μ_d, absorption μ_a, and scattering μ_s. Analogous to the modal extraction coefficient, the effective extinction length $l_{ext} = 1/\mu$ can be defined, which is the distance after which the intensity of light in the mode decreases to 1/e (Fig. 19).

Instead of the extinction length, the number of optical pulses before the intensity of light coupled to mode decreases to 1/e can be quantified. In analogy to optical cavities, this number of optical pulses in radians is denoted as the Q-factor (Fig. 19). The number of optical pulses is related to the frequency (radians per second) and to the wavevector (radians per μm):

$$Q = \frac{\omega}{2\gamma} = \frac{k_{||}}{\mu} \tag{2.7}$$

where γ is the amplitude attenuation in time. Note, that one way how to look on the waveguide is to consider the waveguide as a cavity, where the bottom and top boundaries are mirrors, but the light propagation is not restricted inside the slab plane.

The advantage of the Q-factor analysis is that it can be directly extracted from the angle-resolved transmission efficiency or photoluminescence measurement. The Q-factor is the ratio

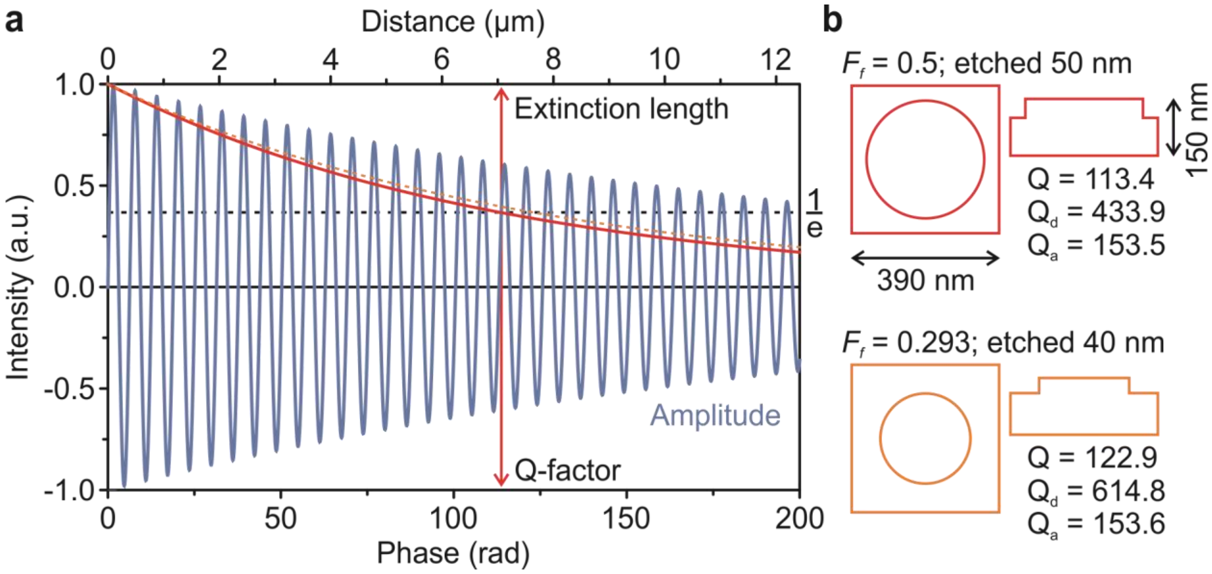

Figure 19: **(a)** The decrease of the intensity of light with distance. The extinction length and *Q*-factor expresses the physical distance and the number of pulses in radians, respectively, before the intensity drops to 1/e of the initial value. Illustration for light with wavelength 738 nm, coupled to mode with N_{eff} = 1.891, which corresponds to in-plane wavevector $k_{||}$ = 16.1 μm^{-1}, and Q = 113.4 (red line) and Q = 122.9 (orange dashed line). The extraction length and *Q*-factor was simulated for diamond PhC slabs (absorption coefficient of diamond 850 cm^{-1}) shown in **(b)** – top view and side view of the unit cell. Both structures have similar $k_{||}$ = 16.1 μm^{-1} and thus similar modal absorption length and Q_a (*Q*-factor when only absorption is considered). The structure on top has ideal fill factor (F_f) and slightly higher depth of etching and thus the light is extracted faster from the layer.

of the mode linewidth to the frequency/wavelength of the cavity mode as defined in Eq. 1.19. However, the care must be taken not to measure the linewidth near the high degeneracy points because the linewidth may be artificially broadened by the presence of multiple modes with slightly shifted frequency (band splitting).

The *Q*-factor can be further divided into three parts Q_a, Q_s, and Q_d accordingly to Eq. 1.20, which corresponds to absorption, scattering, and Bragg diffraction of modes, respectively. The absorption is undesired for light extraction, and the absorption length depends on the absorption coefficient of the material and on the spatial overlap of the mode with the absorbing material. The overlap may be reduced by choosing very thin waveguides. Nevertheless, the LDOS is reduced in such case and this method has no practical meaning for the structures that we use (the waveguide is formed solely by diamond). The scattering depends on the scattering coefficient of the material and on the spatial overlap with the scattering material. It improves the extraction efficiency in principle. However, it does not produce directed output and may be thus undesired in some cases.

The extraction length due to Bragg diffraction depends on the dimensions of the photonic structure and on the order of the diffraction process that leads to the extraction of light from the material. As with absorption and scattering, the Bragg diffraction depends also on the spatial overlap of the mode with the periodic structure, which is typically placed on top of the slab. The deeper is the PhC etched into the slab, the shorter is the extraction (and extinction) length. Fig. 19a shows an example for the PhC structure based on diamond in which the extinction length is approximately 7 μm which is almost 18 lattice periods. Note that the absorption *Q*-factor (Q_a) is lower than extraction *Q*-factor (Q_d) and the majority of light is absorbed. The fraction of extracted light may be increased by improving the material properties (lower absorption coefficient) or by etching the PhC deeper into the material. On the other hand, too deep etching causes the bending of photonic bands and opening of band gap, which decreases the degeneracy at the Γ-point. Thus, it is not advantageous when the directionality of light and spectral selectivity is of importance.

For simulations of the mode spreading in PhC, the structure can be separated in two layers. The continuous bottom layer has the refractive index of the slab material (diamond in our case), and the top layer is composed of the slab material and air (diamond columns in air in our case). For simulations, the effective refractive index of the top layer can be defined as

$$n_{PhC}^2 = F_f n_a^2 + \left(1 - F_f\right) n_s^2 \tag{2.7}$$

where n_s is the refractive index of the slab material (diamond $n_s \approx 2.41$ in our case) n_a is the refractive index of the surrounding material (air, $n_a = 1$), and F_f the fill factor that quantifies the ratio of area in the top layer occupied by the slab material with regard to the total area. For the highest efficiency of Bragg diffraction, the fill factor must be close to 0.5 [29]. If the fill factor is lower or higher, the columns have lower effect on the propagating modes, and thus the extraction is slower. This can be simply understood as the refractive index contrast is maximized for fill factor around 0.5. The effect of higher-order diffraction processes can be neglected in the first approximation because their extraction length is much larger than the extinction length caused by absorption and scattering for polycrystalline diamond.

The wavelength of the mode at the Γ-point depends on a number of parameters: lattice type, lattice constant, refractive index, thickness (height) of the non-perturbed slab layer, and height and diameter of the columns. For the efficient extraction of light, the LDOS inside the layer as well as the overlap with the PhC must be maximized (by choosing correct thickness). A care must be taken not to make the PhC too high, which may result in the band bending and decrease of degeneracy. In the same time, the fill factor must be kept around 0.5. Slight adjustment of the parameters may be then used to tune the spectral position of leaky modes to the desired wavelength without significantly reducing the extraction efficiency. The Q-factor and the extinction length can be estimated from simulations.

The extraction length is of importance also with regard to the collection optics. When the extinction length is known, a suitable optics can be then used for the collection of light. An example is the use of an objective with a large numerical aperture (Fig. 18b) in confocal regime. Despite collecting light almost in the whole escape cone, the overall collection efficiency may be low, because the objective collects light only from small part of the sample, which may be smaller than the extinction length. On the other hand, the short extinction length (low Q-factor) means that the modes have large bandwidth. The result for light at certain wavelength is that the leaky modes are spread over broader angular spectrum. Minimizing the extinction length is thus not desired for applications, where the directionality of light is of importance and for applications where the spectral selectivity is employed such as sensing.

2.2.4 Real structures

The real PhC slabs support not only the TE_0 mode but also the TM_0 mode and eventually higher order modes. Similar considerations as for the TE_0 mode may be done for the TM_0 mode as well, the spectral position of which is shifted to shorter wavelengths. The difference from the TE_0 mode is that the TM_0 mode has a zero component of the electric field transversal to the propagation direction. Thus, the polarizations for coupling into the structure must be opposite than for the TE_0 mode. For instance, light at 575 nm polarized in the x-direction is coupled to the modes propagating in the x-direction (for situation in Fig. 16a). The TM_0 mode is spatially localized near the slab boundaries of the structure (Fig. 4) and thus interacts strongly with the PhC located on top of the slab. This reduces its extraction length, which is expressed in Fig. 17 as more pronounced minima of transmission efficiency achieved for the TM_0 mode compared to the TE_0 mode.

The separation of emission into the individual modes is given by the location and orientation of emitters within the PhC structure and by the LDOS of the PhC slab modes according to the Fermi's golden rule. The LDOS follows the intensity profile of the modes and the orientation of the emitters depends on the material under study. In the case of polycrystalline diamond, the emitters are localized either on the boundaries between the diamond grains, which orientation is random, or inside the grains where the orientation of the emitter (typically a color center) depends on the orientation of the crystal lattice. Nevertheless, there are 4 equivalent directions in one grain and the grains have usually no preferred orientation, which means that the emitters inside the grains have also random orientation.

The photonic structure may be also used to couple the excitation beam into the leaky modes for effective excitation of the PL as was first observed for planar TiO_2 PhC slabs with surface deposited quantum dots [99] and is denoted as the resonant excitation. There are several angles in Fig. 15 for which the resonant excitation is achieved with a 442 nm laser beam. For instance, s-polarized light incident under 22.5° along the Γ-X direction is coupled to the TE_0 mode.

Because the weak PhC slabs are mostly asymmetric, the TE_0 and TM_0 modes are coupled to each other and the energy can slowly flow from one to another. Strictly speaking, the modes cannot be denoted as TE and TM anymore, because of the coupling. Nevertheless, the coupling can be neglected because it is only weak and thus negligible amount of energy is exchanged within the extinction length, which is typically several to tens of micrometers long.

Another effect present in real structures is the re-emission of the photons after they are absorbed in the material. This may slightly improve the overall extraction efficiency because the light that is originally coupled to the modes that are not extracted (missing parts of the green circle in Fig. 18e) may be re-emitted into the mode propagating in a different direction and can be finally extracted. The improvement of extraction efficiency depends also on the ratio of absorption, scattering and Bragg diffraction of the modes. The effect of re-emission is only important for structures with absorption dominating over scattering and Bragg diffraction, which are, however, not usually used in real applications.

2.3 Strong PhC slabs

2-D PhC slabs in the strong regime have sufficient modulation of refractive index, which causes the photonic band bending and opening of the band gap (Fig. 14b). In principle, the strong PhC slabs can be composed of dielectric rods in air or air holes in the dielectric slab. Nevertheless, strong PhC slabs require the symmetry in the vertical direction, otherwise the TE and TM modes are coupled to each other and the band gap is lost. The usual way to obtain a symmetric structure is removing the substrate material which is much easier to achieve for the case of dielectric slab with holes. We were thus interested mainly in the structures with holes, which possess a photonic band gap for the TE-like modes. Structures composed of dielectric rods have the band gap for the TM modes. Note that even for the structures with mirror symmetry in vertical direction and for only one polarization, the photonic band gap is incomplete due to the presence of radiative modes (Fig. 14b).

There is an optimal thickness of the waveguide to achieve the largest ratio of the band gap size to the middle frequency of the band gap. The optimal thickness for slabs with holes is approximately half of the wavelength in the dielectric material [77]. When the thickness is smaller, the fundamental mode is not so well confined in the layer. On the other hand, higher order modes are supported for larger thicknesses (see Fig. 5), which decreases the band gap size.

In contrast to the weak PhC slabs discussed in the previous section, the strong PhC slabs are not suitable for diffraction of modes into the vertical direction because the degeneracy at the Γ-point is lifted due to the band bending caused by the large modulation of refractive index. Instead, the strong PhC slabs with a photonic band gap can be used to improve the collection efficiency by suppressing the propagation of light in the plane of the slab or as starting structures for the fabrication of PhC waveguides and cavities, where the bandgap is utilized for light confinement. The approach in which the in-plane light propagation is suppressed due to the existence of the band gap is, however, not efficient for several reasons [100]. Firstly, the extracted light is not directed into any specific direction and it has Lambertian radiation pattern. Secondly, the presence of the band gap not only prevents the light propagation inside the PhC slabs, but it also decreases the LDOS with respect to the emitter in the homogeneous medium. This leads to the decrease of the radiative transition rate, which follows from Fermi's golden rule. Moreover, the non-radiative emission rate remains unchanged and efficiency of photon emission is thus decreased. Thirdly, the propagation of light is suppressed only for one polarization as was already discussed and thus part of the light is still trapped inside the guided modes.

PhC waveguides and cavities can be created by introducing defects into the periodic structure of the strong PhC slabs. For instance, by omitting a row of holes in the PhC slab, a linear defect that works as a linear waveguide is created. Light cannot penetrate to the surrounding PhC structure because of the existence of the band gap. It cannot couple to the radiative modes either, because it lies below the light line. The simplest defect that can be used as a waveguide is the W1 defect that is made of one missing line of holes inside the PhC slab [101,102]. The second type of defects are point defects that can be used to confine light in all 3 directions and create an optical resonator. An example of such cavity is plotted in Fig. 13c.

2.3.1 Photonic crystal cavities

The PhC cavities are composed of the strong PhC slab with a band gap that contains a point defect in the PhC lattice. The cavity modes are spatially localized in the slab plane due to the band gap and also in the vertical direction due to the total internal reflection. The PhC slabs with holes have band gap usually only for the TE polarized modes. TM polarized modes can propagate in the slab and, therefore, the coupling between TE and TM modes must be suppressed to obtain cavities with low losses and thus high quality factors. To completely suppress the coupling, the structures must possess mirror symmetry in the vertical direction as discussed in previous sections. PhC cavities are thus usually fabricated in suspended dielectric membranes. An alternative to the planar PhC cavities is the use of beam PhC cavities, where the light is confined in two directions by total internal reflection and in one direction by the periodic structure [77].

There are countless planar PhC cavity designs with various mode properties. In this work, we concentrate on the L3 cavity design that is formed by 3 missing holes in the hexagonal lattice. The advantage of this cavity design is that the modes supported by the cavity have a specific polarization and they can thus be differentiated by polarization measurement [103]. There are also cavities with even smaller volume such as the H0 cavity (holes are only shifted) or the H1 cavity (one missing hole) [104,105]. However, the modes of such cavities are either unpolarized, or the cavities support degenerate modes with multiple polarizations.

The single defect cavity usually supports more than one cavity mode. The H1 cavity supports the unpolarized monopole mode, polarized (but degenerate) dipole modes, and also quadrupole and hexapole modes. On the other hand, the L3 cavity supports a fundamental mode, which is analogous to the waveguide modes in the W1 waveguide with reflections from the end of the cavity. Furthermore, it supports also higher order modes with main electric field component aligned either parallel or perpendicular to the long cavity axis. All modes exhibit a linear polarization [103]. The fundamental mode has usually significantly higher quality factor than the other modes. Note that, in this case, the labeling of fundamental and higher order modes is related to the distribution of electromagnetic field in the slab plane and not to the vertical distribution of the field as when the slab thickness was discussed. The slab thickness is considered small enough to support only one TE_0 and one TM_0 mode.

The presence of the PhC cavity significantly alters the LDOS and the spontaneous emission rate can be significantly increased due to Purcell effect for the cavity modes (Eq. 1.21). The mode volume can be in the order of λ^3, which is significantly smaller than for Fabry-Perot cavities, and which increases the Purcell effect. Moreover, the LDOS is increased only for the modes of the cavity, while it is reduced for neighboring wavelengths (for TE polarized emitters) because of the band gap. This effect was already discussed in the previous chapter and it may be used to improve the count-rate of one transition (e.g., the zero-phonon line of diamond color centers) while reducing the count-rate of the other transitions (e.g. the phonon side band of diamond color centers), which improves the radiative branching ratio. This effect is not present for Fabry-Perot cavities, where the LDOS is not reduced for other wavelengths. On the other hand, the PhC cavities bring new problems that must be resolved in order to use the cavities for efficient light generation.

The optical losses of the cavity, which limit the obtainable Q-factor, are caused by the coupling of light from the cavity modes to the radiative modes and to the guided modes supported by the slab. Besides coupling to the guided modes with opposite polarization, which may be prevented by keeping the mirror symmetry in the vertical direction, the cavity modes can also couple to waveguide modes of the same polarization. This happens when the number of holes around the cavity is limited as in Fig. 20, where only five holes surround the cavity on each side. The light tunnels through the structure with the band gap and causes the gradual leak of power from the cavity. To reduce the leakage, the number of holes around cavity must be increased.

The coupling of light to radiative modes, may be reduced by designing the shape of PhC cavities. Structures with large band gap and with the cavity mode located in the middle of the band gap are optimal to reduce the coupling of cavity modes to radiative modes. The position

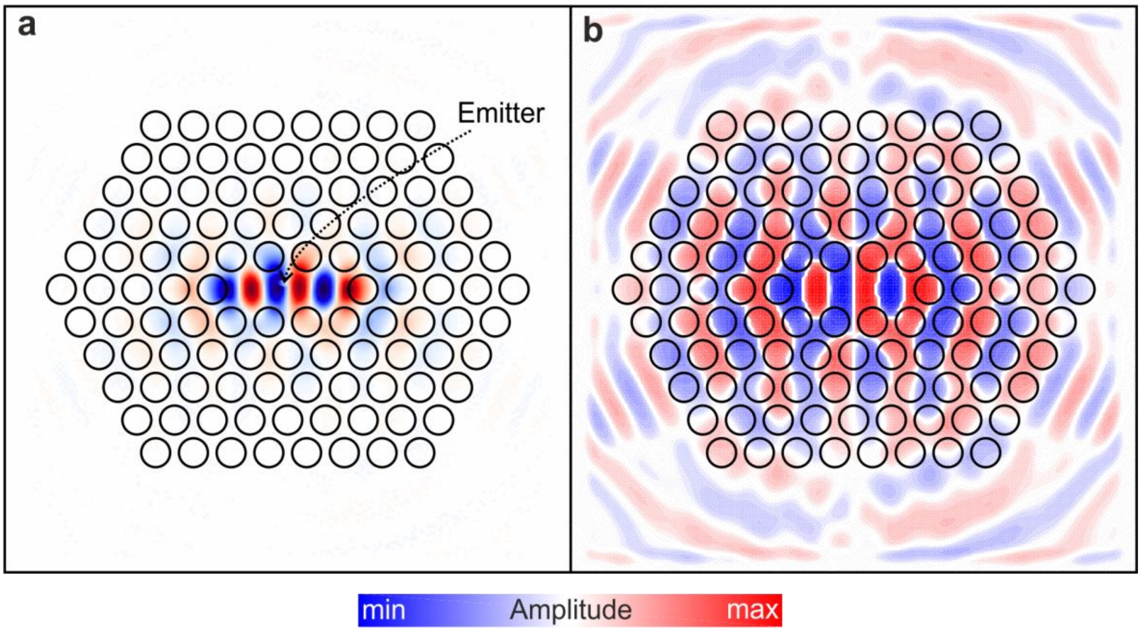

Figure 20: Top view of a simulated PhC cavity in a diamond slab (index of refraction 2.41, layer thickness 250 nm, lattice constant 300 nm, and hole diameter 230 nm). The cavity supports a mode at 740 nm (spectrally near to the zero-phonon line of SiV centers). The electric field amplitude in the middle of the slab was computed using 3-D FDTD simulation (MEEP software package). The amplitude is shown **(a)** in linear and **(b)** in logscale in order to show the part of field that escapes into the slab because of the low number of holes around the cavity.

of modes inside the band gap depends on the shape of the cavity and the diameter of the surrounding holes. Fig. 20 shows the top-view of the L3 cavity and the fundamental mode of such cavity. The radiative losses depend on the smoothness of the transition between the defect and the surrounding PhC slab. When the transition is abrupt then the cavity losses are largest. To improve the *Q*-factor, the transition must be smoothened, which can be done simply by increasing the defect size. However, the volume also increases in such a case, which lowers the Purcell factor. A more convenient way is to slightly adjust the diameter or position of holes around the cavity [60,106,107]. The figure of merit in such case is the ratio between the *Q*-factor and volume of the cavity mode. The optimization may be done by Fourier analysis of the mode field as discussed later in this section.

The *Q*-factor can be greatly reduced by fabrication imperfections. The critical factor is the verticality of the sidewalls of the holes in the PhC slab [63]. Usually, the diameter of the holes is larger on top of the structure than on the bottom. Subsequently, the mirror symmetry of the structure in the vertical direction is broken, which causes that part of the light from the trapped TE mode is coupled to the TM mode. The effect of other fabrication imperfections, such as small differences in the hole diameter, is usually minor. The *Q*-factor also depends on the material properties of the cavity. The additional losses may be caused by scattering or absorption inside the material. The scattering is reduced for cavities formed in a material with small surface roughness.

In accordance with Eq. 1.20, the total *Q*-factor is given by

$$\frac{1}{Q}=\frac{1}{Q_{TM}}+\frac{1}{Q_{guided}}+\frac{1}{Q_{rad}}+\frac{1}{Q_{scat}}+\frac{1}{Q_{abs}} \tag{2.5}$$

where Q_{TM}, Q_{guided}, Q_{rad}, Q_{scat}, and Q_{abs} characterizes the losses caused by coupling to TM mode, guided modes, radiation modes, and by scattering and absorption, respectively. The lowest partial Q has the largest impact on the total Q-factor, and it must be increased in order to improve the total Q-factor. For instance, low Q_{TM} indicates poor verticality of holes, or low Q_{guided} indicates the low number of holes around the cavity. It is pointless to improve factor that has low impact on the total Q factor.

When the cavity is used to enhance the count-rate of the emitters in the material, the modes have to spectrally overlap with the emission line of the emitter. The spectral position of modes in PhC cavities cannot be tuned as easily as in the case of Fabry-Perot cavities (by controlling the distance between the mirrors, e.g. with piezo actuators). Therefore, the structures must be designed to have a band gap and modes in the proper spectral region. The PhC dimensions for achieving overlap may be easily obtained by performing simulations (e.g. finite-difference time-domain simulation, see next chapter). Nevertheless, the position of modes cannot be controlled as precisely as needed to achieve an ideal spectral overlap with emitters with narrow emission lines due to fabrication imperfections. To obtain the spectral overlap, the fine-tuning of modes after the fabrication must be done by a slight adjustment of the cavity dimensions. This can be done, for instance, by condensation of water or gases on the PhC structure, which is a reversible method [108]. Other methods are based on the etching of the top layers of the cavity or on the deposition of thin layer on top [43,109].

The PhC cavities are often used to enhance the count rate of single photon emitters (e.g. in diamond [62,110–115]). In such a case, the emitter must be precisely placed into the place, where the cavity mode has an anti-node to obtain the highest enhancement. It is challenging to fabricate the single-photon source placed in the right position inside the cavity [116,112]. Instead, the opposite procedure is usually followed, in which the single photon emitter is first prepared in the planar slab, found in the optical microscope, and then the PhC cavity is fabricated around it [62]. Note, that the orientation of the emitter (dipole source) with respect to the polarization of modes (TE) is also a crucial issue. The orientation of single photon emitters can be controlled to some extent, e.g. in crystalline materials where the emitters are oriented in some preferential direction.

The enhancement of the count-rate of a single emitter must be accompanied by an efficient light collection, which can be improved by directing the light from the cavity into some significant direction. The far-field radiation pattern is given by the spatial Fourier transformation of the cavity mode electric field. The Fourier transformed spectrum in k-space is divided to the radiation part lying inside the escape cone (white circle in Fig. 21b,c) and confined part that lies outside the circle. By integration of the whole spectrum and the radiation part, the ratio between total power trapped inside the cavity and the radiated power, respectively, may be estimated. The ratio of these values corresponds to the Q-factor of the cavity mode [106]. The far-field emission pattern of the PhC cavity mode corresponds to the shape of the field inside the escape cone of the Fourier transformed spectrum.

There are two basic contributions affecting the k-space elements of the cavity modes. The first contribution comes from the sinusoidal wave with wavelength λ and corresponds to the standing wave inside the cavity. This contribution is located outside the escape cone in the Fourier spectra (two lobes with highest intensity in Fig. 21b). The second contribution comes from the confinement of the field inside the cavity, which is very abrupt for standard PhC

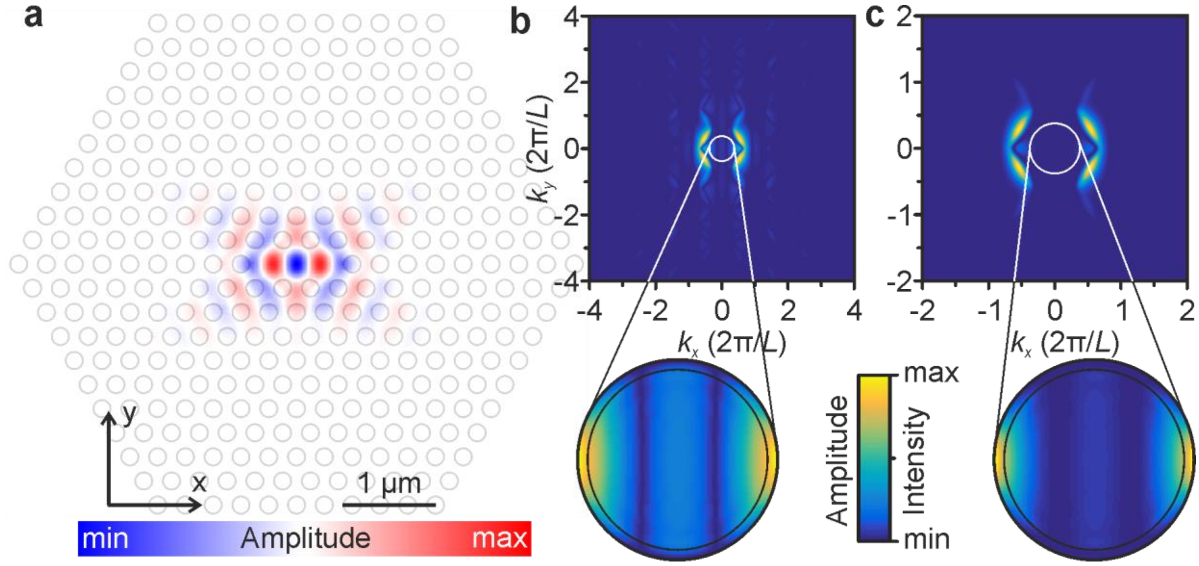

Figure 21: **(a)** Top view of a simulated PhC cavity in a diamond slab (index of refraction 2.33, layer thickness 200 nm, lattice constant 300 nm, and hole diameter 185 nm). The cavity supports the fundamental mode at 794 nm. The electric field amplitude in the middle of the slab was computed using 3-D FDTD simulation (MEEP software). **(b)** Elements of the electric field in k-space (computed as the spatial Fourier transformation of field in (a)). The bottom part shows the detail of the escape cone. The inner circle shows the part collected with microscope objective with NA = 0.9. The shape of the field in the escape cone corresponds to the far-field radiation pattern. **(c)** Same as (b) for quadrate of the electric field. Note that the amplitude/intensity scale of the bottom pictures differs from the top pictures in order to maximize the contrast in radiation pattern.

cavities. The abrupt change then leads to the Fourier components spread over large areas in the k-space, which contribute also to the escape cone. The places that contribute most to the escape cone can be detected by performing inverse Fourier transform of the escape cone area [117].

The electric field of the cavity mode may be modified by adjustment of the diameter and position of the holes around the cavity [60,106,107,117]. Some designs lead to the smoothing of the cavity mode, which decreases the intensity of the radiative part inside the escape cone and increases the *Q*-factor, while the volume of the cavity is not significantly increased. Similar approach can be used to control the radiation pattern of the cavity modes. For instance, a cavity design that leads to a directional emission from the cavity was proposed in Ref. [118].

Each mode has a different distribution of the field inside the cavity, and thus the *Q*-factor and far-field radiation pattern differ for each mode. Note that the cavity is symmetric in the vertical direction and thus the radiation propagates equally into both directions, and the collection efficiency thus cannot exceed 50%. A reflector may be placed on one side to direct the emission into one direction [119].

2.3.2 On-chip photonic circuits

In the above paragraphs, the collection of light from the cavity was considered only via coupling to radiative modes. Another approach is possible where the cavity is coupled to a waveguide fabricated in the slab plane. The waveguide works as an input/output channel for the cavity (Fig. 22) [120,121]. This approach improves the collection efficiency when the losses to output channel are optimized. The optimization of output losses can be done by changing the number of holes between the cavity and the waveguide. The optimal losses to output channel should be high enough, so that most of the photons leaves the cavity via the output channel

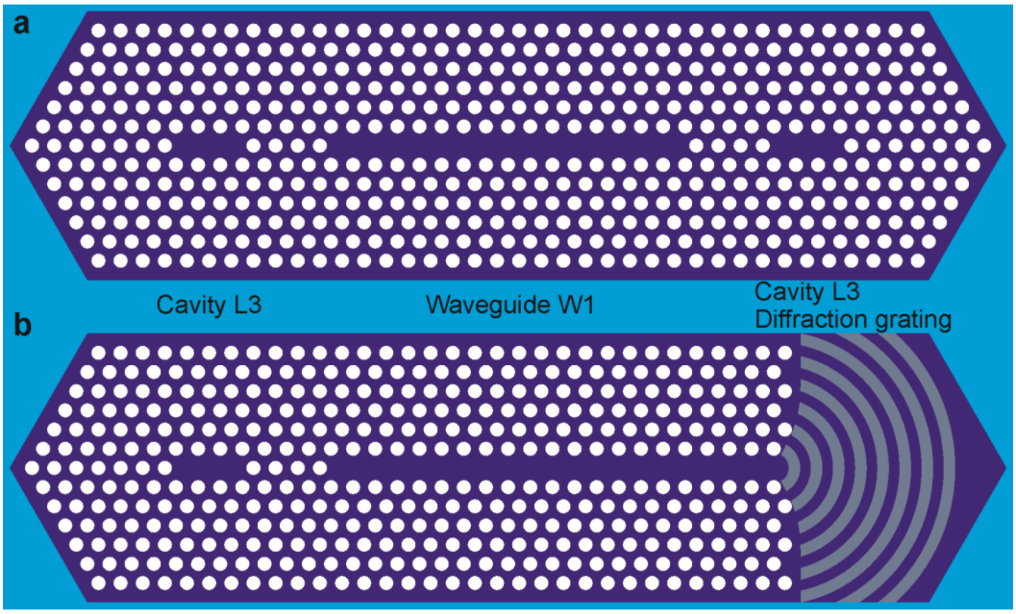

Figure 22: Sketch of the simple integrated photonic structures: **(a)** Two L3 PhC cavities coupled via W1 PhC waveguide. **(b)** L3 PhC cavity coupled to W1 PhC waveguide, and periodic diffractive grating for Bragg diffraction of light from the slab plane into the space.

rather than through other loss mechanisms, but not too high to significantly reduce the *Q*-factor of the cavity.

The waveguide can be further coupled to other photonic structures. For instance, two PhC cavities can be coupled via the waveguide (Fig. 22a). When the other PhC cavity supports mode at the same frequency as the first one the setup can be used, for example, to prepare entangled states between single photon emitters placed inside such cavities. Another possibility is to use a periodic structure to Bragg diffract the light from the slab into the space (Fig. 22b). The mode of the waveguide propagates in one direction and thus directional light beam may be obtained after the diffraction. These basic structures can be further integrated to create photonic circuits on a single chip for realization of various optical setups [122–124].

2.4 Computer simulations

There are various methods for simulation of PhC properties [77]. In this work we use mainly three simulation methods: rigorous coupled-wave analysis (RCWA), finite-difference time-domain (FDTD), and computation of definite-frequency eigenstates of Maxwell's equation. These complementary methods allow us to compute both the macroscopic (photonic bands and band gaps, far-field radiation) and the microscopic (local electric field distribution and propagation) PhC properties.

In the RCWA method, the planar periodic structure is divided into layers which are uniform in the direction perpendicular to the PhC plane [125–127]. The electromagnetic field is represented as a sum over coupled waves and each coupled wave is related to one of the Fourier harmonics that represent the periodic permittivity function. Subsequently, the Maxwell's equations in each layer are solved in the Fourier domain. Finally, the boundary conditions at interfaces between the layers are solved.

We employed the commercial software DiffractMOD+ (RSoft) for performing RCWA simulations. DiffractMOD is a design and simulation tool for diffractive optical structures such as diffractive optical elements, subwavelength periodic structures, or PhCs. The RCWA technique is implemented using advanced algorithms including fast Fourier factorization and generalized transmission line formulation. It allows to output the total reflection, transmission, and absorption, and reflection and transmission efficiencies of the individual diffractive orders. Moreover, it allows to output the vector field distribution inside and in the vicinity of the computed structure.

In the FDTD simulation method, the space is divided into discrete grid and the electromagnetic field is computed by solving the Maxwell's equations at boundaries between the units in discrete time steps [128]. The advantage of the time domain method is the solving of wide frequency range in one simulation run. Thus, it is advantageous for finding resonant frequencies and optimizing dimensions of photonic structures. We used MEEP (MIT Electromagnetic Equation Propagation) free/open-source software package to perform 2-D and 3-D FDTD simulations [129]. We used it to investigate the propagation of light inside photonic structures, to find the optimal thickness of diamond PhC slabs, and to find resonant modes of PhC cavities and their characteristics.

Computation of definite-frequency eigenstates of Maxwell's equations was done using MPB (MIT Photonic-Bands) free/open-source software package [130]. It is a frequency domain method for computation of photonic band structures (dispersion diagrams) and the associated electromagnetic modes of periodic structures. Although the software is designed to compute strictly periodic structures, the PhC slabs and PhC cavities can be modeled by using superlattices. We used MPB to find photonic structures with broad band gaps, and resonant modes and electromagnetic fields of PhC cavities.

3. Diamond

Diamond is a material well-known for its natural beauty, hardness, and high price. It is not surprising that throughout history people devoted plenty of time and endeavor to prepare synthetic diamonds. Nevertheless, the knowledge and technology were not adequate to fabricate artificial diamonds until the middle of the 20th century. Nowadays, people can prepare synthetic diamonds with various sizes by several techniques. It should be noted that the synthetic diamonds are of a lesser value as jewels, where the natural origin is appreciated. On the other hand, diamond exhibits many superior physical properties [131], which can be used in a broad spectrum of applications ranging from cutting tools through optical and electronic devices to medicine. Thanks to the cheap and accessible synthetic production, diamond can be further studied and utilized in many areas of science and technology.

3.1 Properties of diamond

Diamond is composed of carbon atoms arranged into the diamond cubic crystal lattice (Fig. 23). Each atom is tetrahedrally bonded to its closest neighbors with covalent, sp^3-hybridized bonds. Most of the diamond interesting properties originate from this rigid structure. However, it is necessary to note that diamond is not the thermodynamically most stable allotrope of carbon at standard conditions (room temperature and atmospheric pressure). The most stable form of carbon is graphite [34], where the carbon atoms are bonded with only three closest neighbors by sp^2-hybridized bonds forming sheets that are weakly bonded to each other. The transformation of diamond into graphite leads to the overall decrease of Gibbs free energy and this transformation is, thus, thermodynamically favored [132]. Nevertheless, the potential barrier for the transition is so high that the transition rate is negligible at standard conditions, i.e. diamond is the metastable allotrope of carbon. The metastability of diamond makes its preparation very difficult because the formation of graphite is preferred. Diamond can thus be formed from carbon either at very high pressures (around 7 GPa), where it becomes more stable than graphite [131], or using special growth procedures which suppress the formation of graphite as will be described in this chapter.

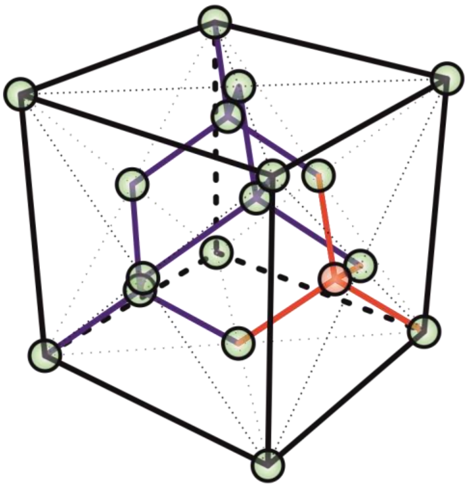

Figure 23: Model of the diamond cubic crystal lattice. Each atom is bonded with its 4 closest neighbors as indicated for one atom (red color).

Thanks to its rigid lattice, diamond is the hardest naturally occurring mineral and it is thus used to improve performance of cutting and drilling tools. Diamond has also the highest thermal conductivity of all known materials (> 1000 $Wm^{-1}K^{-1}$) due to low phonon scattering on the crystal lattice [133,134]. Diamond substrates may thus be used as heat spreaders for effective cooling of integrated electronic circuits. Chemically pure diamond is electrically insulating. By doping with boron and phosphorus, p-type conductivity and n-type may be achieved, respectively. Subsequently, diamond can be used for direct fabrication of semiconductor devices [135]. Diamond has also a high carrier mobility (> 1000 $cm^2/V/s$ [136]) and a broad electronic band gap, which is an attractive feature for some electronic applications.

Another attractive property of diamond is its chemical inertness. Hard and chemically inert materials are ideal for the use as protective coatings. Thanks to its biocompatibility, diamond finds also use in various biological and medical applications [137].

Last but not least, diamond has also very interesting optical properties [138]. Diamond transmits both near-UV, and near and short-wavelength IR radiation due to its broad band gap (5.5 eV). Despite the fact that the chemically pure diamond is in principle transparent for visible light, in reality diamond may contain defects in crystal lattice (sp^2 phase, various impurity atoms), which causes absorption and/or photoluminescence of diamond. The optically active defect centers will be treated in section "3.3 Diamond color centers" in detail. Diamond has also relatively high refractive index ($n \approx 2.41$) in the region of visible light and it is, thus, suitable for photonic applications. Monocrystalline diamond is more suitable for optical applications than the polycrystalline diamond since light is scattered by the grain boundaries in the latter.

3.2 Diamond fabrication

The natural diamonds originate from the Earth's mantle at depth around 200 km, where high pressure (7 – 8 GPa) and high temperature (1400 – 1600°C) occurs [131]. At these conditions, diamond is thermodynamically stable, and it is spontaneously created from carbon-rich melts. Diamonds are then transported to the surface during volcanic eruptions.

3.2.1 High pressure synthesis

The first method developed for the synthesis of diamond reproduces the physical conditions in the Earth's mantle [139]. With the reference to the physical conditions, the method is called high pressure high temperature (HPHT) synthesis. A mechanical press is used to apply a pressure on the carbon-rich melts produced by heating graphite or other carbon rich materials. Monocrystalline diamonds with sizes up to few millimeters can be grown using this technique [140]. The concentration of chemical impurities may be controlled during the fabrication process, which enables the production of very pure or, on the other hand, intentionally doped diamonds.

Diamond can be produced also by the detonation of certain explosives (e.g. trinitrotoluene or RDX) [141]. The pressure and temperature are elevated for a short time period during the explosion, which may be sufficient for the creation of the diamond phase from carbon atoms contained in the explosives or carbon atoms added in the form of graphite. In comparison with the HPHT method, the impure diamond particles with the nanoscale dimensions (usually 4 –

15 nm [141]) are produced during the detonation synthesis. The detonation nanodiamonds (DNDs) have a broad spectrum of applications, e.g. seeding of substrate materials for the chemical vapor deposition (CVD) growth, metal plating, polishing or lubrification. Nanodiamonds with fluorescent defects (details in "3.3 Diamond color centers" subchapter) are attractive for the use in biology and medicine. Recently, other methods based on the pulsed-laser irradiation [142] or ultrasound cavitation [143] were demonstrated for nanodiamond synthesis.

3.2.2 CVD synthesis

The CVD synthesis fundamentally differs from the preceding methods because diamond is not thermodynamically stable at the growth conditions. In contrast to the natural genesis, the pressure is lower by many orders of magnitude ($1 - 10^5$ Pa). It can be used to deposit thin layers of monocrystalline or polycrystalline diamond. The growth of bulk diamonds is possible when longer deposition times are used [144]. In this work, we use the CVD diamond synthesis for sample preparation and therefore we describe this method in detail.

The CVD synthesis is used to grow thin diamond layers on suitable substrate materials. The substrates are loaded into the deposition chamber, which is filled with precursor gases. Usually, mixture of methane and hydrogen is used. The gases are activated into radicals by certain source of energy (microwaves, hot filament, arc discharge, or combustion flame [145]). Chemical reactions proceed between the activated species in the gas phase and on the surface of the substrate [146]. When the parameters are optimized, the diamond layer grows on the substrate.

In this process, methane acts only as the source of carbon atoms and its concentration is usually low (1 – 10%). Other hydrocarbons may eventually be used instead of methane to supply carbon atoms. On the other hand, hydrogen is the key component which facilitates the diamond growth through several mechanisms. Firstly, it effectively etches sp^2-hybridized bonds between carbon atoms and suppresses the growth of graphite, which is thermodynamically more stable than diamond [146]. Diamond sp^3-hybridized bonds are also partially etched by hydrogen radicals but with a significantly slower rate. If the conditions are well balanced (by pressure, power, temperature, gas dilution) the difference in etching rates enables the growth of pure diamond phase. Secondly, atomic hydrogen enhances the activation of hydrocarbons. Finally, hydrogen atoms terminate the dangling bonds on the surface of diamond and prevents the surface graphitization.

Additional gases (e.g. O_2, Ar, CO_2 [145]) may be used to tune the properties of diamond such as grain size, chemical purity (the ratio between sp^3 and sp^2 phase), or optical properties. Other gases (e.g. N_2, SiH_4 [147]) are used to introduce dopants into diamond which may, for instance, increase its conductivity or create optical centers. Impurities may also originate from the substrate material or chamber walls, which may be partially etched by reactive species during growth. On the other hand, ultrapure diamond with impurity concentration < 5 ppb can also be prepared using the CVD synthesis [148]. It is also possible to use isotopically enriched methane for growth, which results in a better physical properties (longer coherence time of color centers, thermal conductivity) of the diamond layers [149,133].

The growth of diamond strongly depends on the properties of a substrate material. The simplest situation is when diamond grows homoepitaxially on the diamond substrate. In the case of a non-diamond substrate material, the growth of diamond begins with the so called spontaneous nucleation process, when the first stable clusters of carbon atoms with diamond structure are created in the gas phase or on the substrate surface [34]. Clusters must overcome the energetic barrier (achieve a given size) in order to become stable. The size of energetic barrier (denoted as nucleation barrier) is given by the deposition conditions – deposition system, gas mixture, pressure, or temperature [150] – and by the substrate material. The nucleation process may be enhanced by various methods such as scratching, biasing, or coating of the substrate [146]. The growth on non-diamond substrate usually results in a formation of polycrystalline diamond layer, although the growth of single crystal diamond, so-called heteroepitaxy, was demonstrated on some substrates (e.g. on Ir [151]).

As the spontaneous nucleation process is typically slow and nucleation density (i.e. number of diamond clusters per unit area) relatively low for growing continuous films, the substrate material is often seeded with diamond powder before deposition (e.g. in ultrasonic bath). Subsequently, diamond grows directly on the present diamond nanoparticles from the powder. Since the diamond nanoparticles are randomly oriented after seeding, the process results in the formation of a polycrystalline diamond layer with predominantly random orientation of individual crystals.

High temperature (> 500°C) is usually used for diamond growth, which is not suitable for growth on temperature sensitive substrate materials (semiconductors, glass, plastics, or amorphous Si) [146,152]. For instance, defects, which deteriorate their electronic properties, may be created in semiconductors at elevated temperatures. Moreover, high strain may be induced inside the material, when there is large difference between coefficient of thermal expansion of diamond and the substrate material. In some cases, it may cause cracking and delamination of thin diamond layers. Those unwanted effects may be reduced by performing the diamond growth at lower temperatures (even below 100°C [153]). Nevertheless, the low temperature decreases the growth rate and may worsen the quality (material purity, grain size) of the diamond layer.

3.3 Color centers in diamond

Spatially localized electronic states may be introduced into the diamond band gap due to the crystal lattice defects. The presence of some defects causes that the diamond crystal is not transparent for the whole visible region anymore and the crystal shows some specific color. These defects are thus called color centers. The color centers are linked to specific types of crystal defects, such as impurity atoms (N, Si, Ge, etc.) often accompanied with neighboring vacancy in the crystal lattice.

Optically active color centers not only absorb light, but they are capable of emitting light at particular wavelengths during the radiative transition. Since the energy of the emitted light lies inside the band gap of diamond, the emission of color centers is not absorbed. The energy of electronic states of color centers is strictly defined for individual impurities and, thus, characteristic spectrally narrow zero-phonon lines (ZPL) may be observed in the PL spectra of diamond. ZPLs are often accompanied by phonon sidebands at longer wavelengths, which originate from excitation of lattice vibrations (phonons) during electronic transition. Diamond can host more than 500 luminescent centers with various spectral positions of ZPLs and various optical properties [138,69]. However, only some of them are associated with the impurity atom and their electronic structure is known.

Isolated color centers are often referred to as artificial atoms because of their strictly defined electronic levels. Their advantage over classical atoms or molecules lies in their fixed spatial position inside the diamond lattice. The color centers can thus be directly addressed, and their PL may be collected. When the individual color centers are spatially isolated, they have the properties of single photon sources – they emit maximally one photon in one excitation cycle.

The ability of the color centers to act as single photon sources attracted wide interest [69,149,154–156]. The ideal single photon source emits exactly one photon on demand in one excitation cycle [69] and the emitted light has antibunching photon statistics. The diamond color centers resemble the properties of ideal single photon sources and thus have a potential to be the basic components for building quantum networks and quantum computers [157–159]. Nevertheless, there are also other attractive applications, such as the detection of weak magnetic fields [160] or the realization of fundamental quantum mechanical experiments [161], based on the color centers. Moreover, the photoluminescence of the color centers that are placed near the diamond surface depends on the properties of the surrounding environment. Therefore, diamond with color centers can be used also for sensing applications [137,162–164].

Some other systems may also act as single photon sources, e.g. non-linear optical effects in some materials, organic molecules or quantum dots [67]. Nevertheless, the advantage of the diamond color centers lies in their reproducibility, which originates from diamond rigid crystal lattice, color centers photostability even at room temperature, narrow PL bandwidth, and long coherence times [69]. Recently discovered color centers in other materials, particularly in silicon carbide (SiC) or Si, seem to be an interesting alternative for the diamond color centers. The color centers in SiC and Si are advantageous for long-range communication because they emit light in the telecommunication windows [73,74,165]. Moreover, the fabrication techniques for Si and SiC are more developed in comparison to diamond.

3.3.1 Color centers fabrication

Color centers are present in both natural and synthetic diamonds. Nevertheless, fabrication of synthetic diamonds offers the possibility to control the amount of impurities and also to support or suppress the creation of the color centers. Color centers may be created during the CVD synthesis if the corresponding impurity atoms are present inside the chamber. Impurities may be added into the chamber intentionally. For example, the addition of small concentration of SiH_4 or N_2 between precursor gases results in the formation of Si- and N-related color centers in diamond, respectively [147]. Similarly, silicon wafers placed near the active plasma region in the reactor serve as a source of Si atoms [166,167]. The plasma partially etches the silicon wafer surface, and Si atoms fill the chamber. On the other hand, unwanted color centers formation may occur during the growth. It can be caused by the plasma etching of the substrate material or the deposition chamber. Beside this, the chamber may be contaminated with impurities from previous depositions or with residual atmospheric gases (mainly N_2), which remain inside the chamber.

Parameters during the growth determines if the impurity atoms form optically active color centers [168]. It may happen that the light-emitting color centers are not formed despite the presence of impurity atoms in diamond. For instance, the color centers photoluminescence is quenched in the diamond layers with large stress or in the diamond layers grown with high concentration of methane, which results in the formation of large number of material defects that act as nonradiative recombination centers [169]. Quenching could be also caused by the aggregation of multiple impurity atoms in one place when the concentration of impurity atoms is too large. Moreover, some color centers (e.g. N- or Cr- related) are not created directly during the growth and postprocessing, which involve creation of vacancies (e.g. by electron irradiation) and thermal annealing, is required.

The disadvantage of the creation of color centers during the CVD growth is that this method offers only limited control over their position. The vertical position (with respect to the growth direction) of the color centers can be controlled in the delta doping technique when the precursor gas with impurity atoms (e.g. N_2) is introduced into the chamber in a pulse only for a short period of time [170]. When the concentration of impurity atoms is low (below 1 ppb), individually optically addressable color centers can be produced by the CVD in the monocrystalline diamond [171]. However, there is no control over the lateral position of color centers on the sample.

The second method of the color centers preparation is the ion implantation. In this method, accelerated ions impact on the surface of a natural or synthetic diamond and penetrate into the diamond crystal structure. The depth of penetration depends on the ion energy and may be predicted by the Monte Carlo methods (e.g. stopping and range of ions in matter (SRIM) [172]). Nevertheless, diamond color centers are not created during the implantation itself. The impacted ions are not properly incorporated into the lattice positions and the diamond crystal lattice is damaged by the impact of the ions, which causes unwanted nonradiative transitions. Therefore, diamond must be annealed after the implantation. During the annealing the diamond lattice is partially recovered. At temperatures above 700°C the vacancies in diamond become mobile [173]. They are usually trapped by the implanted ions, because it is energetically favorable, and the color centers are created.

The ion implantation method offers high control over the lateral position of color centers [156]. Impurity density and location may be precisely controlled by the ion dose and the ion optics [174]. On the other hand, the yield of optically active centers is low. Single photon emission was first achieved by Wang et al. in monocrystalline diamond implanted with N ions in 2005 [175]. The ion implantation method can be used to create single photon sources inside diamond nanostructures [176]. To obtain very high lateral resolution (in nm scale) an AFM tip with small hole has been used as an aperture during the implantation process [177]. This method was used to create NV centers inside PhC cavities [112]. Nevertheless, the more common approach is to identify the position of color centers first and create the cavity around the pre-selected color centers in the next step [62].

3.3.2 Nitrogen-vacancy center

The nitrogen-vacancy center is the most extensively studied color center in diamond. It is formed by the substitutional nitrogen atom and the adjacent vacancy in the diamond lattice (Fig. 24a). Two charge configurations of NV centers exist, which differ in the spectral positions of the ZPL (Fig. 24b). The ZPL of neutrally charged NV^0 center is located at 575 nm with a broad and intense phonon sideband ranging from 580 to 650 nm. The negatively charged NV^- center

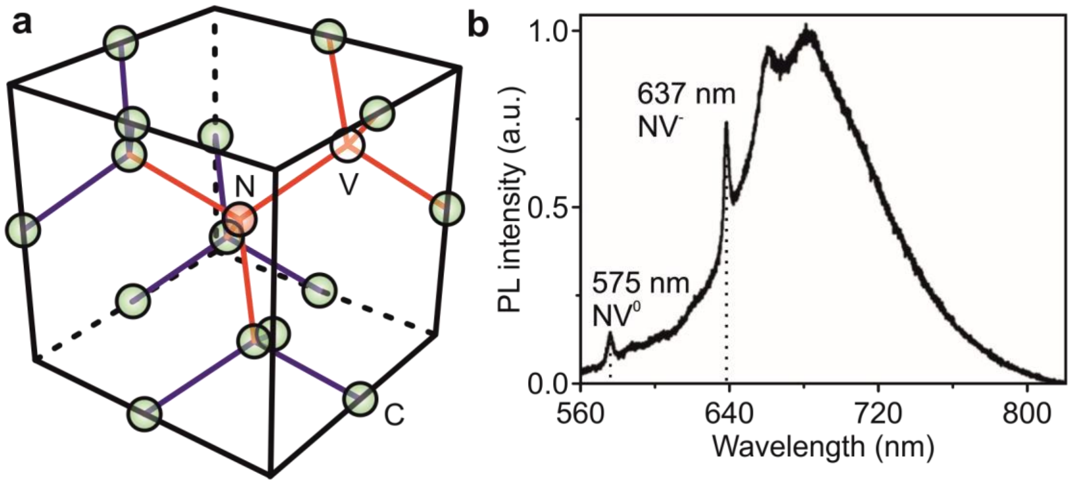

Figure 24: **(a)** Diamond lattice with NV center, which is formed by N atom adjacent to a vacancy (V). **(b)** Room temperature PL spectrum showing ZPL of neutral (575 nm) and negatively charged (637 nm) NV center with their phonon sidebands. (b) is reproduced from [69].

has one additional electron that is trapped at the color center, and its ZPL is shifted to the red part of the PL spectra to 637 nm, again with the intense phonon sideband sprawling up to 800 nm.

There are many prospective applications of diamonds with NV centers. When the NV centers are placed near the diamond surface (e.g. NV centers in nanodiamonds) the charge configuration may change depending on the local environment [163,178,179]. This property is promising for applications in sensing. The NV^- centers exhibits optically detected magnetic resonance (ODMR) [180] and the measurement of very weak magnetic fields using NV^- centers was already demonstrated [160,181,182]. Isolated NV centers were also demonstrated to act as single photon sources [154,183] that may be fabricated even by the CVD method [155].

A property that makes NV^- centers especially suitable for single qubits in a quantum information processing is their very long coherence time [69]. The ground and excited states of NV^- centers form spin triplets, where the $m_s = 0$ and $m_s = \pm 1$ lines can be observed at low temperature. The transition between these two spin polarizations may be induced and controlled by microwaves [63]. Thanks to the rigid diamond lattice, the spin-orbit coupling is reduced. This leads to very long spin-lattice relaxation time which reaches to 5 ms at room temperature and hours at cryogenic temperatures [149]. The spin coherence time can be as high as microseconds at room temperature and seconds at the cryogenic temperatures [184].

This long coherence time is very sensitive to the crystal defects in the neighborhood of the center. For instance, the spin relaxation time is reduced in nanodiamonds and polycrystalline diamonds with small grains due to the proximity of surface states [185]. Furthermore, the presence of impurities in the diamond crystal can decrease the spin coherence times due to their interaction with NV centers. To achieve very long coherence times the concentration of impurities and of ^{13}C carbon (natural abundance 1.1% [186]) must be reduced, which may be achieved during the CVD growth with isotopically purified methane or by the HPHT method.

Despite the many interesting properties (long spin coherence times or single photon emission), the usage of NV centers is limited by their strong phonon coupling. The Debye-Waller factor, which is the ratio of the ZPL intensity to the total PL intensity of the center is only 0.05 even at low temperature [187]. Only 5% of photons are emitted into the narrow ZPL, while the rest of the photons are emitted into the broad phonon sideband. Therefore, the properties of other color centers are being investigated to find more suitable single photon sources.

3.3.3 Silicon-vacancy center

The silicon-vacancy center is formed by Si atom placed in a split position between two adjacent vacancies in the diamond lattice (Fig. 25). The most common state is the negatively charged SiV$^-$ center, which has the ZPL located at 738 nm (Fig. 25) with weak phonon sideband centered at 757 nm and the Debye-Waller factor at room temperature around 0.7. The Debye-Waller factor is significantly better compared to the NV centers. The spectral width of ZPL at room temperature is less than 10 nm, which is also narrower in comparison with the ZPL of the NV centers. The luminescence wavelength in near infrared is favorable for applications in medicine due to low absorption and background luminescence of tissues in this spectral region.

Thermodynamically stable SiV centers were observed in nanodiamonds smaller than 2 nm [188], while the NV centers are unstable in such small nanodiamonds. Other advantage over the NV centers is the easy fabrication of SiV centers, which are created spontaneously when Si atoms are present in the CVD chamber during the diamond growth. On the other hand, the amount of spontaneously created SiV centers is usually very high and special methods must be employed to prepare single SiV centers capable of acting as single-photon sources by the CVD [171,189]. Present studies show that SiV centers can be used for similar applications as NV centers: single photon sources for quantum information processing [171], sensing [190], or biomarking [191].

The first experiments have shown lower intensity of SiV centers in comparison with NV centers [69], which is caused by the complicated electronic structure of the SiV center. The electronic structure forms a three-level system, where the individual levels are split due to the spin-orbital coupling [192]. The electron from the upper excited state quickly decays to the PL active state. Nevertheless, it may then transit either radiatively to the ground state or non-

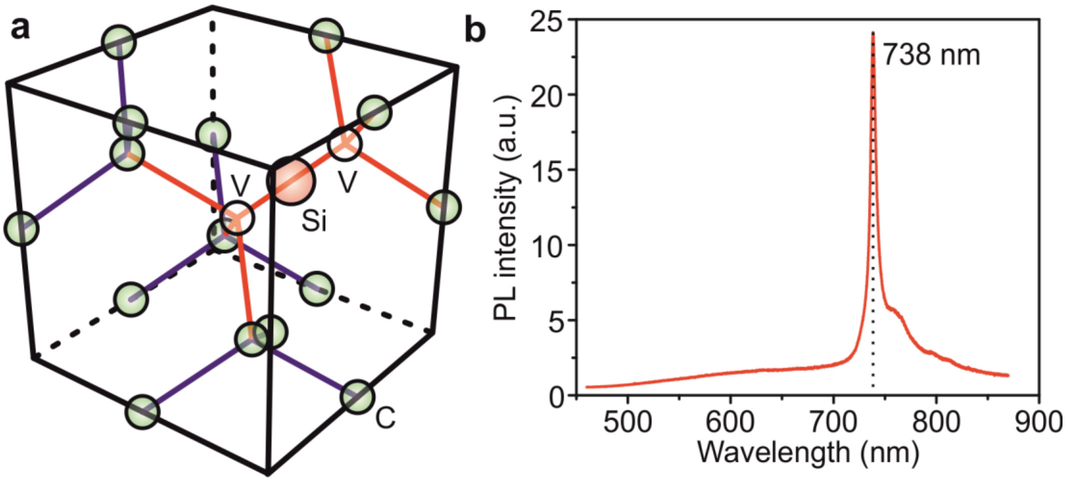

Figure 25: **(a)** Diamond lattice with SiV center, which is formed by Si atom in a split position between two vacancies (V). **(b)** Room temperature PL spectrum showing ZPL of SiV center (738 nm) with the phonon sideband (757 nm).

radiatively to a shelving state. The metastable shelving state is responsible for the lower count rate of SiV centers when compared to NV centers. However, it was shown later that the transition to the metastable state can be suppressed in some cases (e.g. in high-purity diamonds [193]) or the life-time of the metastable state can be reduced in nano-diamonds [75], which leads to the increased count rate by up to three orders of magnitude. The count rate and the intensity of SiV centers in nanodiamonds then exceeds the count rate of NV centers.

The model described in Ref. [192] places the SiV ground state 2.05 eV below the conduction band edge. Nevertheless, a new model, which is based on the photoluminescence excitation spectroscopy and ab-initio theoretical modelling, have been suggested recently, which includes also change of electronic levels during excitation and de-excitation processes [194,40]. SiV centers have also neutrally charged state (SiV^0), ZPL of which is located at 945 nm. Nevertheless, the intensity of SiV^0 centers is low and its practical utilization is, thus, questionable. The generally accepted model of the SiV center electronic structure is still missing.

4. Fabrication of photonic structures in diamond

The fabrication of photonic structures in diamond can be done by standard lithographic methods where parts of the sample are selectively removed (top-down) or by direct growth of photonic structures on the patterned substrate (bottom-up). The methods for top-down approach are very precise and well established in semiconductors technology (mainly for silicon). Nevertheless, the processing of diamond is complicated due to its hardness and chemical inertness. Specific procedures or parameters are thus required, which limits the range of possible applications. Moreover, the top-down approach is often available only for creating small structures on a limited number of samples (e.g. for research) and its up-scaling is both expensive and time-consuming.

On the other hand, the bottom-up approach is, for the case of diamond, based on the growth of a diamond layer on the already patterned substrates. This approach substitutes the complicated structuring of the diamond by the structuring of the substrate, which is typically easier and can be up-scaled. However, it often suffers from difficulties with the diamond growth on foreign substrates. For instance, the change of the substrate topography alters the diamond nucleation and growth, or some substrates cannot be used for the depositions at elevated temperatures. Moreover, the CVD method that is used in the bottom-up approach from a seeding layer or by the spontaneous nucleation results mostly in the polycrystalline layer. The polycrystalline diamond layer is not suitable for some applications, e.g. for single photon sources, due to its worse optical properties in comparison with monocrystalline layer.

Top-down and bottom-up approaches are often combined, e.g. the top-down approach is used to pattern the non-diamond substrate for the subsequent CVD growth, or the bottom-up approach is used to create mask for the top-down fabrication. These combined methods are attractive for up-scaling the processed area that is necessary for the practical usage of photonic structures.

Many photonic structures require the usage of monocrystalline diamond to achieve the optimal performance [62,110,195]. Nevertheless, the preparation of monocrystalline diamond and the subsequent fabrication is often challenging and requires expensive devices. On the other hand, the advantage of polycrystalline diamond lies in its cost-effective fabrication and in the fact that many photonic structures are based on thin layers that can be easily deposited on various types of substrates using the CVD method [34,146]. The deposition of high-quality monocrystalline layer on a foreign substrate by the CVD method is possible but very challenging [196,197].

The disadvantage of polycrystalline diamond is the inherent optical absorption caused by the presence of non-diamond carbon phase in the boundary between individual grains. Beside the absorption, light is also scattered on the grain boundaries and also on the surface roughness, even though the latter can be reduced by smoothing processes [198]. Moreover, the density of color centers is very difficult to control during the CVD and the background photoluminescence from non-diamond carbon bonds complicates the isolation of photons from single photon sources.

There are also approaches, where the fabrication in diamond is completely avoided by creating the photonic or plasmonic [199–202] structures in other materials. Subsequently, simple diamond samples such as slabs or nanoparticles are placed into the vicinity of these structures. An example of this approach is the fabrication of microscopic Fabry-Perot cavities from silicon, into which the diamond slab with color centers is inserted [48]. Another example is the placement of diamond nanocrystals with color centers into the vicinity of photonic cavities [113] by precise positioning, which can be done by the AFM [114]. These methods benefit from the possibility to choose samples with high material quality, not deteriorated by fabrication procedures or non-ideal diamond growth parameters. However, the placement of color centers is often not ideal with respect to the maximum of the cavity field, which limits the performance of such photonic structures.

4.1 Top down approach

In the top-down processes, bulk diamond or planar diamond layer deposited by the CVD are used as a starting material. Subsequently, part of the material is removed to create photonic structures in the sample. Common methods for the material removing are reactive ion etching (RIE) or focused ion-beam (FIB) milling.

4.1.1 Lithography and reactive ion etching

The RIE a dry etching method where a plasma is ignited near the substrate surface. When the sample is negatively biased, the high energetic ions from plasma attacks the sample surface. The movement of the ions can be controlled by the electric field, and the ions can be directed to hit the sample in some primary direction (usually vertical with regard to the sample surface). The directional movement of the ions results in the anisotropy of the etching process and allows to create deep holes with almost vertical sidewalls inside the properly masked material.

The RIE works at large surface areas and thus allows large scale processing. Nevertheless, to create specific structures selected areas on the sample must be covered by a mask. The simplest method to produce the mask is photolithography [203]. To create the mask, the sample is first covered with a light-sensitive material, called a photoresist, usually by the spin coating. Selected areas on the sample are then exposed to light, which changes the properties of the photoresist. The sample is often illuminated through the mask to achieve selective illumination of the photoresist. This method is advantageous over the direct writing of the pattern with a laser beam, because it allows to process the whole sample area during one exposition step.

Commonly, organic materials that degrade after illumination (positive photoresist) or materials consisting of monomers which polymerize after illumination (negative photoresist) are used as the photoresist. In the case of the positive photoresist, the illuminated part is more prone to dissolve in chemical solution (called developer) and is removed, while the rest of the photoresist stays on the sample. In the case of the negative photoresist, the illuminated part stays on the sample. The individual photoresists differ in various parameters such as sensitivity to light, contrast between the illuminated and not-illuminated part, edge profile, or adherence to the sample.

The developed photoresist can be directly used as the mask for the RIE in some cases. Nevertheless, a metal layer is often deposited over the sample with a developed photoresist mask to improve the resiliency of the mask during the RIE. Subsequently, the photoresist is removed from the sample together with the metal deposited on the top. This method is denoted as lift-off and results in the inverted pattern with regard to the patterns formed by the photoresist after the development (Fig. 26a).

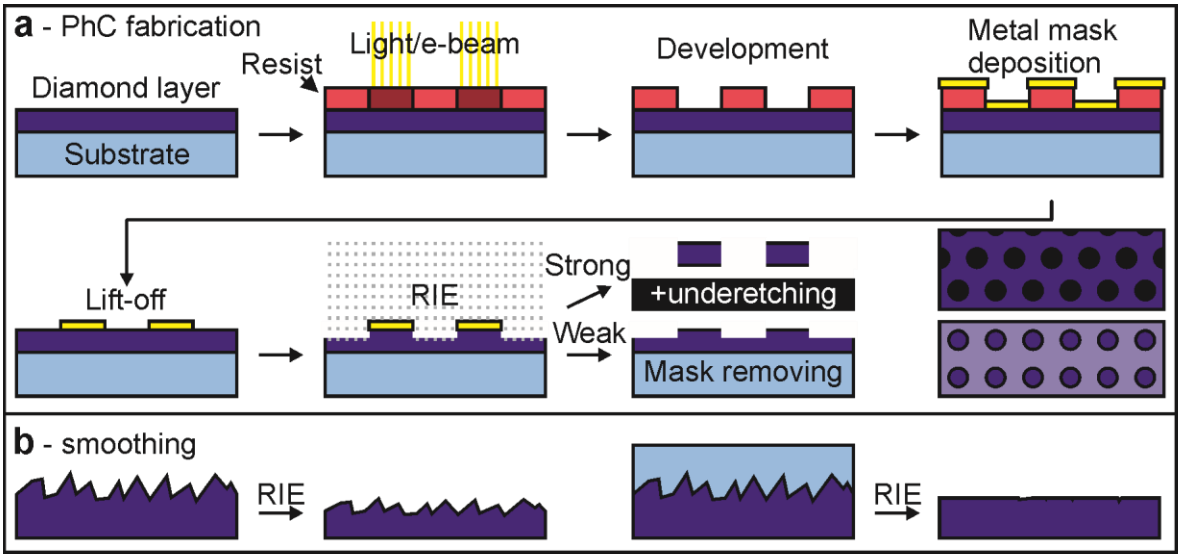

Figure 26: **(a)** Top-down fabrication of PhC structures in diamond: Thin diamond layer on substrate is covered with resist, which is illuminated by light or electron beam. The illuminated parts are removed during development (positive photoresist). Metal mask is deposited on the sample and the excess part is removed by lift-off. The reactive ion-etching (RIE) is applied through the mask, which leads to highly directional etching. Only part of the layer is removed in the case of weak slabs. For strong slabs, holes are etched through the whole diamond layer and part of the substrate is removed by wet etching, which leads to suspended membrane needed for structures with band gap. **(b)** The RIE can be also used for smoothing of the layer. When the RIE is used without mask, the surface roughness is reduced. Lower surface roughness can be achieved when some other material is deposited on top and the RIE with similar etching rate for both materials is applied.

The minimal dimensions (resolution) of the structures produced by photolithography are limited by the wavelength of the employed light. Therefore, UV light is often used for photolithography. Yet, the dimensions of photonic structures often lie below this limit and photolithography thus cannot be used for their fabrication. One solution is to use electromagnetic radiation with shorter wavelength (XUV, X-rays). Nevertheless, simple optical components and masks for visible light cannot be used anymore which makes the devices and fabrication of masks more expensive. These methods are thus mainly used for serial production of components, where the same patterns are produced repeatedly.

An alternative approach is to use the electron beam lithography (EBL) with the resist sensitive to the illumination by electrons. The wavelength of electrons depends on their kinetic energy and they can be focused to spots with the diameter in nanoscale (down to few nm) when they have sufficient kinetic energy. The devices for the EBL are similar to scanning electron microscopes but with the beam path not restricted to the scanning movement. There are several differences between the EBL and photolithography. Firstly, the electron beam is usually used to directly draw the patterns into the resist. Secondly, the electron beams are formed by electromagnetic lenses and the individual electrons in the beam repulse each other, which increases the beam size. Thirdly, the electrons are not absorbed by the material instantly, but lose their kinetic energy during multiple scattering events inside the resist. This results in the further increase of the minimum pattern size, which is typically several tens of nm. All these effects have to be considered when drawing patterns with the electron beam. The combination with a scanning electron microscope, can be used to find specific places on the sample, where the photonic structures are created.

The mask can also be created by bottom-up approaches. For instance, the periodic photonic structures (mostly with hexagonal symmetry) can be prepared by nanosphere lithography, where the mask is composed of spheres with diameter as low as several hundreds of nanometers [204]. The periodic patterns can be formed by self-assembly of micro-spheres, for example, on the surface of liquids. This method does not require any special devices, but there is only limited number of available patterns [89,205].

To create strong PhC slabs the diamond layer must be suspended in the air to prevent coupling between the TE and the TM modes. For this, part of the substrate below the diamond PhC slab must be etched away. Wet etching, which is isotropic is usually used for that purpose. For better control the substrate (e.g. Si) may be covered by a thin sacrificial layer (e.g. SiO_2). The sacrificial layer can be then selectively removed by wet etching (e.g. HF). The etchant reaches the sacrificial layer through the holes in the diamond layer.

The RIE can be used also for the surface roughness reduction [206,207], which is very important for photonic structures, where the scattering of light on rough surface is undesired. The process of the so-called planarization starts with the deposition of a cover layer on the top of the sample by spin coating (Fig. 26b). After the congelation of the cover layer, the RIE is used to etch the surface of the sample. A specific plasma chemistry is selected to achieve similar etching rate for the material of the layer (e.g. diamond) and for the top material. The similar etching rate allows to etch away the top parts of diamond grains, which effectively reduce the surface roughness. Note that when no material is deposited on the top of diamond, the etching rate is similar for peaks and valleys between them and the surface roughness is not significantly affected.

4.1.2 Focused ion beam milling

In the FIB milling method, heavy ions (e.g. gallium or argon) impacts on the surface of sample and causes the removal (sputtering) of atoms from the sample. In contrast to the RIE, the ions form a narrow beam, similarly to the electron beam, that can be used to directly write the patterns into the sample. The ion beam is again manipulated by electromagnetic lenses and the minimal resolution is in the range of tens of nanometers [208].

The limitation of the FIB milling is that it requires conductive samples, otherwise the charge accumulates on the surface and causes defocusing of the beam, which causes additional artefacts and loss of resolution. For non-conductive materials, such as diamond, an additional electron beam can be used to neutralize the sample, or the sample must be covered by a thin conductive layer before the fabrication in order to channel off the excess charge. Another drawback is that the sputtered atoms may be re-deposited back onto the sample and contaminate the surface.

An advantage of the FIB milling is that it is often combined with electron microscope and thus the obtained structures can be characterized in-situ [62]. The images can be also taken directly with the ion-beam, which may provide additional information about the sample. The FIB milling can also be used to decrease the surface roughness of the sample [209], which may be advantageous when the photonic structures are built in polycrystalline diamond.

4.2.3 Hydrogenated amorphous Si micro-structuring

The micro-structuring of a thin hydrogenated amorphous silicon (a-Si:H) layer that utilizes conductive atomic force microscope (AFM) is not as widespread as the previously described standard lithography methods. Nevertheless, we used this alternative approach in this work to create patterned layers of a-Si:H for further bottom-up diamond growth. The advantage of this method for us was the presence of the conductive atomic force microscope in our laboratory and existing prior experiments.

Thanks to the absence of long-range order, amorphous silicon (a-Si) differs from crystalline silicon in many physical properties. Most importantly the band structure and band gap width are modified. This leads to various applications, in which a-Si outperforms crystalline Si. For instance a-Si can be used for light generation [210], photovoltaics [211], or fabrication of electronic elements (e.g. transistors or photodetectors) [212]. Apart from the absence of long-range order, some Si atoms are not bonded to four closest neighbors and the material contain unsatisfied dangling bonds. The dangling bonds scatter electrons and deteriorate the electronic properties (causes low conductivity) of a-Si. Nevertheless, the dangling bonds may be passivated by hydrogen in hydrogenated amorphous silicon (a-Si:H), which is usually used for fabrication of the devices [213–215].

The CVD method is commonly used for preparation of thin a-Si or a-Si:H layers. Silane (SiH_4) is used as a precursor gas. Additional gases may be used to prepare layers with high hydrogen content (H_2 and He) or for doping (PH_3 or B_2H_6). There are no special requirements on the substrate material because the deposition can be done at low temperatures (< 200°C).

When heated above 600°C, the a-Si crystallizes into micro- or nano-crystalline silicon, which consist of small Si crystals with amorphous phase between them. Micro-crystalline silicon is also used for fabrication of some devices (e.g. solar cells [216]). The crystallization temperature may be decreased when certain silicide forming metals (e.g. Ni or Cr), which act as catalyzers, are present [217]. Furthermore, the crystallization may be induced by application of electric field. The crystallization may then occur even at room temperature in the process called field-enhanced metal-induced solid phase crystallization (FE-MISPC) [218].

The AFM tip can be used to locally apply the electric field to a thin layer (~200 nm) of a-Si:H and to cause local crystallization of a-Si:H through the FE-MISPC process [213]. To achieve crystallization at room temperature, a-Si:H with high hydrogen content in layers (20 – 45 at. %) must be used. Moreover, it must be deposited on silicide forming metal substrate (e.g. glass coated with 40 nm Ni film) which acts both as crystallization catalyzer and as electrode for supplying voltage. During the crystallization process, the volume of material decreases, and a microscopic pit is created (Fig. 27).

Application of the electric field in a constant current regime leads to better control over the process when compared to constant voltage regime. The size and the shape of the pits depend on the current magnitude and the properties of the AFM tip [213]. It was shown that by using special circuitry (metal over semiconductor field-effect transistor (MOSFET) and feedback circuitry) for a better control over the electric current, non-conductive pits can be prepared [220]. The material in those pits remains amorphous and their size is better defined. It was deduced that the crystallizations occur during discharging of parasitic capacitance when special circuitry is not used and uncontrolled electric current flows through the sample.

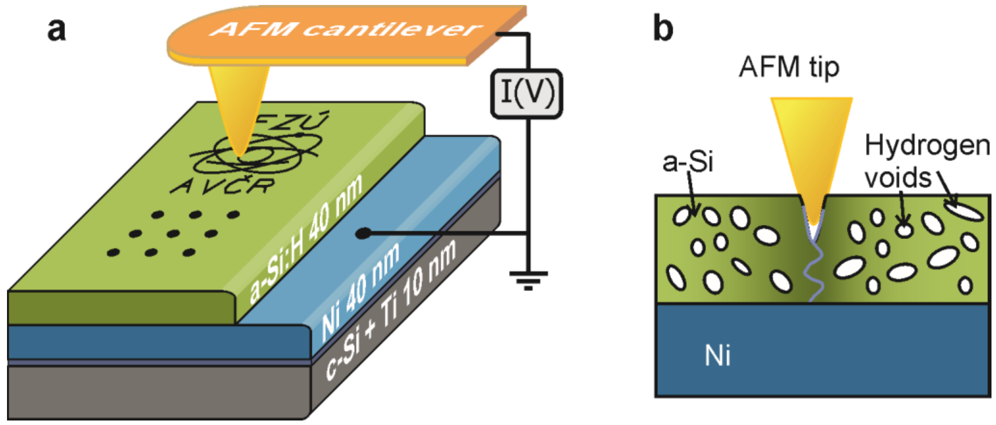

Figure 27: **(a)** Schematic drawing of the experimental setup for a-Si:H patterning. Reproduced from [219] **(b)** The volume of a-Si:H decreases after the local application of the electric field by conductive AFM because hydrogen leaves the layer. The crystallization of a-Si may be prevented by controlling the maximal current flowing through the layer.

Subsequently, it was shown that the pits (both conductive and non-conductive) can be used for selective deposition of silicon nanocrystals using CVD deposition of Si [215]. The creation of nanocrystals was evidenced by increased conductivity inside the pits after the deposition, which was not observed prior the deposition, and also by Raman micro-spectroscopy. The pits act as nucleation sites for creation of the nanocrystals [221,222] during subsequent deposition of silicon by CVD. There are more factors that can cause the preferential nucleation inside the pits such as the presence of material defects (cracks, non-homogeneities) in a-Si:H layer, higher mechanical strain in the layer, or higher concentration of precursor gases inside the pits. Most probably, a combination of these factors is responsible for the nucleation. Such nanostructures could be used also as template for bottom-up growth of diamond structures.

4.2 Bottom-up approach

Bottom-up approach for creating nanostructures relies on the self-assembly of small building blocks, usually atoms and molecules, into complex systems. The CVD diamond growth can be considered as self-assembly of carbon atoms under specific conditions. Complex molecules can be modified to directly create complex shapes by self-assembly [223]. This is not the case of diamond, and some external input must be used, usually in the form of patterned substrate, to achieve growth of complex shapes. Generally, the bottom-up fabrication process is not well controlled, and many structural defects may be present. Bottom-up process in diamond is thus not effective for creating structures that demand high precision of fabrication, such as the strong PhC slabs or the PhC cavities. On the other hand, weak PhC slabs are not as sensitive to the structural imperfections and the bottom-up approach offers a cost-effective alternative to the expensive top-down fabrication.

For the bottom-up approach, the substrate material is patterned prior to the diamond deposition usually by one of the top-down approaches described earlier. The diamond then either grows more or less homogeneously on the whole substrate and simply copies the substrate geometry to create desired structures (such as in Ref. [20], Fig. 28a), or it grows only on the selected surface areas, while the growth is suppressed on others (Fig. 28b-d) [224,225]. The bottom-up approach thus allows to create structures in the material that can be easily processed, such as silicon or glass, and to completely skip the process of creating structures in diamond.

Nevertheless, this method brings new problems due to specific conditions that are needed to achieve diamond growth on foreign substrates.

4.2.1 Spontaneous nucleation of diamond

It is relatively easy to achieve homogeneous diamond growth over the whole sample by completely covering (seeding) the sample with diamond powder before deposition (e.g. in the ultrasonic bath with suspension of diamond nanocrystals). When only a part of the sample is selectively seeded, e.g. by using photolithography (Fig. 28b,c) [226], diamond preferentially grows at these areas and can create complex patterns. At the locations without the seeding, the spontaneous nucleation can be detrimental. On the other hand, spontaneous nucleation can be enhanced at the selected locations, which can also result in formation of complex patterns (Fig. 28d).

Without the seeding, the growth starts with creation of diamond nuclei during the spontaneous nucleation process. The nuclei emerge at the energetically favorable places (such as structural or crystal defects), which are denoted as the nucleation sites. The spontaneous nucleation rate is quantified by the nucleation density – the number of the nuclei per unit area [34]. The nucleation density depends both on the properties of the surface material, e.g. type of material, surface roughness, or carbon concentration on the surface [146], and on the parameters of the CVD deposition (type of CVD system, temperature, pressure, or methane concentration).

The spontaneous nucleation can be effectively initialized or suppressed by surface modification [146]. For instance, diamond preferentially nucleates in the nano- or micro-scale pits on the substrate, which may be artificially created by scratching the substrate [34]. The nucleation process is then controlled by the deposition conditions. The simplest method is to change the methane concentration in the chamber. Higher methane concentration usually leads to higher nucleation density and vice versa. Using this process, the deposition can be tuned to achieve growth only at the selected locations on the sample.

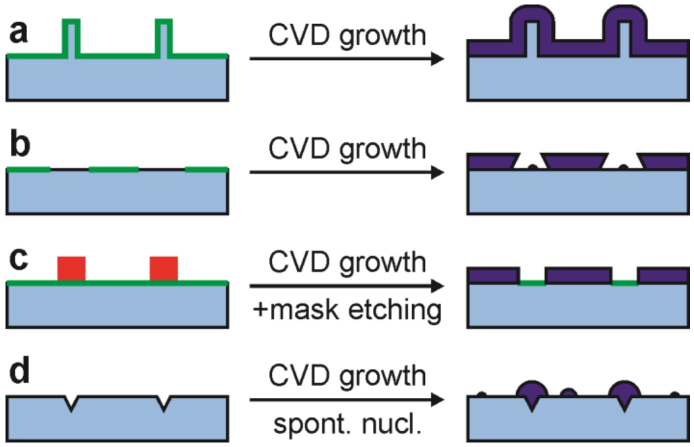

Figure 28: Schematic drawing of bottom-up processes: **(a)** The nucleation layer (green) covers the whole substrate, where topographical features are created by top-down processes. **(b)** The nucleation layer is deposited only to selected parts of the sample. Parasitic spontaneous nucleation or diamond nanocrystals coming from seeding layer may cause growth in the areas not originally intended for the diamond growth. **(c)** The nucleation layer is partially masked by material suppressing spontaneous nucleation of diamond (red). **(d)** Spontaneous growth of diamond in artificially prepared defects on substrate. Again, parasitic spontaneous nucleation may be present.

5. Experimental methods

5.1 Diamond deposition

In our work, two different chemical vapor deposition reactors were employed for the diamond growth: (i) focused microwave (MW) plasma reactor (*Aixtron P6*) using an ellipsoidal cavity resonator and (ii) linear antenna MW plasma system (*Roth & Rau AK 400*) equipped with two linear antennas working in a pulsed regime (Fig. 29) [227]. In the focused plasma system, the plasma is located in the vicinity of the substrates (1 – 2 mm) and high pressure is used during growth (1 – 20 kPa). This results in fast growth rate (typically ≈ 0.2 nm/s), heating of the substrate (typically 350°C – 1100°C), non-homogeneous growth rate over large samples, and may also result in the etching of the substrate. The etching of the substrate may be used to dope diamond with impurity atoms such as Si or Ge for creating SiV or GeV centers, respectively. The creation of SiV centers was also observed when no Si samples were placed inside the reactor [228]. The Si atoms originated most probably from the etching of the quartz bell jar that encloses the region with plasma.

The linear plasma system differs in the location of the plasma and in its better homogeneity over the sample. The plasma is typically located 7 – 10 cm far from the sample surface and lower pressure (10 – 1000 Pa) is used, which results in the slow growth rate (typically 0.01 nm/s) and enables the low temperature deposition (surface temperature as low as ≈ 100°C can be used).

For the growth of diamond layers for PhC slabs, both deposition systems were used, and the deposition parameters were chosen to grow diamond layers with high optical quality (low absorption). Bare Si wafer was placed near the samples in the focused plasma system as a supply of Si atoms for creation of SiV centers. In the case of spontaneous nucleation process, the parameters were chosen to achieve the highest nucleation density on Si wafer while keeping low temperature during deposition (max. ≈ 350 °C). The focused plasma system was used, in order to obtain optically active SiV centers, despite the linear plasma system is more advantageous for the diamond growth at low temperature.

Before the growth of samples for photonic structures, the substrates were ultrasonically cleaned in acetone and isopropyl alcohol and were rinsed in deionized water. Subsequently, the seeding was carried out by ultrasonic bath in aqueous dispersion of nanodiamond particles (NanoAmando, nanodiamond size 4.8 ± 0.6 nm) diluted by deionized water 1:40 v:v. The seeding for selective growth using a-Si:H mask was done by immersing the samples in the colloidal solution of FDP (Fumed Diamond Powder, NanoCarbon Research Institute, nanodiamond size 3.1 ± 0.6 nm) detonation nanodiamonds. Detailed description of the employed parameters can be found in the enclosed articles (attached at the end of the thesis).

5.2 Fabrication

Top-down and bottom-up strategies were used for the fabrication of diamond PhC slabs and PhC cavities. In the top-down process the diamond layer was first deposited using the CVD method on the planar substrate and subsequently the PhC was fabricated on the top of the layer. On the other hand, the substrate was patterned first in the bottom-up process and the diamond layer was deposited on the patterned substrate with no further modification.

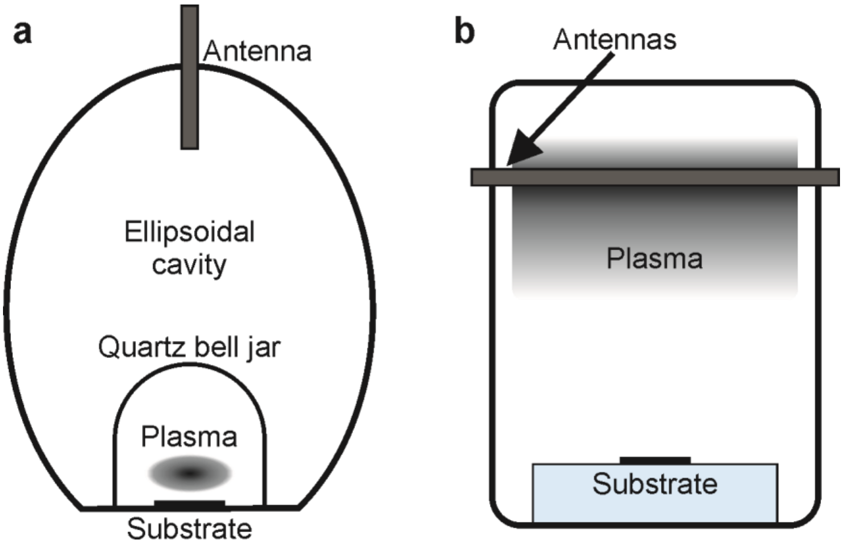

Figure 29: Schematic drawing of diamond deposition systems: **(a)** focused microwave (MW) plasma reactor (*Aixtron P6*) using an ellipsoidal cavity resonator, and **(b)** linear antenna MW plasma system (*Roth & Rau AK 400*) equipped with two linear antennas working in a pulsed regime.

5.2.1 Top-down PhC slabs and cavities

Quartz glass substrates (10×10 mm^2) were used as substrates for the fabrication of PhC slabs. After the diamond growth, the top part of the diamond layer was patterned to periodically ordered columns using electron beam lithography (EBL) and reactive ion etching (RIE). The electron sensitive polymer (PMMA, thickness ≈ 100 nm) was first patterned by EBL and gold (thickness ≈ 70 nm) was evaporated over the patterned PMMA. The mask was created by lift-off process. Not-covered parts of the sample were partially etched in the capacitively coupled O_2/CF_4 plasma RIE. Finally, the metal mask was removed by wet etching. Each of the PhC slabs was at least 1×1 mm^2 large. Only samples with square lattice symmetry were fabricated for simplicity.

In the case of PhC cavities, the diamond was deposited on Si wafer covered with the thin (> 1 µm) layer of SiO_2 prepared by oxidation of Si. After the diamond growth, the Al layer (thickness ≈ 80 nm) was deposited on the top by sputtering. The electron sensitive polymer layer (AR-P 617.06, thickness ≈ 200 nm) was patterned by EBL. The Al layer was partially removed by using an inductively coupled plasma reactive ion etching $SiCl_4$/Ar to create a mask for diamond etching. The polymer layer was fully removed in O_2/Ar plasma. The patterning of the diamond layer was done again in the capacitively coupled O_2/CF_4 plasma RIE. The metal mask was removed by wet etching. To create suspended membranes, the SiO_2 layer below diamond was locally removed by wet etching in the buffered oxide etchant (BOE) solution (7:1 volume ratio of 40% NH_4F in water to 40% HF in water).

5.2.2 Bottom-up PhC slabs

For the bottom-up growth of PhC slabs, the quartz glass was patterned using EBL and RIE. The process of metal mask preparation (Ti/Au with thicknesses ≈ 5 nm and ≈ 50 nm) is similar to diamond patterning described in the previous paragraph. The quartz glass was patterned in capacitively coupled radio frequency SF_6 plasma RIE. Samples with both the square and the hexagonal lattice symmetry were fabricated.

5.2.3 Hydrogenated amorphous Si

The structure of the samples used for a-Si:H micro-structuring is illustrated in Fig. 27a. The bottom electrode (Ni or Pt) was deposited using vacuum thermal evaporation on the substrate (monocrystalline Si) with 10 nm Ti adhesion layer. Thin layer of a-Si:H (thickness 40 ± 5 nm controlled by deposition length) was deposited using plasma-enhanced CVD. High hydrogen content (20–45 at. %) that is necessary for micro-structuring was achieved by using 0.02% of SiH_4 (1 sccm) diluted in helium (5000 sccm), and low temperature (50°C) of the CVD process. Constant electric current (0.5–15 nA) was locally applied to the sample using the Ni film (negative polarity) and the AFM tip as electrodes (see the section about AFM for details).

For the selective diamond deposition, the a-Si:H layer was deposited on Pt coated Si seeded with nanodiamonds. The layer was patterned by standard photolithography process (positive photoresist, 6 s exposition with UV light, 40 s in the developer) and dry etching in SF_6 plasma. The SF_6 plasma selectively removed a-Si:H on the parts of the sample not-covered by photoresist and revealed the seeding layer. The rest of the photoresist was removed in acetone bath.

5.3 Optical characterization

5.3.1 Raman micro-spectroscopy

Raman micro-spectroscopy was used for the material characterization of the samples. Two different systems with different excitation wavelengths were used: *Renishaw inVia Reflex*, excitation wavelength 442 nm, objective 100×; and *Horiba XploRA*, excitation wavelength 532 nm, objective 100×. The spatial resolution of both systems is below 1 μm.

The chemical purity of diamond layers (sp^3/sp^2 ratio) was estimated from the ratio of the area of diamond peak located at ~1331 cm^{-1} to the combined area of graphite band centered at ~1580 cm^{-1} and disordered graphite band centered at ~1360 cm^{-1} [150]. Note that this ratio does not show the actual ratio of sp^3 and sp^2 bonds in the sample, because the Raman scattering cross-section of sp^2 bonds is higher by approximately two orders of magnitude compared to sp^3 bonds. Moreover, the efficiency depends on the excitation wavelength. Diamond peak is more pronounced when the light with shorter wavelength is used. Nevertheless, the chemical purity of samples measured with the same excitation wavelength can be compared.

Amorphous and crystalline silicon was distinguished using Raman spectroscopy. The crystalline silicon has sharp (FWHM < 5 cm^{-1}) peak centered at approximately 520 cm^{-1} in Raman spectra. In contrast, a-Si has broad Raman band ranging from app. 420 cm^{-1} to 540 cm^{-1} due to non-defined bond energies and lengths. For microcrystalline silicon, the fraction of the amorphous phase may be determined from the ratio of these Raman peaks. Moreover, the Si-H and Si-H_2 bonds are evidenced around 2000 cm^{-1} [229] and the hydrogen content in a-Si:H can thus be estimated from the Raman spectra.

5.3.2 Micro-PL setup

The *Renishaw inVia Reflex* Raman system with excitation wavelength 442 nm was also used to measure the photoluminescence (PL) of the samples. Various objectives were used for the measurement: objective magnification 100× (NA = 0.9), 50× (NA = 0.5), 20× (NA = 0.4), and

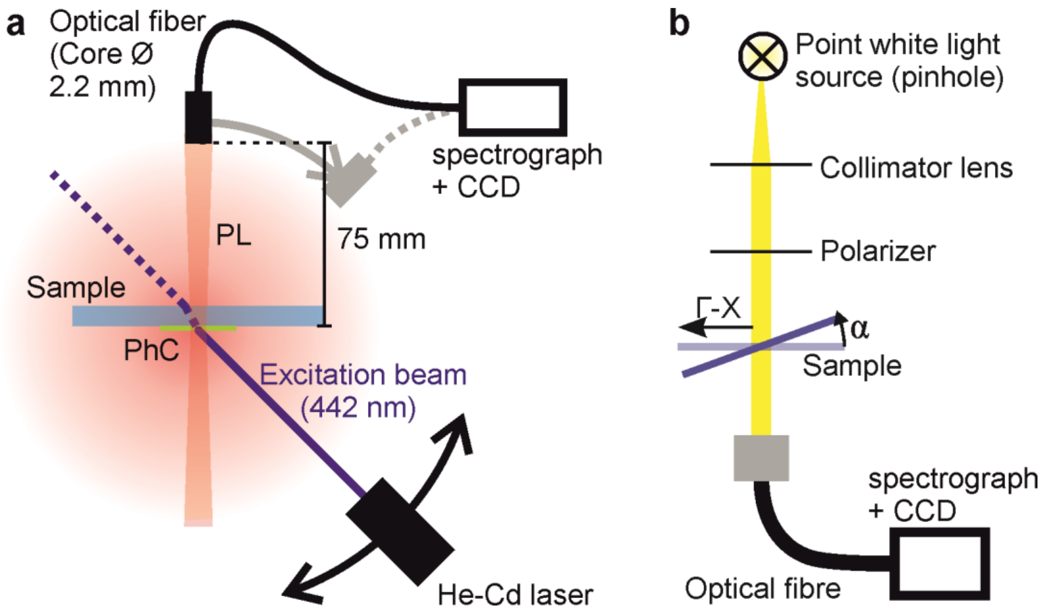

Figure 30: **(a)** Schematic picture of the setup used for angle-resolved PL. **(b)** Schematic picture of the setup used for angle-resolved transmission measurement.

5× (NA = 0.12). The 100× objective has large collection half angle (64.2°), which allows to measure weak signals (e.g. from diamond nano-crystals). On the other hand, the 5× objective has small collection half angle (6.9°) and, thus, it collects only signals propagating near to the vertical direction. We have used it to detect the leaky modes from PhC slabs.

5.3.3 Angle-resolved PL

The PL of the PhC slabs was probed also on another setup, which allows measuring the PL directed into very narrow solid angle (see Fig. 30a). Using this setup, we were able to measure light propagating into the vertical direction (near the Γ-point in the k-space, Fig. 18) with high degeneracy of leaky modes and thus the highest enhancement factor. This configuration greatly improves the spectral selectivity and is thus attractive for applications in sensing.

The signal was collected by a multimode fiber (core diameter 2.2 mm, NA = 0.22, angular resolution = 0.9°) coupled to a spectrograph (*Andor, Shamrock 303i* and detected by a cooled CCD camera). The distance between the sample and the fiber aperture was 75 mm. The angle of incidence of the excitation beam (HeCd CW laser, 442 nm) on the sample was adjustable. The diameter of the laser spot on the sample was approximately 0.5 mm. For the angle-resolved PL measurements with a fixed excitation angle, the optical fiber was rotated around the sample along the Γ-X direction (Fig. 30a).

The PhC was oriented towards the excitation laser beam. If it were oriented oppositely, then the laser beam would refract on the boundary between the air and quartz and it would lead to a spatial shift of the excited region during the change of the excitation angle. It was not possible to use angles close to the sample normal (angle of incidence <15°) for the excitation. In such case, the excitation beam would excite parasitic luminescence in the optical fiber. Nevertheless, we were mainly interested in the resonant excitation angles with the angles of incidence lying between 40° and 60° for 442 nm excitation beam.

5.3.4 Angle-resolved transmission measurement

The angle-resolved transmission measurement, which allows to map the spectral position of leaky modes for different angles of incidence, was realized on the setup shown in Fig. 30b. A broadband tungsten lamp was employed as a light source. A collimated light beam of a small divergence (angular spread lower than 0.3°) was obtained using a pinhole and a series of lenses. Polarizer was used to define light polarization. Transmitted light was detected using an optical fiber connected to a spectrometer with an intensified CCD camera (*Andor*) at the output. The sample was covered by a black paper with square aperture (that matched the size of one PhC structure) and vertically mounted to a rotational stage. Subsequently, the sample was rotated around the axis perpendicular to one of the main symmetry directions of the PhC. For each angle (step of 27 arcminutes) the transmission spectrum was measured. The obtained results were compared with the simulations performed by the RCWA method.

5.3.5 Reflectance interferometry

Thickness of the diamond layers was measured by reflectance interferometry. A white light source and a spectrometer were used to measure reflectance spectra with interference fringes. The data were evaluated by a commercially available *FilmWizard* software (*SCI company*).

5.3.6 Photothermal deflection spectroscopy

The absorption coefficient of diamond layers that was further used for the simulations of photonic structures and for the *Q*-factor calculations was measured by the photothermal deflection spectroscopy (PDS) [230]. The absorption is measured indirectly in PDS technique via measuring the thermal changes of the refractive index of the medium surrounding the sample (liquid with large dependence of refractive index on temperature). First, the sample is immersed into the liquid and the pump beam impacts on the probed sample. Part of the light is absorbed by the sample. The absorbed energy is converted mostly to heat, which causes heating of the surrounding medium. These changes are detected by the probe beam, which propagates parallel to the sample in a close vicinity to its surface. The probe is deflected, depending on the temperature gradient, which is proportional to the absorption coefficient of the sample. The PDS method is particularly suitable for measurement of absorption coefficient of thin layers, where the volume of the absorbing material is proportional to the layer thickness. In comparison with other methods, only directly absorbed light is evaluated, and the effect of other optical losses (reflections, scattering) is excluded.

5.4 Characterization of Fabry-Perot cavities

For the characterization of the Fabry-Perot cavities in the red part of spectra a continuous narrowband external-cavity diode tunable laser (*Toptica DL Pro HP 637*) was used. The tuning of laser over broad spectral region (635 nm – 641 nm) was used to find the free spectral range of cavities. The laser wavelength was measured by wavemeter (*Toptica Photonics*). The width (FWHM) of cavity modes was measured by modulating the laser wavelength and comparing the width with the free spectral range of the Fabry-Perot cavity etalon (1 GHz).

The finesse of the Fabry-Perot cavities in the near infra-red region were measured by tunable laser *EXFO T100S-HP/O*. Again, the tuning of the laser over broad spectral region (1260 nm – 1360 nm) was used to find the free spectral range of cavities. For very short cavities, the free spectral range exceeded the wavelength range of the laser. The cavity length was obtained from the spectral position of the fundamental and higher order modes, and from the radius of curvature of the mirrors in such case. The radius of curvature (R_{oc}) is related to the cavity length L_{cav} by

$$R_{oc} = \frac{L_{cav}}{1 - \left[\cos\left(\frac{1}{p+q}\Delta\nu_{00\leftrightarrow pq}\frac{2L\pi}{c}\right)\right]^2} \tag{5.1}$$

where (p,q) is the Hermite-Gaussian beam order, $\Delta\nu_{00\leftrightarrow pq}$ is the frequency difference between $TEM_{0,0}$ and $TEM_{p,q}$ Gaussian mode, and c is the speed of light [48]. The free spectral range can be then computed as $\Delta\nu_{FSR} = c/2L_{cav}$. The cavity linewidth was measured by scanning the laser over the cavity resonance while a 200 MHz sideband modulation was applied, and the observed linewidth was compared with the known splitting of the sidebands.

5.4.2 White light interferometry

White light interferometer (Filmetrics Profilm 3D) was used to characterize micro-mirrors on the Si chips, particularly to measure their radius of curvature. In comparison with AFM, the white light interferometer is a contactless characterization method that prevents damages caused by the physical contact between the sample surface and the AFM tip. Moreover, the speed of the measurement is significantly faster than the AFM measurement as the whole picture is recorded in one exposition. This allows the characterization of large sample areas (e.g. hundreds of mirrors on one chip), which is not feasible with the AFM.

5.4 Other characterization methods

5.4.1 Atomic force microscopy

Atomic force microscopy (*AFM Veeco DI3100 IV AFM*) was used both for fabrication of microscopic patterns in the a-Si:H layer and for the characterization of the samples. The fabrication of microscopic patterns was done in the contact mode. The AFM was equipped with conductive metal coated Si tips (*ContE-G, BudgetSensors*, force constant 0.2 N/m). Constant electrical current was locally applied to the sample using the tip and metal (Ni or Pt) layer below the a-Si:H layer as electrodes. External source (*Keithley K237*) was used as a current source and voltage monitor. Same tips were used for the measurement of the conductivity of the samples.

Characterization of the topography was done on the same AFM microscope or on another device (*NT-MDT NTEGRA Prima AFM*) using the intermittent (tapping) regime (tips *Tap300Al-G, BudgetSensors*, force constant 40 N/m). The measurements were analyzed by *Gwyddion*, Free and Open Source software package for data visualization and analysis [231]. AFM was also used to measure the surface roughness of diamond layers.

5.4.2 Scanning electron microscopy

Scanning electron microscopy (SEM) was used for the EBL and to investigate the morphology of the samples. The surface morphology of diamond samples was investigated primarily by *Raith e_LiNe workstation* in standard configuration.

Tescan Maia3 was used to measure morphology of the sample with a-Si:H and also to characterize changes of the secondary electron emission using an in-beam detector. The back-scattered electrons were used for the visualization of material contrast.

5.4.3 X-ray photoelectron spectroscopy

Chemical composition of some samples was analyzed by the X-ray photoelectron spectroscopy (XPS; *AXIS Supra, Kratos*) with hemispheric analyzer and monochromatic Al Kα X-ray source, 1486.6eV; high resolution spectra pass energy 20 eV. The XPS spectra were acquired from the area of 700×300 μm^2 with the take-off angle 90°. XPS allows to analyze the concentration of individual elements and also the concentration of different types of bonds (e.g. sp^3 bonds and sp^2 bonds in diamond).

6. Results and discussion

In this thesis we studied various approaches for improving the collection efficiency of light from color centers, primarily ensembles of SiV centers, in diamond. Particularly, we used weak PhC slabs to study the improvement of light collection due to Bragg diffraction of leaky modes [20,21,232], PhC crystal cavities to study coupling of SiV centers to cavity modes [233], Fabry-Perot micro-cavities to study coupling of NV centers to cavity modes [234], and we attempted to grow isolated diamond nanocrystals with SiV centers [219,225]. In the following sections we briefly point out the main achievements. The details about the performed research with an extensive discussion can be found in the respective journal articles that are enclosed at the end of this thesis.

6.1 Weak photonic crystal slabs

We used both the bottom-up and top-down approaches to fabricate the weak PhC slabs. Our motivation was to use the weak PhC slabs to extract and collect the light emitted by photoluminescent processes in diamond. We were particularly interested in the following: (i) maximizing the extraction of light from thin diamond layers, (ii) directing the extracted light into the vertical direction where it can be easily collected with simple optics with low NA, and (iii) achieving the spectral overlap between the leaky modes and the SiV centers ZPL.

In our first article [20] we introduced a new bottom-up method for the fabrication of PhC slabs based on the diamond growth on pre-patterned substrates (the bottom-up approach). This method allowed us to fabricate diamond PhC slabs without directly processing the diamond layer, which is complicated due to the diamond hardness and chemical stability. Instead, the quartz glass substrate is patterned, which can be done relatively easily, and which can be cost-effectively up-scaled to larger areas using, for instance, nanoimprint lithography [235].

Even more importantly, we have shown that the method allows tuning the spectral position of leaky modes by changing the diamond deposition time, which results in the varying thickness of the deposited diamond layer. The observed phenomenon was also successfully numerically simulated. Using the optimal deposition time and the physical dimensions of patterns, which we determined from numerical simulations, the spectral overlap of leaky modes with the SiV centers ZPL has been achieved. The observed peak enhancement factor at the SiV centers ZPL was more than 14 when the photoluminescence intensity measured on the as-deposited diamond layer with a comparable thickness was taken as a reference (Fig. 31a,b).

PhCs with both the square and hexagonal lattice symmetries were fabricated, and their performance was compared. The maximal enhancement factor was observed on the PhC with the hexagonal lattice symmetry, which well agrees with the theoretical prediction. The higher enhancement is caused by the degeneracy at the Γ-point for the hexagonal lattice when compared with the square lattice. The maximal enhancement factor achieved with the PhCs with the square lattice symmetry was approximately 10, and the ratio of the enhancement factors between these two lattice symmetries corresponds with the ratio of the degeneracy.

The disadvantage of the bottom-up approach is that the shape of PhCs is not fully controlled, which might have negative effect on the performance of the PhC slabs. Therefore, we have prepared another set of PhCs by top-down approach for our second article [21], which allowed us to fabricate structures with better control over their structural quality. In this case, only the

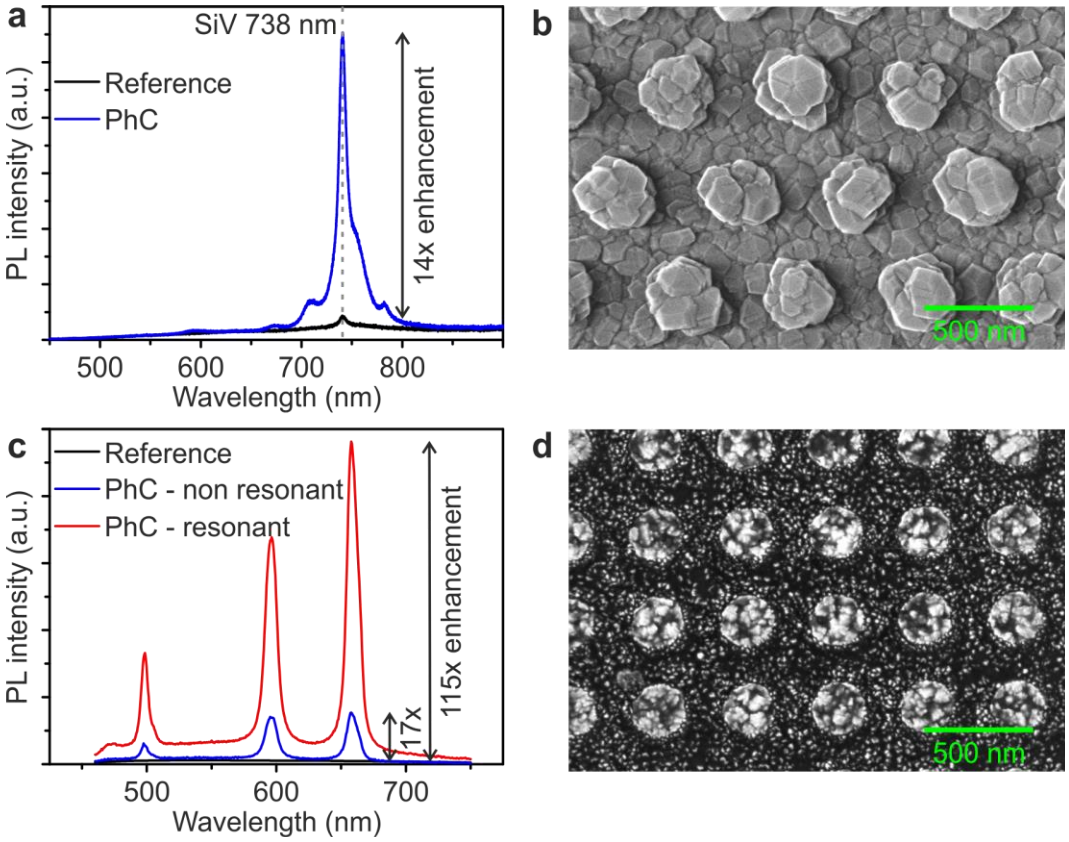

Figure 31: **(a)** PL intensity from reference non-patterned layer (black) and from the PhC slab fabricated by bottom-up approach (blue). The enhancement factor is 14 at the SiV center ZPL. **(b)** SEM image of the bottom-up grown sample. **(c)** PL intensity from reference non-patterned layer (black) and from the PhC slab fabricated by top-down approach under non-resonant (blue) and resonant (red) excitation. The enhancement factor exceeds 100 if the resonant excitation is used. **(d)** SEM image of the top-down fabricated sample.

PhCs with the square lattice symmetry were fabricated for simplicity. The dimensions of the samples were designed to obtain as high extraction efficiency as possible. Moreover, the effect of resonant excitation, where the excitation laser beam is coupled into the leaky modes of PhCs to extend the excitation beam path length inside diamond and thus the excitation efficiency, was implemented to further increase the intensity of the emitted light. On the other hand, we have not aimed to match the position of leaky modes with the emission lines of color centers in this study. Instead, we demonstrated the PL enhancement on the broadband PL from diamond in the red part of the visible region.

By using the resonant excitation and the resonant extraction via leaky modes, we have achieved up to 115-fold enhancement of PL intensity into the vertical direction (Fig. 31c,d). To achieve such high enhancement factor, the thickness of the diamond layer was optimized (using 3-D FDTD numerical simulation) to maximize the coupling efficiency of light emitted from diamond optical centers to the extraction leaky mode. Moreover, we have shown that using the fundamental TE-like (TE_0) mode both for the excitation and for the extraction enables to further increase the extracted PL intensity. The fundamental TE_0 leaky mode is the most advantageous for the case when the emitters are placed directly inside the layer. TE_0 mode has the highest overlap between its electric field spatial profile and the diamond layer and thus provides both the most efficient excitation of color centers and the most efficient coupling of emission to the extraction leaky mode. The electric field of the modes was simulated using RCWA simulations to support our claims. In contrast, the TM-like fundamental mode provides lower PL enhancement. Nevertheless, its electric field is localized near the surface of the structure and thus it is more sensitive to changes in the surroundings as well as more advantageous for the PL enhancement from surface deposited emitters.

In Ref. [232] we studied the effect of the diamond layer morphology on the PhC performance. We found out that the size of grains in diamond layer significantly affects the fabrication process. The PhCs fabricated in layers with large diamond grains contained large number of structural defects and the maximal observed enhancement factor was only 12×. This is only slightly higher than the enhancement observed on PhCs with square lattice symmetry fabricated by bottom-up approach.

Currently, we are working on a combination of the bottom-up and top-down approach. The top-down approach provides well-defined structures with optimal dimensions to achieve high enhancement of the PL intensity. The procedure similar to the bottom-up approach is then used to tune the spectral position of the leaky modes and achieve the spectral overlap with the desired emission lines in diamond.

More details about our research on the weak PhC slabs can be found in the attached journal articles entitled *Enhanced extraction of silicon-vacancy centers light emission using bottom-up engineered polycrystalline diamond photonic crystal slabs* [20], *Maximized vertical photoluminescence from optical material with losses employing resonant excitation and extraction of photonic crystal modes* [21], and *Effect of CVD diamond morphology on the photoluminescence extraction by photonic crystal slabs* [232].

6.2 Photonic crystal cavities

As with the weak PhC slabs, our motivation was to use PhC cavities for the extraction of light emitted by diamond color centers, SiV centers in particular. We tested both top-down techniques, focused ion-beam (FIB) milling and electron beam lithography (EBL) with subsequent reactive ion etching (RIE) for the fabrication of the PhC cavities. Fig. 32 shows the resulting photonic structures. The fabrication with FIB was complicated due to the charge accumulation on the sample, which resulted in the drift of the ion-beam and non-ideal periodicity of the photonic structures (Fig. 32a). The drift of the sample was slightly improved when the diamond layer was covered by the thin film of titanium to prevent the charge accumulation. Nevertheless, the periodicity was not sufficient for the observation of the photonic effects. We concluded that the FIB instrument that we used is not applicable for the fabrication of the PhC cavities in diamond.

Better results were obtained when the EBL and RIE techniques were used for the fabrication of PhC cavities (Fig. 32b) as we describe in Ref. [233]. We obtained the spectral overlap between the cavity modes and the SiV centers zero-phonon line. To achieve the overlap, we have developed a new method for the fabrication of the PhC cavities that does not require fine tuning of the mode spectral position by using postprocessing methods, e.g. sublimation of ice on top of the structure, that were mentioned in the theoretical part of this thesis. Instead, our method was based on growing polycrystalline diamond layer with varying thickness over the substrate. This can be achieved easily in the deposition system when the plasma is placed close to the sample, which causes non-homogeneous heating of the sample and the distribution of growth radicals coming from the plasma. Subsequently, multiple cavities with different spectral

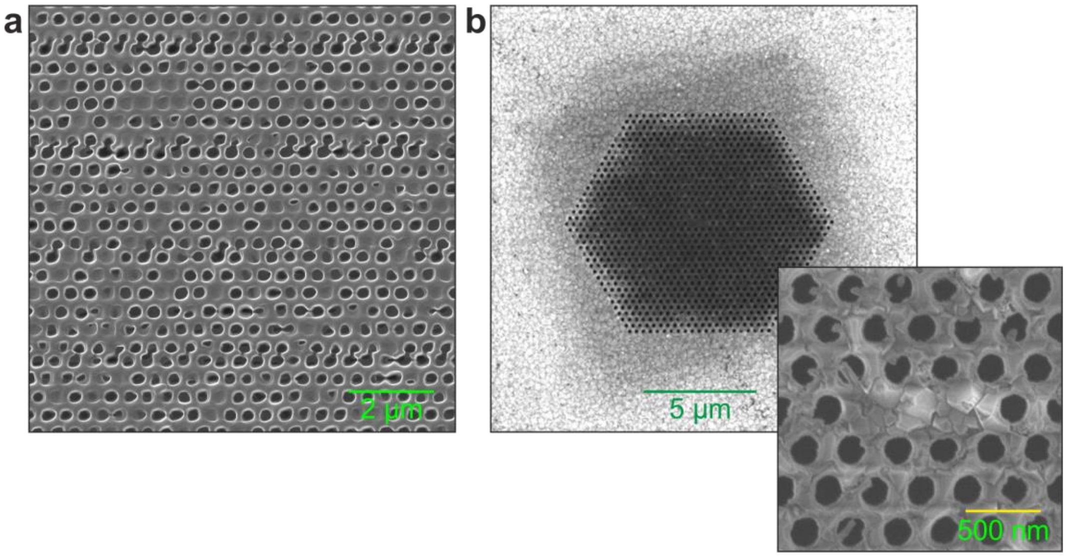

Figure 32: **(a)** SEM image of the PhC slab fabricated by FIB. **(b)** SEM image of the PhC structure fabricated by combination of EBL and RIE. The inset shows the central part, where three missing holes form the L3 cavity.

positions of modes due to varying thickness of the layer were fabricated over the sample. The cavities with the optimal spectral position (overlapping the SiV center ZPL) of cavity modes were selected during the characterization.

The theoretical *Q*-factor of the cavity modes was more than 700 for the fundamental cavity mode and 100 – 200 for the other, higher-order, modes. The *Q*-factor was further reduced by the absorption and scattering losses in polycrystalline diamond. We experimentally observed *Q*-factor of 292 for the fundamental cavity mode and around 100 for the higher-order modes. No change of the diameter or position of holes around the cavity was applied as the losses caused by absorption and scattering dominated and thus, no significant improvement is possible without further reduction of the concentration of sp^2 phase in diamond and reduction of the surface roughness.

The observed enhancement factor at the SiV center ZPL was more than 2.5 with regard to the surrounding PhC structure (strong PhC slab). The observed enhancement is lower than the maximal enhancement corresponding to the theoretical Purcell factor of the cavity mode into which the PL of SiV centers is coupled. The main reason for the lower observed enhancement is the presence of the ensemble of SiV centers that are distributed randomly in the material and not located in the ideal position with the highest electric field of the mode. Similar results were observed earlier on PhC cavities made in monocrystalline diamond with the ensemble of SiV centers [43].

The obtained results are very promising for cheap and fast fabrication of PhC cavities. The cavity performance can be improved by reducing the absorption and scattering losses, e.g. by etching the non-diamond phase in acids or by planarization. Subsequently, the modified cavity design can be applied to further improve the *Q*-factor of the cavity modes. More details about our research on the diamond PhC cavities can be found in the attached journal article entitled *Photonic crystal cavity-enhanced emission from silicon vacancy centers in polycrystalline diamond achieved without postfabrication fine-tuning* [233].

6.3 Fabry-Perot microcavities

We studied the Fabry-Perot micro-cavities during my research stay in the group of Dr. Michael Trupke at the University of Vienna. The aim was to enhance the photon count-rate from a single photon source and simultaneously couple the emitted photons into a single mode optical fiber. The efficient collection with the optical fiber is necessary for the realization of further experiments, e.g. the generation of entangled photons, as well as for practical realizations as it allows to use the existing fiber networks for sending quantum information.

For the construction of the cavities, we used concave micro-mirrors with the radius of curvature (ROC) lying between 50 μm and 150 μm that were prepared in the 4 inch Si wafer by two-step dry etching process (see Ref. [48,236] for details). The wafer was then diced to 3 mm by 3 mm chips that hosted hundreds of mirrors spaced on a 125 μm grid. Each chip was equipped with optical coatings to achieve very high reflectivity (> 99.7%).

In the first part of my stay, we studied Fabry-Perot cavities suitable for the interaction with NV centers in monocrystalline diamond. The results of this work have not been published yet and thus we describe the work in more detail. We characterized the Fabry-Perot micro-cavities composed of Si chips, and a monocrystalline diamond slab (CVD, purchased from the *Element Six* company) with the approximate thickness of 25 μm (Fig. 33a). Both the Si surface with concave mirrors and the outer diamond surface were coated with high reflectivity multilayers. The diamond surface located inside the cavity was coated with anti-reflection multilayer to reduce the losses at the boundary between the diamond slab and air inside the cavity. Each multilayer was designed to have a maximal performance at 637 nm, where the NV^- centers zero-phonon line is located.

The coarse adjustment of the cavity length was done mechanically using a micro-meter screw, while a piezo actuator was used to finely tune the cavity length and shift the spectral position of the cavity modes into the vicinity of 637 nm. The mirror on the diamond was used as an input/output mirror for coupling light into and out of the cavity. A set of lenses was used to couple the cavity modes to the single-mode optical fiber. The lenses were chosen based on the ROC of the used cavity mirrors to achieve optimal coupling efficiency into the cavity modes.

In order to measure the cavity characteristics, we coupled a laser beam with a tunable wavelength and narrow emission line to the cavity modes and observed the reflected light. The cavity modes correspond to the minima observed in the intensity of the reflected light. By sweeping the laser wavelength over a cavity mode we were able to compare the linewidth of the mode (Fig. 33b) with the free spectral range of reference Fabry-Perot cavity (1 GHz etalon).

The parameters of the best cavities are summarized in Tab. 2 (first column). Anti-reflection coating (500 ppm), concave Si mirror (> 2 ppm), scattering and intrinsic losses in diamond (> 2000 ppm) were all contributing to the total losses inside the cavity. The transmission of the input/output mirror (3000 ppm) was chosen to be equal to the losses inside the cavity in order to extract the photons from the cavity modes efficiently. Lower transmission of this mirror would lead to higher finesse, but majority of photons would be absorbed inside the cavity and lost, in such case. Note that the optimal parameters listed in Tab. 2 were achieved only when the node (minimum electric field) of the optical modes was located at the boundary between air and diamond inside the cavity. We have accomplished that by tuning the wavelength of light.

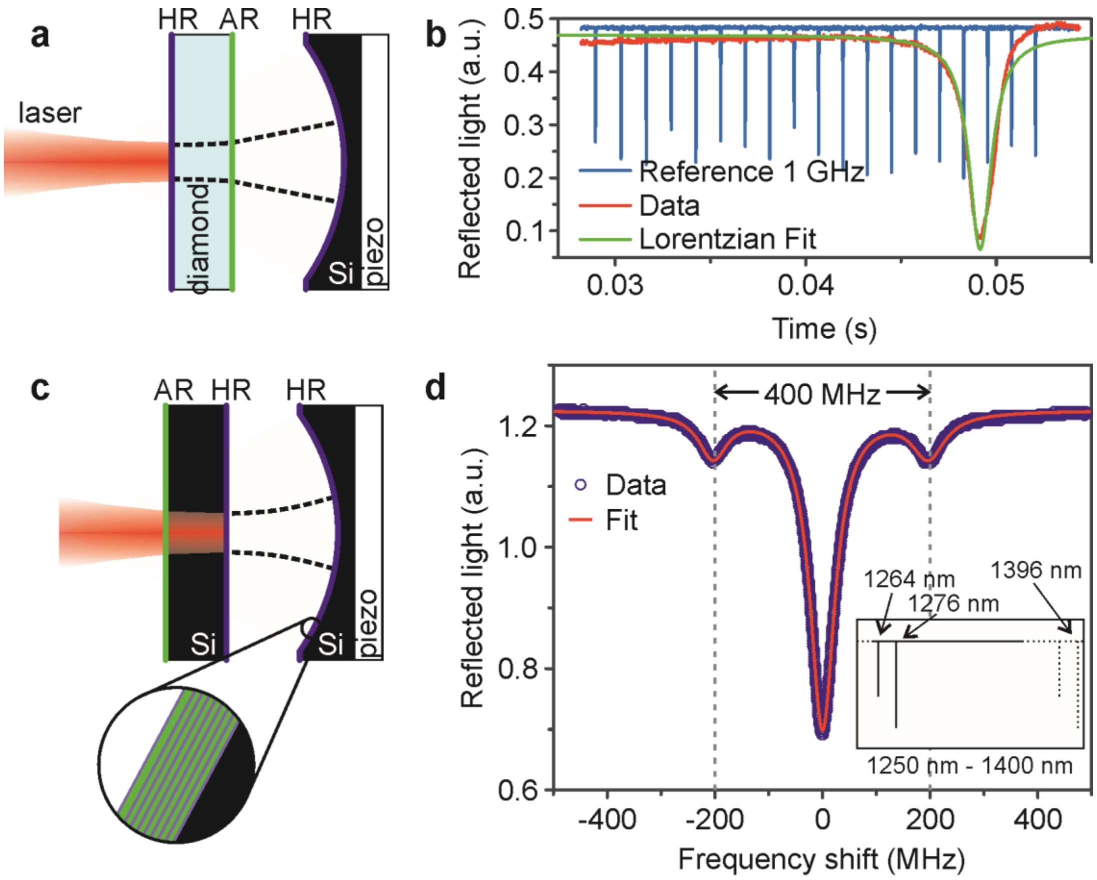

Figure 33: **(a)** Schematic picture of a plano-concave micro-cavity with diamond layer. The surfaces are equipped with high reflectivity (HR) and anti-reflective (AR) coatings. **(b)** The cavity linewidth was measured by modulating the laser over several GHz and comparing the linewidth of the mode with the free spectral range of the Fabry-Perot etalon (1 GHz). **(c)** Schematic picture of a plano-concave micro-cavity working at NIR region. **(d)** The cavity linewidth was measured by sideband modulation and comparing the linewidth with the known distance between sidebands (400 MHz). The inset shows the free spectral range measurement. Only the range denoted by solid line was measured. The free spectral range was computed from the distance between fundamental and higher order cavity mode, and from the radius of curvature of used mirrors that was measured by white light interferometer.

Nevertheless, this was possible only for measuring the cavity properties. When the cavity is used for collection of light from NV centers the wavelength is given by the ZPL, and the phase of the mode on the boundary depends solely on the thickness of the diamond slab. For a fixed wavelength, the finesse over 1000 was achieved approximately for 10% of the cavities on a chip due to the non-homogeneous thickness of the used diamond slab. In other cases, the scattering on the boundary was significantly increased and the finesse dropped to several hundreds.

The measured cavity properties promise the efficiency of generating photons by NV centers at ZPL and their subsequent coupling to the cavity mode and collection by single mode optical fiber to lie between 1% and 3%. The cavity has two beneficial effects. Firstly, the probability of emission of photons into ZPL is enhanced thanks to the increased LDOS inside the cavity (amounts less than 3% for NV centers in bulk diamond). Secondly, the photons are preferentially emitted into the cavity modes and their collection efficiency is also increased (amounts less than 4.5% in bulk diamond, leading to a total collection efficiency of < 0.1% in the bulk diamond). With the cavity values achieved above, this low efficiency could be increased by a factor of 10 – 30. For further improvement of the efficiency, the surface roughness of diamond (currently between 1 nm and 2 nm) could be reduced. For instance, the surface roughness below 0.5 nm would lead to finesse around 4000 and the overall efficiency exceeding 10%.

Subsequently, we attempted to localize and observe single NV centers inside the cavities. However, the localization of a single NV center in the available samples was not possible due to the low density of NV centers in the ultrapure material. Nonetheless, the achieved results show promise for the enhanced collection of photons from optical centers in diamond slabs in these microcavities.

In the second part of my stay, we studied the properties of Si cavities designed for the near-infrared (NIR) region (1280 nm). This region is interesting for long-range quantum communication because the photons can be sent through existing fiber network (telecom O-band). Moreover, single photon emitters for this region, such as vanadium (V) center in silicon carbide (SiC) and G center in Si, were discovered recently [74,165]. The advantage of Si and SiC are their superb optical properties and the better availability of methods for fabrication (e.g. surface roughness reduction) when compared with diamond. On the other hand, there is only limited information about the optical properties of the color centers in SiC and Si and it is questionable if they meet all requirements for the use in quantum information processing.

Again, the plano-concave cavities were formed by Si chip with the concave mirror facing a planar chip (Fig. 33c). In this time, however, no material was placed inside the cavities and only the properties of free cavities have been analyzed so far. A material with color centers will be placed into the cavity in the next experiments. A shift to the infrared region allowed us to use Si also for the input/output mirror as Si is transparent for these wavelengths. The surface roughness of Si can be easily reduced to the level of 0.2 nm by polishing [48], and the scattering is also reduced for longer wavelengths (see Eq. 1.6). As a result, the parameters of cavities were significantly better than those achieved with diamond with finesse reaching to 500 000 (Fig. 33d, Tab. 2, middle column).

In order to further reduce the cavity length, we glued the two Si chips together. We also selected a chip with very small ROC (≈ 65 μm) of mirrors to reduce the volume of the cavity modes. On the other hand, the cavity length was not controlled by the piezo-actuator anymore. Moreover, the free spectral range was of the order of 100 nm, which further reduced the probability of obtaining a cavity mode near 1280 nm. In order to obtain cavities with different length, a spacer with ≈ 16 μm thickness, was inserted between the Si chips on one side, forming a narrow wedge with ≈ 0.3° tilt. By measuring multiple cavities over the chip, we were able to find cavities with modes located near 1280 nm and optical length as low as 7.4 μm. The parameters of the best cavity are summarized in Tab. 2 (last column).

Tab. 2: Parameters of the Fabry-Perot cavities: wavelength (λ), Q-factor (Q), finesse (F), total round-trip optical losses (l_{rt}), and optical length (L_{opt})

Material	**Si + Diamond**	**Si (empty)**	
Cavity type	**Piezo actuator**	**Piezo actuator**	**Glued chips**
λ (nm)	637	1280	1276
Q ($/10^6$)	0.38	16	4
F ($/10^3$)	10.7	490	350
l_{rt} (ppm)	5900	13	18
d (μm)	110	17	7.4

In comparison with the previous experiments, the cavity length was significantly reduced while the finesse remained high. The optical volume of these cavities was as low as 23 λ^3, which is only one order of magnitude higher than for the PhC cavities. The observed $(Q/V)/\lambda^3 \approx 1.7 \times 10^5$ value is almost three times larger than for other types of open-access microcavities [46,237]. The experiments with inserted SiC and Si chips are planned in the near future. More details about the research on the Fabry-Perot cavities in NIR can be found in the attached article entitled *High finesse telecom O-band microcavities* [234].

6.4 Diamond growth in a-Si:H microstructures

The last part of the work was devoted to amorphous silicon (a-Si) thin layers and their potential usage as templates for the selective growth of diamond. We show in Ref. [219] that complex nano-patterns may be prepared in thin (~40 nm) layers of hydrogenated a-Si (a-Si:H) deposited on a thin (~40 nm) electrode (Ni or Pt) placed on various substrates (glass, Si wafer) by using locally applied electric field in an atomic force microscope (AFM). The difference from previous works [215,220] is the usage of much thinner layer, 40 nm vs. ~200 nm.

We found that only very shallow pits (max. 10 nm) can be prepared in the thin a-Si:H layer, when the tip is not moving during deposition. In the beginning of the pit formation, the depth of pits increases as a function of exposure time. However, it saturates after ~10 s and may even decrease, which is accompanied by voltage drop. We argue that the voltage grown on the AFM tip may be released during the electric discharge. Similarly, when the applied electric current is too high (~1 nA), the process leads to electric discharge, which results in a formation of large pits with no control over their dimensions.

We showed that sweeping (local modulation of the tip position) of the tip during exposition stabilizes the process of the pit formation and leads to the creation of better-defined features. This allows usage of larger electric currents (up to 3 nA) and longer exposition times (more than 30 s) for the pit formation. Using this method, pits with more than 30 nm depth and 100 nm diameter in lateral direction can be created in a-Si:H layer. We showed that the process is reproducible and around 100 pits with similar dimensions may be created on the sample using one AFM tip. Furthermore, we show that complex movements across the sample may be also applied and line-art patterns may be scribed into the a-Si:H film (Fig. 34). The processed area does not show only topographical changes, but also changes in electrical conductivity (which is decreased on the processed area), electron emission (increased), and Raman spectra. We proposed that the observed changes are caused by the decreased content of hydrogen inside the a-Si:H layer. The change of hydrogen content was evidenced by Raman micro-spectroscopy. The modified properties of the patterns may become useful as universal templates for growth of nano-materials and nanostructures.

Subsequently, we studied the nucleation of diamond on substrates covered by the thin layer of a-Si:H [225]. Originally, we wanted to achieve the nucleation of diamond nanocrystals inside the pits created by AFM in the a-Si:H layer. However, the low temperature deposition of diamond (substrate temperature ~350 °C) must be used to prevent the a-Si:H layer from crystallization, which causes the dissolution of patterns created by AFM. We found that the spontaneous nucleation of diamond is suppressed on a-Si:H layers when low temperature is used. Nonetheless, diamond nano-crystals with optically active SiV centers grew on monocrystalline silicon under the same deposition conditions.

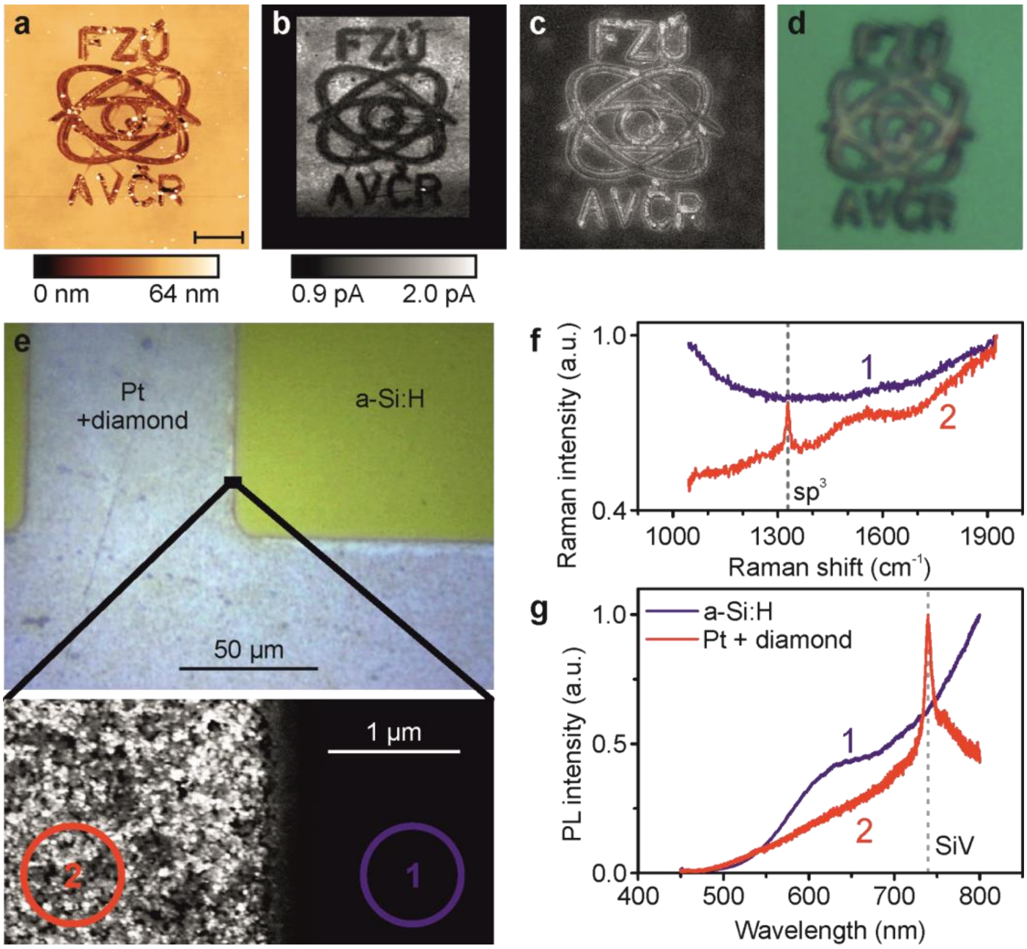

Figure 34: Nanopatterning of the a-Si:H layer by conductive AFM: **(a)** AFM topography of the patterns scribed into the a-Si:H layer (scale bar 2 µm), **(b)** map of the local electric current (measured with bias voltage 3.5 V), **(c)** SEM image of the secondary electron emission, **(d)** bright field optical microscope image in reflected light. Selective growth of diamond: **(e)** Optical microscope image (top) and SEM morphology (bottom) of the sample with an a-Si:H layer patterned by photolithography and subsequent diamond growth, **(f)** Raman spectra taken on the a-Si:H and on the NCD part of the sample; the grey dashed line denotes the position of the sp^3 diamond peak, **(g)** PL intensity taken on the a-Si:H and on the NCD part of the sample; the grey dashed line denotes the spectral position of the SiV peak.

To achieve the selective growth, we used the thin layer of a-Si:H to create a mask on the nucleated sample, which suppresses the growth of diamond. We deposited a 200 nm thin a-Si:H layer over the substrates (Si coated with Pt) seeded with diamond nanoparticles. The a-Si:H layer was partially removed by using photolithography and reactive ion etching. We demonstrated the selective growth of diamond on such substrate with no diamond nucleation on the masked regions. Moreover, the material quality of diamond was sufficient for the observation of photoluminescence from the SiV centers. The size of the features can be further reduced by using different techniques (e.g. the demonstrated patterning using the AFM, or EBL or FIB milling) for patterning of the a-Si:H layer. More details about the research on the a-Si:H micro-structuring and the selective growth of photoluminescent diamond using such micro-structures can be found in the attached journal articles entitled *Complex nano-patterning of structural, optical, electrical and electron emission properties of amorphous silicon thin films by scanning probe* [219] and *Nucleation of diamond micro-patterns with photoluminescent SiV centers controlled by amorphous silicon thin films* [225], respectively.

Conclusions and outlooks

In this thesis, we prepared and investigated various photonic structures that can be used to improve the collection efficiency of light emitted by diamond color centers. We achieved following results:

- We developed a new bottom-up method for the fabrication of polycrystalline diamond PhC slabs, which allowed us to tune the spectral position of leaky modes. Using this method, we achieved a spectral overlap of leaky modes with the ZPL of SiV color centers located at ~738 nm. The enhancement factor of 14 was observed at the SiV center emission line. The bottom-up method represents an affordable alternative to the top-down fabrication methods, which require specialized equipment and procedures for diamond processing, while allowing to finely-control the spectral position of the leaky modes. This allows up-scaling and cost-effective production of PhC slabs for diamond-based photonics and biosensor applications.
- By using the novel approach of resonant excitation and resonant extraction, we achieved 115-fold enhancement of the PL intensity from polycrystalline diamond layers. The enhancement was demonstrated in PhC slabs fabricated by top-down approach. We showed both theoretically and experimentally that the same type of the leaky mode must be used for the excitation and the extraction in order to maximize the enhancement. This approach is advantageous for effective optical excitation of dielectric materials with optical losses, which may find use in photovoltaic energy harvesting or biosensor applications based on photoluminescence observation (e.g. from diamond color centers).
- We developed a new method to fabricate polycrystalline diamond PhC cavities with modes located at the SiV color centers ZPL without the need of post-processing. We obtained 2.5-fold intensity enhancement of the light emitted by the ensemble of SiV centers due to the Purcell effect. These results are comparable with the enhancement achieved on the ensembles of SiV centers in the monocrystalline diamond, while the fabrication method is cheaper and faster, which opens a way for the use of diamond PhC cavities in many fields (e.g. biosensors), for which the traditional approaches are too expensive.
- We showed that Fabry-Perot cavities built with Si micro-mirrors and thin diamond slab promise a significant improvement of the collection efficiency in comparison with the bare slab. The observed cavity finesse (> 1000) was limited by the scattering losses due to the surface roughness (1 - 2 nm) of the used diamond sample. Higher finesse (> 4000) and photon collection efficiency > 10% is expected for samples with the surface roughness < 0.5 nm. This result promises to significantly enhance the photon collection efficiencies of ZPL photons from the single NV centers in diamond, which are currently at the order of 0.1% for setups based on solid immersion lenses or diffraction gratings. The photon collection efficiency is the limiting factor for quantum information processing in diamond-based photonic devices.
- We assembled cavities for NIR region, where we achieved very high finesse (350 000) and simultaneously very low volume of the cavity mode (23 λ^3). The reported value of $(Q/V)/\lambda^3 \approx 1.8 \times 10^5$, which governs the Purcell enhancement, exceeds the performance of all open-access optical microcavities to the best of our knowledge, and is almost three times larger than for the other types of open-access microcavities. High Purcell

enhancement is pivotal for applications requiring enhancement of the interaction of light with matter, such as spin-photon interfaces or cavity-cooling of nanoparticles.

- We fabricated complex patterns with interesting optical and electrical properties in the layer of hydrogenated amorphous Si by using conductive AFM microscope. This may be useful for various applications of a-Si:H itself or as a template for selective growth and self-assembly of nano-materials for photovoltaics or photonics.
- We showed that the diamond nucleation can be efficiently suppressed by hydrogenated amorphous Si. We demonstrated the ability of the hydrogenated amorphous Si to work as a mask for the selective depositions of diamond with optically active SiV centers. The growth of precisely placed diamond crystals and structures can be favorably used to create electronic elements and sensors, photonic structures, and eventually single photon sources for quantum communication based on luminescence of diamond color centers (SiV, NV).

Outlooks

There are various prospective applications of the photonic structures in diamond that can benefit from our results. Polycrystalline diamond layers are advantageous for bio-sensing thanks to the diamond bio-compatibility and low toxicity, and because polycrystalline layers can be cost-effectively deposited over large surface areas of various samples. The color centers alone can be used for sensing applications as was already demonstrated by several groups. The addition of photonic effects improves the collection efficiency of light from color centers. Moreover, the photonic structures are sensitive for the changes of refractive index in their neighborhood, and thus they can be used as independent detection mechanism for the sensors.

Weak PhC slabs are particularly interesting for bio-sensing as they can be easily fabricated over large areas of the substrate. We are currently working on the fabrication of PhC slabs with (i) spectral overlap between modes at Γ-point and SiV centers ZPL, (ii) SiV placed only in the surface layer, and (iii) maximized extraction efficiency of the modes. We will carry out preliminary experiments to compare this design with current bio-sensing devices. The PhC cavities may also be used for sensing in principle, which is, however, hindered by the complex fabrication process. The presented method of tuning of the cavity modes can be utilized for the construction of diamond PhC cavities sensors.

Another promising application is the use of color centers in diamond as single photon sources for quantum information processing. The color centers are perspective for the use as nods of the future quantum networks, as they are suitable for preparation of entangled photon states. Efficient collection of photons is of critical importance for achieving reliable single photon sources for these quantum networks. Both the Fabry-Perot cavities and the PhC cavities can be used for the improvement of light collection from single photon sources. However, in this work only Fabry-Perot cavities were demonstrated in monocrystalline diamond, which is necessary to reduce absorption and scattering on diamond grains. The results achieved on PhC cavities will be extended towards monocrystalline diamond with single photon sources in future.

The disadvantage of color centers in diamond is their spectral position in the red part of spectra with considerable light scattering. The shift to NIR spectral region, e.g. utilizing the color centers in SiC or Si, is anticipated in the near future. Fabry-Perot cavities investigated in this work will be further used to host SiC slab with vanadium color centers. A more distant goal is to use the vanadium color centers coupled to Fabry-Perot cavities as a source of single photons for long-distance quantum communication.

Apart from diamond, the photonic structures offer improvement in other applications. Our achievements may be particularly interesting for photovoltaic applications, where the resonant excitation via leaky modes of PhC slabs promises enhanced absorption efficiency in the progressive field of thin film organic, dye sensitized, and perovskite solar cells. PhC slabs are of interest for lighting applications, where the inverse effect of extraction of light via leaky modes is utilized. More complex photonic structures (e.g. PhC cavities and waveguides) can be used for the construction of photonic chips with applications in photonics and electronics.

References to literature

[1] M. Planck, M. Masius, The theory of heat radiation, Philadelphia, P. Blakiston's Son & Co, 1914.

[2] G.B. Rybicki, A.P. Lightman, Radiative Processes in Astrophysics, John Wiley & Sons, 1991.

[3] R.G. Driggers, Encyclopedia of Optical Engineering, CRC Press, 2003.

[4] S. Nakamura, T. Mukai, M. Senoh, Candela-class high-brightness InGaN/AlGaN double-heterostructure blue-light-emitting diodes, Appl. Phys. Lett. APLCLASS2019 (1998) 1687–1689. https://doi.org/10.1063/1.111832.

[5] E.F. Schubert, Y. -H. Wang, A.Y. Cho, L. -W. Tu, G.J. Zydzik, Resonant cavity light-emitting diode, Appl. Phys. Lett. 60 (1992) 921–923. https://doi.org/10.1063/1.106489.

[6] H. Hirayama, Quaternary InAlGaN-based high-efficiency ultraviolet light-emitting diodes, J. Appl. Phys. 97 (2005) 091101. https://doi.org/10.1063/1.1899760.

[7] S. Kamimura, H. Yamada, C.-N. Xu, Strong reddish-orange light emission from stress-activated Srn+1SnnO3n+1:Sm3+ (n = 1, 2, ∞) with perovskite-related structures, Appl. Phys. Lett. 101 (2012) 091113. https://doi.org/10.1063/1.4749807.

[8] S. Nizamoglu, E. Mutlugun, T. Özel, H.V. Demir, S. Sapra, N. Gaponik, A. Eychmüller, Dual-color emitting quantum-dot-quantum-well CdSe-ZnS heteronanocrystals hybridized on InGaN∕GaN light emitting diodes for high-quality white light generation, Appl. Phys. Lett. 92 (2008) 113110. https://doi.org/10.1063/1.2898892.

[9] Q. Sun, Y.A. Wang, L.S. Li, D. Wang, T. Zhu, J. Xu, C. Yang, Y. Li, Bright, multicoloured light-emitting diodes based on quantum dots, Nat. Photonics. 1 (2007) 717–722. https://doi.org/10.1038/nphoton.2007.226.

[10] P. Bamfield, Chromic Phenomena: Technological Applications of Colour Chemistry, Royal Society of Chemistry, 2007.

[11] I. Pelant, J. Valenta, Luminescence Spectroscopy of Semiconductors, Oxford University Press, 2012.

[12] N. Mizuochi, T. Makino, H. Kato, D. Takeuchi, M. Ogura, H. Okushi, M. Nothaft, P. Neumann, A. Gali, F. Jelezko, J. Wrachtrup, S. Yamasaki, Electrically driven single-photon source at room temperature in diamond, Nat. Photonics. 6 (2012) 299–303. https://doi.org/10.1038/nphoton.2012.75.

[13] B. Tegetmeyer, C. Schreyvogel, N. Lang, W. Müller-Sebert, D. Brink, C.E. Nebel, Electroluminescence from silicon vacancy centers in diamond p–i–n diodes, Diam. Relat. Mater. 65 (2016) 42–46. https://doi.org/10.1016/j.diamond.2016.01.022.

[14] E.F. Schubert, Light-Emitting Diodes, 2nd ed., Cambridge University Press, Cambridge, 2006. https://www.cambridge.org/core/books/lightemitting-diodes/81ADC32DA2266AA8C0CB3AFABB9FB127 (accessed June 2, 2020).

[15] M. Fox, Quantum Optics: An Introduction, OUP Oxford, 2006.

[16] P. Ewart, Atomic Physics, Morgan & Claypool Publishers, 2019.

[17] J.R. Lakowicz, Principles of Fluorescence Spectroscopy, Springer Science & Business Media, 2013.

[18] B.E.A. Saleh, M.C. Teich, Fundamentals of Photonics, John Wiley & Sons, 2019.

[19] H. Buckley, The whitened cube as a precision integrating photometer, J. Inst. Electr. Eng. 59 (1921) 143–152. https://doi.org/10.1049/jiee-1.1921.0007.

[20] L. Ondič, M. Varga, K. Hruška, J. Fait, P. Kapusta, Enhanced Extraction of Silicon-Vacancy Centers Light Emission Using Bottom-Up Engineered Polycrystalline Diamond Photonic Crystal Slabs, ACS Nano. 11 (2017) 2972–2981. https://doi.org/10.1021/acsnano.6b08412.

[21] J. Fait, M. Varga, K. Hruška, Z. Remeš, V. Jurka, A. Kromka, B. Rezek, L. Ondič, Maximized vertical photoluminescence from optical material with losses employing resonant excitation and extraction of photonic crystal modes, Nanophotonics. 8 (2019) 1041–1050. https://doi.org/10.1515/nanoph-2019-0042.

[22] J.J. Wierer, D.A. Steigerwald, M.R. Krames, J.J. O'Shea, M.J. Ludowise, G. Christenson, Y.-C. Shen, C. Lowery, P.S. Martin, S. Subramanya, W. Götz, N.F. Gardner, R.S. Kern, S.A. Stockman, High-power AlGaInN flip-chip light-emitting diodes, Appl. Phys. Lett. 78 (2001) 3379–3381. https://doi.org/10.1063/1.1374499.

[23] E. Matioli, C. Weisbuch, Impact of photonic crystals on LED light extraction efficiency: approaches and limits to vertical structure designs, J. Phys. Appl. Phys. 43 (2010) 354005. https://doi.org/10.1088/0022-3727/43/35/354005.

[24] J.J. Wierer, A. David, M.M. Megens, III-nitride photonic-crystal light-emitting diodes with high extraction efficiency, Nat. Photonics. 3 (2009) 163–169. https://doi.org/10.1038/nphoton.2009.21.

[25] M.R. Krames, O.B. Shchekin, R. Mueller-Mach, G.O. Mueller, L. Zhou, G. Harbers, M.G. Craford, Status and Future of High-Power Light-Emitting Diodes for Solid-State Lighting, J. Disp. Technol. 3 (2007) 160–175. https://doi.org/10.1109/JDT.2007.895339.

[26] O.B. Shchekin, J.E. Epler, T.A. Trottier, T. Margalith, D.A. Steigerwald, M.O. Holcomb, P.S. Martin, M.R. Krames, High performance thin-film flip-chip InGaN–GaN light-emitting diodes, Appl. Phys. Lett. 89 (2006) 071109. https://doi.org/10.1063/1.2337007.

[27] V. Haerle, B. Hahn, S. Kaiser, A. Weimar, S. Bader, F. Eberhard, A. Plössl, D. Eisert, High brightness LEDs for general lighting applications Using the new ThinGaN^{TM}-Technology, Phys. Status Solidi A. 201 (2004) 2736–2739. https://doi.org/10.1002/pssa.200405119.

[28] J.K. Kim, S. Chhajed, M.F. Schubert, E.F. Schubert, A.J. Fischer, M.H. Crawford, J. Cho, H. Kim, C. Sone, Light-Extraction Enhancement of GaInN Light-Emitting Diodes by Graded-Refractive-Index Indium Tin Oxide Anti-Reflection Contact, Adv. Mater. 20 (2008) 801–804. https://doi.org/10.1002/adma.200701015.

[29] C. Wiesmann, K. Bergenek, N. Linder, U. t. Schwarz, Photonic crystal LEDs – designing light extraction, Laser Photonics Rev. 3 (2009) 262–286. https://doi.org/10.1002/lpor.200810053.

[30] G. Harbers, S.J. Bierhuizen, M.R. Krames, Performance of High Power Light Emitting Diodes in Display Illumination Applications, J. Disp. Technol. 3 (2007) 98–109.

[31] A. Wilm, Requirements on LEDs in etendue limited light engines, in: Photonics Multimed. II, International Society for Optics and Photonics, 2008: p. 70010F. https://doi.org/10.1117/12.781199.

[32] T. Markvart, The thermodynamics of optical étendue, J. Opt. Pure Appl. Opt. 10 (2007) 015008. https://doi.org/10.1088/1464-4258/10/01/015008.

[33] W.S. Wong, T. Sands, N.W. Cheung, M. Kneissl, D.P. Bour, P. Mei, L.T. Romano, N.M. Johnson, Fabrication of thin-film InGaN light-emitting diode membranes by laser lift-off, Appl. Phys. Lett. 75 (1999) 1360–1362. https://doi.org/10.1063/1.124693.

[34] A. Kromka, O. Babchenko, Š. Potocký, B. Rezek, Sveshnikov, Diamond nucleation and seeding techniques for tissue regeneration, in: Diam.-Based Mater. Biomed. Appl., Elsevier, 2013.

[35] M. Hammer, 1-D multilayer slab waveguide mode solver, (2020). https://www.computational-photonics.eu/oms.html.

[36] C. McDonagh, C.S. Burke, B.D. MacCraith, Optical Chemical Sensors, Chem. Rev. 108 (2008) 400–422. https://doi.org/10.1021/cr068102g.

[37] T. Mayr, T. Abel, B. Enko, S. Borisov, C. Konrad, S. Köstler, B. Lamprecht, S. Sax, E.J.W. List, I. Klimant, A planar waveguide optical sensor employing simple light coupling, Analyst. 134 (2009) 1544–1547. https://doi.org/10.1039/B904536H.

[38] M. Wang, S. Uusitalo, C. Liedert, J. Hiltunen, L. Hakalahti, R. Myllylä, Polymeric dual-slab waveguide interferometer for biochemical sensing applications, Appl. Opt. 51 (2012) 1886–1893. https://doi.org/10.1364/AO.51.001886.

[39] W.H. Louisell, Quantum statistical properties of radiation, John Wiley & Sons Canada, Limited, 1973.

[40] A. Gali, J.R. Maze, Ab initio study of the split silicon-vacancy defect in diamond: Electronic structure and related properties, Phys. Rev. B. 88 (2013) 235205. https://doi.org/10.1103/PhysRevB.88.235205.

[41] E. Purcell, Spontaneous emission probabilities at radio frequencies, in: Phys. Rev., 1946: p. 681. https://doi.org/10.1007/978-1-4615-1963-8_40.

[42] P.T. Kristensen, C.V. Vlack, S. Hughes, Generalized effective mode volume for leaky optical cavities, Opt. Lett. 37 (2012) 1649–1651. https://doi.org/10.1364/OL.37.001649.

[43] J. Riedrich-Möller, L. Kipfstuhl, C. Hepp, E. Neu, C. Pauly, F. Mücklich, A. Baur, M. Wandt, S. Wolff, M. Fischer, S. Gsell, M. Schreck, C. Becher, One- and two-dimensional photonic crystal microcavities in single crystal diamond, Nat. Nanotechnol. 7 (2012) 69–74. https://doi.org/10.1038/nnano.2011.190.

[44] M. Trupke, E.A. Hinds, S. Eriksson, E.A. Curtis, Z. Moktadir, E. Kukharenka, M. Kraft, Microfabricated high-finesse optical cavity with open access and small volume, Appl. Phys. Lett. 87 (2005) 211106. https://doi.org/10.1063/1.2132066.

[45] C.J. Hood, H.J. Kimble, J. Ye, Characterization of high-finesse mirrors: Loss, phase shifts, and mode structure in an optical cavity, Phys. Rev. A. 64 (2001) 033804. https://doi.org/10.1103/PhysRevA.64.033804.

[46] A. Muller, E.B. Flagg, J.R. Lawall, G.S. Solomon, Ultrahigh-finesse, low-mode-volume Fabry-Perot microcavity, Opt. Lett. 35 (2010) 2293–2295. https://doi.org/10.1364/OL.35.002293.

[47] D. Hunger, T. Steinmetz, Y. Colombe, C. Deutsch, T.W. Hänsch, J. Reichel, A fiber Fabry–Perot cavity with high finesse, New J. Phys. 12 (2010) 065038. https://doi.org/10.1088/1367-2630/12/6/065038.

[48] G. Wachter, S. Kuhn, S. Minniberger, C. Salter, P. Asenbaum, J. Millen, M. Schneider, J. Schalko, U. Schmid, A. Felgner, D. Hüser, M. Arndt, M. Trupke, Silicon microcavity arrays with open access and a finesse of half a million, Light Sci. Appl. 8 (2019) 37. https://doi.org/10.1038/s41377-019-0145-y.

[49] S. Bogdanović, S.B. van Dam, C. Bonato, L.C. Coenen, A.-M.J. Zwerver, B. Hensen, M.S.Z. Liddy, T. Fink, A. Reiserer, M. Lončar, R. Hanson, Design and low-temperature characterization of a tunable microcavity for diamond-based quantum networks, Appl. Phys. Lett. 110 (2017) 171103. https://doi.org/10.1063/1.4982168.

[50] K.J. Vahala, Optical microcavities, Nature. 424 (2003) 839–846. https://doi.org/10.1038/nature01939.

[51] I. Aharonovich, A.D. Greentree, S. Prawer, Diamond photonics, Nat. Photonics. 5 (2011) 397–405. https://doi.org/10.1038/nphoton.2011.54.

[52] C. Schneider, T. Heindel, A. Huggenberger, P. Weinmann, C. Kistner, M. Kamp, S. Reitzenstein, S. Höfling, A. Forchel, Single photon emission from a site-controlled quantum dot-micropillar cavity system, Appl. Phys. Lett. 94 (2009) 111111. https://doi.org/10.1063/1.3097016.

[53] Y. Zhang, M. Lončar, Submicrometer diameter micropillar cavities with high quality factor and ultrasmall mode volume, Opt. Lett. 34 (2009) 902–904. https://doi.org/10.1364/OL.34.000902.

[54] K. Srinivasan, O. Painter, Mode coupling and cavity--quantum-dot interactions in a fiber-coupled microdisk cavity, Phys. Rev. A. 75 (2007) 023814. https://doi.org/10.1103/PhysRevA.75.023814.

[55] C.F. Wang, Y.-S. Choi, J.C. Lee, E.L. Hu, J. Yang, J.E. Butler, Observation of whispering gallery modes in nanocrystalline diamond microdisks, Appl. Phys. Lett. 90 (2007) 081110. https://doi.org/10.1063/1.2709626.

[56] V.S. Ilchenko, X.S. Yao, L. Maleki, Pigtailing the high-Q microsphere cavity: a simple fiber coupler for optical whispering-gallery modes, Opt. Lett. 24 (1999) 723–725. https://doi.org/10.1364/OL.24.000723.

[57] Y.-S. Park, A.K. Cook, H. Wang, Cavity QED with Diamond Nanocrystals and Silica Microspheres, Nano Lett. 6 (2006) 2075–2079. https://doi.org/10.1021/nl061342r.

[58] T.M. Babinec, J.T. Choy, K.J.M. Smith, M. Khan, M. Lončar, Design and focused ion beam fabrication of single crystal diamond nanobeam cavities, J. Vac. Sci. Technol. B. 29 (2011) 010601. https://doi.org/10.1116/1.3520638.

[59] P.B. Deotare, M.W. McCutcheon, I.W. Frank, M. Khan, M. Lončar, High quality factor photonic crystal nanobeam cavities, Appl. Phys. Lett. 94 (2009) 121106. https://doi.org/10.1063/1.3107263.

[60] Y. Akahane, T. Asano, B.-S. Song, S. Noda, High-*Q* photonic nanocavity in a two-dimensional photonic crystal, Nature. 425 (2003) 944–947. https://doi.org/10.1038/nature02063.

[61] A. Faraon, C. Santori, Z. Huang, V.M. Acosta, R.G. Beausoleil, Coupling of Nitrogen-Vacancy Centers to Photonic Crystal Cavities in Monocrystalline Diamond, Phys. Rev. Lett. 109 (2012) 033604. https://doi.org/10.1103/PhysRevLett.109.033604.

[62] J. Riedrich-Möller, C. Arend, C. Pauly, F. Mücklich, M. Fischer, S. Gsell, M. Schreck, C. Becher, Deterministic Coupling of a Single Silicon-Vacancy Color Center to a Photonic Crystal Cavity in Diamond, Nano Lett. 14 (2014) 5281–5287. https://doi.org/10.1021/nl502327b.

[63] I. Bayn, B. Meyler, A. Lahav, J. Salzman, R. Kalish, B.A. Fairchild, S. Prawer, M. Barth, O. Benson, T. Wolf, P. Siyushev, F. Jelezko, J. Wrachtrup, Processing of photonic crystal nanocavity for quantum information in diamond, Diam. Relat. Mater. 20 (2011) 937–943. https://doi.org/10.1016/j.diamond.2011.05.002.

[64] E.D. Black, An introduction to Pound–Drever–Hall laser frequency stabilization, Am. J. Phys. 69 (2000) 79–87. https://doi.org/10.1119/1.1286663.

[65] H.J. Kimble, The quantum internet, Nature. 453 (2008) 1023–1030. https://doi.org/10.1038/nature07127.

[66] C. Santori, M. Pelton, G. Solomon, Y. Dale, Y. Yamamoto, Triggered Single Photons from a Quantum Dot, Phys. Rev. Lett. 86 (2001) 1502–1505. https://doi.org/10.1103/PhysRevLett.86.1502.

[67] M.D. Eisaman, J. Fan, A. Migdall, S.V. Polyakov, Invited Review Article: Single-photon sources and detectors, Rev. Sci. Instrum. 82 (2011) 071101. https://doi.org/10.1063/1.3610677.

[68] A. Kuhn, M. Hennrich, G. Rempe, Deterministic Single-Photon Source for Distributed Quantum Networking, Phys. Rev. Lett. 89 (2002) 067901. https://doi.org/10.1103/PhysRevLett.89.067901.

[69] I. Aharonovich, S. Castelletto, D.A. Simpson, C.-H. Su, A.D. Greentree, S. Prawer, Diamond-based single-photon emitters, Rep. Prog. Phys. 74 (2011) 076501. https://doi.org/10.1088/0034-4885/74/7/076501.

[70] L. Mandel, E. Wolf, Optical Coherence and Quantum Optics, Cambridge University Press, 1995.

[71] A.D. Boozer, A. Boca, R. Miller, T.E. Northup, H.J. Kimble, Cooling to the Ground State of Axial Motion for One Atom Strongly Coupled to an Optical Cavity, Phys. Rev. Lett. 97 (2006) 083602. https://doi.org/10.1103/PhysRevLett.97.083602.

[72] I. Aharonovich, S. Castelletto, D.A. Simpson, A. Stacey, J. McCallum, A.D. Greentree, S. Prawer, Two-Level Ultrabright Single Photon Emission from Diamond Nanocrystals, Nano Lett. 9 (2009) 3191–3195. https://doi.org/10.1021/nl9014167.

[73] C. Kasper, D. Klenkert, Z. Shang, D. Simin, A. Gottscholl, A. Sperlich, H. Kraus, C. Schneider, S. Zhou, M. Trupke, W. Kada, T. Ohshima, V. Dyakonov, G.V. Astakhov, Influence of Irradiation on Defect Spin Coherence in Silicon Carbide, Phys. Rev. Appl. 13 (2020) 044054. https://doi.org/10.1103/PhysRevApplied.13.044054.

[74] L. Spindlberger, A. Csóré, G. Thiering, S. Putz, R. Karhu, J.U. Hassan, N.T. Son, T. Fromherz, A. Gali, M. Trupke, Optical Properties of Vanadium in 4H Silicon Carbide for Quantum Technology, Phys. Rev. Appl. 12 (2019) 014015. https://doi.org/10.1103/PhysRevApplied.12.014015.

[75] E. Neu, D. Steinmetz, J. Riedrich-Möller, S. Gsell, M. Fischer, Matthias Schreck, C. Becher, Single photon emission from silicon-vacancy colour centres in chemical vapour deposition nano-diamonds on iridium, New J. Phys. 13 (2011) 025012. https://doi.org/10.1088/1367-2630/13/2/025012.

[76] J.P. Hadden, J.P. Harrison, A.C. Stanley-Clarke, L. Marseglia, Y.-L.D. Ho, B.R. Patton, J.L. O’Brien, J.G. Rarity, Strongly enhanced photon collection from diamond defect centers under microfabricated integrated solid immersion lenses, Appl. Phys. Lett. 97 (2010) 241901. https://doi.org/10.1063/1.3519847.

[77] J.D. Joannopoulos, S.G. Johnson, J.N. Winn, R.D. Meade, Photonic Crystals: Molding the Flow of Light, Second Edition, Princeton University Press, 2011.

[78] J.D. Jackson, Classical Electrodynamics, 3rd ed., Wiley India Pvt. Limited, 2007.

[79] Lord Rayleigh, XVII. On the maintenance of vibrations by forces of double frequency, and on the propagation of waves through a medium endowed with a periodic structure, Philos. Mag. 24 (1887) 145–159. https://doi.org/10.1080/14786448708628074.

[80] E. Yablonovitch, Inhibited Spontaneous Emission in Solid-State Physics and Electronics, Phys. Rev. Lett. 58 (1987) 2059–2062. https://doi.org/10.1103/PhysRevLett.58.2059.

[81] S. John, Strong localization of photons in certain disordered dielectric superlattices, Phys. Rev. Lett. 58 (1987) 2486–2489. https://doi.org/10.1103/PhysRevLett.58.2486.

[82] M. Koshiba, Wavelength division multiplexing and demultiplexing with photonic crystal waveguide couplers, J. Light. Technol. 19 (2001) 1970–1975. https://doi.org/10.1109/50.971693.

[83] T.A. Birks, J.C. Knight, P.S.J. Russell, Endlessly single-mode photonic crystal fiber, Opt. Lett. 22 (1997) 961–963. https://doi.org/10.1364/OL.22.000961.

[84] L. Zeng, Y. Yi, C. Hong, J. Liu, N. Feng, X. Duan, L.C. Kimerling, B.A. Alamariu, Efficiency enhancement in Si solar cells by textured photonic crystal back reflector, Appl. Phys. Lett. 89 (2006) 111111. https://doi.org/10.1063/1.2349845.

[85] A. Chutinan, N.P. Kherani, S. Zukotynski, High-efficiency photonic crystal solar cell architecture, Opt. Express. 17 (2009) 8871–8878. https://doi.org/10.1364/OE.17.008871.

[86] D. Zhou, R. Biswas, Photonic crystal enhanced light-trapping in thin film solar cells, J. Appl. Phys. 103 (2008) 093102. https://doi.org/10.1063/1.2908212.

[87] E. Chow, S.Y. Lin, S.G. Johnson, P.R. Villeneuve, J.D. Joannopoulos, J.R. Wendt, G.A. Vawter, W. Zubrzycki, H. Hou, A. Alleman, Three-dimensional control of light in a two-dimensional photonic crystal slab, Nature. 407 (2000) 983–986. https://doi.org/10.1038/35039583.

[88] C. Vieu, F. Carcenac, A. Pépin, Y. Chen, M. Mejias, A. Lebib, L. Manin-Ferlazzo, L. Couraud, H. Launois, Electron beam lithography: resolution limits and applications, Appl. Surf. Sci. 164 (2000) 111–117. https://doi.org/10.1016/S0169-4332(00)00352-4.

[89] C.L. Haynes, R.P. Van Duyne, Nanosphere Lithography: A Versatile Nanofabrication Tool for Studies of Size-Dependent Nanoparticle Optics, J. Phys. Chem. B. 105 (2001) 5599–5611. https://doi.org/10.1021/jp010657m.

[90] D. Haefliger, A. Stemmer, Structuring of aluminum films by laser-induced local oxidation in water, Appl. Phys. Mater. Sci. Process. 74 (2002) 115. https://doi.org/10.1007/s003390100974.

[91] T. Banno, M. Tachiki, H. Seo, H. Umezawa, H. Kawarada, Fabrication of diamond single-hole transistors using AFM anodization process, Diam. Relat. Mater. 11 (2002) 387–391. https://doi.org/10.1016/S0925-9635(01)00655-0.

[92] R.M. Nyffenegger, R.M. Penner, Nanometer-Scale Surface Modification Using the Scanning Probe Microscope: Progress since 1991, Chem. Rev. 97 (1997) 1195–1230. https://doi.org/10.1021/cr960069i.

[93] G.P. Lopinski, D.D.M. Wayner, R.A. Wolkow, Self-directed growth of molecular nanostructures on silicon, Nature. 406 (2000) 48–51. https://doi.org/10.1038/35017519.

[94] S.C. Buswell, V.A. Wright, J.M. Buriak, V. Van, S. Evoy, Specific detection of proteins using photonic crystal waveguides, Opt. Express. 16 (2008) 15949–15957. https://doi.org/10.1364/OE.16.015949.

[95] J. García-Rupérez, V. Toccafondo, M.J. Bañuls, J.G. Castelló, A. Griol, S. Peransi-Llopis, Á. Maquieira, Label-free antibody detection using band edge fringes in SOI planar photonic crystal waveguides in the slow-light regime, Opt. Express. 18 (2010) 24276–24286. https://doi.org/10.1364/OE.18.024276.

[96] Y. Liu, S. Wang, D. Zhao, W. Zhou, Y. Sun, High quality factor photonic crystal filter at k=0 and its application for refractive index sensing, Opt. Express. 25 (2017) 10536–10545. https://doi.org/10.1364/OE.25.010536.

[97] S.G. Johnson, S. Fan, P.R. Villeneuve, J.D. Joannopoulos, L.A. Kolodziejski, Guided modes in photonic crystal slabs, Phys. Rev. B. 60 (1999) 5751–5758. https://doi.org/10.1103/PhysRevB.60.5751.

[98] M. Rattier, H. Benisty, E. Schwoob, C. Weisbuch, T.F. Krauss, C.J.M. Smith, R. Houdré, U. Oesterle, Omnidirectional and compact guided light extraction from Archimedean photonic lattices, Appl. Phys. Lett. 83 (2003) 1283–1285. https://doi.org/10.1063/1.1600831.

[99] N. Ganesh, W. Zhang, P.C. Mathias, E. Chow, J. a. N.T. Soares, V. Malyarchuk, A.D. Smith, B.T. Cunningham, Enhanced fluorescence emission from quantum dots on a photonic crystal surface, Nat. Nanotechnol. 2 (2007) 515–520. https://doi.org/10.1038/nnano.2007.216.

[100] S. Fan, P.R. Villeneuve, J.D. Joannopoulos, E.F. Schubert, High Extraction Efficiency of Spontaneous Emission from Slabs of Photonic Crystals, Phys. Rev. Lett. 78 (1997) 3294–3297. https://doi.org/10.1103/PhysRevLett.78.3294.

[101] M. Lončar, D. Nedeljković, T. Doll, J. Vučković, A. Scherer, T.P. Pearsall, Waveguiding in planar photonic crystals, Appl. Phys. Lett. 77 (2000) 1937–1939. https://doi.org/10.1063/1.1311604.

[102] S. Olivier, H. Benisty, M. Rattier, C. Weisbuch, M. Qiu, A. Karlsson, C.J.M. Smith, R. Houdré, U. Oesterle, Resonant and nonresonant transmission through waveguide bends in a planar photonic crystal, Appl. Phys. Lett. 79 (2001) 2514–2516. https://doi.org/10.1063/1.1410338.

[103] W. Fan, Z. Hao, E. Stock, J. Kang, Y. Luo, D. Bimberg, Comparison between two types of photonic-crystal cavities for single-photon emitters, Semicond. Sci. Technol. 26 (2010) 014014. https://doi.org/10.1088/0268-1242/26/1/014014.

[104] M. Minkov, V. Savona, Automated optimization of photonic crystal slab cavities, Sci. Rep. 4 (2014) 1–8. https://doi.org/10.1038/srep05124.

[105] F. Wang, R.E. Christiansen, Y. Yu, J. Mørk, O. Sigmund, Maximizing the quality factor to mode volume ratio for ultra-small photonic crystal cavities, Appl. Phys. Lett. 113 (2018) 241101. https://doi.org/10.1063/1.5064468.

[106] J. Vuckovic, M. Loncar, H. Mabuchi, A. Scherer, Optimization of the Q factor in photonic crystal microcavities, IEEE J. Quantum Electron. 38 (2002) 850–856. https://doi.org/10.1109/JQE.2002.1017597.

[107] K. Srinivasan, O. Painter, Momentum space design of high-Q photonic crystal optical cavities, Opt. Express. 10 (2002) 670–684. https://doi.org/10.1364/OE.10.000670.

[108] J.L. Zhang, S. Sun, M.J. Burek, C. Dory, Y.-K. Tzeng, K.A. Fischer, Y. Kelaita, K.G. Lagoudakis, M. Radulaski, Z.-X. Shen, N.A. Melosh, S. Chu, M. Lončar, J. Vučković, Strongly Cavity-Enhanced Spontaneous Emission from Silicon-Vacancy Centers in Diamond, Nano Lett. 18 (2018) 1360–1365. https://doi.org/10.1021/acs.nanolett.7b05075.

[109] S. Kim, J.E. Fröch, J. Christian, M. Straw, J. Bishop, D. Totonjian, K. Watanabe, T. Taniguchi, M. Toth, I. Aharonovich, Photonic crystal cavities from hexagonal boron nitride, Nat. Commun. 9 (2018) 1–8. https://doi.org/10.1038/s41467-018-05117-4.

[110] J.L. Zhang, S. Sun, M.J. Burek, C. Dory, Y.-K. Tzeng, K.A. Fischer, Y. Kelaita, K.G. Lagoudakis, M. Radulaski, Z.-X. Shen, N.A. Melosh, S. Chu, M. Lončar, J. Vučković, Strongly Cavity-Enhanced Spontaneous Emission from Silicon-Vacancy Centers in Diamond, Nano Lett. 18 (2018) 1360–1365. https://doi.org/10.1021/acs.nanolett.7b05075.

[111] L. Liebermeister, F. Petersen, A. v Münchow, D. Burchardt, J. Hermelbracht, T. Tashima, A.W. Schell, O. Benson, T. Meinhardt, A. Krueger, A. Stiebeiner, A. Rauschenbeutel, H. Weinfurter, M. Weber, Tapered fiber coupling of single photons emitted by a deterministically positioned single nitrogen vacancy center, Appl. Phys. Lett. 104 (2014) 031101. https://doi.org/10.1063/1.4862207.

[112] J. Riedrich-Möller, S. Pezzagna, J. Meijer, C. Pauly, F. Mücklich, M. Markham, A.M. Edmonds, C. Becher, Nanoimplantation and Purcell enhancement of single nitrogen-vacancy centers in photonic crystal cavities in diamond, Appl. Phys. Lett. 106 (2015) 221103. https://doi.org/10.1063/1.4922117.

[113] J. Wolters, A.W. Schell, G. Kewes, N. Nüsse, M. Schoengen, H. Döscher, T. Hannappel, B. Löchel, M. Barth, O. Benson, Enhancement of the zero phonon line emission from a single nitrogen vacancy center in a nanodiamond via coupling to a photonic crystal cavity, Appl. Phys. Lett. 97 (2010) 141108. https://doi.org/10.1063/1.3499300.

[114] A.W. Schell, G. Kewes, T. Schröder, J. Wolters, T. Aichele, O. Benson, A scanning probe-based pick-and-place procedure for assembly of integrated quantum optical hybrid devices, Rev. Sci. Instrum. 82 (2011) 073709. https://doi.org/10.1063/1.3615629.

[115] J. Benedikter, H. Kaupp, T. Hümmer, Y. Liang, A. Bommer, C. Becher, A. Krueger, J.M. Smith, T.W. Hänsch, D. Hunger, Cavity-Enhanced Single-Photon Source Based on the Silicon-Vacancy Center in Diamond, Phys. Rev. Appl. 7 (2017) 024031. https://doi.org/10.1103/PhysRevApplied.7.024031.

[116] J. Meijer, S. Pezzagna, T. Vogel, B. Burchard, H.H. Bukow, I.W. Rangelow, Y. Sarov, H. Wiggers, I. Plümel, F. Jelezko, J. Wrachtrup, F. Schmidt-Kaler, W. Schnitzler, K. Singer, Towards the implanting of ions and positioning of nanoparticles with nm spatial resolution, Appl. Phys. A. 91 (2008) 567–571. https://doi.org/10.1007/s00339-008-4515-1.

[117] T. Nakamura, Y. Takahashi, Y. Tanaka, T. Asano, S. Noda, Improvement in the quality factors for photonic crystal nanocavities via visualization of the leaky components, Opt. Express. 24 (2016) 9541–9549. https://doi.org/10.1364/OE.24.009541.

[118] N.-V.-Q. Tran, S. Combrié, A. De Rossi, Directive emission from high-Q photonic crystal cavities through band folding, Phys. Rev. B. 79 (2009) 041101. https://doi.org/10.1103/PhysRevB.79.041101.

[119] S.-H. Kim, S.-K. Kim, Y.-H. Lee, Vertical beaming of wavelength-scale photonic crystal resonators, Phys. Rev. B. 73 (2006) 235117. https://doi.org/10.1103/PhysRevB.73.235117.

[120] A. Faraon, E. Waks, D. Englund, I. Fushman, J. Vučković, Efficient photonic crystal cavity-waveguide couplers, Appl. Phys. Lett. 90 (2007) 073102. https://doi.org/10.1063/1.2472534.

[121] E. Waks, J. Vuckovic, Coupled mode theory for photonic crystal cavity-waveguide interaction, Opt. Express. 13 (2005) 5064–5073. https://doi.org/10.1364/OPEX.13.005064.

[122] A.Z. Subramanian, E. Ryckeboer, A. Dhakal, F. Peyskens, A. Malik, B. Kuyken, H. Zhao, S. Pathak, A. Ruocco, A.D. Groote, P. Wuytens, D. Martens, F. Leo, W. Xie, U.D. Dave, M. Muneeb, P.V. Dorpe, J.V. Campenhout, W. Bogaerts, P. Bienstman, N.L. Thomas, D.V. Thourhout, Z. Hens, G. Roelkens, R. Baets, Silicon and silicon nitride photonic circuits for spectroscopic sensing on-a-chip [Invited], Photonics Res. 3 (2015) B47–B59. https://doi.org/10.1364/PRJ.3.000B47.

[123] G. Kim, J.W. Park, I.G. Kim, S. Kim, S. Kim, J.M. Lee, G.S. Park, J. Joo, K.-S. Jang, J.H. Oh, S.A. Kim, J.H. Kim, J.Y. Lee, J.M. Park, D.-W. Kim, D.-K. Jeong, M.-S. Hwang, J.-K. Kim, K.-S. Park, H.-K. Chi, H.-C. Kim, D.-W. Kim, M.H. Cho, Low-voltage high-performance silicon photonic devices and photonic integrated circuits operating up to 30 Gb/s, Opt. Express. 19 (2011) 26936–26947. https://doi.org/10.1364/OE.19.026936.

[124] M. Davanco, J. Liu, L. Sapienza, C.-Z. Zhang, J.V. De Miranda Cardoso, V. Verma, R. Mirin, S.W. Nam, L. Liu, K. Srinivasan, Heterogeneous integration for on-chip quantum photonic circuits with single quantum dot devices, Nat. Commun. 8 (2017) 1–12. https://doi.org/10.1038/s41467-017-00987-6.

[125] R. Petit, ed., Electromagnetic Theory of Gratings, Springer-Verlag, Berlin Heidelberg, 1980.

[126] M.G. Moharam, T.K. Gaylord, Rigorous coupled-wave analysis of planar-grating diffraction, JOSA. 71 (1981) 811–818. https://doi.org/10.1364/JOSA.71.000811.

[127] L. Li, New formulation of the Fourier modal method for crossed surface-relief gratings, JOSA A. 14 (1997) 2758–2767. https://doi.org/10.1364/JOSAA.14.002758.

[128] A. Taflove, S.C. Hagness, Computational Electrodynamics: The Finite-Difference Time-Domain Method, 3 edition, Artech House, Boston, 2005.

[129] A.F. Oskooi, D. Roundy, M. Ibanescu, P. Bermel, J.D. Joannopoulos, S.G. Johnson, Meep: A flexible free-software package for electromagnetic simulations by the FDTD method, Comput. Phys. Commun. 181 (2010) 687–702. https://doi.org/10.1016/j.cpc.2009.11.008.

[130] S.G. Johnson, J.D. Joannopoulos, Block-iterative frequency-domain methods for Maxwell’s equations in a planewave basis, Opt. Express. 8 (2001) 173–190. https://doi.org/10.1364/OE.8.000173.

[131] R.S. Balmer, J.R. Brandon, S.L. Clewes, H.K. Dhillon, J.M. Dodson, I. Friel, P.N. Inglis, T.D. Madgwick, M.L. Markham, T.P. Mollart, N. Perkins, G.A. Scarsbrook, D.J. Twitchen, A.J. Whitehead, J.J. Wilman, S.M. Woollard, Chemical vapour deposition synthetic diamond: materials, technology and applications, J. Phys. Condens. Matter. 21 (2009) 364221. https://doi.org/10.1088/0953-8984/21/36/364221.

[132] N.-M. Hwang, D.-K. Lee, Charged nanoparticles in thin film and nanostructure growth by chemical vapour deposition, J. Phys. Appl. Phys. 43 (2010) 483001. https://doi.org/10.1088/0022-3727/43/48/483001.

[133] L. Wei, P.K. Kuo, R.L. Thomas, T.R. Anthony, W.F. Banholzer, Thermal conductivity of isotopically modified single crystal diamond, Phys. Rev. Lett. 70 (1993) 3764–3767. https://doi.org/10.1103/PhysRevLett.70.3764.

[134] A. Ward, D.A. Broido, D.A. Stewart, G. Deinzer, Ab initio theory of the lattice thermal conductivity in diamond, Phys. Rev. B. 80 (2009) 125203. https://doi.org/10.1103/PhysRevB.80.125203.

[135] S. Koizumi, K. Watanabe, M. Hasegawa, H. Kanda, Ultraviolet Emission from a Diamond pn Junction, Science. 292 (2001) 1899–1901. https://doi.org/10.1126/science.1060258.

[136] J. Isberg, J. Hammersberg, E. Johansson, T. Wikström, D.J. Twitchen, A.J. Whitehead, S.E. Coe, G.A. Scarsbrook, High Carrier Mobility in Single-Crystal Plasma-Deposited Diamond, Science. 297 (2002) 1670–1672. https://doi.org/10.1126/science.1074374.

[137] A. S. Barnard, Diamond standard in diagnostics: nanodiamond biolabels make their mark, Analyst. 134 (2009) 1751–1764. https://doi.org/10.1039/B908532G.

[138] A.M. Zaitsev, Optical Properties of Diamond: A Data Handbook, Springer Science & Business Media, 2013.

[139] F.P. Bundy, H.T. Hall, H.M. Strong, R.H.W. Jun, Man-Made Diamonds, Nature. 176 (1955) 51–55. https://doi.org/10.1038/176051a0.

[140] Y. Zhang, C. Zang, H. Ma, Z. Liang, L. Zhou, S. Li, X. Jia, HPHT synthesis of large single crystal diamond doped with high nitrogen concentration, Diam. Relat. Mater. 17 (2008) 209–211. https://doi.org/10.1016/j.diamond.2007.12.018.

[141] V.Y. Dolmatov, Detonation-synthesis nanodiamonds: synthesis, structure, properties and applications, Russ. Chem. Rev. 76 (2007) 339. https://doi.org/10.1070/RC2007v076n04ABEH003643.

[142] S. Hu, J. Sun, X. Du, F. Tian, L. Jiang, The formation of multiply twinning structure and photoluminescence of well-dispersed nanodiamonds produced by pulsed-laser irradiation, Diam. Relat. Mater. 17 (2008) 142–146. https://doi.org/10.1016/j.diamond.2007.11.009.

[143] A.Kh. Khachatryan, S.G. Aloyan, P.W. May, R. Sargsyan, V.A. Khachatryan, V.S. Baghdasaryan, Graphite-to-diamond transformation induced by ultrasound cavitation, Diam. Relat. Mater. 17 (2008) 931–936. https://doi.org/10.1016/j.diamond.2008.01.112.

[144] Y. Mokuno, A. Chayahara, H. Yamada, Synthesis of large single crystal diamond plates by high rate homoepitaxial growth using microwave plasma CVD and lift-off process, Diam. Relat. Mater. 17 (2008) 415–418. https://doi.org/10.1016/j.diamond.2007.12.058.

[145] M. Schwander, K. Partes, A review of diamond synthesis by CVD processes, Diam. Relat. Mater. 20 (2011) 1287–1301. https://doi.org/10.1016/j.diamond.2011.08.005.

[146] D. Das, R.N. Singh, A review of nucleation, growth and low temperature synthesis of diamond thin films, Int. Mater. Rev. 52 (2007) 29–64. https://doi.org/10.1179/174328007X160245.

[147] V. Sedov, V. Ralchenko, A.A. Khomich, I. Vlasov, A. Vul, S. Savin, A. Goryachev, V. Konov, Si-doped nano- and microcrystalline diamond films with controlled bright photoluminescence of silicon-vacancy color centers, Diam. Relat. Mater. 56 (2015) 23–28. https://doi.org/10.1016/j.diamond.2015.04.003.

[148] I. Akimoto, Y. Handa, K. Fukai, N. Naka, High carrier mobility in ultrapure diamond measured by time-resolved cyclotron resonance, Appl. Phys. Lett. 105 (2014) 032102. https://doi.org/10.1063/1.4891039.

[149] D.D. Awschalom, R. Hanson, J. Wrachtrup, B.B. Zhou, Quantum technologies with optically interfaced solid-state spins, Nat. Photonics. 12 (2018) 516–527. https://doi.org/10.1038/s41566-018-0232-2.

[150] T. Izak, A. Sveshnikov, P. Demo, A. Kromka, Enhanced spontaneous nucleation of diamond nuclei in hot and cold microwave plasma systems, Phys. Status Solidi B. 250 (2013) 2753–2758. https://doi.org/10.1002/pssb.201300117.

[151] M. Fischer, S. Gsell, M. Schreck, R. Brescia, B. Stritzker, Preparation of 4-inch Ir/YSZ/Si(001) substrates for the large-area deposition of single-crystal diamond, Diam. Relat. Mater. 17 (2008) 1035–1038. https://doi.org/10.1016/j.diamond.2008.02.028.

[152] T. Ižák, O. Babchenko, Š. Potocký, Z. Remeš, H. Kozák, E. Verveniotis, B. Rezek, A. Kromka, Low Temperature Diamond Growth, in: Nanodiamond, Royal Society of Chemistry, 2013: pp. 290–342.

[153] K. Tsugawa, M. Ishihara, J. Kim, Y. Koga, M. Hasegawa, Nanocrystalline diamond film growth on plastic substrates at temperatures below 100°C from low-temperature plasma, Phys. Rev. B. 82 (2010) 125460. https://doi.org/10.1103/PhysRevB.82.125460.

[154] C. Kurtsiefer, S. Mayer, P. Zarda, H. Weinfurter, Stable Solid-State Source of Single Photons, Phys. Rev. Lett. 85 (2000) 290–293. https://doi.org/10.1103/PhysRevLett.85.290.

[155] J.R. Rabeau, A. Stacey, A. Rabeau, S. Prawer, F. Jelezko, I. Mirza, J. Wrachtrup, Single Nitrogen Vacancy Centers in Chemical Vapor Deposited Diamond Nanocrystals, Nano Lett. 7 (2007) 3433–3437. https://doi.org/10.1021/nl0719271.

[156] L. Marseglia, K. Saha, A. Ajoy, T. Schröder, D. Englund, F. Jelezko, R. Walsworth, J.L. Pacheco, D.L. Perry, E.S. Bielejec, P. Cappellaro, Bright nanowire single photon source based on SiV centers in diamond, Opt. Express. 26 (2018) 80–89. https://doi.org/10.1364/OE.26.000080.

[157] J. Wrachtrup, F. Jelezko, Processing quantum information in diamond, J. Phys. Condens. Matter. 18 (2006) S807. https://doi.org/10.1088/0953-8984/18/21/S08.

[158] K. Nemoto, M. Trupke, S.J. Devitt, A.M. Stephens, B. Scharfenberger, K. Buczak, T. Nöbauer, M.S. Everitt, J. Schmiedmayer, W.J. Munro, Photonic Architecture for Scalable Quantum Information Processing in Diamond, Phys. Rev. X. 4 (2014) 031022. https://doi.org/10.1103/PhysRevX.4.031022.

[159] H.J. Kimble, M. Dagenais, L. Mandel, Photon Antibunching in Resonance Fluorescence, Phys. Rev. Lett. 39 (1977) 691–695. https://doi.org/10.1103/PhysRevLett.39.691.

[160] S. Hong, M.S. Grinolds, L.M. Pham, D.L. Sage, L. Luan, R.L. Walsworth, A. Yacoby, Nanoscale magnetometry with NV centers in diamond, MRS Bull. 38 (2013) 155–161. https://doi.org/10.1557/mrs.2013.23.

[161] V. Jacques, E. Wu, F. Grosshans, F. Treussart, P. Grangier, A. Aspect, J.-F. Roch, Experimental Realization of Wheeler’s Delayed-Choice Gedanken Experiment, Science. 315 (2007) 966–968. https://doi.org/10.1126/science.1136303.

[162] C.E. Nebel, B. Rezek, D. Shin, H. Uetsuka, N. Yang, Diamond for bio-sensor applications, J. Phys. Appl. Phys. 40 (2007) 6443. https://doi.org/10.1088/0022-3727/40/20/S21.

[163] V. Petráková, A. Taylor, I. Kratochvílová, F. Fendrych, J. Vacík, J. Kučka, J. Štursa, P. Cígler, M. Ledvina, A. Fišerová, P. Kneppo, M. Nesládek, Luminescence of Nanodiamond Driven by Atomic Functionalization: Towards Novel Detection Principles, Adv. Funct. Mater. 22 (2012) 812–819. https://doi.org/10.1002/adfm.201101936.

[164] Y. Mei, D. Fan, S. Lu, Y. Shen, X. Hu, SiV center photoluminescence induced by C=O termination in nanocrystalline diamond and graphite loops hybridized films, J. Appl. Phys. 120 (2016) 225107. https://doi.org/10.1063/1.4972026.

[165] C. Beaufils, W. Redjem, E. Rousseau, V. Jacques, A.Yu. Kuznetsov, C. Raynaud, C. Voisin, A. Benali, T. Herzig, S. Pezzagna, J. Meijer, M. Abbarchi, G. Cassabois, Optical properties of an ensemble of G-centers in silicon, Phys. Rev. B. 97 (2018) 035303. https://doi.org/10.1103/PhysRevB.97.035303.

[166] J. Barjon, E. Rzepka, F. Jomard, J.-M. Laroche, D. Ballutaud, T. Kociniewski, J. Chevallier, Silicon incorporation in CVD diamond layers, Phys. Status Solidi A. 202 (2005) 2177–2181. https://doi.org/10.1002/pssa.200561920.

[167] S. Stehlik, M. Varga, P. Stenclova, L. Ondic, M. Ledinsky, J. Pangrac, O. Vanek, J. Lipov, A. Kromka, B. Rezek, Ultrathin Nanocrystalline Diamond Films with Silicon Vacancy Color Centers via Seeding by 2 nm Detonation Nanodiamonds, ACS Appl. Mater. Interfaces. 9 (2017) 38842–38853. https://doi.org/10.1021/acsami.7b14436.

[168] A.M. Edmonds, M.E. Newton, P.M. Martineau, D.J. Twitchen, S.D. Williams, Electron paramagnetic resonance studies of silicon-related defects in diamond, Phys. Rev. B. 77 (2008) 245205. https://doi.org/10.1103/PhysRevB.77.245205.

[169] T. Feng, B.D. Schwartz, Characteristics and origin of the 1.681 eV luminescence center in chemical-vapor-deposited diamond films, J. Appl. Phys. 73 (1993) 1415–1425. https://doi.org/10.1063/1.353239.

[170] K. Ohno, F. Joseph Heremans, L.C. Bassett, B.A. Myers, D.M. Toyli, A.C. Bleszynski Jayich, C.J. Palmstrøm, D.D. Awschalom, Engineering shallow spins in diamond with nitrogen delta-doping, Appl. Phys. Lett. 101 (2012) 082413. https://doi.org/10.1063/1.4748280.

[171] L.J. Rogers, K.D. Jahnke, T. Teraji, L. Marseglia, C. Müller, B. Naydenov, H. Schauffert, C. Kranz, J. Isoya, L.P. McGuinness, F. Jelezko, Multiple intrinsically identical single-photon emitters in the solid state, Nat. Commun. 5 (2014) 4739. https://doi.org/10.1038/ncomms5739.

[172] J.F. (James F.) Ziegler, U. Littmark, J.P. Biersack, The stopping and range of ions in solids / J.F. Ziegler, J.P. Biersack, U. Littmark, Pergamon, New York, 1985.

[173] G. Davies, S.C. Lawson, A.T. Collins, A. Mainwood, S.J. Sharp, Vacancy-related centers in diamond, Phys. Rev. B. 46 (1992) 13157–13170. https://doi.org/10.1103/PhysRevB.46.13157.

[174] T. Schenkel, A. Persaud, S.J. Park, J. Meijer, J.R. Kingsley, J.W. McDonald, J.P. Holder, J. Bokor, D.H. Schneider, Single ion implantation for solid state quantum computer development, J. Vac. Sci. Technol. B Microelectron. Nanometer Struct. Process. Meas. Phenom. 20 (2002) 2819–2823. https://doi.org/10.1116/1.1518016.

[175] C. Wang, C. Kurtsiefer, H. Weinfurter, B. Burchard, Single photon emission from SiV centres in diamond produced by ion implantation, J. Phys. B At. Mol. Opt. Phys. 39 (2006) 37. https://doi.org/10.1088/0953-4075/39/1/005.

[176] B.J.M. Hausmann, T.M. Babinec, J.T. Choy, J.S. Hodges, S. Hong, I. Bulu, A. Yacoby, M.D. Lukin, M. Lončar, Single Color Centers Implanted in Diamond Nanostructures, New J. Phys. 13 (2011) 045004. https://doi.org/10.1088/1367-2630/13/4/045004.

[177] J. Meijer, S. Pezzagna, T. Vogel, B. Burchard, H.H. Bukow, I.W. Rangelow, Y. Sarov, H. Wiggers, I. Plümel, F. Jelezko, J. Wrachtrup, F. Schmidt-Kaler, W. Schnitzler, K. Singer, Towards the implanting of ions and positioning of nanoparticles with nm spatial resolution, Appl. Phys. A. 91 (2008) 567–571. https://doi.org/10.1007/s00339-008-4515-1.

[178] K.-M.C. Fu, C. Santori, P.E. Barclay, R.G. Beausoleil, Conversion of neutral nitrogen-vacancy centers to negatively charged nitrogen-vacancy centers through selective oxidation, Appl. Phys. Lett. 96 (2010) 121907. https://doi.org/10.1063/1.3364135.

[179] M.V. Hauf, B. Grotz, B. Naydenov, M. Dankerl, S. Pezzagna, J. Meijer, F. Jelezko, J. Wrachtrup, M. Stutzmann, F. Reinhard, J.A. Garrido, Chemical control of the charge state

of nitrogen-vacancy centers in diamond, Phys. Rev. B. 83 (2011) 081304. https://doi.org/10.1103/PhysRevB.83.081304.

[180] E. Bernardi, R. Nelz, S. Sonusen, E. Neu, Nanoscale Sensing Using Point Defects in Single-Crystal Diamond: Recent Progress on Nitrogen Vacancy Center-Based Sensors, Crystals. 7 (2017) 124. https://doi.org/10.3390/cryst7050124.

[181] M.W. Dale, G.W. Morley, Medical applications of diamond magnetometry: commercial viability, ArXiv170501994 Cond-Mat Physicsphysics Physicsquant-Ph. (2017).

[182] L. Rondin, J.-P. Tetienne, T. Hingant, J.-F. Roch, P. Maletinsky, V. Jacques, Magnetometry with nitrogen-vacancy defects in diamond, Rep. Prog. Phys. 77 (2014) 056503. https://doi.org/10.1088/0034-4885/77/5/056503.

[183] A. Gruber, A. Dräbenstedt, C. Tietz, L. Fleury, J. Wrachtrup, C. von Borczyskowski, Scanning Confocal Optical Microscopy and Magnetic Resonance on Single Defect Centers, Science. 276 (1997) 2012–2014. https://doi.org/10.1126/science.276.5321.2012.

[184] N. Mizuochi, P. Neumann, F. Rempp, J. Beck, V. Jacques, P. Siyushev, K. Nakamura, D.J. Twitchen, H. Watanabe, S. Yamasaki, F. Jelezko, J. Wrachtrup, Coherence of single spins coupled to a nuclear spin bath of varying density, Phys. Rev. B. 80 (2009) 041201. https://doi.org/10.1103/PhysRevB.80.041201.

[185] R.G. Ryan, A. Stacey, K.M. O’Donnell, T. Ohshima, B.C. Johnson, L.C.L. Hollenberg, P. Mulvaney, D.A. Simpson, Impact of Surface Functionalization on the Quantum Coherence of Nitrogen-Vacancy Centers in Nanodiamonds, ACS Appl. Mater. Interfaces. 10 (2018) 13143–13149. https://doi.org/10.1021/acsami.7b19238.

[186] P.L. Stanwix, L.M. Pham, J.R. Maze, D. Le Sage, T.K. Yeung, P. Cappellaro, P.R. Hemmer, A. Yacoby, M.D. Lukin, R.L. Walsworth, Coherence of nitrogen-vacancy electronic spin ensembles in diamond, Phys. Rev. B. 82 (2010) 201201. https://doi.org/10.1103/PhysRevB.82.201201.

[187] P. Siyushev, V. Jacques, I. Aharonovich, F. Kaiser, T. Müller, L. Lombez, M. Atatüre, S. Castelletto, S. Prawer, F Jelezko, J. Wrachtrup, Low-temperature optical characterization of a near-infrared single-photon emitter in nanodiamonds, New J. Phys. 11 (2009) 113029. https://doi.org/10.1088/1367-2630/11/11/113029.

[188] I.I. Vlasov, A.A. Shiryaev, T. Rendler, S. Steinert, S.-Y. Lee, D. Antonov, M. Vörös, F. Jelezko, A.V. Fisenko, L.F. Semjonova, J. Biskupek, U. Kaiser, O.I. Lebedev, I. Sildos, P.R. Hemmer, V.I. Konov, A. Gali, J. Wrachtrup, Molecular-sized fluorescent nanodiamonds, Nat. Nanotechnol. 9 (2014) 54–58. https://doi.org/10.1038/nnano.2013.255.

[189] L.J. Rogers, K.D. Jahnke, M.W. Doherty, A. Dietrich, L.P. McGuinness, C. Müller, T. Teraji, H. Sumiya, J. Isoya, N.B. Manson, F. Jelezko, Electronic structure of the negatively charged silicon-vacancy center in diamond, Phys. Rev. B. 89 (2014) 235101. https://doi.org/10.1103/PhysRevB.89.235101.

[190] T. Müller, C. Hepp, B. Pingault, E. Neu, S. Gsell, M. Schreck, H. Sternschulte, D. Steinmüller-Nethl, C. Becher, M. Atatüre, Optical signatures of silicon-vacancy spins in diamond, Nat. Commun. 5 (2014) 3328. https://doi.org/10.1038/ncomms4328.

[191] A. S. Barnard, I. I. Vlasov, V. G. Ralchenko, Predicting the distribution and stability of photoactive defect centers in nanodiamond biomarkers, J. Mater. Chem. 19 (2009) 360–365. https://doi.org/10.1039/B813515K.

[192] E. Neu, M. Agio, C. Becher, Photophysics of single silicon vacancy centers in diamond: implications for single photon emission, Opt. Express. 20 (2012) 19956. https://doi.org/10.1364/OE.20.019956.

[193] K. Iakoubovskii, G.J. Adriaenssens, Optical detection of defect centers in CVD diamond, Diam. Relat. Mater. 9 (2000) 1349–1356. https://doi.org/10.1016/S0925-9635(00)00248-X.

[194] S. Häußler, G. Thiering, A. Dietrich, N. Waasem, T. Teraji, J. Isoya, Takayuki Iwasaki, M. Hatano, F. Jelezko, A. Gali, A. Kubanek, Photoluminescence excitation spectroscopy of SiV- and GeV- color center in diamond, New J. Phys. 19 (2017) 063036. https://doi.org/10.1088/1367-2630/aa73e5.

[195] A. Faraon, P.E. Barclay, C. Santori, K.-M.C. Fu, R.G. Beausoleil, Resonant enhancement of the zero-phonon emission from a colour centre in a diamond cavity, Nat. Photonics. 5 (2011) 301–305. https://doi.org/10.1038/nphoton.2011.52.

[196] M. Schreck, B. Stritzker, Nucleation and Growth of Heteroepitaxial Diamond Films on Silicon, Phys. Status Solidi A. 154 (1996) 197–217. https://doi.org/10.1002/pssa.2211540116.

[197] S. Gsell, T. Bauer, J. Goldfuß, M. Schreck, B. Stritzker, A route to diamond wafers by epitaxial deposition on silicon via iridium/yttria-stabilized zirconia buffer layers, Appl. Phys. Lett. 84 (2004) 4541–4543. https://doi.org/10.1063/1.1758780.

[198] X. Checoury, D. Néel, P. Boucaud, C. Gesset, H. Girard, S. Saada, P. Bergonzo, Nanocrystalline diamond photonics platform with high quality factor photonic crystal cavities, Appl. Phys. Lett. 101 (2012) 171115. https://doi.org/10.1063/1.4764548.

[199] S. Schietinger, M. Barth, T. Aichele, O. Benson, Plasmon-Enhanced Single Photon Emission from a Nanoassembled Metal−Diamond Hybrid Structure at Room Temperature, Nano Lett. 9 (2009) 1694–1698. https://doi.org/10.1021/nl900384c.

[200] N.P. de Leon, B.J. Shields, C.L. Yu, D.E. Englund, A.V. Akimov, M.D. Lukin, H. Park, Tailoring Light-Matter Interaction with a Nanoscale Plasmon Resonator, Phys. Rev. Lett. 108 (2012) 226803. https://doi.org/10.1103/PhysRevLett.108.226803.

[201] J.T. Choy, B.J.M. Hausmann, T.M. Babinec, I. Bulu, M. Khan, P. Maletinsky, A. Yacoby, M. Lončar, Enhanced single-photon emission from a diamond–silver aperture, Nat. Photonics. 5 (2011) 738. https://doi.org/10.1038/nphoton.2011.249.

[202] R. Kolesov, B. Grotz, G. Balasubramanian, R.J. Stöhr, A.A.L. Nicolet, P.R. Hemmer, F. Jelezko, J. Wrachtrup, Wave–particle duality of single surface plasmon polaritons, Nat. Phys. 5 (2009) 470. https://doi.org/10.1038/nphys1278.

[203] P. Rai-Choudhury, Handbook of Microlithography, Micromachining, and Microfabrication: Microlithography, IET, 1997.

[204] M. Domonkos, M. Varga, L. Ondič, L. Gajdošová, A. Kromka, Microsphere lithography for scalable polycrystalline diamond-based near-infrared photonic crystals fabrication, Mater. Des. 139 (2018) 363–371. https://doi.org/10.1016/j.matdes.2017.10.076.

[205] C.L. Haynes, A.D. McFarland, M.T. Smith, J.C. Hulteen, R.P. Van Duyne, Angle-Resolved Nanosphere Lithography: Manipulation of Nanoparticle Size, Shape, and Interparticle Spacing, J. Phys. Chem. B. 106 (2002) 1898–1902. https://doi.org/10.1021/jp013570+.

[206] C. Vivensang, L. Ferlazzo-Manin, M.F. Ravet, G. Turban, F. Rousseaux, A. Gicquel, Surface smoothing of diamond membranes by reactive ion etching process, Diam. Relat. Mater. 5 (1996) 840–844. https://doi.org/10.1016/0925-9635(95)00368-1.

[207] J. Heupel, N. Felgen, R. Merz, M. Kopnarski, J.P. Reithmaier, C. Popov, Development of a Planarization Process for the Fabrication of Nanocrystalline Diamond Based Photonic Structures, Phys. Status Solidi A. 216 (2019) 1900314. https://doi.org/10.1002/pssa.201900314.

[208] J. Orloff, L. Swanson, M. Utlaut, High Resolution Focused Ion Beams: FIB and its Applications: The Physics of Liquid Metal Ion Sources and Ion Optics and Their Application to Focused Ion Beam Technology, Springer Science & Business Media, 2003.

[209] Y. Li, H. Takino, F. Frost, Ion beam planarization of diamond turned surfaces with various roughness profiles, Opt. Express. 25 (2017) 7828–7838. https://doi.org/10.1364/OE.25.007828.

[210] K. Luterová, I. Pelant, P. Fojtík, M. Nikl, I. Gregora, J. Kočka, J. Dian, J. Valenta, P. Malý, J. Kudrna, J. Štěpánek, A. Poruba, P. Horváth, Visible photoluminescence and electroluminescence in wide-bandgap hydrogenated amorphous silicon, Philos. Mag. B. 80 (2000) 1811–1832. https://doi.org/10.1080/13642810008216508.

[211] D.E. Carlson, C.R. Wronski, Amorphous silicon solar cell, Appl. Phys. Lett. 28 (1976) 671–673. https://doi.org/10.1063/1.88617.

[212] R.A. Street, Hydrogenated Amorphous Silicon, Cambridge University Press, 2005.

[213] B. Rezek, E. Šípek, M. Ledinský, P. Krejza, J. Stuchlík, A. Fejfar, J. Kočka, Spatially localized current-induced crystallization of amorphous silicon films, J. Non-Cryst. Solids. 354 (2008) 2305–2309. https://doi.org/10.1016/j.jnoncrysol.2007.10.045.

[214] B. Rezek, E. Šípek, M. Ledinský, J. Stuchlík, A. Vetushka, J. Kocka, Creating nanocrystals in amorphous silicon using a conductive tip, Nanotechnology. 20 (2009) 045302. https://doi.org/10.1088/0957-4484/20/4/045302.

[215] E. Verveniotis, B. Rezek, E. Šípek, J. Stuchlík, M. Ledinský, J. Kočka, Impact of AFM-induced nano-pits in a-Si:H films on silicon crystal growth, Nanoscale Res. Lett. 6 (2011) 145. https://doi.org/10.1186/1556-276X-6-145.

[216] J. Meier, J. Spitznagel, U. Kroll, C. Bucher, S. Faÿ, T. Moriarty, A. Shah, Potential of amorphous and microcrystalline silicon solar cells, Thin Solid Films. 451–452 (2004) 518–524. https://doi.org/10.1016/j.tsf.2003.11.014.

[217] L.K. Lam, S. Chen, D.G. Ast, Kinetics of nickel-induced lateral crystallization of amorphous silicon thin-film transistors by rapid thermal and furnace anneals, Appl. Phys. Lett. 74 (1999) 1866–1868. https://doi.org/10.1063/1.123695.

[218] I. Pelant, P. Fojtík, K. Luterová, J. Kočka, A. Poruba, J. Štěpánek, Electric-field-enhanced metal-induced crystallization of hydrogenated amorphous silicon at room temperature, Appl. Phys. A. 74 (2002) 557–560. https://doi.org/10.1007/s003390100913.

[219] J. Fait, J. Čermák, J. Stuchlík, B. Rezek, Complex nano-patterning of structural, optical, electrical and electron emission properties of amorphous silicon thin films by scanning probe, Appl. Surf. Sci. 428 (2018) 1159–1165. https://doi.org/10.1016/j.apsusc.2017.09.228.

[220] E. Verveniotis, E. Šípek, J. Stuchlík, J. Kočka, B. Rezek, Generating ordered Si nanocrystals via atomic force microscopy, J. Non-Cryst. Solids. 358 (2012) 2118–2121. https://doi.org/10.1016/j.jnoncrysol.2011.12.018.

[221] R.P. Sear, Nucleation: theory and applications to protein solutions and colloidal suspensions, J. Phys. Condens. Matter. 19 (2007) 033101. https://doi.org/10.1088/0953-8984/19/3/033101.

[222] A.J. Page, R.P. Sear, Heterogeneous Nucleation in and out of Pores, Phys. Rev. Lett. 97 (2006) 065701. https://doi.org/10.1103/PhysRevLett.97.065701.

[223] M. Endo, Y. Yang, H. Sugiyama, DNA origami technology for biomaterials applications, Biomater. Sci. 1 (2013) 347–360. https://doi.org/10.1039/C2BM00154C.

[224] O. Babchenko, T. Izak, E. Ukraintsev, K. Hruska, B. Rezek, A. Kromka, Toward surface-friendly treatment of seeding layer and selected-area diamond growth, Phys. Status Solidi B. 247 (2010) 3026–3029. https://doi.org/10.1002/pssb.201000124.

[225] J. Fait, Š. Potocký, Š. Stehlík, J. Stuchlík, A. Artemenko, A. Kromka, B. Rezek, Nucleation of diamond micro-patterns with photoluminescent SiV centers controlled by amorphous silicon thin films, Appl. Surf. Sci. 480 (2019) 1008–1013. https://doi.org/10.1016/j.apsusc.2019.03.064.

[226] H. Kozak, A. Kromka, O. Babchenko, B. Rezek, Directly Grown Nanocrystalline Diamond Field-Effect Transistor Microstructures, Sens. Lett. 8 (2010) 482–487. https://doi.org/10.1166/sl.2010.1298.

[227] M. Varga, V. Vretenar, T. Izak, V. Skakalova, A. Kromka, Carbon nanotubes overgrown and ingrown with nanocrystalline diamond deposited by different CVD plasma systems, Phys. Status Solidi B. 251 (2014) 2413–2419. https://doi.org/10.1002/pssb.201451176.

[228] Š. Potocký, J. Holovský, Z. Remeš, M. Müller, J. Kočka, A. Kromka, Si-related color centers in nanocrystalline diamond thin films, Phys. Status Solidi B. 251 (2014) 2603–2606. https://doi.org/10.1002/pssb.201451177.

[229] V.A. Volodin, D.I. Koshelev, Quantitative analysis of hydrogen in amorphous silicon using Raman scattering spectroscopy, J. Raman Spectrosc. 44 (2013) 1760–1764. https://doi.org/10.1002/jrs.4408.

[230] W.B. Jackson, N.M. Amer, A.C. Boccara, D. Fournier, Photothermal deflection spectroscopy and detection, Appl. Opt. 20 (1981) 1333–1344. https://doi.org/10.1364/AO.20.001333.

[231] D. Nečas, P. Klapetek, Gwyddion: an open-source software for SPM data analysis, Open Phys. 10 (2012) 181–188. https://doi.org/10.2478/s11534-011-0096-2.

[232] J. Fait, M. Varga, K. Hruška, A. Kromka, B. Rezek, L. Ondič, Effect of CVD diamond morphology on the photoluminescence extraction by photonic crystal slabs, (to be submitted).

[233] L. Ondič, M. Varga, J. Fait, K. Hruška, V. Jurka, A. Kromka, J. Maňák, P. Kapusta, J. Nováková, Photonic crystal cavity-enhanced emission from silicon vacancy centers in polycrystalline diamond achieved without postfabrication fine-tuning, Nanoscale. 12 (2020) 13055–13063. https://doi.org/10.1039/c9nr10580h.

[234] J. Fait, S. Putz, G. Wachter, J. Schalko, U. Schmid, M. Arndt, M. Trupke, High finesse telecom O-band microcavities, (submitted to Optica).

[235] J. Xavier, J. Probst, F. Back, P. Wyss, D. Eisenhauer, B. Löchel, E. Rudigier-Voigt, C. Becker, Quasicrystalline-structured light harvesting nanophotonic silicon films on nanoimprinted glass for ultra-thin photovoltaics, Opt. Mater. Express. 4 (2014) 2290–2299. https://doi.org/10.1364/OME.4.002290.

[236] G.W. Biedermann, F.M. Benito, K.M. Fortier, D.L. Stick, T.K. Loyd, P.D.D. Schwindt, C.Y. Nakakura, R.L. Jarecki, M.G. Blain, Ultrasmooth microfabricated mirrors for quantum information, Appl. Phys. Lett. 97 (2010) 181110. https://doi.org/10.1063/1.3511743.

[237] D. Najer, M. Renggli, D. Riedel, S. Starosielec, R.J. Warburton, Fabrication of mirror templates in silica with micron-sized radii of curvature, Appl. Phys. Lett. 110 (2017) 011101. https://doi.org/10.1063/1.4973458.

List of publications

Published articles related to the thesis

- L. Ondič, M. Varga, K. Hruška, J. Fait, P. Kapusta, *Enhanced Extraction of Silicon-Vacancy Centers Light Emission Using Bottom-Up Engineered Polycrystalline Diamond Photonic Crystal Slabs*, ACS Nano (2017), doi: 10.1021/acsnano.6b08412
    - Citations: WOS: 18 (incl. 7 auto citations), SCOPUS: 19 (incl. 9 auto citations)
- J. Fait, J. Čermák, J. Stuchlík, B. Rezek, *Complex nano-patterning of structural, optical, electrical and electron emission properties of amorphous silicon thin films by scanning probe*, Applied Surface Science (2018), doi: 10.1016/j.apsusc.2017.09.228
    - WOS citations: 4 (incl. 1 auto citation), SCOPUS: 3 (incl. 1 auto citation)
- J. Fait, M. Varga, K. Hruška, Z. Remeš, V. Jurka, A. Kromka, B. Rezek, L. Ondič, *Maximized vertical photoluminescence from non-homogeneous optical material with losses employing resonant excitation and extraction of photonic crystal modes*, Nanophotonics (2019), doi: 10.1515/nanoph-2019-0042
    - Citations: SCOPUS: 1 auto citation
- J. Fait, Š. Potocký, Š. Stehlík, J. Stuchlík, A. Artemenko, A. Kromka, B. Rezek, *Nucleation of diamond micro-patterns with photoluminescent SiV centers controlled by amorphous silicon thin films*, Applied Surface Science (2019), doi: 10.1016/j.apsusc.2019.03.064
- L. Ondič, M. Varga, J. Fait, K. Hruška, V. Jurka, A. Kromka, J. Maňák, P. Kapusta, J. Nováková, *Photonic crystal cavity-enhanced emission from silicon vacancy centers in polycrystalline diamond achieved without postfabrication fine-tuning*, Nanoscale (2020), doi: 10.1039/c9nr10580h

Submitted/Prepared for submission articles related to the thesis

- J. Fait, S. Putz, G. Wachter, M. Trupke, *High finesse telecom O-band micro cavities*, Submitted to Optica
- J. Fait, M. Varga, K. Hruška, A. Kromka, B. Rezek, L. Ondič, *Effect of CVD diamond morphology on the photoluminescence extraction by photonic crystal slabs*, Prepared for submission

Other publications in impacted journals

- J. Čermák, L. Mihai, D. Sporea, Y. Galagan, J. Fait, A. Artemenko, P. Štenclová, B. Rezek, M. Straticiuc, I. Burducea, *Proton irradiation induced changes in glass and polyethylene terephthalate substrates for photovoltaic solar cells*, Solar Energy Materials and Solar Cells (2018), doi: 10.1016/j.solmat.2018.06.046
    - Citations: WOS: 3 (incl. 1 auto citation), SCOPUS: 3 (incl. 1 auto citation)

- Š. Stehlík, L. Ondič, M. Varga, J. Fait, A. Artemenko, T. Glatzel, A. Kromka, B. Rezek, *Silicon-vacancy centers in ultra-thin nanocrystalline diamond films*, Micromachines (2018), doi: 10.3390/mi9060281
    - Citations: WOS: 2 (incl. 1 auto citation), SCOPUS: 2 (incl. 1 auto citation)
- L. Ondič, J. Fait, M. Varga, J. Maňák, and J. Nováková, *Polycrystalline diamond photonic crystal slabs prepared by focused ion beam milling*, Novel Optical Materials and Applications (2018), doi: 10.1364/NOMA.2018.NoTu4J.6

List of contributions on conferences and seminars

- J. Fait, Š. Potocký, J. Stuchlík, A. Kromka, B. Rezek: “Spontaneous nucleation of diamond suppressed by amorphous and microcrystalline silicon”, Hasselt Diamond Workshop 2017 – SBDD XXII, Hasselt, Belgium, March 2017; poster
- J. Fait, J. Čermák, J. Stuchlík, B. Rezek: “Complex nano-patterning of amorphous silicon thin films by scanning probe”, SPM Workshop 2017, Lednice, Czech Republic, March 2017; oral
- J. Fait: “Complex nano-patterning of amorphous silicon thin films by scanning probe”, Department seminar, CTU Prague, Czech Republic, April 2017; oral
- J. Fait, L. Ondič, M. Varga, K. Hruška, A. Kromka, B. Rezek: “Effect of diamond deposition system on optical properties of polycrystalline diamond 2D photonic crystal slabs”, 16th IUVSTA International Summer School on Physics at Nanoscale, Devět Skal, Czech Republic, June 2017; poster
- J. Fait, J. Čermák, A. Kromka, B. Rezek: “Precise nanoscale patterning of amorphous silicon for electronics and photonics”, Cena Nadace ČEZ, Prague, Czech Republic, June 2017; poster
- J. Fait, L. Ondič, M. Varga, K. Hruška, A. Kromka, B. Rezek: “Structural and material properties of nanocrystalline diamond photonic crystal slabs for high light extraction efficiency”, Nanocon 2017, Brno, Czech Republic, October 2017; oral
- J. Fait, L. Ondič, M. Varga, K. Hruška, A. Kromka, B. Rezek: “Structural and material properties of nanocrystalline diamond photonic crystal slabs for high light extraction efficiency”, The Sixth International Education Forum on Environment and Energy Science, Tenerife, Spain, December 2017; oral
- J. Fait, J. Čermák, A. Kromka, B. Rezek: “Precise nanoscale patterning of amorphous silicon films for electronics and photonics”, International Workshop on Teaching Photovoltaics, Prague, March 2018; poster
- J. Fait, L. Ondič, M. Varga, K. Hruška, A. Kromka, B. Rezek: “Resonant excitation and extraction: A way to maximized vertical light emission from diamond photonic crystal slabs”, ICN+T 2018, Brno, Czech Republic, July 2018; oral
- J. Fait, L. Ondič, M. Varga, K. Hruška: “Silicon vacancy centers light emission rerouted into vertical direction via leaky modes of a photonic crystal slab”, 29th International Conference on Diamond and Carbon Materials, Dubrovnik, Croatia, September 2018; oral
- J. Fait, Š. Potocký, J. Stuchlík, A. Artemenko, A. Kromka, B. Rezek: “Diamond Nanocrystals Nucleation Controlled by Amorphous and Nanocrystalline Silicon Thin

Films”, 29th International Conference on Diamond and Carbon Materials, Guildford, United Kingdom, September 2018; poster

- J. Fait, Š. Potocký, J. Stuchlík, A. Artemenko, A. Kromka, B. Rezek: “Selective growth of photoluminescent nanocrystalline diamond micropatterns by using hydrogenated amorphous silicon film”, Nanocon 2018, Brno, Czech Republic, October 2018; oral
- J. Fait, M. Varga, K. Hruška, A. Kromka, B. Rezek, L. Ondič “Effect of polycrystalline diamond morphology on the PL extraction with photonic crystal slabs” Hasselt Diamond Workshop 2019 – SBDD XXIV, Hasselt, Belgium, March 2019; poster

Own contribution of the author

In the research related to the dissertation thesis, participation of more authors was necessary. I contributed to the research by performing the majority of numerical simulations (RCWA – program RSoft, FDTD – program MEEP, MPB program) for the design of photonic structures and for the interpretation of the results. I also performed the measurements of angle-resolved photoluminescence, micro-photoluminescence, Raman micro-spectroscopy, AFM, white-light interferometry, and processed the obtained data. I developed a new method for patterning a thin a-Si:H layer by using conductive AFM microscope. I also participated in the discussions regarding the parameters of the CVD diamond growth and a-Si:H deposition. However, specialized technological methods were used for the depositions as well as for the patterning of samples and they were performed by experts in this field.

Regarding the publication of results, I wrote the majority of the articles, where I was the first author. I also prepared the figures, graphs and illustrations in these articles. The articles were further reviewed and improved based on the remarks of other authors. I also communicated with the editor and referees during the publication process. I participated on the publication of other articles that I co-authored during meetings with other authors and by making notes and improvements to the texts.

Participation on projects

I was a principal investigator of the SGS project for PhD students (SGS17/179/OHK4/3T/13) with the topic *Diamond Photonic Structures and Their Influence on the Intensity of SiV Centers Photoluminescence*. This project was finished after the first year because of recommendation to merge SGS projects of more students with similar topics to enable better exploitation of the resources. After that I became a principal investigator of a new SGS project (SGS18/179/OHK4/3T/13) with a broader topic *Opto-electronic and photonic properties of diamond nanostructures and their interfaces with organic molecules investigated by experimental and computational methods* covering my research and research of my fellow PhD students Daria Miliaieva and Petra Matunová.

During my stay in Vienna I was working on an Aktion program scholarship project that was devoted to enhancement of photon collection efficiency from single photon emitters in monocrystalline diamond and in silicon carbide.

I was participating on the GAČR project (16-09692Y) with topic “Studying effects of photonic crystal structures on photoluminescence of silicon-vacancy centers in diamond” under the lead of RNDr. Lukáš Ondič, PhD., the supervisor-specialist of this thesis.

Part of the activities was also funded by the Centre for Advanced Photovoltaics (European Regional Development Fund project CZ.02.1.01/0.0/0.0/15 003/000046).

Awards

The article *Complex nano-patterning of structural, optical, electrical and electron emission properties of amorphous silicon thin films by scanning probe* published in Applied Surface Science has gained recognition by the Elsevier Physics Twitter channel and was granted with promotional access for three months.

I was awarded with the Aktion scholarship for 5 months for a visiting PhD stay at the University of Vienna. I spent 9 months in Vienna in total as the rest of the stay was financed by the Mobility program of the Czech Technical University. During this period, I was working in the Quantum optics group (led by prof. Philip Walther) at the University of Vienna in the team of Dr. Michael Trupke. Under his supervision, I was studying the properties of optical micro-resonators, which can be used for the enhancement of photon collection efficiency from single photon emitters.

I was awarded 2nd place in a competition of the ČEZ company "Cena Nadace ČEZ 2017". The topic of my project was *Precise nanoscale patterning of amorphous silicon for electronics and photonics*.

I was nominated for the Milan Odehnal award in 2020 of the Czech Physics Society (http://ipnp.cz/cfs/index.php/cena-milana-odehnala). The results were not yet announced at the time of the thesis submission.

List of attachments

1. L. Ondič, M. Varga, K. Hruška, J. Fait, P. Kapusta, Enhanced Extraction of Silicon-Vacancy Centers Light Emission Using Bottom-Up Engineered Polycrystalline Diamond Photonic Crystal Slabs, ACS Nano (2017), doi: 10.1021/acsnano.6b08412

2. J. Fait, M. Varga, K. Hruška, Z. Remeš, V. Jurka, A. Kromka, B. Rezek, L. Ondič, *Maximized vertical photoluminescence from non-homogeneous optical material with losses employing resonant excitation and extraction of photonic crystal modes*, Nanophotonics (2019), doi: 10.1515/nanoph-2019-0042

3. J. Fait, M. Varga, K. Hruška, A. Kromka, B. Rezek, L. Ondič, *Effect of CVD diamond morphology on the photoluminescence extraction by photonic crystal slabs*, Prepared for submission

4. L. Ondič, M. Varga, J. Fait, K. Hruška, V. Jurka, A. Kromka, J. Maňák, P. Kapusta, J. Nováková, *Photonic crystal cavity-enhanced emission from silicon vacancy centers in polycrystalline diamond achieved without postfabrication fine-tuning*, Nanoscale (2020), doi: 10.1039/c9nr10580h

5. J. Fait, S. Putz, G. Wachter, J. Schalko, U. Schmid, M. Arndt, M. Trupke, *High finesse telecom O-band microcavities,* submitted to Optica

6. J. Fait, J. Čermák, J. Stuchlík, B. Rezek, *Complex nano-patterning of structural, optical, electrical and electron emission properties of amorphous silicon thin films by scanning probe*, Applied Surface Science (2018), doi: 10.1016/j.apsusc.2017.09.228

7. J. Fait, Š. Potocký, Š. Stehlík, J. Stuchlík, A. Artemenko, A. Kromka, B. Rezek, *Nucleation of diamond micro-patterns with photoluminescent SiV centers controlled by amorphous silicon thin films,* Applied Surface Science (2019), doi: 10.1016/j.apsusc.2019.03.064

Please note that the numbering of figures, tables, equations, and references is done separately within the articles that form compact works. Please also note that the symbols used for individual quantities may differ from the symbols used in the theoretical part of this thesis and it may also differ between individual articles.

ACS NANO
www.acsnano.org
ARTICLE

Enhanced Extraction of Silicon-Vacancy Centers Light Emission Using Bottom-Up Engineered Polycrystalline Diamond Photonic Crystal Slabs

Lukáš Ondič,*,† Marian Varga,† Karel Hruška,† Jan Fait,†,‡ and Peter Kapusta§

†Institute of Physics, Academy of Sciences of the Czech Republic, v.v.i., Cukrovarnická 10, CZ-162 00, Prague 6, Czech Republic
‡Faculty of Electrical Engineering, Czech Technical University in Prague, Technická 2, CZ-166 27, Prague 6, Czech Republic
§J. Heyrovský Institute of Physical Chemistry, Academy of Sciences of the Czech Republic, v.v.i., Dolejškova 3, CZ-182 23, Prague 8, Czech Republic

Supporting Information

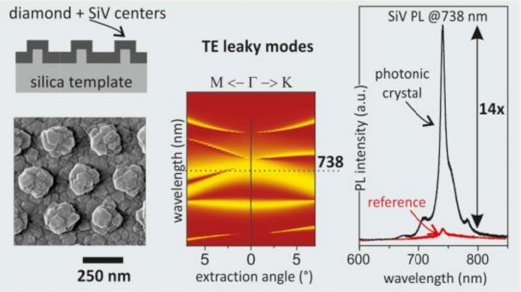

ABSTRACT: Silicon vacancy (SiV) centers are optically active defects in diamond. The SiV centers, in contrast to nitrogen vacancy (NV) centers, possess narrow and efficient luminescence spectrum (centered at ≈738 nm) even at room temperature, which can be utilized for quantum photonics and sensing applications. However, most of light generated in diamond is trapped in the material due to the phenomenon of total internal reflection. In order to overcome this issue, we have prepared two-dimensional photonic crystal slabs from polycrystalline diamond thin layers with high density of SiV centers employing bottom-up growth on quartz templates. We have shown that the spectral overlap between the narrow light emission of the SiV centers and the leaky modes extracting the emission into almost vertical direction (where it can be easily detected) can be obtained by controlling the deposition time. More than 14-fold extraction enhancement of the SiV centers photoluminescence was achieved compared to an uncorrugated sample. Computer simulation confirmed that the extraction enhancement originates from the efficient light-matter interaction between light emitted from the SiV centers and the photonic crystal slab.

KEYWORDS: *silicon-vacancy center, photoluminescence, photonic crystal slab, leaky modes, polycrystalline diamond*

Diamond has a wide bandgap of 5.5 eV and the strongest UV emission line positioned at 5.27 eV (235 nm) at room temperature.[1] Nevertheless, luminescence in the visible spectrum from diamond can be achieved by introducing defects and impurities[2] during the fabrication process, which leads to the formation of light-emitting color centers. This makes diamond a material very attractive for integrated and quantum photonics[3−5] but also in biology for labeling[6,7] and sensing applications.[8]

One of the very promising color centers in diamond, especially for quantum information processing and single photon generation, are negatively charged silicon-vacancy (SiV) centers which are created when a single Si atom substitutes for two C atoms in the split vacancy configuration.[9] Compared to the well-known and extensively investigated nitrogen vacancy (NV) centers with broad room temperature emission spectrum (width of about 100 nm),[3,10−12] the SiV centers exhibit very narrow zero-phonon-line (ZPL) of width of 5 nm even at room temperature, which is centered at ≈738 nm.[13] Another important advantage of the SiV centers compared to other diamond optical centers is that 70% of its luminescence is concentrated in the ZPL.[14] Fast decay times in the range of nanoseconds along with single photon emitters properties,[15−18] makes SiV centers great candidates for practical applications as they would not require cooling to low temperatures.

SiV centers can be fabricated by ion implantation into the diamond[15] or directly during deposition of the diamond layers by adjusting growth parameters.[16,19] Recently, we have successfully fabricated polycrystalline diamond films with

Received: December 15, 2016
Accepted: February 25, 2017
Published: February 26, 2017

DOI: 10.1021/acsnano.6b08412
ACS Nano 2017, 11, 2972−2981

brightly luminescent SiV centers by employing microwave-plasma chemical vapor deposition.[20] This approach presents relatively inexpensive and flexible way of diamond films fabrication across large areas, possibility to adjust material properties, and flexibility in coating other materials. However, the challenge to increase the optical quality of the prepared layers in the visible spectral range and thereby to increase the luminescence intensity from SiV centers is still an issue. Different ways how to increase quantum yield of the SiV centers photoluminescence (PL) are investigated.

The efficiency of PL from optically active diamond color centers can be improved also indirectly by combining them with plasmonic (metallic)[21−27] or photonic (dielectric) nanostructures. For example, the NV centers PL was coupled to the modes of diamond microdisk[28] and microring resonators,[29] to a photonic crystal cavity[30] or nanowires.[10] Interestingly, even though a number of photonic structures have been demonstrated both on single-crystal[5,31−33] and polycrystalline diamond,[34−36] only a few works exist on the photonic nanostructures with the SiV centers. Recently, Becher *et al.* have obtained 2.8 enhancement of the SiV centers PL *via* the Purcell effect by spectrally tuning the photonic crystal cavity mode by oxidizing the diamond film.[37] The same group has also shown that a single SiV center can be coupled to a photonic crystal cavity prepared in a single-crystal diamond and they achieved 19-fold enhancement of the SiV center PL.[38] For the polycrystalline diamond, 2D arrays of diamond nanopillars[39,40] enabled to manipulate the PL from SiV centers, however, no significant enhancement of the PL was achieved.

For the case of the optical centers embedded in thin layers, the PL efficiency can be also increased by enhancing the extraction efficiency from the layer, for example, by fabricating a 2D photonic crystal (PhC) on the top of it. The mechanism is such that light emitted in the layer first couples into the leaky modes of the PhC and then radiates to air under defined angles.[41,42] In ref 36 and in more detail in ref 43, we have introduced this approach to polycrystalline diamond layers. We have etched the surface of a diamond layer into the shape of a square-lattice PhC in order to increase intensity of the spectrally broad “white” emission of diamond which, however, did not contain optically active SiV centers. In ref 44, we have shown that light emission from surface-deposited Si quantum dots on such PhC can be also enhanced.

In order to employ the leaky modes concept for the SiV centers light emission, the fabrication technique must enable to obtain perfect spectral overlap of the leaky modes with the narrow PL of the SiV centers. Furthermore, the overlap with vertically propagating modes is desirable from the application point of view, for example in photonics or sensing, because it simplifies light collection from such device. The typically employed structuring techniques such as focused ion beam milling[45−47] or reactive ion etching[32,36,43,48,49] of the diamond surface through a periodic mask defined by an electron beam lithography could be employed. However, due to very narrow emission spectrum of the SiV centers, these methods would require many testing samples to obtain the requested spectral overlap with the vertically propagating leaky modes. At least for polycrystalline diamond, these structuring methods appear not cost-efficient for this particular case. Furthermore, we have an experience that the ion etching of the polycrystalline diamond often results in relatively low structural quality of the samples.[44]

Here, on the contrary, we present an efficient yet relatively simple method to obtain 2D PhC slabs on polycrystalline diamond layers having leaky modes spectrally overlapping the narrow emission line of the SiV centers. It is based on growing the diamond layer on a patterned quartz substrate and it thus avoids etching of the diamond itself. The electron beam lithography and reactive ion etching is employed only for etching the quartz template with a demand on precision, which is easily achievable without any time-consuming testing. The precise spectral overlap of the narrow PL spectrum of the SiV centers with the vertical leaky modes is achieved by subsequent growth of the polycrystalline diamond layer. It takes an advantage from the fact that the spectral position of the leaky mode resonances varies with the thickness of the diamond waveguiding layer, which is a parameter easily controlled by deposition time. Strength of this method is first demonstrated on a series of samples having different thickness of the diamond layer. Samples with optimal thickness are then employed to enhance the PL extraction efficiency of the embedded SiV centers. We will show that by using this approach, the PL extraction efficiency can be increased more than 14 times compared to the emission from the SiV centers in an unpatterned layer. Furthermore, the structure was designed such that the PL emission was directed almost in the vertical direction, which simplifies light collection.

RESULTS AND DISCUSSION

Dimensions of the PhC slabs were designed employing rigorous-coupled wave-analysis (RCWA) technique. The primary goal was to achieve a spectral overlap of the SiV centers PL emission with the leaky modes located near the Γ-point of the reciprocal lattice by tuning the diamond layer thickness. These modes exhibit low group velocity[50,51] and efficient coupling into the exterior[52] and thus should enable an efficient extraction of light emitted by the embedded SiV centers. Another reason why the leaky modes around the Γ-point are preferred extraction channels is that these modes are extracted in vertical or almost vertical directions, which is favorable for optical applications. Figure 1a shows a cross-section of the PhC structure used in the simulation. As a result of the computation, a set of parameters specified in the Figure 1a were obtained for the PhC composed of columns ordered into square and hexagonal lattice symmetries. In the simulation we assume that the speed of the lateral growth is comparable to the horizontal one. In such case, the diamond columns diameter is equal to the sum of the silica column diameter d_{sub} and twice the thickness of the overgrown diamond h, *i.e.*, $d = d_{sub} + 2h$.

To elucidate our approach, Figure 1b shows the simulated normal incidence transmission spectra of hexagonal PhCs with different thickness of the diamond layer h. Leaky modes are in the transmission spectra manifested as Fano resonances due to the fact that light of a given wavelength incident on the PhC from outside under a given angle can couple into the leaky mode of the PhC when it fulfills the Bragg diffraction condition.[53,54] By decreasing the thickness of the layer, the fundamental TE and TM mode resonances shift toward lower wavelengths and for the PhC with $h = 110$ nm, the TE mode overlaps with the SiV center emission band. The choice of the overlap with the TE-mode is based on its lower Q-factor compared to the TM-mode given by the clearly (except for the $h = 175$ nm) spectrally broader resonance. The advantage of the low Q-factor is (i) easily achievable spectral overlap with desired wavelengths, and (ii) shorter extraction length and thus only a limited interaction of the radiation with optical losses in

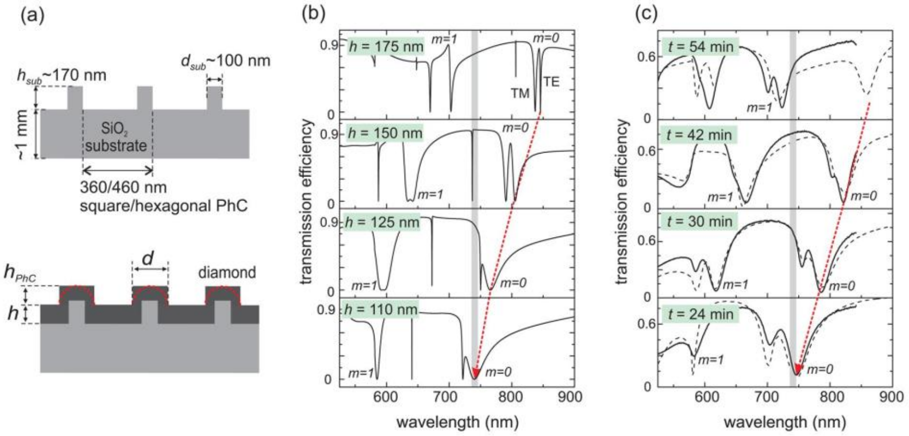

Figure 1. (a) Schematic cross section of a quartz periodic template (top) and the resulting PhC after the diamond growth—the ideal case with the cylindrical columns (dark gray) *vs* the more-realistic case with the dome-shaped pillars (dashed red curve) are depicted (bottom). (b) Simulated transmission spectra for normally incident light on the hexagonal PhC structures with ideal cylindrical columns (shown in a) and having different thickness of the diamond layer h and the column diameter $d = d_{sub} + 2h$, which demonstrates the tunability of the leaky resonances with the diamond layer thickness. Deep minima in transmission curves are the TE or TM leaky modes of different order m ($m = 0$ is a fundamental mode). The gray rectangle depicts spectral position of the SiV center PL band. (c) Measured transmission spectra (solid curves) for the normally incident light on the hexagonal PhC samples grown for different deposition time t and thus differing in thicknesses and diameters of the columns. The gray rectangle depicts spectral position of the SiV center PL band. The dashed black curves depict the computed transmission spectra simulated taking into account the real properties of the fabricated samples (dome-shaped pillars, thickness h, and optical losses).

the system. As the polarization of light emitted by the SiV centers is random due to the random orientation of the diamond grains forming the layer, it might appear that only the part of emission coupled to the TE leaky modes will be extracted using this scheme. Nevertheless, as it will be shown experimentally, also a number of TM modes exist at this wavelength around the Γ-point for the case of the PhCs with the hexagonal lattice symmetry. Therefore, also the SiV centers light emission coupled to the TM leaky modes will be efficiently extracted in the almost vertical directions and covered by the narrow collection angle of the detection. Fundamental modes were chosen as the extraction channels because their Gaussian like spatial distribution of electric field with only one maximum allows for their efficient feeding by the SiV centers.

It should be noted that the computed parameters were simulated using values of refractive index taken from the index database and supposing structures with perfect structural quality. From our previous experience, we anticipated that the resulting structures may have, except for the lattice constant, slightly different parameters (refractive index, diameter of the columns, shape of the columns). These differences are a consequence of many fabrication steps involved, which often lead to structural imperfections, and also a consequence of the polycrystalline nature of the material. Nevertheless, as it was not easy to estimate the exact trend of the diamond growth in advance, the results of the simulation served as a very good starting point for the subsequent fabrication.

The fabrication process was divided into two main steps which are schematically depicted in Figure 1a. First, quartz substrates were nanostructured with a periodicity and dimensions predicted by a computer simulation employing electron beam lithography technique and reactive ion etching (RIE). Namely, 4 identical periodic structures (each having 1 × 1 mm^2) comprising columns (diameter ≈ 100 nm, height ≈ 170 nm) with square lattice symmetry (lattice constant $a = 360$ nm) and 4 identical structures composed of similarly high columns with hexagonal symmetry ($a = 460$ nm) were fabricated on the quartz substrates. As a second step, the periodic patterns were seeded with diamond nanopowder and subsequently overgrown with diamond layers yielding polycrystalline diamond PhC slabs. SiV centers were formed during the growth in a plasma reactor by placing a source of Si close to the sample. Thickness of the diamond layer was controlled by the deposition time. In order to experimentally demonstrate the effect of different diamond layer thicknesses on photonic properties of the structures, deposition times of 54, 42, 30, and 24 min were used. Figure 2 shows SEM images of the fabricated PhC slabs. It is evident that with decreasing the deposition time, the diameter of the columns decreases and their shape slightly changes. We have verified by the AFM measurements that the height of the columns h_{PhC} remained almost equal to the height of the etched silica columns h_{sub}. The diamond-covered columns had a slightly dome-like shape as measured by the SEM and AFM (see Supporting Information). Due to a geometrical difference between the real samples and the ideal simulated ones, mainly in the shape of the pillars (dome-like shape pillars *vs* cylindrical columns), the thickness h of the grown samples needed to be in some cases increased compared to the simulated one in order to demonstrate a similar trend of the leaky modes shifting in the experimental data. The thicknesses of the grown diamond layers were ≈285, 215, 155, and 115 nm going from the longest deposition time to the shortest one. The difference between the predicted (with the ideal columns) and the real thickness is negligible for the shortest deposition time. However, it increases with increasing the deposition time meaning that the longer time grown

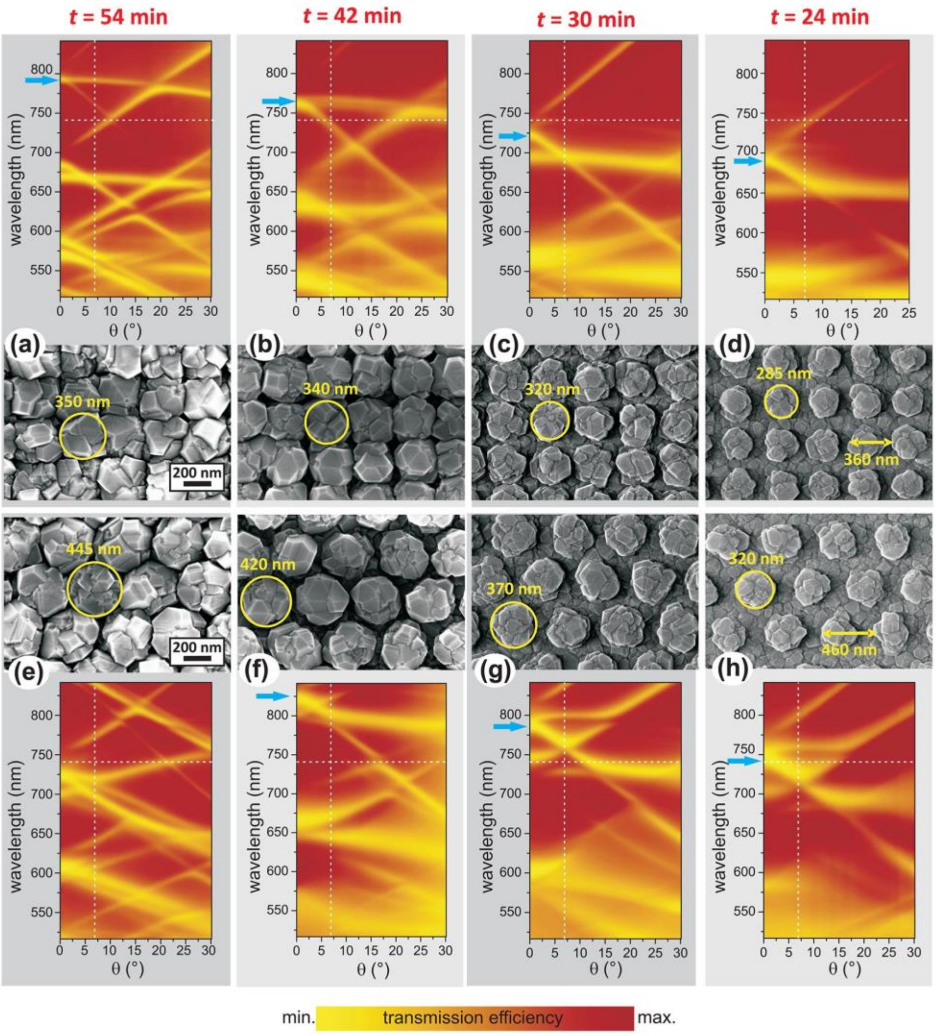

Figure 2. SEM images of the fabricated diamond PhC slabs with square (a−d) and hexagonal (e−h) lattice symmetry and the corresponding angle-resolved S-polarized transmission spectra in the Γ−X direction for the square lattice and in the Γ−K direction for the hexagonal lattice PhCs. Leaky modes are visible as bands in the maps of transmission efficiency plotted as a function of wavelength and the angle of incidence θ. The blue arrows depict TE fundamental modes of the given sample. The horizontal and vertical white dashed lines depict a spectral position of the SiV center PL maximum and the boundary of the collection cone defined by the numerical aperture of the objective used in micro PL measurements, respectively.

structures cannot be anymore well approximated by the ideal case of the cylindrical columns. In the following, we will show that the photonic properties of the fabricated PhCs can be very well reproduced by taking into account the real shape of the columns in the simulation. We would like to note that it is out of scope of this study to describe in more detail the diamond growth process as it depends in a nontrivial way on many parameters of the prepatterned quartz template such as lattice constant, filling factor, *etc.*

After the diamond growth, we probed the leaky mode resonances of the fabricated PhCs employing angle and polarization resolved transmission spectroscopy. The measured normal incidence transmission spectra of the hexagonal lattice PhCs prepared with different deposition times, plotted in Figure 1c, qualitatively follow the trend predicted by the simulation shown in Figure 1b. Note that for the sample with deposition time of $t = 54$ min we could not see the fundamental leaky mode due to the spectral limitation of the detector but we can clearly identify the first order modes.

In order to describe the measured spectra by the simulation, the real dimensions of the sample extracted from the SEM images, dome-like shape of the columns and optical losses were included for the simulated structure (see the Methods section for details). A very good quantitative agreement was obtained between the measurement and the theory for the structures grown for 24, 30 and also 42 min (Figure 1c, solid *vs* dashed

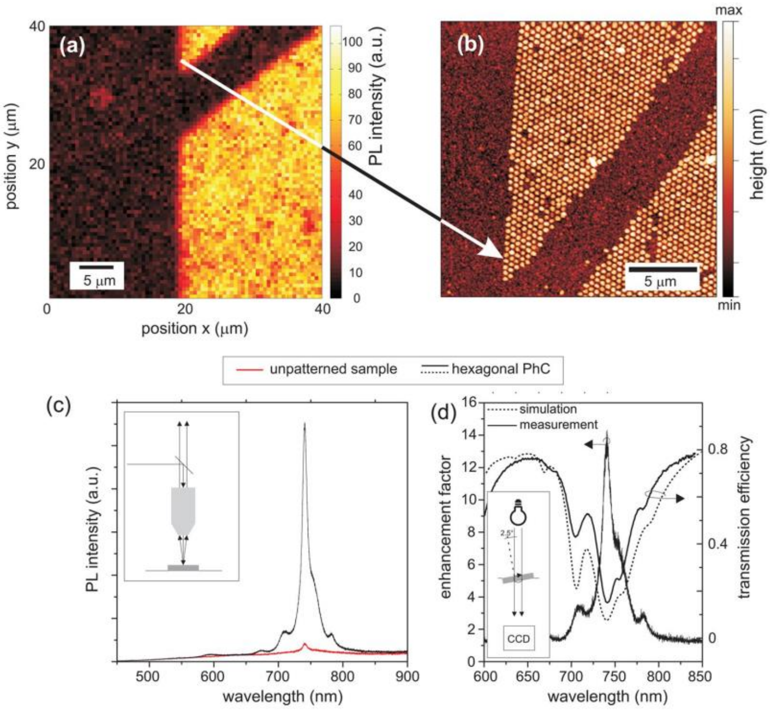

Figure 3. (a) Spectrally integrated (740 ± 13 nm) confocal PL image of the edge of the PhC structure. The strongly light emitting surface on the right side represents the PhC structure, while the less emitting part on the left side is the unpatterned part of the diamond layer. Scratch that removed some columns at the upper part of the PhC structure is also visible. (b) AFM image of the edge of the PhC structure corresponding to the part of the image shown in (a). (c) Comparison of PL emission spectrum of the hexagonal PhC (black) corresponding to the SEM micrograph in Figure 2h and that of an unpatterned diamond sample (red). (d) Enhancement factor, defined as ratio of the PL intensity from the PhC to that from the unpatterned sample, is compared to the measured and simulated transmission curves obtained with S-polarized light along the Γ−K direction and incident angle of 2.5° for the hexagonal lattice PhC. Insets show simplified sketches of the experimental setups used for acquiring the plotted data.

line). For the structure grown for 54 min, the theoretical curve is slightly different from the measured one due to very irregular shape of the diamond pillars.

When the angle-resolved transmission efficiency is plotted as a function of wavelength and the angle of incidence, it forms a photonic band diagram of the studied PhC slab[41,52,55] in the angle-wavelength representation. Naturally, only those modes of the structure which couple with air modes can be mapped by this approach. Figure 2 shows the measured photonic band diagrams corresponding to the fabricated structures whose SEM images are displayed in parallel. Photonic bands are formed by the deep minima in transmission curves. Only those photonic band diagrams measured with S-polarized light propagating along the Γ−X direction for the square and along the Γ−K direction for the hexagonal lattice PhCs, respectively, are shown. Photonic band diagrams of the leaky modes of all the fabricated structures measured with S and P polarized light along the significant directions are included in Supporting Information. For the PhC samples grown for 54 min, it clearly holds that the fundamental leaky modes are spectrally red-shifted with respect to the SiV center PL emission. For the square lattice, the fundamental leaky mode at the Γ-point is located at around 790 nm and for the hexagonal lattice the mode is out of the detection window of our experimental setup. By gradually shortening the deposition time, the fundamental leaky mode resonances blue shift toward the SiV center PL band which is in Figure 2 schematically depicted by horizontal dashed lines. The goal to get an overlap of the SiV center PL with modes at or close to the Γ-point is almost perfectly satisfied for the square lattice PhC grown for 30 min and for the hexagonal lattice PhC grown for 24 min. For the square PhC, however, the resonances around the SiV center PL maximum are shallow and not very well pronounced in the transmission spectra whereas for the hexagonal one the opposite is true. The very deep minima suggest high extraction efficiency of these modes due to the reciprocity between the in- and out-coupling of light. Therefore, in the following, we will mostly focus on discussing the properties of this particular sample with hexagonal symmetry and deposition time t = 24 min. For the other PhC structures the overlap occurs at higher angles of incidence where the extraction efficiency is lower than that for the modes being close to the Γ-point. It should be noted that due to well estimated growth conditions for the short deposition times, already the structure grown for 24 min had the desired photonic properties. Nevertheless, if this were not the case, our method enables us to fine-tune the leaky modes by changing the deposition time in small time-steps.

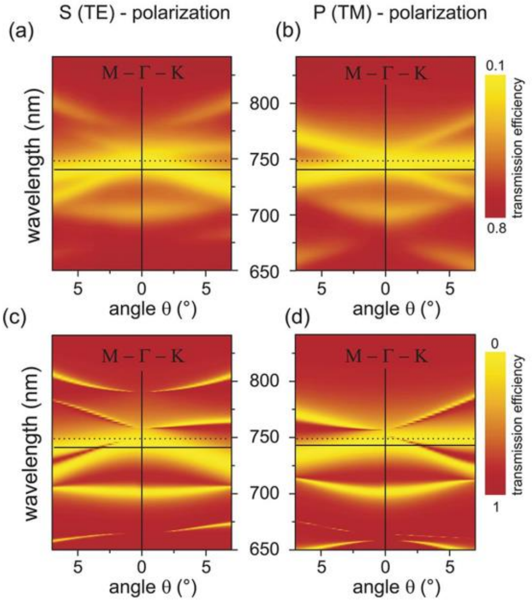

Figure 4. (a, b) Measured and (c, d) RCWA simulated photonic band diagrams of the (best-performing) hexagonal photonic crystal slab (shown in Figure 2h) for the S- and P-polarized light incident along the Γ−K and Γ−M direction of the reciprocal lattice. The solid horizontal line is positioned at the spectral maximum of the SiV centers PL. For the discussion on the dashed horizontal line see the text. The diagrams are shown only within the range of the relevant incident angles with respect to the collection angle. The diagrams are extracted from transmission curves measured/simulated as a function of the incident angle (zero being the normal incidence).

Next, a scanning confocal microscope was employed to qualitatively map the SiV centers PL in the fabricated PhC structures. Figure 3a shows a spectrally integrated (740 ± 13 nm) PL intensity map obtained by scanning the boundary of the hexagonal PhC structure grown for 24 min (Figure 2h) and the surrounding unpatterned layer. As evidenced by the AFM scan shown in Figure 3b, the PhC structure is located at the right side of the image and the unpatterned reference is at the left side. The scanning confocal image thus clearly demonstrates that the intensity of light extracted from the PhC is much higher than that extracted from the unpatterned reference diamond layer.

Then the performance of the samples with respect to the extraction efficiency was quantitatively evaluated by a micro-PL setup, which includes an objective with a collection half angle of 6.9° (NA = 0.12). The narrow collection angle of the objective was chosen in order to detect only the modes propagating in the vertical or almost vertical direction. Figure 3c shows the micro-PL spectrum of the hexagonal PhC (t = 24 min) in comparison with the micro-PL spectrum of the unpatterned diamond layer of a similar thickness h. In the plotted emission spectra, the SiV centers light emission is revealed as a relatively narrow peak centered at around 740 nm superimposed on a broad emission band. The broad emission band originates from various optically active defects introduced unintentionally during the diamond growth. The increase of the extracted SiV centers PL intensity is in the case of the PhC more than 14-fold as demonstrated by plotting the enhancement factor in Figure 3d. The enhancement factor was computed as a ratio of the micro PL spectrum of the PhC to the unpatterned part of the same sample. By comparison with micro-PL spectra of the other samples (see Supporting Information), we have confirmed our expectation that the hexagonal PhC grown for 24 min has the best-performance with respect to the extraction efficiency of the SiV centers PL. Considering the low NA of the objective, the extracted PL is confined within a relatively narrow angle simplifying practical usage of such device. It means that sophisticated optics to collect the extracted emission would not be necessary but a simple well aligned lens would be sufficient to collect the PL.

The measured effect of the PL extraction enhancement is mostly related to Bragg diffraction. The almost perfect intensity coincidence between the measured PL spectra from the PhC and the reference at wavelength regions 500−550, 610−650 and 850−900 nm (see Figure 3c), *i.e.*, outside the leaky modes, shows that the effects of increased number of SiV centers in the PhC compared to the reference sample (due to the diamond material deposited on the columns sides) or increased PL emitting surface are negligible. Next, the cavity-enhanced spontaneous emission *via* the Purcell effect[56] is absent in the studied sample as verified by the time-resolved PL measurements of the SiV centers within the PhC and outside (see Supporting Information, Figure S14). Neither the effect of inhibited spontaneous emission into waveguide modes[57,58] is relevant for our structure which cannot possess a photonic bandgap because of its laterally asymmetric nature and low refractive index contrast between the diamond layer and the silica substrate. Hence, the obtained enhancement factor does not need any corrections and directly shows the amount of light extraction *via* leaky modes.

The extraction angle depends on the polarization of the mode and the direction of its propagation within the PhC slab, defined by the k-vector. For example, by studying the measured transmission curves for the S-polarized light incident along the Γ−K direction on the best-performing hexagonal lattice PhC we have found that the in-coupling of light at the wavelength of the SiV center PL occurs for the incident angle of 2.5°. This transmission curve is plotted by a solid line in Figure 3d and it is clear that its deep minimum spectrally coincides with the enhancement factor maximum at ≈740 nm (being at the SiV peak maximum). This implies that for the case of the light extraction from the layer, which is a reciprocal situation to the coupling of light, part of the light emission from the SiV centers is coupled into this leaky mode and efficiently radiates into the surrounding under the angle of 2.5°. Nevertheless, also other modes propagating in different crystal directions that are within the spatial detection range of the objective (boundary of the collection angle of the objective at 6.9° is depicted by the vertical dotted lines in Figure 2) and spectrally overlap with the PL of the SiV centers contribute to the PL extraction enhancement.

Figure 4 shows the measured and simulated photonic band diagrams of the best-performing hexagonal PhC (t = 24 min) for our detection-scheme-relevant incident angles. Intentionally, the simulated band diagrams take into account real dimensions of the sample except optical losses in order to clearly resolve the photonic bands. Spectra simulated with the optical losses are plotted in Supporting Information (Figure S11). Due to the character of the photonic band diagram given by the symmetry of the hexagonal lattice, high density of modes (both TE and TM) exist around the Γ-point. Clearly, the SiV centers PL peak maximum, depicted by the solid horizontal line in Figure 4, is not tuned to overlap exactly the leaky mode at the Γ-point (dashed line) but it is positioned spectrally slightly below it. Thanks to this, it overlaps leaky modes of both polarizations (TE and TM), which makes the employed extraction scheme independent of the source polarization. It is interesting to discuss how the extraction would be affected if the PhC was tailored such that the SiV centers PL perfectly overlapped the almost horizontal very deep transmission minimum (TM mode) in the Γ−K direction (right part of the dotted horizontal line in Figure 4b,d). The answer can be extracted directly from the PL spectra shown in Figure 3c in which the effect of this mode on the PL spectrum is manifested as the long-wavelength shoulder of the SiV centers PL peak at around 750 nm. The extraction enhancement factor at this wavelength is approximately 7 (see Figure 3d), which is half of the extraction enhancement measured for the SiV centers PL peak. The reason for this lower enhancement is the higher Q-factor of the almost "horizontal" TM mode (in Figure 4) compared to some of the "inclined" modes, and the overall lower density of modes at this wavelength. It should be noted that at exactly the Γ-point (≈750 nm), this "horizontal" mode has a character of the TE-mode even though the mode is excited with the P(TM)-polarization. Clearly, this follows from the symmetry of the structure for the case of the normal incidence. The Γ-point TM-like mode is located at around 700 nm in this case.

In order to further support the interpretation of the extraction enhancement origin we will compare the extraction efficiency of the best-performing hexagonal PhC sample ($t = 24$ min) with another PhC structure. As a representative sample, we have chosen the PhC with square lattice symmetry grown for 54 min (Figure 2a), which has larger fill factor and thickness than the hexagonal PhC. Namely, its parameters are as follows: lattice constant = 360 nm, diameter of the columns ≈ 350 nm, height of the dome-shaped columns ≈ 180 nm, height of the diamond layer ≈ 285 nm. PL spectrum along with the enhancement factor of this sample are plotted in Figure 5. In this case, the SiV center PL peak of the unpatterned layer and the PhC crystal perfectly overlaps in intensity (Figure 5a) revealing that there is no effect of the PhC on this emission within the collection angle covered by the objective. This arises due to the fact the SiV center PL spectrally does not coincide with any leaky modes located close to the Γ-point, within the collection angle. Furthermore, as in the previous case of the hexagonal PhC, the perfect overlap in the PL intensity everywhere except at the positions of the leaky modes also evidences that there is no other mechanism, such as excitation laser in-coupling or slightly increased volume of the PhC with respect to the reference layer, contributing to the extraction enhancement than the out-coupling *via* leaky modes. On the other hand, other wavelengths of the emission from diamond defects are considerably enhanced. For example almost 7-fold enhancement was obtained for the PL emission at 790 nm (see the enhancement factor in Figure 5b) which spectrally coincides with the fundamental leaky modes around the Γ-point (see photonic band diagram in Figure 2a and Figure S10 in Supporting Information). These relatively narrow peaks in the PL spectrum are thus generated as an effect of the periodic pattern on the broad luminescence of diamond and should not be mistaken for some new strongly emitting optical centers.

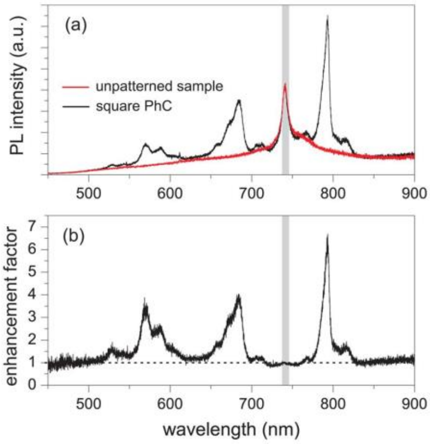

Figure 5. (a) Micro-PL spectrum of the PhC with square lattice symmetry grown for 54 min (shown in Figure 2a) compared to the spectrum of the unpatterned diamond layer. (b) Enhancement factor of the emission signal from the square lattice PhC shown in (a). The gray rectangle depicts the PL band of the SiV centers.

Finally, we would like to compare briefly the performance of the hexagonal and the square lattice PhCs considering the extraction efficiency *via* the leaky modes. For the SiV centers PL, the highest enhancement factor achieved with the square lattice symmetry was ≈8 and that was in the sample grown for 30 min (see Figure S13a in Supporting Information). This lower enhancement compared to the best-performing hexagonal PhC grown for 24 min might be both due to lower density of the leaky modes around the Γ-point and/or due to not perfectly spectrally tuned leaky modes with respect to the emission wavelength of the SiV centers (see photonic band diagram in Figure 2c and Figure S8 in Supporting Information). On the other hand, the density of the leaky modes can be, in the case of the square lattice, increased by decreasing the spectral separation of the fundamental TE and TM modes. This can be practically realized by increasing the thickness of the layer. The square PhC grown for 42 min can serve as an example of this effect (see photonic band diagram in Figure 2b and Figure S9 in Supporting Information). Nevertheless, even such optimized structure gives extraction enhancement factors not higher than 10 (Figure S13b in Supporting Information). The enhancement factor of 10 was obtained at other wavelength than that of the SiV center PL. However, as there is no other effect contributing to the extraction enhancement than the PL coupling to the leaky modes, it is reasonable to expect that the same results would be obtained if the leaky modes were spectrally coincident with the SiV centers PL. Another fact that supports this expectation is that for the PhC with hexagonal symmetry grown for 42 min, the enhancement factor of 14 (Figure S13b in Supporting Information) was measured at the wavelength of 805 nm, which is the similar enhancement as was obtained also for the SiV centers PL with the hexagonal PhC grown for 24 min. We can thus conclude that in our case, the hexagonal lattice PhCs possess within the studied (narrow) collection angle better performance with respect to light extraction than the square lattice PhCs due to (i) higher density of modes around the Γ-point and (ii) lower Q-factor of the leaky modes. Furthermore, the enhancement factor of 14 seems to be a maximal achievable value with this type of structures and material. It is slightly lower (14 *vs* 19) than that achieved for the SiV centers embedded in a single-crystal diamond PhC cavity[38] due to a different enhancement scheme employed (Purcell effect in ref 38 and leaky modes in our case) and due to optical losses present in the polycrystalline diamond. On the other hand, this is counterbalanced by cheaper and relatively easily up-scalable fabrication approach presented in this paper.

CONCLUSIONS

In summary, we have reported an experimental demonstration of 2D photonic crystal slabs with efficient extraction of the SiV centers luminescence. We have shown that the extraction of the SiV center luminescence can be more than 14 times increased compared to the uncorrugated diamond layer when the periodic structure on diamond layer is carefully designed and fabricated. It was evidenced by an experimental characterization of the sample and by the computer simulation that such enhancement was obtained thanks to the spectral overlap of the SiV centers emission with the leaky modes of the photonic crystal slabs. We have introduced a fabrication method that allowed for avoiding the structuring of the diamond itself by a direct growth on a patterned quartz substrates. It enables us to tune relatively easily yet effectively the spectral position of leaky modes by changing the deposition time while keeping the similar type of the quartz template. Furthermore, the etching of quartz, being relatively easy, can be cost-effectively up-scaled to larger areas using for example nanoimprint-lithography requiring only limited machine processing time.[59] Coupling of SiV centers to the leaky modes of the PhC based on polycrystalline diamond marks pivotal progress toward the usage of such structures in diamond-based photonics or as optical sensors. Although demonstrated with an ensemble of active centers in this work, coupling of spatially separated emitters or emitters located only close to the surface should be also possible using the techniques described here. Therefore, in addition to the fundamental interest in manipulating light emission from the SiV centers, these structures present potential applications for future optical components, for example as light sources with directional and efficient light extraction.

METHODS

Fabrication. Diamond growth was realized on a quartz substrate which was periodically patterned. The quartz glass (1×1 cm^2) was coated with an electron sensitive polymer (PMMA). Then, the electron beam was employed to nanopattern the PMMA into the form of the base matrix. Then, a Ti/Au (5/50 nm) masking matrix was evaporated. Finally, dry plasma etching in capacitively coupled RF-plasma in a SF_6 gas was performed yielding geometrically ordered quartz columns (diameter of ≈100 nm, height of ≈170 nm) with the square (lattice constant of 360 nm) or hexagonal lattice (lattice constant of 460 nm) symmetry. Altogether, 8 periodic patterns were fabricated: 4 with hexagonal symmetry and 4 with square lattice symmetry, each of them having 1×1 mm^2.

These structured substrates were ultrasonically seeded in a water-based suspension with detonation diamond powder. The diamond growth was performed by focused microwave plasma chemical vapor deposition using an ellipsoidal cavity resonator from a hydrogen and methane gas mixture. The growth of the continuous diamond layer followed the primary template created in the quartz. Parameters used for the diamond deposition: deposition time t = 24, 30, 42, 54 min; pressure p = 60 mbar, gas flow of hydrogen H_2 equal to 300 sccm, gas flow of methane CH_4 equal to 3 sccm, H_2 to CH_4 ratio equal to 100, power of microwave source P = 3000 W and approximate surface temperature of samples T = 750 °C. The main source of Si was a piece of crystalline Si wafer. Another source of Si atoms was a quartz substrate itself. Due to this the depth distribution of SiV centers can be slightly nonuniform; however, this has no negative effect on the performance of the PhC slab. The layout of each sample was such that always two periodic templates, each having 1×1 mm^2, one with square and the other one with hexagonal lattice symmetry were prepared on a single quartz substrate in order to have a comparable diamond thickness for both symmetries after the diamond growth with a single deposition time. The real thicknesses of the diamond layers were extracted from cross-sectional SEM images of the planar diamond samples (see Figure S1 in Supporting Information) grown side-by-side with PhC samples. The obtained values are in a very good agreement with the values measured on the uncorrugated part of the PhC samples by the reflection measurements.

Optical Methods. *Confocal Imaging.* We used the MicroTime200 (PicoQuant) confocal time-resolved microscope platform.[60] The sample was excited with a 2 μW average power in the diffraction limited confocal observation spot by 470 nm diode laser through 100× magnification air spaced objective (Olympus, NA = 0.8). The PL was collected in epifluorescence observation mode by the same objective, passed through a 75 μm diameter pinhole and detected by a Si-avalanche photodiode (PerkinElmer SPCM-AQR-14) through an optical filter transmitting 740 ± 13 nm (Semrock). Pixel resolution was 533 nm.

Angle-Resolved Transmission Spectra. A broadband tungsten lamp was employed as a light source. A collimated light beam of small divergence (angular spread lower than 0.3°) was obtained using a pinhole and a series of lenses. Polarizer was used to define light polarization. Transmitted light was detected using an optical fiber connected to a spectrometer with an intensified CCD camera (Andor) at the output. The sample was covered by a black paper with square aperture (that matched the size of one photonic crystal) and vertically mounted to a rotational stage. Subsequently, the sample was rotated around the axis perpendicular to one of the main symmetry directions of the PhC. For each angle (step of 27 arcminutes) the transmission spectrum was measured. The same process was repeated without the photonic structure (only with the aperture) afterward. The transmission spectrum for each angle was obtained as the ratio of intensity from these two measurements. The same measurement was done for both polarizations and for both main symmetry directions of the PhC.

Micro-PL Setup. The sample was excited by a HeCd cw laser (442 nm) and the spectrally resolved PL was detected with a silicon CCD camera. The photoluminescence was excited and measured in a direction perpendicular to the sample plane employing a Leica objective with NA = 0.12, which corresponds to a maximum collection angle ≈ 6.9° from a normal. The excitation spot diameter was ≈2 μm. Intensity of photoluminescence from places with and without photonic structures (both on the same sample) was measured and compared.

All the measurements were performed at room temperature.

Computer Simulation. RCWA technique based simulation tool DiffractMOD (RSoft) was employed for (i) designing the photonic structures and (ii) for simulating the results of optical experiments. When designing the structures, the computed parameters of the PhC structures were simulated using values of refractive index taken from the index database, supposing structures with perfect structural quality, and the pillars having perfectly cylindrical shape. We would like to point out different lattice constant of the hexagonal (460 nm) and square (360 nm) PhC. This is a result of the simulation, the goal of which was (i) to get the spectral overlap of the fundamental leaky modes with the emission line of the SiV centers and (ii) simultaneously to have the thickness of a diamond film not smaller than 80 nm in order to obtain a fully closed diamond layer of required quality.

In order to find a good match between the measured data and the simulation presented in Figure 1c and Figure 4, the following approach was employed. First, values for the diameter of the dome-shaped columns were extracted from SEM measurements. Second, dome-like shape of the columns was included. Third, the thickness of the layer was iterated in order to get the best agreement between the simulation and the experiment, *i.e.*, to get the spectral coincidence between the respective minima. The obtained thicknesses were within the error similar to those extracted from the cross-sectional SEM images and the reflection measurements. Finally, optical losses were added to the simulated structure in order to account also for the shape and intensity of the measured spectrum and to get also a quantitative agreement. For lossless material, all the resonances in the PhC transmission spectrum usually reach zero transmitivity,[53] which is confirmed by the simulation. However, losses make the minima shallower.[44] The optical losses are present due to reabsorption of light inside the layer and due to scattering on the structural imperfections. The simulation could be slightly further improved by taking into account the real refractive index of the layer; however, the value of the bulk diamond refractive index is sufficient for our purposes.

ASSOCIATED CONTENT

Supporting Information

The Supporting Information is available free of charge on the ACS Publications website at DOI: 10.1021/acsnano.6b08412.

> SEM images of the PhC sample at different stages of the fabrication process, cross-sectional images of the reference samples, representative AFM topography and height profiles of the diamond pillars; photonic band diagrams of the leaky modes measured with S- and P-polarized light on all the studied samples and leaky mode band diagrams of the hexagonal PhC (t = 24 min) simulated with optical losses are included; results of micro-PL measurements performed on all the PhC samples and enhancement factors for the relevant PhC structures; PL decay curves of the SiV centers embedded in the hexagonal PhC grown for 24 min and the reference are compared (PDF)

AUTHOR INFORMATION

Corresponding Author

*E-mail: ondic@fzu.cz.

ORCID

Lukáš Ondič: 0000-0002-9980-8573
Marian Varga: 0000-0002-9613-4614
Jan Fait: 0000-0003-3084-3220

Notes

The authors declare no competing financial interest.

ACKNOWLEDGMENTS

This work was supported by the grant GACR 16-09692Y and MSMT project No. LD15003. This article is also based upon work from COST Action MP1403 "Nanoscale Quantum Optics". P.K. was supported by the grant P208/12/G016 – GACR Project of Excellence. We would like to thank Prof. I. Pelant (IoP, ASCR), Dr. A. Kromka (IoP, ASCR) and Dr. B. Rezek (Faculty of Electrotechnical Engineering, Czech Technical University in Prague) for fruitful discussions.

REFERENCES

(1) Watanabe, H.; Hayashi, K.; Takeuchi, D.; Yamanaka, S.; Okushi, H.; Kajimura, K.; Sekiguchi, T. Strong Excitonic Recombination Radiation from Homoepitaxial Diamond Thin Films at Room Temperature. *Appl. Phys. Lett.* **1998**, *73*, 981−983.

(2) Zaitsev, A. M. *Optical Properties of Diamond: A Data Handbook*; Springer-Verlag: Berlin, 2001.

(3) Prawer, S.; Greentree, A. D. Applied Physics - Diamond for Quantum Computing. *Science* **2008**, *320*, 1601−1602.

(4) van der Sar, T.; Wang, Z. H.; Blok, M. S.; Bernien, H.; Taminiau, T. H.; Toyli, D. M.; Lidar, D. A.; Awschalom, D. D.; Hanson, R.; Dobrovitski, V. V. Decoherence-Protected Quantum Gates for a Hybrid Solid-State Spin Register. *Nature* **2012**, *484*, 82−86.

(5) Aharonovich, I.; Greentree, A. D.; Prawer, S. Diamond Photonics. *Nat. Photonics* **2011**, *5*, 397−405.

(6) Faklaris, O.; Joshi, V.; Irinopoulou, T.; Tauc, P.; Sennour, M.; Girard, H.; Gesset, C.; Arnault, J.-C.; Thorel, A.; Boudou, J.-P.; Curmi, P. A.; Treussart, F. Photoluminescent Diamond Nanoparticles for Cell Labeling: Study of the Uptake Mechanism in Mammalian Cells. *ACS Nano* **2009**, *3*, 3955−3962.

(7) Rojas, S.; Gispert, J. D.; Martín, R.; Abad, S.; Menchón, C.; Pareto, D.; Víctor, V. M.; Álvaro, M.; García, H.; Herance, J. R. Biodistribution of Amino-Functionalized Diamond Nanoparticles. *In Vivo* Studies Based on 18F Radionuclide Emission. *ACS Nano* **2011**, *5*, 5552−5559.

(8) Nebel, C. E.; Rezek, B.; Shin, D.; Uetsuka, H.; Yang, N. Diamond for Bio-Sensor Applications. *J. Phys. D: Appl. Phys.* **2007**, *40*, 6443−6466.

(9) Goss, J. P.; Jones, R.; Breuer, S. J.; Briddon, P. R.; Öberg, S. The Twelve-Line 1.682 eV Luminescence Center in Diamond and the Vacancy-Silicon Complex. *Phys. Rev. Lett.* **1996**, *77*, 3041−3044.

(10) Babinec, T. M.; Hausmann, B. J. M.; Khan, M.; Zhang, Y.; Maze, J. R.; Hemmer, P. R.; Lončar, M. A Diamond Nanowire Single-Photon Source. *Nat. Nanotechnol.* **2010**, *5*, 195−199.

(11) Hausmann, B. J. M.; Shields, B.; Quan, Q.; Maletinsky, P.; McCutcheon, M.; Choy, J. T.; Babinec, T. M.; Kubanek, A.; Yacoby, A.; Lukin, M. D.; Lončar, M. Integrated Diamond Networks for Quantum Nanophotonics. *Nano Lett.* **2012**, *12*, 1578−1582.

(12) Inam, F. A.; Grogan, M. D. W.; Rollings, M.; Gaebel, T.; Say, J. M.; Bradac, C.; Birks, T. A.; Wadsworth, W. J.; Castelletto, S.; Rabeau, J. R.; Steel, M. J. Emission and Nonradiative Decay ofNanodiamond NV Centers in a Low Refractive Index Environment. *ACS Nano* **2013**, *7*, 3833−3843.

(13) Feng, T.; Schwartz, B. D. Characteristics and Origin of the 1.681 eV Luminescence Center in Chemical-Vapor-Deposited Diamond Films. *J. Appl. Phys.* **1993**, *73*, 1415−1425.

(14) Aharonovich, I.; Neu, E. Diamond Nanophotonics. *Adv. Opt. Mater.* **2014**, *2*, 911−928.

(15) Wang, C.; Kurtsiefer, C.; Weinfurter, H.; Burchard, B. Single Photon Emission from SiV Centres in Diamond Produced by Ion Implantation. *J. Phys. B: At., Mol. Opt. Phys.* **2006**, *39*, 37.

(16) Neu, E.; Steinmetz, D.; Riedrich-Möller, J.; Gsell, S.; Fischer, M.; Schreck, M.; Becher, C. Single Photon Emission from Silicon-Vacancy Colour Centres in Chemical Vapour Deposition Nano-Diamonds on Iridium. *New J. Phys.* **2011**, *13*, 025012.

(17) Becker, J. N.; Gorlitz, J.; Arend, C.; Markham, M.; Becher, C. Ultrafast All-Optical Coherent Control of Single Silicon Vacancy Colour Centres in Diamond. *Nat. Commun.* **2016**, *7*, 13512.

(18) Liu, Y.; Siyushev, P.; Rong, Y.; Wu, B.; McGuinness, L. P.; Jelezko, F.; Tamura, S.; Tanii, T.; Teraji, T.; Onoda, S.; Ohshima, T.; Isoya, J.; Shinada, T.; Zeng, H.; Wu, E. Investigation of the Silicon Vacancy Color Center for Quantum Key Distribution. *Opt. Express* **2015**, *23*, 32961−32967.

(19) Potocký, S.; Holovský, J.; Remeš, Z.; Müller, M.; Kočka, J.; Kromka, A. Si-related Color Centers in Nanocrystalline Diamond Thin Films. *Phys. Status Solidi B* **2014**, *251*, 2603−2606.

(20) Potocký, S.; Ižák, T.; Varga, M.; Kromka, A. Influence of Gas Chemistry on Si-V Color Centers in Diamond Films. *Phys. Status Solidi B* **2015**, *252*, 2580−2584.

(21) Schell, A. W.; Kewes, G.; Hanke, T.; Leitenstorfer, A.; Bratschitsch, R.; Benson, O.; Aichele, T. Single Defect Centers in Diamond Nanocrystals as Quantum Probes for Plasmonic Nanostructures. *Opt. Express* **2011**, *19*, 7914−7920.

(22) Huck, A.; Kumar, S.; Shakoor, A.; Andersen, U. L. Controlled Coupling of a Single Nitrogen-Vacancy Center to a Silver Nanowire. *Phys. Rev. Lett.* **2011**, *106*, 096801.

(23) Schietinger, S.; Barth, M.; Aichele, T.; Benson, O. Plasmon-Enhanced Single Photon Emission from a Nanoassembled Metal-

Diamond Hybrid Structure at Room Temperature. *Nano Lett.* **2009**, *9*, 1694−1698.

(24) de Leon, N. P.; Shields, B. J.; Yu, C. L.; Englund, D. E.; Akimov, A. V.; Lukin, M. D.; Park, H. Tailoring Light-Matter Interaction with a Nanoscale Plasmon Resonator. *Phys. Rev. Lett.* **2012**, *108*, 226803.

(25) Kolesov, R.; Grotz, B.; Balasubramanian, G.; Stöhr, R. J.; Nicolet, A. A. L.; Hemmer, P. R.; Jelezko, F.; Wrachtrup, J. Wave-Particle Duality of Single Surface Plasmon Polaritons. *Nat. Phys.* **2009**, *5*, 470−474.

(26) Choy, J. T.; Hausmann, B. J. M.; Babinec, T. M.; Bulu, I.; Khan, M.; Maletinsky, P.; Yacoby, A.; Lončar, M. Enhanced Single-Photon Emission from a Diamond-Silver Aperture. *Nat. Photonics* **2011**, *5*, 738−743.

(27) Choy, J. T.; Bulu, I.; Hausmann, B. J. M.; Janitz, E.; Huang, I.-C.; Lončar, M. Spontaneous Emission and Collection Efficiency Enhancement of Single Emitters in Diamond *via* Plasmonic Cavities and Gratings. *Appl. Phys. Lett.* **2013**, *103*, 161101.

(28) Lee, J. C.; Magyar, A. P.; Bracher, D. O.; Aharonovich, I.; Hu, E. L. Fabrication of Thin Diamond Membranes for Photonic Applications. *Diamond Relat. Mater.* **2013**, *33*, 45−48.

(29) Faraon, A.; Barclay, P. E.; Santori, C.; Fu, K.-M. C.; Beausoleil, R. G. Resonant Enhancement of the Zero-Phonon Emission from a Colour Centre in a Diamond Cavity. *Nat. Photonics* **2011**, *5*, 301−305.

(30) Faraon, A.; Santori, C.; Huang, Z.; Acosta, V. M.; Beausoleil, R. G. Coupling of Nitrogen-Vacancy Centers to Photonic Crystal Cavities in Monocrystalline Diamond. *Phys. Rev. Lett.* **2012**, 033604.

(31) Fairchild, B. A.; Olivero, P.; Rubanov, S.; Greentree, A. D.; Waldermann, F.; Taylor, R. A.; Walmsley, I.; Smith, J. M.; Huntington, S.; Gibson, B. C.; Jamieson, D. N.; Prawer, S. Fabrication of Ultrathin Single-Crystal Diamond Membranes. *Adv. Mater.* **2008**, *20*, 4793−4798.

(32) Hiscocks, M. P.; Ganesan, K.; Gibson, B. C.; Huntington, S. T.; Ladouceur, F.; Prawer, S. Diamond Waveguides Fabricated by Reactive Ion Etching. *Opt. Express* **2008**, *16*, 19512−19519.

(33) Burek, M. J.; Chu, Y.; Liddy, M. S. Z.; Patel, P.; Rochman, J.; Meesala, S.; Hong, W.; Quan, Q.; Lukin, M. D.; Lončar, M. High Quality-Factor Optical Nanocavities in Bulk Single-Crystal Diamond. *Nat. Commun.* **2014**, *5*, 5718.

(34) Wang, C. F.; Hanson, R.; Awschalom, D. D.; Hu, E. L.; Feygelson, T.; Yang, J.; Butler, J. E. Fabrication and Characterization of Two-Dimensional Photonic Crystal Microcavities in Nanocrystalline Diamond. *Appl. Phys. Lett.* **2007**, *91*, 201112.

(35) Checoury, X.; Néel, D.; Boucaud, P.; Gesset, C.; Girard, H.; Saada, S.; Bergonzo, P. Nanocrystalline Diamond Photonics Platform with High Quality Factor Photonic Crystal Cavities. *Appl. Phys. Lett.* **2012**, *101*, 171115.

(36) Ondič, L.; Dohnalová, K.; Ledinský, M.; Kromka, A.; Babchenko, O.; Rezek, B. Effective Extraction of Photoluminescence from a Diamond Layer with a Photonic Crystal. *ACS Nano* **2011**, *5*, 346−350.

(37) Riedrich-Möller, J.; Kipfstuhl, L.; Hepp, C.; Neu, E.; Pauly, C.; Mücklich, F.; Baur, A.; Wandt, M.; Wolff, S.; Fischer, M.; Gsell, S.; Schreck, M.; Becher, C. One- and Two-Dimensional Photonic Crystal Microcavities in Single Crystal Diamond. *Nat. Nanotechnol.* **2012**, *7*, 69−74.

(38) Riedrich-Möller, J.; Arend, C.; Pauly, C.; Mücklich, F.; Fischer, M.; Gsell, S.; Schreck, M.; Becher, C. Deterministic Coupling of a Single Silicon-Vacancy Color Center to a Photonic Crystal Cavity in Diamond. *Nano Lett.* **2014**, *14*, 5281−5287.

(39) Felgen, N.; Naydenov, B.; Turner, S.; Jelezko, F.; Reithmaier, J. P.; Popov, C. Incorporation and Study of SiV Centers in Diamond Nanopillars. *Diamond Relat. Mater.* **2016**, *64*, 64−69.

(40) Singh, S.; Thomas, V.; Martyshkin, D.; Kozlovskaya, V.; Kharlampieva, E.; Catledge, S. A. Spatially Controlled Fabrication of a Bright Fluorescent Nanodiamond-Array with Enhanced Far-Red Si-V Luminescence. *Nanotechnology* **2014**, *25*, 045302.

(41) Joannopoulous, J. D.; Johnson, S. G.; Winn, J. N.; Meade, R. D. *Photonic Crystals: Molding the Flow of Light*; Princeton University Press: Princeton, 2008.

(42) Wierer, J. J.; David, A.; Megens, M. M. III-Nitride Photonic-Crystal Light-Emitting Diodes with High Extraction Efficiency. *Nat. Photonics* **2009**, *3*, 163−169.

(43) Ondič, L.; Kůsová, K.; Cibulka, O.; Pelant, I.; Dohnalová, K.; Rezek, B.; Kromka, A.; Babchenko, O.; Ganesh, N. Enhanced Photoluminescence Extraction Efficiency from a Diamond Photonic Crystal *via* Leaky Modes. *New J. Phys.* **2011**, *13*, 063005.

(44) Ondič, L.; Babchenko, O.; Varga, M.; Kromka, A.; Čtyroký, J.; Pelant, I. Diamond Photonic Crystal Slab: Leaky Modes and Modified Photoluminescence Emission of Surface-Deposited Quantum Dots. *Sci. Rep.* **2012**, *2*, 914.

(45) Martin, A. A.; Randolph, S.; Botman, A.; Toth, M.; Aharonovich, I. Maskless Milling of Diamond by a Focused Oxygen Ion Beam. *Sci. Rep.* **2015**, *5*, 8958.

(46) Bayn, I.; Bolker, A.; Cytermann, C.; Meyler, B.; Richter, V.; Salzman, J.; Kalish, R. Diamond Processing by Focused Ion Beam-Surface Damage and Recovery. *Appl. Phys. Lett.* **2011**, *99*, 183109.

(47) Lesik, M.; Spinicelli, P.; Pezzagna, S.; Happel, P.; Jacques, V.; Salord, O.; Rasser, B.; Delobbe, A.; Sudraud, P.; Tallaire, A.; Meijer, J.; Roch, J. F. Maskless and Targeted Creation of Arrays of Colour Centres in Diamond Using Focused Ion Beam Technology. *Phys. Status Solidi A* **2013**, *210*, 2055−2059.

(48) Leech, P. W.; Reeves, G. K.; Holland, A. Reactive Ion Etching of Diamond in CF_4, O_2, O_2 and Ar-based Mixtures. *J. Mater. Sci.* **2001**, *36*, 3453−3459.

(49) Ando, Y.; Nishibayashi, Y.; Kobashi, K.; Hirao, T.; Oura, K. Smooth and High-Rate Reactive Ion Etching of Diamond. *Diamond Relat. Mater.* **2002**, *11*, 824−827.

(50) Sakoda, K. Enhanced Light Amplification due to Group-Velocity Anomaly Peculiar to Two- and Three-Dimensional Photonic Crystals. *Opt. Express* **1999**, *4*, 167−176.

(51) Ondič, L.; Pelant, I. Efficient Light Amplification in Low Gain Materials due to a Photonic Band Edge Effect. *Opt. Express* **2012**, *20*, 7071−7080.

(52) Wiesmann, C.; Bergenek, K.; Schwarz, U. T. Photonic Crystal LEDs - Designing Light Extraction. *Laser Photonics Rev.* **2009**, *3*, 262−286.

(53) Fan, S.; Joannopoulos, J. D. Analysis of Guided Resonances in Photonic Crystal Slabs. *Phys. Rev. B: Condens. Matter Mater. Phys.* **2002**, *65*, 235112.

(54) Fan, S.; Villeneuve, P. R.; Joannopoulos, J. D.; Schubert, E. F. High Extraction Efficiency of Spontaneous Emission from Slabs of Photonic Crystals. *Phys. Rev. Lett.* **1997**, *78*, 3294−3297.

(55) Astratov, V. N.; Whittaker, D. M.; Culshaw, I. S.; Stevenson, R. M.; Skolnick, M. S.; Krauss, T. F.; De La Rue, R. M. Photonic Band-Structure Effects in the Reflectivity of Periodically Patterned Waveguides. *Phys. Rev. B: Condens. Matter Mater. Phys.* **1999**, *60*, R16255−R16258.

(56) Purcell, E. M. Spontaneous Emission Probabilities at Radio Frequencies. *Phys. Rev.* **1946**, *69*, 681.

(57) Fujita, M.; Takahashi, S.; Tanaka, Y.; Asano, T.; Noda, S. Simultaneous Inhibition and Redistribution of Spontaneous Light Emission in Photonic Crystals. *Science* **2005**, *308*, 1296−1298.

(58) Lodahl, P.; Van Driel, F. A.; Nikolaev, I. S.; Irman, A.; Overgaag, K.; Vanmaekelbergh, D.; Vos, W. L. Controlling the Dynamics of Spontaneous Emission from Quantum Dots by Photonic Crystals. *Nature* **2004**, *430*, 654−657.

(59) Becker, C.; Wyss, P.; Eisenhauer, D.; Probst, J.; Preidel, V.; Hammerschmidt, M.; Burger, S. 5*x*5 cm^2 Silicon Photonic Crystal Slabs on Glass and Plastic Foil Exhibiting Broadband Absorption and High-Intensity Near-Fields. *Sci. Rep.* **2014**, *4*, 5886.

(60) Koberling, F.; Wahl, M.; Patting, M.; Rahn, H.-J.; Kapusta, P.; Erdmann, R. Two-Channel Fluorescence Lifetime Microscope with Two Colour Laser Excitation, Single-Molecule Sensitivity, and Submicrometer Resolution. *Proc. SPIE* **2003**, *5143*, 181−192.

DE GRUYTER Nanophotonics 2019; aop

Research article

Jan Fait*, Marián Varga, Karel Hruška, Zdeněk Remeš, Vlastimil Jurka, Alexander Kromka, Bohuslav Rezek and Lukáš Ondič

Maximized vertical photoluminescence from optical material with losses employing resonant excitation and extraction of photonic crystal modes

https://doi.org/10.1515/nanoph-2019-0042
Received February 12, 2019; revised March 29, 2019; accepted April 16, 2019

Abstract: Optical losses of a host material together with the total internal reflection phenomenon can significantly reduce photoluminescence external quantum efficiency of embedded light-emitters. This is not only the case for light-emitting color centers in thin layers of nanocrystalline diamond, but also for silicon nanocrystals in silica dioxide matrices and for some types of perovskite materials. Here, we show that a significant boost (more than 100-fold enhancement) of the directional light emission efficiency from light-emitters in diamond can be achieved by using two-dimensional photonic crystal slabs (PhCs) to extract the light emission into vertical direction (resonant extraction) and at the same time to couple the excitation beam into the structure (resonant excitation). We have further shown that this so-called resonant extraction and excitation scheme provides the highest enhancement when the overlap between the electric field distribution of extraction leaky mode and the region of the excited light-emitters is maximized. This can be achieved by using the same type of the photonic mode for both extraction and excitation, and by optimizing the thickness of a diamond layer. The usage of the same type of modes appears to be more significant than tuning of the Q-factors of the excitation and extraction leaky modes individually. The results of our measurements are supported by the outputs of computer simulations. Our findings may be helpful in designing future PhCs for extraction of luminescence originating from various optoelectronic and sensor devices making use of the unique properties of the diamond. Moreover, our concept can be easily extended to other light-emitting materials with optical losses.

Keywords: photonic crystal slab; leaky modes; nanocrystalline diamond; photoluminescence centers; light extraction.

1 Introduction

Low optical quality of a material with otherwise perfect physical and chemical properties can significantly reduce its practical application in the field of photonics. One such material is the nanocrystalline diamond, which shares high mechanical and chemical stability [1], or the ability to host single-photon sources [2, 3] with the monocrystalline diamond. However, its optical quality is significantly worse due to the optical losses and light scattering on grain boundaries [4–6]. Another material in which optical quality hinders its usage as an efficient light source, for example, as an alternative to the materials used nowadays for organic light-emitting diodes, are halide perovskites [7, 8]. In addition to the optical losses, the relatively high refractive index causes that only a small portion of light within an escape cone is radiated out from the thin layers of these materials [9]. The major part of the emitted light is coupled to guided modes supported by the layer and then gradually absorbed [10]. The extraction is slightly enhanced due to the scattering on inhomogeneities [11, 12]. Nevertheless, the emission has a Lambertian radiation pattern, which requires the usage of sophisticated optical elements in order to achieve reasonable collection efficiency [13].

***Corresponding author: Jan Fait,** Institute of Physics CAS, Cukrovarnická 10, 16200 Prague, Czech Republic; and Faculty of Electrical Engineering, Czech Technical University in Prague, Technická 27, 16627 Prague, Czech Republic, e-mail: fait@fzu.cz. https://orcid.org/0000-0003-3084-3220
Marián Varga, Karel Hruška, Zdeněk Remeš, Vlastimil Jurka, Alexander Kromka and Lukáš Ondič: Institute of Physics CAS, Cukrovarnická 10, 16200 Prague, Czech Republic
Bohuslav Rezek: Institute of Physics CAS, Cukrovarnická 10, 16200 Prague, Czech Republic; and Faculty of Electrical Engineering, Czech Technical University in Prague, Technická 27, 16627 Prague, Czech Republic

Various photonic structures can be used for manipulating light emission from materials with absorption and scattering losses [14–18]. For instance, both the total internal reflection and the amount of absorbed light can be reduced by fabricating a suitable two-dimensional photonic crystal (PhC) on the top of a thin layer [19–23]. Luminescence of the embedded light-emitters couples to the leaky photonic modes of the PhCs which then radiate to air under defined directions via the Bragg diffraction phenomenon [24]. The extracted emission is thus strongly directional and the far-field radiation pattern can be tuned based on the required application by dimensions of the PhC [25].

This is particularly important for etendue limited applications [26] because then the extracted light can be easily collected by a simple optical system or sent directly onto a detector. Moreover, the amount of absorbed radiation is reduced due to relatively short optical path [27]. Recently, we have shown that by using 2D PhCs on a polycrystalline diamond, up to 14-fold extraction efficiency enhancement of the vertical light emission on a peak wavelength can be achieved [28]. The vertical extraction provides the highest emission intensity with respect to other extraction directions due to the degeneracy of the vertically out-coupled modes [29].

When optical excitation is used for generating emission, the PhC structure can be designed so that the excitation beam is coupled into the layer through an excitation leaky mode. This causes a significant increase of the excitation efficiency and by this also the enhancement of the photoluminescence (PL) intensity without the need to increase the excitation power. The concept which combines excitation and collection via leaky modes was first introduced in 2007 by Ganesh et al. [30, 31], and is called the resonant excitation and extraction, and it is successfully employed for the materials with negligible optical losses and surface deposited light-emitters. The authors argued, and their experiments proved that the main factor affecting the efficiency of this process, are the Q-factors of the excitation and extraction modes. Namely, the high Q-factor of the excitation mode enables the long-lasting localization of the pumping beam within the layer and, on the other hand, the low Q-factor of the extraction mode causes fast out-coupling of the emitted radiation to the desired direction.

In this contribution we demonstrate that the enhancement of the PL intensity into vertical direction from light-emitters distributed homogeneously inside a thin layer with low optical quality can be also significantly enhanced by accommodating the resonant excitation and extraction scheme, but in a specific regime. Namely, we propose and verify that employing one type of the leaky mode for both the excitation and the extraction in combination with maximized coupling of the emission to the extraction mode is pivotal when the emitters are distributed homogeneously inside the material. Further we show that the Q-factor analysis must also include absorption and scattering of light in the material with low optical quality. On the example of a nanocrystalline diamond layer with a PhC on its surface, we demonstrate up to 115-fold PL intensity enhancement at the wavelength of the extraction leaky mode using this approach. The nanocrystalline diamond was chosen because it comprises optical losses due to absorption and scattering [4], and in the same time it possesses spectrally broad visible PL [32]. The latter enabled us to elaborate this scheme for both the fundamental TE and TM modes on the similar sample. Finally, we demonstrate that our experimental results agree with the outputs of the simulations.

2 Sample design

The PhCs were designed with a goal to achieve resonant excitation with blue (or green) laser and, at the same time, efficient resonant extraction of the wavelengths within a red spectral region. The resonant excitation and resonant extraction scheme includes the following steps (Figure 1A): (1) in-coupling of blue excitation beam into the leaky mode of the photonic structure, (2) absorption of the in-coupled light by the material, (3) emission of red PL from the excited emitters and its subsequent coupling into the extraction leaky mode, and (4) out-coupling of the light via the extraction leaky mode into the vertical direction. Some other effects such as direct absorption of laser beam or direct emission from the material into space also contribute to the observed PL intensity in a vertical direction. However, their contribution is marginal, and we concentrate solely on the resonant excitation and extraction scheme.

The steps (1), (2), and (4) depend on the dimensions of the PhC and their efficiency can be described by the Q-factors of the excitation and extraction leaky modes. The total Q-factor of the mode is composed of three contributions, which quantify the losses caused by individual mechanisms:

$$\frac{1}{Q}=\frac{\omega_0}{\Delta\omega}=\frac{1}{Q_{\mathrm{dif}}}+\frac{1}{Q_{\mathrm{abs}}}+\frac{1}{Q_{\mathrm{scat}}}, \qquad (1)$$

where ω_0 is the central frequency of the leaky mode and $\Delta\omega$ is the leaky mode full width at half maximum and Q_{dif}, Q_{abs}, and Q_{scat} characterizes the losses caused by Bragg

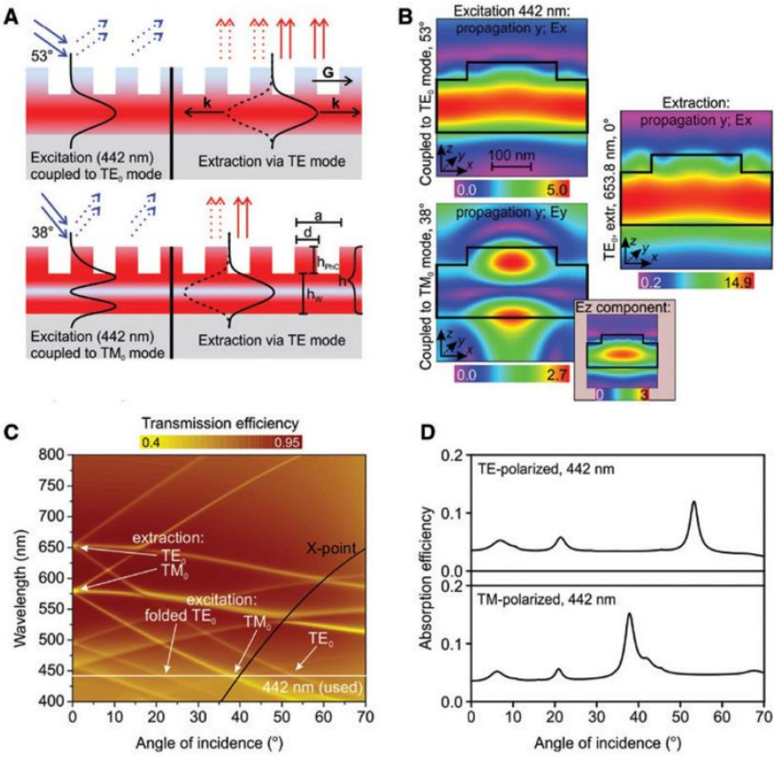

Figure 1: Principle of light extraction via leaky modes and the properties of leaky modes.
(A) Schematic sketch of the resonant excitation (left part of the image) and extraction (right part) of photoluminescence (PL) via Bragg diffraction of leaky modes. Excitation laser (blue solid arrows) is coupled into the leaky mode of the photonic crystal (PhC) (black solid curve). While propagating in the material, it is partially absorbed (red region) and partially diffracted out (blue dashed arrows). The excited emitters (located in red region) then emit light that partially couples to the extraction leaky mode (black solid and dashed curves) and is diffracted out from the material (red arrows). Spatial overlap of the excited region (defined by the excitation leaky mode) with the extraction leaky mode is crucial for maximizing PL enhancement using the resonant excitation/extraction scheme. (B) Simulated electric field intensity for the PhC-A sample (see Figure 2) for TE$_0$ and TM$_0$ excitation mode (left) and TE$_0$ extraction mode (right). Note that the TM$_0$ mode has two nonzero components of E-field with different distributions. The black line shows the boarders of PhC unit cell. The intensity of the field is normalized to the unit amplitude of the incident wave. See Figure S5 in Suppl. info for simulations of field components of all modes relevant for the discussion throughout the paper. (C) Simulated photonic band diagram of PhC-A sample for angles of incidence between 0° and 70°. The graph shows the transmission efficiency of unpolarized light for given wavelength and angle of incidence. (D) Simulated absorption efficiency of PhC-A as a function of the angle of incidence (between 0° and 70°). Increased absorption at 442 nm matches the position of leaky modes in (C). The effects of scattering and fabrication defects are not included.

diffraction, absorption, and scattering (both on material inhomogeneities and on defects caused by fabrication) of light, respectively. The out-coupling efficiency of a leaky mode from the PhC slab is maximized when the Q_{dif} is minimized, and simultaneously Q_{abs} and Q_{scat} are maximized. Subsequently, most of the light is diffracted into defined direction instead of being absorbed or randomly scattered. On the other hand, the excitation efficiency is maximized when Q_{abs} is minimized, and Q_{dif} and Q_{scat} are maximized. The low Q_{abs} implies high absorption and high Q_{dif} and Q_{scat} extend the optical path of the mode in the material. The absorption and scattering losses are given by characteristics of the material, which we do not try to tune (although it is possible by changing the deposition conditions). Nevertheless, all, Q_{dif}, Q_{abs}, and Q_{scat}, can be changed by the physical dimensions of the PhC. Note that it follows from the above-discussion, that the Q_{dif} and Q_{abs} requirements on the extraction and excitation leaky modes are exactly opposite.

The efficiency of step (3) depends on the single-mode local density of optical states (SM-LDOS) that quantifies the power that is coupled to the specific mode from the dipole source. Note that the total LDOS is higher than SM-LDOS because it includes also light that couples to other modes and the light that is directly radiated to space. The spatial profile of the SM-LDOS is proportional to the electric field distribution of the respective mode. The efficiency of step (3) is thus proportional to the spatial integral overlap between the electric field distribution of the extraction mode (black curve in the right part of Figure 1A) and the region of excited light-emitters (red-colored region in Figure 1A), in accordance with Fermi's golden rule [33]. The distribution of excited light-emitters follows the intensity profile of the excitation leaky mode, when resonant excitation is used. Figure 1A outlines this situation for two cases of the excitation mode: fundamental TE (TE_0) and fundamental TM (TM_0). Clearly, the highest spatial overlap between the excited region and the electric field distribution of extraction mode is achieved when both excitation and extraction is done via the leaky modes with similar intensity distributions (Figure 1A top), i.e. modes of the same type (TE or TM) and order. When two different modes are used (e.g. TM_0 for excitation and TE_0 for extraction Figure 1A bottom) the spatial overlap is reduced. The simulated electric field distribution for the modes is shown in Figures 1B and S5 in the Suppl. info. We chose the TE_0 mode for extraction and excitation as it has the highest overlap of the electric field distribution with the layer, and thus provides the highest SM-LDOS, when the light-emitters are distributed homogeneously in the layer, as we confirmed also experimentally. On the other hand, TM_0 mode is advantageous when the emitters are located near the surface because its electric field distribution is localized near edges of the structure (Figure 1B).

Overall, for maximizing the efficiency of the whole excitation/extraction process, we require high Q_{dif} for excitation leaky mode, low Q_{dif} for extraction leaky mode, and the usage of the same type and order of the excitation and extraction leaky mode. However, it is not possible to fulfill all the three requirements in the same time as the Q-factors on one photonic mode branch cannot be tuned separately. As we will show, the excitation/extraction scheme realized via the similar mode is for the case of materials with low optical quality, and emitters inside the material more important than choosing different types of modes with ideal Q-factors.

The other factor that influences the efficiency of the step (3) is the thickness of the diamond layer. Optimal layer thickness, for which the SM-LDOS in PhC is maximized, exist for each mode [34]. Both LDOS and SM-LDOS can be estimated by performing 3D finite-difference time-domain (FDTD [35]) simulations. For the case of waveguide that supports only fundamental modes, the FDTD simulation directly shows the amount of light coupled to the respective photonic mode, which is proportional to the SM-LDOS of that mode [36]. We performed simulations for the dipole source placed in the middle, in the top and bottom quarter, and on the top and bottom edge of the planar diamond waveguide (Suppl. info section: 2. coupling efficiency to modes). The simulation confirms that the coupling efficiency depends on the electric field distribution of the modes. For instance, the highest portion of light is coupled to the TE_0 mode for the dipole source positioned in the middle of the waveguide, because the TE_0 mode has maximal electric field there. Moreover, we used a wide-frequency source, which allows to detect the optimal thickness-to-wavelength ratio for obtaining optimal coupling of emitted light to the guided mode (the ratio for which the SM-LDOS of the extraction mode is maximized).

The optimal thickness of diamond layers ($n_D = 2.32$, see Figure S7 in Suppl. info) on SiO_2 substrate ($n_{SiO_2} = 1.45$) for red light (around 650 nm) coupling to the TE_0 mode lies in the range of 78 and 124 nm as follows from the FDTD simulation (see Figures S2–S4 in Suppl. info). For light source located in the middle of the layer with optimal thickness, the TE_0 mode carries more than 77% of the total power, which would be emitted by the same source into homogeneous medium. The basic idea of excitation and extraction via the same type of leaky mode is valid also for structures, which support higher order modes at the extraction wavelength. Nevertheless, the PL can couple to all supported modes and the efficiency of coupling into the specific extraction leaky mode is reduced.

Upon acquiring the optimal thickness (h_w) for the main waveguiding layer, we computed dimensions (lattice constant a, column diameter d, and column height h_{PhC}, see the schematic image in Figure 1A) of square-lattice PhCs to be fabricated on the top of it. We designed and fabricated two PhC structures (Figure 2) to support vertical extraction of the PL in red spectral region via TE_0 leaky mode. The first structure (PhC-A) had waveguiding layer (h_w, see Figure 1A) within the range of the optimal thickness. The second structure (PhC-B) was designed to have low Q_{dif} on extraction wavelength, which denotes more effective out-coupling of the extraction leaky mode into the vertical direction. The total thickness ($h = h_w + h_{PhC}$) was 160 nm for both samples. The main idea was to show that the effect of efficient coupling to extraction mode (pronounced in PhC-A) leads to better overall enhancement than high efficiency in out-coupling of the extraction leaky mode alone (PhC-B; Figure S13 in Suppl. info shows the TE_0 mode profile of this sample). The square symmetry was chosen because it has less complicated photonic band structure than the hexagonal one and the effect of resonant excitation/extraction can be thus more easily demonstrated.

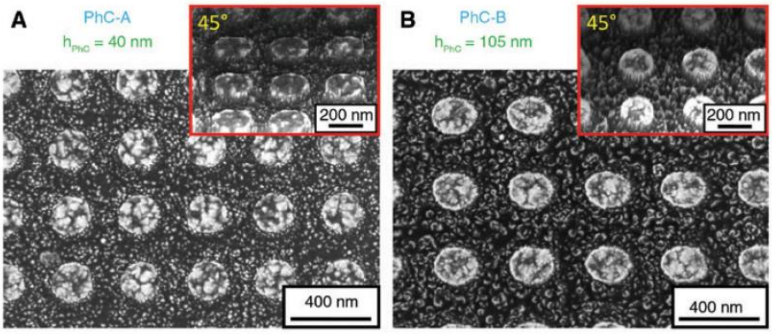

Figure 2: Scanning electron microscopy micrographs of the diamond-based 2D PhCs.
(A) PhC-A: lattice constant $a = 345$ nm, column diameter $d = 205$ nm, thickness of diamond layer before etching $h = 160$ nm, and thickness of diamond layer after etching $h_w = 120$ nm. (B) PhC-B: lattice constant $a = 390$ nm, column diameter $d = 215$ nm, thickness of diamond layer before etching $h = 160$ nm, and thickness of diamond layer after etching $h_w = 55$ nm. The insets show the morphology of respective samples under 45° angle.

3 Results

3.1 PL enhancement

The sample was excited with the TE (s) or TM (p) polarized cw laser beam (442 nm) incident along the Γ-X [37] direction of high symmetry. The excitation angle of incidence was varied from 7.5° to 67.5° and the PL signal was collected with an optical fiber being perpendicular with respect to the sample surface in order to collect only the normally extracted leaky modes within a small collection cone. An example of such a PL spectrum for the nonresonant excitation of the PhC-A is shown in Figure 3A. The extraction leaky modes are manifested as sharp resonances at particular wavelengths. Their spectral positions are in agreement with the computed ones (Figure 1C).

Figure 3B plots the measured PL intensity at the wavelength of the TE_0 extraction mode as a function of the excitation angle for the TE excitation of the PhC-A. The two PL signal maxima, one at around 22.5° and the other at 54.3°, occur at the similar angles as the leaky modes in the simulated curve of the transmission efficiency of the excitation laser, which implies that the enhancement of the signal is due to resonant in-coupling of the excitation laser into the structure. Similarly, the TM polarized excitation beam is coupled to TM_0 mode when incident at 42.9° (Figure 3C). Here the correspondence with the computed transmission spectrum is not perfect, which is caused by the inaccuracy of numerical simulation for TM_0 mode as explained in Suppl. info (Figure S12).

As a next step, the performance of the PhCs with respect to the light emission enhancement was evaluated via an enhancement factor, which we define as a ratio of the PL intensity measured on the PhC (I_{PhC}) to the PL intensity measured on the unpatterned diamond layer (I_{ref}) with thickness h. Figure 3D and E shows the dependence of the enhancement factor on the emission wavelength for the resonant excitation via TE_0 and TM_0, respectively, in comparison to the nonresonant excitation for the PhC-A. The total enhancement factor (EF_{tot}) can be written as

$$EF_{tot}(\lambda) = \frac{I_{PhC}(\lambda)}{I_{ref}(\lambda)} = EF_{leaky}(\lambda) + EF_{Lamb} - 1 \tag{2}$$

where the EF_{leaky} is the contribution of leaky modes to the PL and the EF_{Lamb} is the spectrally independent enhancement of the Lambertian radiation (further denoted as a Lambertian enhancement factor) being simply the enhancement of the radiation not coupled to guided or leaky modes. The correction –1 must be added so that the total enhancement remains 1 if both the EF_{Lamb} and EF_{leaky} are equal to 1 (i.e. the PL is not enhanced). Numerical values of the PL enhancement factors at the peak wavelengths of the extraction modes are summarized in Table 1. For the PhC-A, various combinations of the extraction and excitation leaky modes were evaluated, whereas for the PhC-B, only the combination relevant for the discussion is listed.

As Table 1 shows for the PhC-A, the listed values of the Lambertian enhancement factor depend on the polarization of the excitation beam mainly because they reflect the enhancement with the resonant excitation. The radiation resonantly coupled to the TE_0 excitation leaky mode has higher spatial overlap with the emitters than the TM_0 mode and thus it provides higher excitation efficiency and subsequently the increase of the overall PL. The EF_{Lamb} values then naturally remain approximately constant

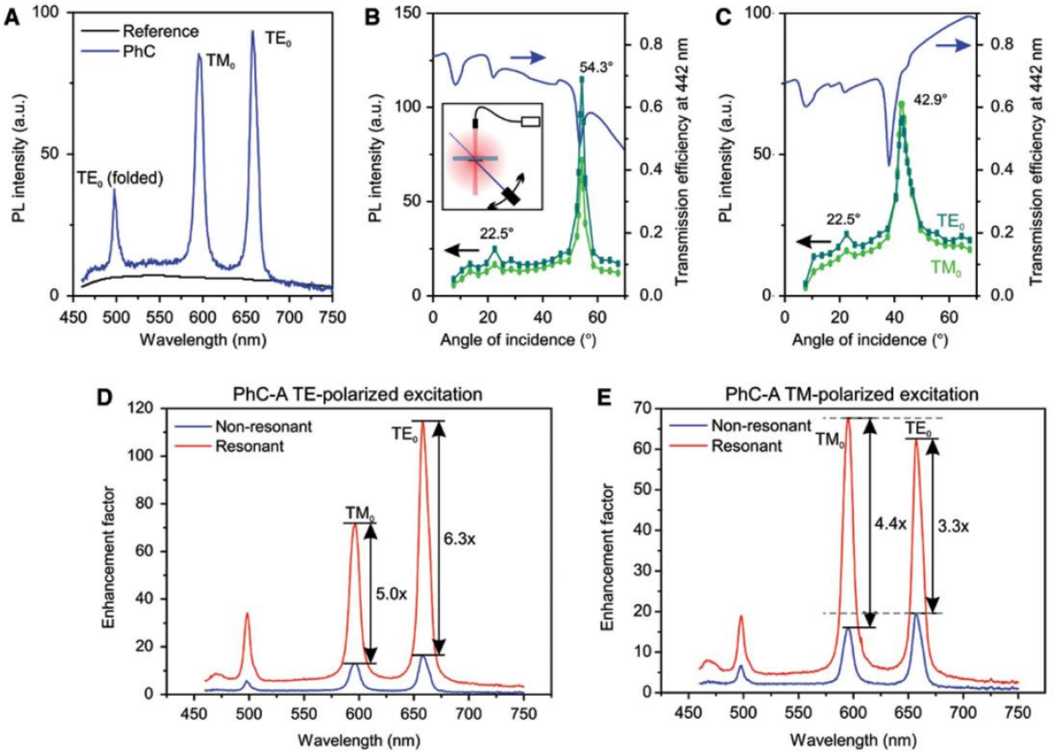

Figure 3: PL spectra and enhancement factor under non-resonant and resonant excitation.
(A) The comparison of PL intensity measured on plain diamond layer (black) and on PhC-A (blue, nonresonant excitation). (B, C) The normalized PL intensity measured on PhC-A sample at the wavelength of the TE$_0$ (658 nm) and TM$_0$ (596 nm) extraction leaky mode as a function of the angle of incidence of the excitation beam (the connecting lines are guides to the eye), and rigorous coupled-wave analysis (RCWA) simulated transmission efficiency of the excitation beam (442 nm-blue line): (B) TE-polarized excitation beam; inset shows the measurement setup (see Suppl. info for details), (C) TM-polarized excitation beam. (D, E) The enhancement factor of PhC-A sample when excited with (D) TE-polarized and (E) TM-polarized excitation beam.

Table 1: Enhancement factors for the photonic crystal (PhC)-A and PhC-B samples (for detailed explanation see the main text).

	PhC-A				PhC-B
Extraction mode	TE$_0$	TM$_0$	TE$_0$	TM$_0$	TE$_0$
Excitation mode	TE$_0$	TE$_0$	TM$_0$	TM$_0$	TE$_0$
Total enhancement factor	114.7	71.9	62.9	67.6	67.7
Lambertian enh.[a]	6.1	6.1	4.8	4.8	7.6
Leaky mode enh.	109.6	66.8	58.8	63.8	61.1
Extraction enh.	17.4	13.4	17.7	14.4	21.5
Excitation enh.	6.3	5.0	3.3	4.4	2.8

Various combinations of excitation/extraction modes were measured for PhC-A. Note that the excitation enhancement factor includes both, the in-coupling (Q-factor related) and field overlap (between excitation/extraction leaky modes) effects. [a]Lambertian enhancement factor under resonant excitation.

over the whole PL spectrum (we have observed only small variations due to the Fabry-Pérot resonances). The Lambertian enhancement factor is much smaller for nonresonant excitation, where it may be caused by several factors: (1) diffraction of light on the PhC into the first real diffraction order, which changes the electric field distribution of excitation beam inside the sample, (2) different volume and surface of the PhC with respect to the reference layer, and (3) Fabry-Pérot resonances. Overall, the Lambertian enhancement factor presents only about 5% of the total PL enhancement (Table 1). The remaining 95% of the PL enhancement is due to leaky modes enhancement.

The leaky modes enhancement factor (at the wavelength of the leaky mode λ_0) can be divided into (1) pure extraction enhancement factor (EF_{Extr}) measured under nonresonant excitation angle and (2) resonant excitation enhancement factor (EF_{Excit}):

$$EF_{leaky}(\lambda_0) = EF_{Extr} \cdot EF_{Excit} \tag{3}$$

The highest, 110-fold leaky mode enhancement was obtained for the TE_0 resonant excitation and the TE_0 extraction leaky mode of the PhC-A (Figure 3D), which is six times more than for the nonresonant excitation (Table 1). For the TM_0 leaky extraction mode, the enhancement is around 67× when excited with TE_0 mode. On the other hand, for the TM_0 resonant excitation (Figure 3E), the PL enhancement at the TE_0 extraction mode is only around 59× whereas it is higher for the TM_0 extraction (64×). Clearly, the overlap of the excitation and the extraction modes (both TM_0) outweighs the fact that the structure is optimized for the extraction via the TE_0 mode. However, in overall the enhancement factor is much smaller than that obtained at this sample with TE_0 resonant excitation and extraction (Table 1), because the spatial overlap of the TM_0 mode with diamond and hence with the light-emitters is smaller than for the TE_0 mode (Figure 1B). These experimental results confirm our hypothesis that the PL emission can be significantly enhanced when coupling and out-coupling is realized via the photonic modes of the same type and order.

Furthermore, the extraction enhancement factors for a single type of the extraction mode are (within the error of the measurements) similar for both polarizations of the excitation beam, for example 17.4× and 17.7× (Table 1) for the TE_0 extraction mode. This is due to the fact that the diamond light-emitters do not possess any preferential orientation in the layer and thus respond similarly to both polarizations of the excitation beam.

For the case of PhC-B, the total enhancement factor is around 61, which is approximately three times more than for the nonresonant excitation (Table 1). The effect of resonant excitation is significantly lower when compared to PhC-A sample because the thickness of the waveguiding layer (h_w) is not optimized for resonant excitation and extraction scheme. On the other hand, as designed, the sample has higher extraction enhancement factor than PhC-A due to higher spatial overlap of the TE_0 with the PhC structure.

3.2 Q-factor analysis

The excitation and extraction enhancement can be contrasted with the Q-factor analysis. The Q-factors in Table 2 were extracted from measured and simulated band diagrams (Figure 4) and their computation is described in Suppl. info (Section 4, Experimental). The main cause of losses for TE_0 leaky mode is absorption (low Q_{abs}) because this mode is localized in the material and has thus high overlap with the lossy material. On the other hand, the losses of TM_0 mode are caused primarily by Bragg diffraction (low Q_{dif}) and scattering on surface defects (low Q_{scat}) as this mode is localized on the edge of the structure, where the PhC and fabrication defects are located.

Table 2: The total Q-factor (Q) of leaky modes, which we determined from transmission measurement, is divided according to the type of losses: diffraction losses Q_{dif}, absorption losses Q_{abs}, and scattering losses Q_{scat}.

Leaky mode	**PhC-A**				**PhC-B**	
	TE_0		**TM_0**		**TE_0**	
Wavelength (nm)	658	442	596	442	631	442
Q	82		61		36	
Q_{dif}	344	340	187	114	67	29
Q_{abs}	142	116	207	130	242	315
Q_{scat}	445		161		115	

The relationship between Q-factors is given by (1).

For the efficient out-coupling of the leaky modes high Q_{abs} and Q_{scat}, and low Q_{dif} is desirable. This assures that the PL coupled to the leaky mode is diffracted into the desired (normal) direction instead of being absorbed or scattered into random direction on material inhomogeneities and structural defects. When the Q-factors of TE_0 and TM_0 leaky modes of PhC-A are compared (Table 2), the TM_0 mode should work better for out-coupling. However, the highest extraction (i.e. under nonresonant excitation) enhancement factor around 17.5× was obtained with the TE_0 extraction mode (Table 1). The reason is that the Q-factor describes only the out-coupling of leaky modes from the structure and not the initial coupling of the PL to leaky modes, which was optimized for the TE_0 mode via the optimal thickness. Here the higher SM-LDOS of TE_0 mode plays more significant role than the better out-coupling of the TM_0 leaky mode from the structure. This clearly manifests the importance of both the spatial overlap between the extraction mode profile with the distribution of the excited light-emitters and the optimized thickness of the layer for coupling to this TE_0 mode.

In the case of excitation efficiency, the high Q_{dif} and Q_{scat}, and low Q_{abs} are desirable. In such a case the excitation beam stays long in the PhC and is simultaneously efficiently absorbed. Based on the Q-factors (Table 2) the TE_0 mode works best for the excitation efficiency, which is in accordance with the measured excitation enhancement factor (Table 1). Nevertheless, in the value of the excitation enhancement factor, also the overlap between

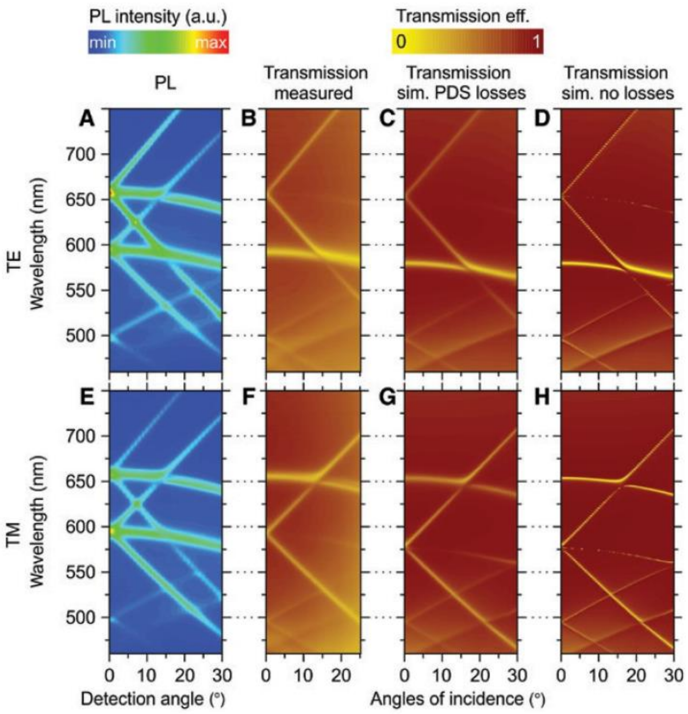

Figure 4: Measured PL spectra (PhC-A) as a function of the extraction angle, and transmission band diagrams.
(A) Angle-resolved PL spectra excited by TE-polarized laser beam incident at the resonant angle of 54.3° and (E) excited by the TM-polarized laser beam incident at the resonant angle of 42.9°. Measured (B), RCWA simulated with losses (C), and simulated without losses (D) transmission efficiency as a function of the angle of incidence (along the Γ-X direction of high symmetry) for the TE-polarized light.
(F–H) Same for the TM-polarized light.

the excitation and extraction mode plays an important role, which is evidenced by dependence of the excitation enhancement (Table 1) on the extraction leaky mode. Note, that although the thickness of the layer is optimized to achieve highest SM-LDOS for TE_0 mode at wavelengths around 650 nm, the excitation TE_0 leaky mode is even more localized in the layer because of shorter wavelength. The reduced SM-LDOS is not important for the absorption efficiency.

The in-coupling of excitation beam into structure is affected not only by the diffraction Q-factor but also by the monochromacy and directivity of light. The high Q_{dif} is advantageous only for monochromatic and highly directional light in this respect. The total excitation enhancement (absorbed energy) can be partially simulated by rigorous coupled-wave analysis (RCWA) simulations (see Figure 1D). Nevertheless, it does not count with the scattering of light and fabrication imperfections, which decrease the overall performance.

For the case of PhC-B the diamond layer is thinner (h_w) than for the PhC-A, whereas the PhC columns are higher (h_{PhC}). The TE_0 mode is thus more spread outside diamond layer, which decreases its single-mode local density of optical states in the diamond and increases its interaction with PhC structure that causes faster diffraction. The effect on Q-factors is that Q_{dif} is low and Q_{abs} high. As a result, the PhC-B should work better for extraction and worse for excitation when compared to the PhC-A sample, which we observed (Table 1).

4 Discussion and conclusion

The importance of spatial overlap of the extraction and excitation leaky mode may be manifested by considering the competition in PL extraction between the supported modes. The 78–124 nm thick diamond layer supports both TE_0 and TM_0 modes at all wavelengths. Each mode is diffracted into vertical direction at different extraction wavelength. The other mode also exists for these wavelengths, but it is extracted into different direction, e.g., the steep TM_0 band crossing the TE_0 extraction wavelength at around 17° (Figure 4A). Nevertheless, Figure 4A clearly shows that the steep TM_0 extraction band is weaker for resonant excitation with TE_0 mode when compared to the resonant excitation with TM_0 mode (Figure 4E). Similarly, the steep TE_0 extraction band is weaker in Figure 4E.

A significant portion of PL intensity coupled to TE_0 (or TM_0) mode is lost due to diffraction into nonvertical angles (flat bands in Figure 4A,E). The light diffracted into these directions can be collected by placing the optical fiber closer to the sample or by using objectives with higher numerical aperture. Nevertheless, it leads to the loss of spectral selectivity of leaky modes, because other wavelengths are also diffracted into these directions. Note that the spectral selectivity is especially important for sensing applications.

Figure 4 also compares the simulated and measured transmission efficiency. The most prominent difference between the simulated and measured transmission efficiency lies in the shift of the TM_0 mode spectral position. The difference originates from localization of electric field of this mode near the diamond surface as described in Suppl. info (Section 6, TM-polarized excitation).

The PhC structures under the study were designed to obtain high vertical PL enhancement in the red part of the visible spectrum. This is spectrally near to zero phonon spectral lines of negatively charged nitrogen vacancy (637 nm) or silicon vacancy (738 nm) color centers [2, 38, 39], which are potential single photon sources [3] and sensing components [40, 41]. Even though there were no (or very few) color centers in the present samples, they can be introduced into the diamond using ion implantation technique or directly during fabrication of new samples [42, 43]. The spectral position of the leaky modes may be shifted to the emission peak of the color center by adjusting the lattice constant [24]. However, due to the fabrication imperfections, tuning of the PhC structures to an exact a priori selected wavelength is not possible. Nevertheless, fine tuning of the extraction resonance spectral position can be done by postprocessing: overgrowth of the PhC structures with thin diamond layer to increase layer height or sample etching to reduce the layer height. The former was used for fabrication and spectral tuning of leaky resonances by bottom-up approach [28]. Also note that the spectral shift of resonances is not detrimental for excitation in-coupling as it only requires slight adjustment of the excitation beam angle of incidence. Furthermore, Figure 1C shows that the same TE_0 excitation mode can be excited also by other wavelengths if the resonant angle is shifted appropriately. Moreover, other resonant angles exist also for the excitation in the other direction of high symmetry, the Γ-M direction. Finally, the TM_0 leaky mode has high field intensity located on the PhC surface (Figure 1B). Combination of near-surface color centers sensitive to the changes of surroundings with a photonic crystal tuned at the TM_0 resonance is, therefore, promising for increased optical sensor sensitivity.

To conclude, we have shown that the resonant excitation/extraction scheme can be used to achieve 115-fold enhancement of PL intensity originating from light-emitters in nanocrystalline diamond-based photonic crystals. Even though that the nanocrystalline diamond possesses relatively high optical losses, the achieved enhancement is comparable to that obtained for a material with negligible losses [30]. In order to reach such enhancement, we have shown that both the spatial overlap between the excitation and the extraction leaky mode, and the spatial overlap between the light-emitters and the extraction leaky mode must be maximized. This condition is fulfilled for the TE_0 leaky mode used both for the excitation in-coupling and for the extraction of PL in the case of nanocrystalline diamond PhCs. The usage of the same mode for both excitation and extraction is more important than tuning of the Q-factors of excitation and extraction leaky modes individually. Moreover, the Q-factor must be separated into the effect of Bragg diffraction, absorption, and scattering in order to reasonably explain the excitation/extraction efficiency of the leaky modes. Our results, even though obtained on a specific material, can be extended towards any dielectric material with optical losses.

Acknowledgments: This work was supported by the Czech Science Foundation (GAČR) (16-09692Y); Czech Technical University (CTU) (SGS18/179/OHK4/3T/13); and projects of Operational Programme Research, Development and Education financed by European Structural and Investment Funds and the Czech Ministry of Education, Youth and Sports (CZ.02.1.01/0.0/0.0/15_003/0000464 and CZ.02.1.01/0.0/0.0/16_019/0000760). It occurred in the frame of LNSM infrastructure. We would like to acknowledge Prof. I. Pelant for fruitful discussions.

References

[1] Philip J, Hess P, Feygelson T, et al. Elastic, mechanical, and thermal properties of nanocrystalline diamond films. Appl Phys 2003;93:2164–71.

[2] Iakoubovskii K, Adriaenssens GJ. Optical detection of defect centers in CVD diamond. Diamond Relate Mater 2000;9: 1349–56.

[3] Aharonovich I, Castelletto S, Simpson DA, Su C-H, Greentree AD, Prawer S. Diamond-based single-photon emitters. Rep Prog Phys 2011;74:076501.

[4] Varga M, Remes Z, Babchenko O, Kromka A. Optical study of defects in nano-diamond films grown in linear antenna microwave plasma CVD from $H_2/CH_4/CO_2$ gas mixture. Phys Status Solidi B 2012;249:2635–9.

[5] Nesládek M, Meykens K, Stals LM, Vaněček M, Rosa J. Origin of characteristic subgap optical absorption in CVD diamond films. Phys Rev B 1996;54:5552–61.

[6] Balmer RS, Brandon JR, Clewes SL, et al. Chemical vapour deposition synthetic diamond: materials, technology and applications. J Phys Condens Matter 2009;21:364221.
[7] Tan Z-K, Moghaddam RS, Lai ML, et al. Bright light-emitting diodes based on organometal halide perovskite. Nat Nanotechnol 2014;9:687–92.
[8] Stranks SD, Snaith HJ. Metal-halide perovskites for photovoltaic and light-emitting devices. Nat Nanotechnol 2015;10:391–402.
[9] Fujii T, Gao Y, Sharma R, Hu EL, DenBaars SP, Nakamura S. Increase in the extraction efficiency of GaN-based light-emitting diodes via surface roughening. Appl Phys Lett 2004;84:855–7.
[10] Ondič L, Kůsová K, Cibulka O. Enhanced photoluminescence extraction efficiency from a diamond photonic crystal via leaky modes. New J Phys 2011;13:063005.
[11] Uzunoglu NK, Fikioris JG. Scattering from an inhomogeneity inside a dielectric-slab waveguide. J Opt Soc Am 1982;72:628–37.
[12] Schnitzer I, Yablonovitch E, Caneau C, Gmitter TJ, Scherer A. 30% external quantum efficiency from surface textured, thin-film light-emitting diodes. Appl Phys Lett 1993;63:2174–6.
[13] Moreno I, Sun C-C. Modeling the radiation pattern of LEDs. Opt Exp 2008;16:1808–19.
[14] Checoury X, Néel D, Boucaud P, et al. Nanocrystalline diamond photonics platform with high quality factor photonic crystal cavities. Appl Phys Lett 2012;101:171115.
[15] Wang CF, Hanson R, Awschalom DD, et al. Fabrication and characterization of two-dimensional photonic crystal microcavities in nanocrystalline diamond. Appl Phys Lett 2007;91:201112.
[16] Kreuzer C, Riedrich-Möller J, Neu E, Becher C. Design of photonic crystal microcavities in diamond films. Opt Exp OE 2008;16:1632–44.
[17] Makarov S, Furasova A, Tiguntseva E, et al. Halide-perovskite resonant nanophotonics. Adv Opt Mater 2019;7:1800784.
[18] Richter JM, Abdi-Jalebi M, Sadhanala A, et al. Enhancing photoluminescence yields in lead halide perovskites by photon recycling and light out-coupling. Nat Commun 2016;7:13941.
[19] Wierer JJ, David A, Megens MM. III-nitride photonic-crystal light-emitting diodes with high extraction efficiency. Nat Photon 2009;3:163–9.
[20] Wiesmann C, Bergenek K, Linder N, Schwarz UT. Photonic crystal LEDs – designing light extraction. Laser Photon Rev 2009;3:262–86.
[21] Matioli E, Weisbuch C. Impact of photonic crystals on LED light extraction efficiency: approaches and limits to vertical structure designs. J Phys D: Appl Phys 2010;43:354005.
[22] Inoue T, Zoysa MD, Asano T, Noda S. Realization of narrowband thermal emission with optical nanostructures. OPTICA 2015;2:27–35.
[23] Krishnan C, Brossard M, Lee K-Y, et al. Hybrid photonic crystal light-emitting diode renders 123% color conversion effective quantum yield. OPTICA 2016;3:503–9.
[24] Joannopoulos JD, Johnson SG, Winn JN, Meade RD. Photonic crystals: molding the flow of light, 2nd ed. Princeton and Oxford, Princeton University Press, 2011.
[25] Wu S, Xia H, Xu J, Sun X, Liu X. Manipulating luminescence of light emitters by photonic crystals. Adv Mater 2018;30:1803362.
[26] Wilm A. Requirements on LEDs in etendue limited light engines, in: photonics in multimedia II. Int Soc Optics Photonics 2008;7001:70010F.
[27] Zelsmann M, Picard E, Charvolin T, et al. Seventy-fold enhancement of light extraction from a defectless photonic crystal made on silicon-on-insulator. Appl Phys Lett 2003;83:2542–4.
[28] Ondič L, Varga M, Hruška K, Fait J, Kapusta P. Enhanced extraction of silicon-vacancy centers light emission using bottom-up engineered polycrystalline diamond photonic crystal slabs. ACS Nano 2017;11:2972–81.
[29] Ondič L, Dohnalová K, Ledinský M, Kromka A, Babchenko O, Rezek B. Effective extraction of photoluminescence from a diamond layer with a photonic crystal. ACS Nano 2011;5:346–50.
[30] Ganesh N, Zhang W, Mathias PC, et al. Enhanced fluorescence emission from quantum dots on a photonic crystal surface. Nat Nano 2007;2:515–20.
[31] Ganesh N, Block ID, Mathias PC, et al. Leaky-mode assisted fluorescence extraction: application to fluorescence enhancement biosensors. Opt Exp 2008;16:21626–40.
[32] Galář P, Dzurňák B, Varga M, Marton M, Kromka A, Malý P. Influence of non-diamond carbon phase on recombination mechanisms of photoexcited charge carriers in microcrystalline and nanocrystalline diamond studied by time resolved photoluminescence spectroscopy. Opt Mater Exp 2014;4:624–37.
[33] Verhart NR, Lepert G, Billing AL, Hwang J, Hinds EA. Single dipole evanescently coupled to a multimode waveguide. Opt Exp OE 2014;22:19633–40.
[34] Brueck SRJ. Radiation from a dipole embedded in a dielectric slab. IEEE J Selected Topics Quant Electron 2000;6:899–910.
[35] Oskooi AF, Roundy D, Ibanescu M, Bermel P, Joannopoulos JD, Johnson SG. Meep: a flexible free-software package for electromagnetic simulations by the FDTD method. Comp Phys Commun 2010;18:687–702.
[36] Taflove A, Johnson SG, Oskooi A. Advances in FDTD computational electrodynamics: photonics and nanotechnology. Boston, Artech House, 2013.
[37] Ondič L, Babchenko O, Varga M, Kromka A, Čtyroký J, Pelant I. Diamond photonic crystal slab: leaky modes and modified photoluminescence emission of surface-deposited quantum dots. Sci Rep 2012;2:srep00914.
[38] Davies G, Lawson SC, Collins AT, Mainwood A, Sharp SJ. Vacancy-related centers in diamond. Phys Rev B 1992;46:13157–70.
[39] Iakoubovskii K, Adriaenssens GJ, Dogadkin NN, Shiryaev AA. Optical characterization of some irradiation-induced centers in diamond. Diamond Relate Mater 2001;10:18–26.
[40] Stehlík Š, Ondič L, Varga M, et al. Silicon-vacancy centers in ultra-thin nanocrystalline diamond films. Micromachines 2018;9:281.
[41] Petráková V, Taylor A, Kratochvílová I, et al. Luminescence of nanodiamond driven by atomic functionalization: towards novel detection principles. Adv Funct Mater 2012;22:812–19.
[42] Barjon J, Rzepka E, Jomard F, et al. Silicon incorporation in CVD diamond layers. Phys Stat Sol A 2005;202:2177–81.
[43] Potocký Š, Holovský J, Remeš Z, Müller M, Kočka J, Kromka A. Si-related color centers in nanocrystalline diamond thin films. Phys Stat Sol B 2014;251:2603–6.

Supplementary Material: The online version of this article offers supplementary material (https://doi.org/10.1515/nanoph-2019-0042).

Effect of CVD diamond morphology on the photoluminescence extraction by photonic crystal slabs

Jan Fait*,[1,2], Marián Varga[1], Karel Hruška[1], Alexander Kromka[1], Bohuslav Rezek[1,2] and Lukáš Ondič[1]

[1] Institute of Physics CAS, Cukrovarnická 10, 16200 Prague, Czech Republic
[2] Faculty of Electrical Engineering, Czech Technical University in Prague, Technická 2, 16627 Prague, Czech Republic

*Corresponding author: e-mail fait@fzu.cz, phone +420 220 318 475

Abstract

Photonic crystal (PhC) slabs may be used to extract the photoluminescence from thin diamond layers and direct it into desired direction. This effect can be used for various sensor devices based on photoluminescence of diamond color centers. The extraction efficiency is limited by the material properties and precision of the PhC fabrication. In this study, we analyze the effect of diamond film morphology on the fabrication of the PhC and subsequently on the extraction efficiency. We show that diamond layer with small grains (< 50 nm) is more convenient both for the PhC slabs fabrication and for the extraction of photoluminescence in comparison with diamond layer with large grains (> 100 nm). We also show that the trend of enhancement factor dependence on the numerical aperture of the collection optics differs for different morphologies of diamond layer.

Keywords

Polycrystalline diamond, photonic crystal slabs, photonic sensors, leaky modes, photoluminescence enhancement

1. Introduction

Photonic crystal (PhC) slabs are commonly used for fabrication of highly efficient sensing devices that are based on the optical transducing mechanism [1–5]. The PhC slabs support optical resonances that can be observed as spectrally sharp features in the transmission and reflection spectra. The light that is resonantly coupled into the PhC slab propagates inside the PhC slab with evanescent tails interfering and interacting with the surrounding environment [6]. A small change in the refractive index in the surrounding environment then leads to the spectral shift of the resonances, which is the basis of the detection mechanism [5].

The PhC slabs are created when a thin layer of material with high refractive index (e.g. TiO_2 [7], ZnO [8], or diamond [9]) is patterned with a 2D periodicity [10]. The PhC slabs mediate the coupling between the guided photonic modes inside the layer and the radiative modes that are propagating in a free space via the phenomenon of Bragg diffraction. Even though external light source was usually proposed for the use in sensing devices, the leaky modes can be also used to extract the light from the light emitters residing inside the PhC [11,12]. The modes, that would be otherwise trapped and guided inside the layer, become leaky, which not only increases the portion of light that radiates from the layer but the extracted light is also directed into defined directions [13], which can be controlled by the PhC slab dimensions. The directionality of the light allows its efficient detection without the usage of complex detection optics [12]. In principle, the spectral shift of extracted light can also be used for sensing, as the same mechanism as for transmission/reflection is employed.

The material that is particularly suitable for fabrication of sensor devices is diamond. Diamond has many properties that are interesting for sensing, such as biocompatibility, chemical inertness, or negative electron affinity [14]. One of the most interesting and intensively studied features are diamond color centers [15,16]. For instance, silicon vacancy (SiV) centers are ideal for sensorics thanks to their narrow emission spectra at NIR. The diamond color centers can not only be used as a passive light source for the detection mechanism, but also as an independent detection mechanism since their photoluminescence (PL) intensity is affected by the changes on the diamond surface [17–19].

The combination of photonic structures with diamond can improve the performance of devices based on the PL of diamond color centers, e.g. SiV, nitrogen-vacancy (NV), etc. [20]. For instance, PhC cavities [21,22] or ring resonators [23] enable to locally increase the emission rate of color centers due to Purcell effect [24]. Recently, we have demonstrated fabrication of PhC cavities in polycrystalline diamond with a notable enhancement of the SiV centers PL [25]. Nevertheless, the emission rate is increased only in a very small volume of the material and sophisticated optical devices are required to collect the light.

In contrast, PhC slabs allow to improve the PL collection efficiency from large-scale samples [26]. This increases the signal on one hand and allows the spatially resolved sensing on the other hand, because the resonance condition depends on the refractive index at a specific location [5]. We have already shown that the PhC slabs can be engineered to efficiently extract the photoluminescence of SiV centers [9] and that the PhC slabs can be fabricated in polycrystalline diamond layers, while keeping excellent performance for light extraction [26]. This is a key property for cost-effective fabrication of sensing devices because thin layers of polycrystalline diamond can be easily deposited on various types of substrates using chemical vapor deposition (CVD) [27,28].

In this study, we evaluate the effect of CVD diamond layer morphology (grain-size), which can be controlled by the CVD deposition parameters, on the fabrication and on the optical properties of diamond PhC slabs. The morphology of the diamond layer affects both the material properties (concentration of non-diamond carbon bonds, surface roughness) and optical properties (absorption coefficient, light scattering, background photoluminescence). We analyze the properties of materials and structures using scanning electron microscopy (SEM), atomic force microscopy (AFM), and photothermal deflection spectroscopy (PDS). We show that the shape of the PhC is better controlled on the layer with small diamond grains (grain size < 50 nm), which leads to better directionality of the PL extraction, than on the layer with large diamond grains (grain size > 100 nm). We also observe, how the PL enhancement depends on the numerical aperture (NA) of the collection optics. Low NA is advantageous for enhancement of narrow spectral peaks, while high NA offers enhancement in broad spectral region. Low NA also allows to place the detection optics in a large distance from the sample, which may be important for some sensing systems.

2. Experimental

For the diamond growth two different CVD reactors were employed: (i) focused microwave (MW) plasma reactor (Aixtron P6) using an ellipsoidal cavity resonator and (ii) linear antenna MW plasma system (Roth & Rau AK 400) equipped with two linear antennas working in a pulsed regime [29]. The quartz substrates were ultrasonically cleaned in acetone and isopropyl alcohol and were rinsed in deionized water. After the cleaning, the quartz substrates were seeded by applying ultrasonic agitation in a nanodiamond colloid (NanoAmando aqueous dispersion of nanodiamond particles, median nanodiamond size 4.8 ± 0.6 nm) diluted by deionized water 1:40 v:v.

Parameters used for diamond deposition in focused MW plasma reactor were as follows: deposition time $t = 80$ min, total gas pressure $p = 5$ kPa, gas flow of hydrogen H_2 equal to 300 sccm, gas flow of methane CH_4 equal to 3 sccm, power of MW source $P = 2.5$ kW, and approximate surface temperature of samples T = 570°C. These parameters lead to a formation of diamond layers with grain size > 100 nm (denoted as large grains). Note that certain procedures (e.g. increasing the ratio of CH_4 to H_2 [30]) would lead to the creation of smaller diamond grains. Nevertheless, it would deteriorate the optical quality of the layer. Therefore, we used the second deposition reactor, which is capable of keeping high optical quality of diamond layer while the grain size is < 50 nm (denoted as small grains). Parameters used for diamond deposition in linear antenna MW plasma system were as follows: deposition time $t = 19$ h, pressure $p = 10$ Pa, gas flow of hydrogen H_2 equal to 200 sccm, gas flow of methane CH_4 equal to 5 sccm, and gas flow of CO_2 equal to 20 sccm, power of microwave source

P = 2×1.7 kW, and approximate surface temperature of samples T = 540°C. The thickness of the layers was between 160 nm and 175 nm in both cases.

The top part of the diamond layer was patterned into the periodically ordered columns using electron beam lithography (EBL) and reactive ion etching (RIE) yielding a PhC slab. The electron sensitive polymer (PMMA, approximate thickness 100 nm) was first patterned by EBL (Fig. 1a). Next, the gold (approximate thickness 70 nm) was evaporated and the mask was created using a lift-off process (Fig. 1b). Not-covered parts of the sample were partially etched in capacitively coupled O_2/CF_4 plasma RIE. Finally, the metal mask was removed by wet etching (Fig. 1c). The total area of the PhC structure on each sample was larger than 1 mm^2. The shape of the PhC was computed using rigorous coupled-wave approximation (RCWA, RSoft DiffractMod software) to support photonic modes at the red part of the visible region. In the same time, very thin samples were designed, which is advantageous for sensing applications. Nevertheless, it might not be optimal for achieving best photonic performance.

The surface morphology of the samples was investigated by SEM (e_LiNe workstation, Raith, Dortmund, Germany) in standard configuration. The surface roughness of as-deposited diamond layer and diamond layer after etching was measured by AFM (Veeco DI3100 IV). The absorption of diamond layers was measured by PDS. The thickness and refractive index of the diamond film (both before and after etching) was measured by the reflectance interferometry and evaluated by a commercially available FilmWizard software (SCI company).

The first type of the PL measurement was performed on a home-made setup with optical fiber placed at a distance of 7.5 cm from the sample. This setup allows to measure the PL with high angular resolution (1°) coming from a large sample area (0.1 mm^2). For the second type of the PL measurement, the *Renishaw inVia Reflex* system was used, where more objectives (5x with NA 0.12; 20x with NA 0.4; 50x with NA 0.5; and 100x with NA 0.9) were used for the collection of signals. The maximal collection angle depends on the NA of the objective and it is specified in the caption of Fig. 2. Also, the size of the probed area depends on the NA, and it is in the order of units of square micrometers for all objectives. This may limit the portion of collected leaky modes as their extraction length may be larger. The depth of focus is larger than the thickness of the samples for all objectives. He-Cd laser (442 nm) was used for the excitation of the PL in both cases. For the simulation of transmission through the sample RCWA approximation was used.

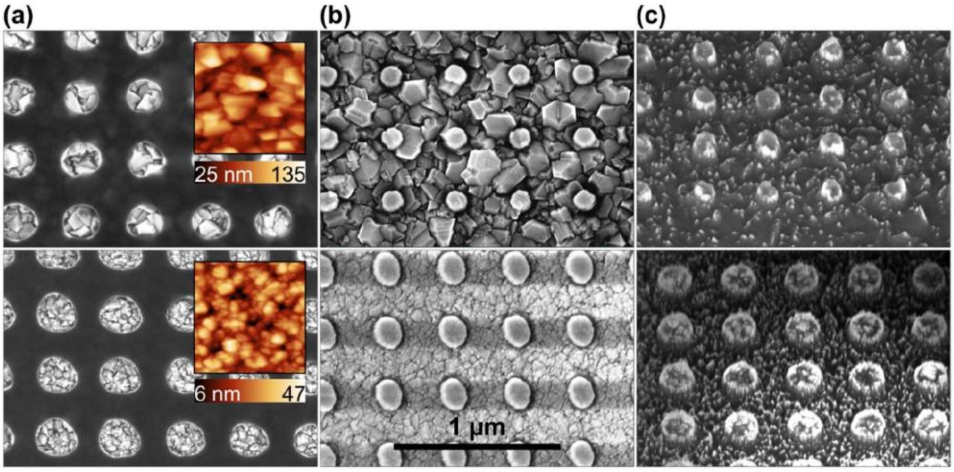

Figure 1 SEM pictures of the various stages during the PhC slab fabrication: (a) EBL patterning of PMMA (the insets show the topography of as-deposited diamond layer measured with AFM), (b) gold mask over the sample after the lift-off process, (c) final diamond-based PhC slabs (under tilting angle 45°). Top and bottom row show the sample with large and small diamond grains, respectively.

3. Results

3.1 PhC characterization

Fig. 1c shows the SEM morphology of the PhC samples under 45° tilting angle. Both structures reveal some shape imperfections, which originates from the polycrystalline character of the diamond film. There are two major aspects, which cause the imperfections. Firstly, the layer is composed of the mixture of the sp^2 (graphitic) and sp^3 (diamond) hybridized carbon phases. The graphitic phase between the diamond grains is etched-away more quickly what finally result in a randomly featured diamond film between the columns. The composition of the layers was measured by Raman spectroscopy (see the spectra in Fig. S2 in Supplementary Information). The ratio of non-diamond sp^2 phase is higher in the sample with large diamond grains.

Secondly, the surface of as-grown diamond layer is rough (insets of Fig. 1a). This results in an irregular shape of PhC columns with sharp edges as is evident on SEM images. Larger imperfections can be seen on the sample with large diamond grains. The presence of large grains (> 100 nm) increases the surface roughness (RMS 19 nm, measured by AFM). Subsequently, the PhC columns are randomly deformed depending on the orientation of grains in the layer. By contrast, the sample with small diamond grains (< 50 nm) reveal smaller surface roughness (RMS 7 nm). This results in a better control over the column shape, which remains more or less identical across the sample.

The PhC dimensions, determined from SEM images, are summarized in Tab. 1. Thickness of the diamond film (both before and after etching) was measured by reflectance interferometry. The height of the columns was determined by AFM measurement. A significant difference between the samples lies in the diameter of PhC columns. The difference originates from fabrication process. Although the diameter of EBL circles and thickness of gold layer (70 nm) were similar on both samples, the diameter of gold-mask circles was different. This is most probably caused by the higher surface roughness of the layer with large diamond grains.

The layer with large diamond grains has more pronounced absorption in the visible region, which is caused by larger content of sp^2 phase. The absorption coefficient of the layer with large and small grains is 875 cm^{-1} and 610 cm^{-1}, respectively, for the wavelength 650 nm as measured with the PDS. The spectral dependence of the absorption coefficient is shown in the Fig. S1b in the Supp. Info.

Finally, the transmission of white light through the samples was measured (Fig. 2). Minima in transmission efficiency are observed when the light is coupled to the leaky modes of the PhC slab at the given angle of incidence and given wavelength. For skewed angle of incidence, the coupling condition is shifted to other wavelengths with respect to the spectral position under the vertically incident beam (Γ-point). The photonic band diagram (for leaky modes) can be reconstructed from this measurement. Fig. 2 shows that there is almost perfect conformity between measured and simulated transmission band diagrams for the sample with small diamond grains. For the sample with large grains, the transmission was measured only for the direction normal to the sample plane (see the Supplementary Information.

Table 1 The dimensions of diamond photonic crystal slabs: *a* lattice constant, *d* diameter of columns, *h* thickness of the as-deposited diamond layer, and *hc* height of the columns (equals to the thickness etched by RIE). The uncertainty of the measurements is 5 nm.

grain size	large (> 100 nm)	small (< 50 nm)
a (nm)	390	390
d (nm)	165	215
h (nm)	175	160
hc (nm)	105	105

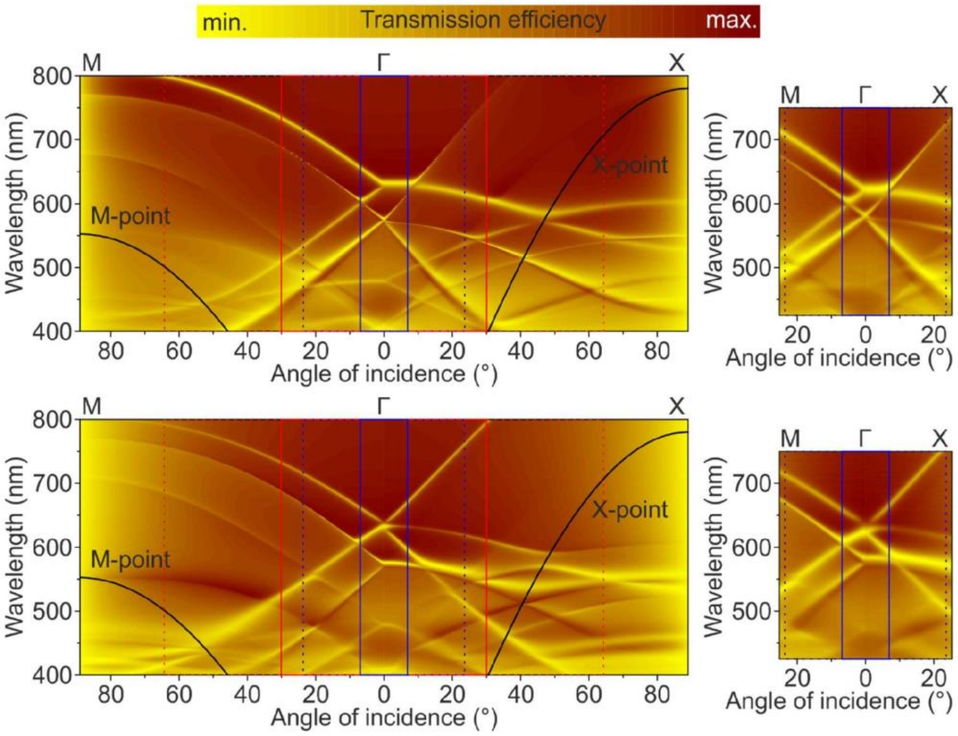

Figure 2 Simulated (left) and measured (right) photonic band diagrams of the sample with small grains for p-polarized (top) and s-polarized (bottom) light. The left part of x-axis of each diagram is for Γ-M direction and the right part for Γ-X direction. The position of X and M points is also indicated in the diagram. Dimensions specified in Tab. 1 were used for the simulation. The vertical lines show the edge of the collection cone of the used objectives (NA 0.12: 6.9°, blue solid lines; NA 0.4: 23.6°, blue dashed lines; NA 0.5: 30°, red solid lines; NA 0.9: 64.2°, red dashed lines).

3.2 PL measurement with the optical fiber

Figure 3 shows the PL signal measured with the optical fiber placed at the vertical direction with regard to the sample plane. Clearly, two peaks are present in the PL spectra measured on the PhC (black line), while there are no such peaks on the as-deposited diamond layer (blue line). The peaks originate from the extraction of the PL signal via leaky modes. Note, that the same intensity of the excitation beam and identical detection time were used for all measurements with the fiber.

In order to evaluate the performance of the PhC structures, we define the enhancement factor as a ratio between the PL intensity measured on the PhC and the PL intensity measured on the as-deposited diamond layer (while using same parameters for both measurements). The peak enhancement factor is 4.1 for the PhC slab on the sample with large grains (TE_0 leaky mode at the wavelength of 643 nm) and 16.7 for the PhC slab on sample with small grains (TE_0 at 631 nm). We also determined the overall enhancement factor, which is the ratio between the total intensity of PL measured on PhC and that measured on as-deposited diamond layer (intensity between 460 nm and 750 nm was integrated). The integral enhancement factor is 1.5 for the sample with large grains and 4.4 for the sample with small grains.

The main mechanism of the PL enhancement is the extraction of leaky modes (narrow spectral peaks at approximately 590 nm and 640 nm). The TE_0 leaky mode offers higher enhancement factor than TM_0 leaky mode for both samples (Fig. 3). However, there are also other effects that contribute to the enhancement factor. Firstly, it is the effect of Fabry-Perot resonances. In our case it enhances the extraction of light (into vertical direction) in the blue and green spectral region (Fig. 3), while the extraction of red light is suppressed. This is in accordance with the numerical simulations of Fabry-Perot resonances (see Fig. S2 in Supp. Info). Secondly, the volume of material is lower on the PhC when compared to as-deposited diamond layer, which affects the number of emitters and thus the overall PL intensity. The ratio between the volume of the material on the as-deposited diamond layer and on the PhC structure is 2.05 and 2.00 for the sample with large and small diamond grains, respectively. Thirdly, different surface area of the PhC with respect to the reference layer may cause the enhancement in the whole spectral region. The higher the surface area is, the more emitters are placed near the diamond surface and may thus emit light directly into space.

In order to exclude all other effects except the extraction of the leaky modes, we approximated the background PL on the PhC by the red dashed lines (shown in Fig. 3) and used this approximation as a reference for determination of the corrected enhancement factor. After this correction, the peak enhancement factor is 2.0 and 4.1 for TM_0 and TE_0 leaky mode, respectively, for the sample with large grains. On the sample with small grains, the peak enhancement factor is 3.6 and 7.0 for TM_0 and TE_0 leaky mode, respectively.

Clearly, the leaky modes offer higher enhancement on the sample with small grains. The better performance of this sample is partially caused by the lower absorption coefficient and better overall homogeneity of the diamond. Better homogeneity decreases the scattering of light that is propagating through the layer, which is a mechanism that compete with the diffraction of leaky modes on the PhC. Reduced scattering thus leads to increased extraction efficiency via leaky modes. Note that, although the scattering improves the extraction of light, the light is not extracted into any specific direction and objectives with high numerical aperture must be used for its collection.

The second factor that leads to the observed better performance of the sample with small grains is the better structural quality of PhC structures. The structural quality of PhC not-only improves the out-coupling efficiency of the leaky modes from the photonic structure but mainly causes that the light is extracted into the specific direction. This is not the case of the sample with large grains, and hence the maximal observed enhancement factor is reduced. Moreover, the samples with small grains have larger column diameter, and the light is extracted more efficiently from the layer [31].

Note that the resonant excitation can be used to additionally enhance the PL by coupling the excitation laser into the leaky mode of PhC [7,26]. The morphology of PhC affects also this so-called resonant excitation enhancement. The maximal observed resonant excitation enhancement for the laser beam incident under the resonant angle was only around 3 on the sample with large grains, while it was more than 5 on the sample with small grains.

3.3 PL measurement with the microscope objectives

Fig. 4 shows the PL spectra measured with the microscope objective with numerical aperture 0.12 (acceptance angle of 6.9°) on both samples. Again, we measured the PL intensity on the PhC slab (black curve) and on the as-deposited diamond layer (blue). The peaks in the PhC spectra are spectrally broadened when compared to those measured with the optical fiber. The reason is that also the leaky modes that propagates slightly skewed with regard to the vertical direction lie within the collection cone of the objective. These modes are spectrally shifted with regard to those extracted directly into the vertical direction, as can be seen on the photonic band diagram (Fig. 2), where the maximal collection angles for all objectives are depicted.

The peak enhancement factor is 3.1 (wavelength 650 nm) and 4.4 (wavelength 631 nm) for the sample with large and small diamond grains, respectively. These values are lower than the peak enhancement factors measured with the optical fiber, which is in accordance with the fact that the PhC offers highly directional emission. At one particular wavelength, the increase of the collection angle leads to the gradual increase of the intensity for the case of the reference and background (not leaky modes enhanced) signal. On the other hand, the signal from the leaky modes does not increase gradually due to the directionality of leaky modes. These two effects lead to the observed decrease of the enhancement factor.

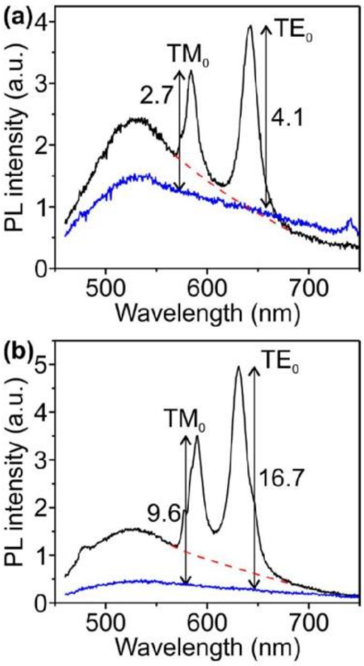

Figure 3 PL intensity measured by fiber with low collection angle (1°) on the PhC slab (black) and on the as-deposited diamond layer (blue) for the sample with (a) large and (b) small diamond grains. The numbers show the peak enhancement factor for TM$_0$ and TE$_0$ leaky modes.

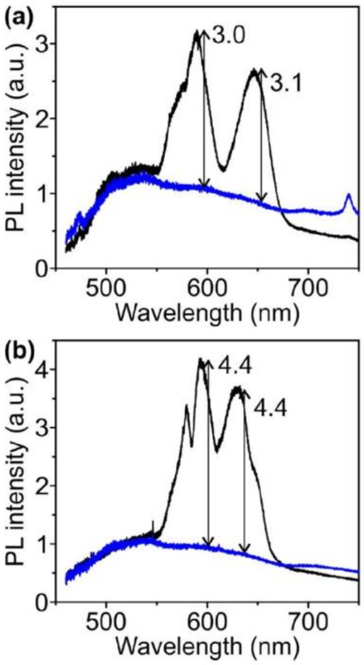

Figure 4 PL intensity measured by 5x objective (NA 0.12) on the PhC slab (black) and on the as-deposited diamond layer (blue) for the sample with (a) large and (b) small diamond grains. The numbers show the peak enhancement factor for TM$_0$ and TE$_0$ leaky modes.

Fig. 5a shows the enhancement factor as a function of the wavelength for the objectives with different NA for the sample with small diamond grains. The figure shows not only that the peaks in PL spectra become wider with higher NA, but also that the peak enhancement factor increases again. The increment of enhancement factor is most probably caused by the integration over large angle, where folded leaky modes contribute to the extraction. Interestingly, no increase of enhancement factor was observed for the sample with small diamond grains (Fig. 5b).

The dependence of the enhancement factor on the NA of the collection optics was investigated on the photonic structures made of TiO_2/PMMA [6] and on the photonic structures in Si-nanocrystals rich glass [32,33], and, in both cases, the enhancement factor remained constant or decreased with the numerical aperture (similarly to diamond layer with large grains in our case). Nevertheless, these studies were performed on materials with different refractive indices, PhC slabs with different dimensions, and employing objectives with max. NA 0.4.

The main reason for the different behavior of our PhC structure compared to other works is probably caused by different dimensions and refractive index of the PhC. It can be seen from the photonic band diagram (Fig. 2) that the X-point is located between 30° and 50° for the relevant wavelengths. The bands are folded in the X-point, which increases the portion of light that is diffracted into large angles. This light can be collected only with the high NA objectives. The reason why the diamond sample with large grains works differently is that the light is scattered and reflected on the boundaries between diamond grains. This causes that a large part of light is scattered from the layer within the Lambertian radiation pattern instead of being diffracted via leaky modes and the effect of leaky modes is thus not as significant as on the sample with small diamond grains.

Another factor responsible for the increase of the enhancement factor with the NA may be that the excitation beam incident under the resonant angle can be coupled into the PhC and thus increase the excitation efficiency. The resonant angles are 24°, 31°, and 54° for p-polarized excitation and 29°, 41°, and 54° for s-polarized light for 442 nm excitation beam (Fig. 2). Therefore, the resonant excitation can be achieved only when the objectives with high numerical aperture are used. Nevertheless, only small fraction of the excitation beam is resonantly coupled into the structure in the case of excitation via the objectives, and we thus expect only small effect on the overall enhancement factor.

Note that the growth of integral enhancement factor (integrated over all wavelengths) with numerical aperture is expectable since each wavelength is Bragg diffracted into different angle. The higher the numerical aperture is, the larger is the spectral bandwidth for which the leaky modes are collected by the objective and the higher is the integral enhancement factor.

Finally, the PL spectra measurements on various places of the PhC itself revealed large-scale inhomogeneities in the geometry, that are more pronounced on the sample with large grains (Fig. S3 in Supp. Info). This may affect the measurement with optical fiber, since the detected signal comes from large area of the sample in that case. This is the reason why larger differences between samples were observed with optical fiber measurement when compared to the measurement with microscope objective.

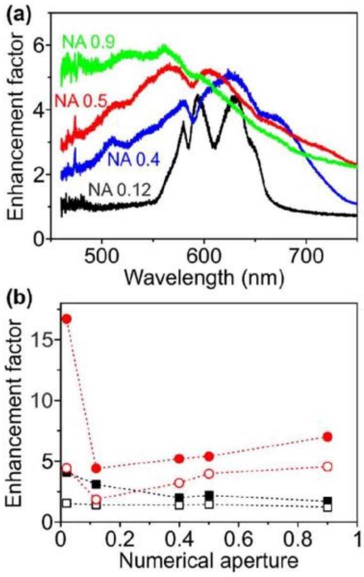

Figure 5 (a) The enhancement factor evaluated from PL intensity measurements with objectives with different numerical aperture (NA) on the sample with small grains. (b) Dependence of the peak (solid symbols) and integral (open symbols) enhancement factor on the numerical aperture of the detection optics for the sample with small (circles; data shown in (a)) and large (squares) diamond grains.

Conclusion

In this study, we showed that the morphology (grain size) of diamond layer significantly affects the fabrication of the PhC slabs. Precise structures fabricated in the sample with small grains (grain size < 50 nm) are essential for obtaining highly directional PL emission from diamond PhC slabs. For the case of the layer with small grains, we also observed that the peak enhancement factor increases with numerical aperture of the collection microscopic objectives. The increase of peak enhancement factor is primarily caused by the extraction via leaky modes that are folded in the X-point of the photonic structure and that can be collected only by using objectives with high numerical aperture. No increase of peak enhancement factor with numerical aperture was observed on the sample with large grains (grain size > 100 nm), which is most probably caused by the scattering of light on the larger diamond grains, which is more pronounced on this sample. The obtained results may be helpful in fabricating diamond photonic structures for sensing applications making use of diamond color centers.

Acknowledgement

This work was supported by the Czech Science Foundation (GAČR) (19-14523S); Czech Technical University (CTU) (SGS18/179/OHK4/3T/13); and European projects (CZ.02.1.01/0.0/0.0/15_003/0000464 and CZ.02.1.01/0.0/0.0/16_019/0000760).

References

[1] C. Blin, Z. Han, H.A. Girard, P. Bergonzo, P. Boucaud, M.E. Kurdi, S. Saada, S. Sauvage, X. Checoury, Surface-sensitive diamond photonic crystals for high-performance gas detection, Opt. Lett. 41 (2016) 4360–4363. https://doi.org/10.1364/OL.41.004360.

[2] H. Inan, M. Poyraz, F. Inci, M.A. Lifson, M. Baday, B.T. Cunningham, U. Demirci, Photonic crystals: emerging biosensors and their promise for point-of-care applications, Chem. Soc. Rev. (2016). https://doi.org/10.1039/C6CS00206D.

[3] M. Lee, P.M. Fauchet, Two-dimensional silicon photonic crystal based biosensing platform for protein detection, Opt. Express. 15 (2007) 4530–4535. https://doi.org/10.1364/OE.15.004530.

[4] R. Shugayev, P. Bermel, Propagation Loss-Immune Biocompatible Nanodiamond Refractive Index Sensors, Adv. Opt. Mater. (n.d.) n/a-n/a. https://doi.org/10.1002/adom.201700487.

[5] G. Pitruzzello, T.F. Krauss, Photonic crystal resonances for sensing and imaging, J. Opt. 20 (2018) 073004. https://doi.org/10.1088/2040-8986/aac75b.

[6] N. Ganesh, I.D. Block, P.C. Mathias, W. Zhang, E. Chow, V. Malyarchuk, B.T. Cunningham, Leaky-mode assisted fluorescence extraction: application to fluorescence enhancement biosensors, Opt. Express. 16 (2008) 21626–21640. https://doi.org/10.1364/OE.16.021626.

[7] N. Ganesh, W. Zhang, P.C. Mathias, E. Chow, J. a. N.T. Soares, V. Malyarchuk, A.D. Smith, B.T. Cunningham, Enhanced fluorescence emission from quantum dots on a photonic crystal surface, Nat. Nanotechnol. 2 (2007) 515–520. https://doi.org/10.1038/nnano.2007.216.

[8] A. Yamilov, X. Wu, H. Cao, Photonic band structure of ZnO photonic crystal slab laser, J. Appl. Phys. 98 (2005) 103102. https://doi.org/10.1063/1.2134880.

[9] L. Ondič, M. Varga, K. Hruška, J. Fait, P. Kapusta, Enhanced Extraction of Silicon-Vacancy Centers Light Emission Using Bottom-Up Engineered Polycrystalline Diamond Photonic Crystal Slabs, ACS Nano. 11 (2017) 2972–2981. https://doi.org/10.1021/acsnano.6b08412.

[10] J.D. Joannopoulos, S.G. Johnson, J.N. Winn, R.D. Meade, Photonic Crystals: Molding the Flow of Light, Second Edition, Princeton University Press, 2011.

[11] J.J. Wierer, A. David, M.M. Megens, III-nitride photonic-crystal light-emitting diodes with high extraction efficiency, Nat. Photonics. 3 (2009) 163–169. https://doi.org/10.1038/nphoton.2009.21.

[12] E. Matioli, C. Weisbuch, Impact of photonic crystals on LED light extraction efficiency: approaches and limits to vertical structure designs, J. Phys. Appl. Phys. 43 (2010) 354005. https://doi.org/10.1088/0022-3727/43/35/354005.

[13] I. Moreno, C.-C. Sun, Modeling the radiation pattern of LEDs, Opt. Express. 16 (2008) 1808–1819. https://doi.org/10.1364/OE.16.001808.

[14] J.E. Field, ed., The Properties of natural and synthetic diamond, Academic Press, London ; San Diego, 1992.

[15] E. Neu, D. Steinmetz, J. Riedrich-Möller, S. Gsell, M. Fischer, Matthias Schreck, C. Becher, Single photon emission from silicon-vacancy colour centres in chemical vapour deposition nano-diamonds on iridium, New J. Phys. 13 (2011) 025012. https://doi.org/10.1088/1367-2630/13/2/025012.

[16] I. Aharonovich, S. Castelletto, D.A. Simpson, C.-H. Su, A.D. Greentree, S. Prawer, Diamond-based single-photon emitters, Rep. Prog. Phys. 74 (2011) 076501. https://doi.org/10.1088/0034-4885/74/7/076501.

[17] V. Petráková, A. Taylor, I. Kratochvílová, F. Fendrych, J. Vacík, J. Kučka, J. Štursa, P. Cígler, M. Ledvina, A. Fišerová, P. Kneppo, M. Nesládek, Luminescence of Nanodiamond Driven by Atomic Functionalization: Towards Novel Detection Principles, Adv. Funct. Mater. 22 (2012) 812–819. https://doi.org/10.1002/adfm.201101936.

[18] C.E. Nebel, B. Rezek, D. Shin, H. Uetsuka, N. Yang, Diamond for bio-sensor applications, J. Phys. Appl. Phys. 40 (2007) 6443. https://doi.org/10.1088/0022-3727/40/20/S21.

[19] S. Stehlik, L. Ondic, M. Varga, J. Fait, A. Artemenko, T. Glatzel, A. Kromka, B. Rezek, Silicon-Vacancy Centers in Ultra-Thin Nanocrystalline Diamond Films, Micromachines. 9 (2018) 281. https://doi.org/10.3390/mi9060281.

[20] I. Aharonovich, A.D. Greentree, S. Prawer, Diamond photonics, Nat. Photonics. 5 (2011) 397–405. https://doi.org/10.1038/nphoton.2011.54.

[21] J. Wolters, A.W. Schell, G. Kewes, N. Nüsse, M. Schoengen, H. Döscher, T. Hannappel, B. Löchel, M. Barth, O. Benson, Enhancement of the zero phonon line emission from a single nitrogen vacancy center in a nanodiamond via coupling to a photonic crystal cavity, Appl. Phys. Lett. 97 (2010) 141108. https://doi.org/10.1063/1.3499300.

[22] J. Riedrich-Möller, C. Arend, C. Pauly, F. Mücklich, M. Fischer, S. Gsell, M. Schreck, C. Becher, Deterministic Coupling of a Single Silicon-Vacancy Color Center to a Photonic Crystal Cavity in Diamond, Nano Lett. 14 (2014) 5281–5287. https://doi.org/10.1021/nl502327b.

[23] A. Faraon, P.E. Barclay, C. Santori, K.-M.C. Fu, R.G. Beausoleil, Resonant enhancement of the zero-phonon emission from a colour centre in a diamond cavity, Nat. Photonics. 5 (2011) 301–305. https://doi.org/10.1038/nphoton.2011.52.

[24] E. Purcell, Spontaneous emission probabilities at radio frequencies, in: Phys. Rev., 1946: p. 681. https://doi.org/10.1007/978-1-4615-1963-8_40.

[25] L. Ondič, M. Varga, J. Fait, K. Hruška, V. Jurka, A. Kromka, J. Maňák, P. Kapusta, J. Nováková, Photonic crystal cavity-enhanced emission from silicon vacancy centers in polycrystalline diamond achieved without postfabrication fine-tuning, Nanoscale. 12 (2020) 13055–13063. https://doi.org/10.1039/c9nr10580h.

[26] J. Fait, M. Varga, K. Hruška, Z. Remeš, V. Jurka, A. Kromka, B. Rezek, L. Ondič, Maximized vertical photoluminescence from optical material with losses employing resonant excitation and extraction of photonic crystal modes, Nanophotonics. 8 (2019) 1041–1050. https://doi.org/10.1515/nanoph-2019-0042.

[27] D. Das, R.N. Singh, A review of nucleation, growth and low temperature synthesis of diamond thin films, Int. Mater. Rev. 52 (2007) 29–64. https://doi.org/10.1179/174328007X160245.

[28] A. Kromka, O. Babchenko, Š. Potocký, B. Rezek, Sveshnikov, Diamond nucleation and seeding techniques for tissue regeneration, in: Diam.-Based Mater. Biomed. Appl., Elsevier, 2013.

[29] M. Varga, V. Vretenar, T. Izak, V. Skakalova, A. Kromka, Carbon nanotubes overgrown and ingrown with nanocrystalline diamond deposited by different CVD plasma systems, Phys. Status Solidi B. 251 (2014) 2413–2419. https://doi.org/10.1002/pssb.201451176.

[30] C. Dawedeit, S.O. Kucheyev, S.J. Shin, T.M. Willey, M. Bagge-Hansen, T. Braun, Y.M. Wang, B.S. El-Dasher, N.E. Teslich, M.M. Biener, J. Ye, L. Kirste, C.-C. Roehlig, M. Wolfer, E. Woerner, A.W. van Buuren, A.V. Hamza, C. Wild, J. Biener, Grain size dependent physical and chemical properties of thick CVD diamond films for high energy density physics experiments, Diam. Relat. Mater. 40 (2013) 75–81. https://doi.org/10.1016/j.diamond.2013.10.001.

[31] C. Wiesmann, K. Bergenek, N. Linder, U. t. Schwarz, Photonic crystal LEDs – designing light extraction, Laser Photonics Rev. 3 (2009) 262–286. https://doi.org/10.1002/lpor.200810053.

[32] L. Ondič, M. Varga, I. Pelant, J. Valenta, A. Kromka, R.G. Elliman, Silicon nanocrystal-based photonic crystal slabs with broadband and efficient directional light emission, Sci. Rep. 7 (2017) 5763. https://doi.org/10.1038/s41598-017-05973-y.

[33] L. Ondič, M. Varga, I. Pelant, A. Kromka, K. Hruška, R.G. Elliman, Two-dimensional photonic crystals increasing vertical light emission from Si nanocrystal-rich thin layers, Beilstein J. Nanotechnol. 9 (2018) 2287–2296. https://doi.org/10.3762/bjnano.9.213.

Nanoscale

PAPER

Cite this: DOI: 10.1039/c9nr10580h

Photonic crystal cavity-enhanced emission from silicon vacancy centers in polycrystalline diamond achieved without postfabrication fine-tuning†

Lukáš Ondič, *[a] Marian Varga, [a] Jan Fait, [a,d] Karel Hruška,[a] Vlastimil Jurka,[a] Alexander Kromka, [a] Jan Maňák,[a] Peter Kapusta [b] and Jaroslava Nováková[c]

Received 14th December 2019,
Accepted 21st May 2020

DOI: 10.1039/c9nr10580h

rsc.li/nanoscale

Diamond optical centers have recently emerged as promising single-photon sources for quantum photonics. Particularly, negatively charged silicon vacancy (SiV^-) centers show great promise due to their narrow zero-phonon emission line present also at room temperature. However, due to fabrication tolerances it is challenging to prepare directly photonic structures with optical modes spectrally matching the emission of SiV^- centers. To reach the spectral overlap, photonic structures must typically undergo complicated post-processing treatment. In this work, suspended photonic crystal cavities made of polycrystalline diamond are engineered and more than 2.5-fold enhancement of the SiV^- center zero-phonon line intensity *via* coupling to the cavity photonic mode is demonstrated. The intrinsic non-homogeneous thickness of the diamond thin layer within the sample is taken as an advantage that enables reaching the spectral overlap between the emission from SiV^- centers and the cavity modes without any post-processing. Even with lower optical quality compared to monocrystalline diamond, the fabricated photonic structures show comparable efficiency for intensity enhancement. Therefore, the results of this work may open up a promising route for the application of polycrystalline diamond in photonics.

1 Introduction

Single-photon emitters are envisioned as basic building blocks of the future quantum optical circuits.[1–3] Diamond optical centers with their high-brightness and long coherence time are promising candidates.[4–7] The photoluminescence (PL) emission rate (number of photons emitted per second) of the optical centers can be improved by incorporating them into nanostructures which also provide a control over their emission pattern.[8,9] A large variety of photonic nanostructures have been demonstrated both on monocrystalline[10–18] and polycrystalline diamond.[19–23] One of the examples of such nanostructures is a photonic crystal (PhC) cavity. Modified local density of optical states within the PhC cavity enables modification of the PL emission rate of the embedded light-emitters *via* the Purcell effect.[24]

Particularly, promising diamond optical centers are negatively-charged silicon vacancy (SiV^-) centers possessing a narrow room-temperature zero-phonon line,[25,26] reasonable (more than 5% quantum yield) brightness,[27,28] and single-photon emitter properties.[29] Their coupling to monocrystalline diamond PhC cavities has been demonstrated too. For example, Becher *et al.* have obtained 2.8 enhancement of the ensemble of SiV^- center PL *via* the Purcell effect by spectrally tuning the photonic crystal cavity mode *via* diamond oxidation.[30] The same group has also shown that a single SiV^- center can be coupled to a photonic crystal cavity prepared in a monocrystalline diamond with 19-fold enhancement of the SiV^- center PL.[31] Even higher enhancement has been obtained by Vučković *et al.*[32] who coupled the SiV^- center into a one-dimensional diamond photonic crystal cavity.

All the above-listed achievements have relied on a relatively complicated and expensive fabrication process. In PhC cavities, the optical modes must be well both spatially and spectrally overlapped with the emitters.[33] Typically, however, the inaccuracies in the fabrication do not enable spectrally matching the cavity mode with the emitter possessing a narrow emission line (such as the SiV^- center) within one processing run.[30,32] Therefore, after fabricating the cavity itself, it must be

---

[a] *Institute of Physics, Czech Academy of Sciences, v.v.i., Cukrovarnická 10, CZ-162 00 Prague 6, Czech Republic. E-mail: ondic@fzu.cz*
[b] *J. Heyrovský Institute of Physical Chemistry, Czech Academy of Sciences, v.v.i., Dolejškova 3, CZ-182 23 Prague 8, Czech Republic*
[c] *Charles University in Prague, Faculty of Mathematics and Physics, Department of Surface and Plasma Science, V Holešovičkách 742/2, 180 00 Prague 8, Czech Republic*
[d] *Faculty of Electrical Engineering, Czech Technical University in Prague, Technická 27, 16627 Prague, Czech Republic*

† Electronic supplementary information (ESI) available. See DOI: 10.1039/C9NR10580H

optically characterized and, based on its properties, post-processed to obtain the desired properties.[34] Post-processing methods take advantage of the fact that the spectral position of the cavity mode strongly depends on the thickness of the layer. Therefore, the cavity modes can be shifted by thinning *via* oxidation[30] or reactive ion etching, *via* the deposition of thin dielectric layers, or *via* gas condensation.[32] The post-processing techniques are either time-consuming or require advanced experimental equipment. For example, the latter approach (gas condensation) relies on creating a thin layer of ice on the cavity and it would be therefore complicated to use it in practice. Furthermore, if a set of cavities is prepared on a single chip, each cavity is slightly different from another and thus in the end only one structure is (after suitable postprocessing) usable with the given type of emitter.

Polycrystalline diamond, even though possessing higher optical losses than monocrystalline diamond, provides one important advantage – a relatively low-cost and large-scale fabrication process on various substrates.[35] Furthermore, by employing suitable approaches, nanoresonators[36] and PhC cavities with *Q*-factors comparable to those obtained on monocrystalline diamond have been acquired[20] and coupling of the broad emission of nitrogen vacancy (NV) centers to the cavity mode has been demonstrated.[19] For example, scattering losses can be minimized by smoothing the surface of polycrystalline diamond.[20,37] However, the fabrication process still contains inaccuracies due to the grain-like structure of polycrystalline diamond, which might be a reason why PhC cavities coupled with SiV$^-$ centers have not been demonstrated for polycrystalline diamond so far.

A hybrid approach that combines diamond optical centers and photonic nanostructures prepared on a well-established material from classical photonics may provide an alternative solution.[38,39] For example, recently, an efficient coupling of an ensemble of NV centers to the modes of Si_3N_4-based PhC cavities has been demonstrated.[40] Similarly, plasmonic based nanostructures combined with nanodiamonds present a promising alternative.[41–47] However, from the point of view of integration and practical applications, the all-diamond device remains the most favorable.

In this contribution, we demonstrate a very simple but efficient approach to reach the spectral overlap of the photonic mode of an all-diamond photonic crystal cavity with the zero-phonon line of the negatively charged SiV$^-$ centers without the need for post-processing. A series of regularly distributed air-suspended photonic crystal cavities are prepared into the diamond thin film containing an ensemble of SiV$^-$ centers. The non-homogeneous thickness of the polycrystalline diamond thin film, which is its intrinsic property arising from the fabrication method, serves then as a tool for in-direct spectral fine-tuning of the cavity modes. By looking at the PL spectrum of each cavity, optical modes in spectral resonance with the emitters are identified. Even though such an approach is partially random (the local changes of the thickness cannot be easily measured and only the average thickness is known), it leads to the desired output without the need to employ complicated post-processing. We show by micro-PL measurements that up to 2.5-fold PL intensity enhancement of the zero-phonon emission line of the SiV$^-$ centers can be obtained by coupling the emission into the cavity mode. On such a chip, one has to choose the well-performing structures and realize the experiments on them. The same holds for practical applications where the properly functional cavities could be selectively coupled to the photonic circuits.

2 Results and discussion

Sample design and fabrication

As a proof-of-concept, we have designed a photonic crystal cavity composed of three missing holes in the hexagonal lattice two-dimensional photonic crystal, the so-called L3 cavity. We have tuned the dimensions of the PhC structure such that the SiV$^-$ center zero-phonon emission line would couple to higher order modes of the L3 cavity. As will be shown, these modes are spectrally close to each other (Fig. 2(d)) which simplifies the emission-mode matching. The drawback of these modes compared to the fundamental cavity mode is their lower theoretical *Q*-factor[48] and thus the lower expected Purcell enhancement of the emission. This constrains dimensions of the PhC to a lattice constant of 300 nm, a layer thickness of 190 nm, and a hole diameter of 185 nm.

The fabrication process is in detail described in the Methods section and schematically sketched in Fig. S1 in the ESI.† Briefly, we have fabricated a thin polycrystalline diamond layer (approx. 170–190 nm thick) on a SiO_2 buffer layer (1 μm thick) grown on a Si substrate. The SiV$^-$ centers were incorporated during the growth with homogeneous distribution as verified by scanning the PL from the large area of the sample (not shown). The density of the centers was not estimated; however, it is relatively high based on the fact that the PL is not saturated even with few mW of the excitation power. By combining electron beam lithography and reactive ion etching, a series of PhC cavities within a single diamond layer possessing varying thickness have been created. An overall metallic mask of a selected PhC cavity is shown in Fig. 1(a) with details displayed in Fig. 1(c). Fig. 1(b) shows a SEM image of the PhC cavity after reactive ion etching through the mask. Fig. 1(d) shows details of another PhC cavity. After removing the mask, the diamond layer has been under-etched in buffered HF in order to obtain a slab surrounded by air (Fig. 1e). Clearly, the polycrystalline nature of the diamond causes the surface of the layer to remain rough (surface roughness RMS ≈ 31 nm from AFM measurements).

Enhancement of the SiV$^-$ center emission intensity

The cavity modes can be mapped using a micro-PL setup. In our case, 442 nm laser light was focused *via* an objective on the sample and the PL was collected employing the same objective. We have used objective with high numerical aperture (NA = 0.9) in order to reach high spatial resolution and to

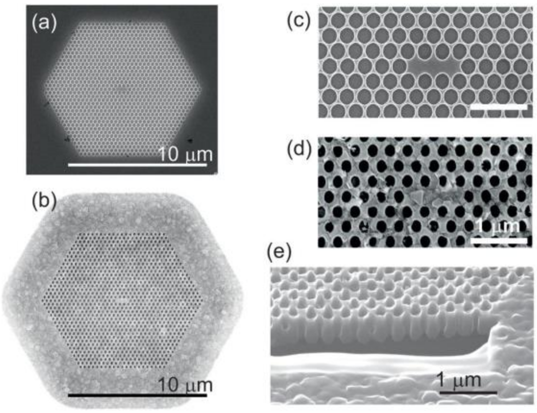

Fig. 1 SEM images of the fabricated photonic crystal cavities. (a) Metallic mask on the diamond layer and (b) the resulting PhC cavity. The photonic crystal is under-etched also around its boundaries giving the contrast in (b). Details of the photonic crystal cavity – (c) metallic mask and (d) the final diamond structure. (e) Angle-view SEM image of the photonic crystal.

collect all the photonic modes overlapping the emission spectrum of polycrystalline diamond.

Fig. 2b shows the room-temperature micro PL spectrum of the selected PhC cavity, the one providing the highest enhancement of the SiV^- center PL with respect to the surrounding PhC structure. Furthermore, the PL spectra of the surrounding PhC structure and the adjacent homogeneous diamond suspended slab are also plotted in Fig. 2b. The zero-phonon line of the SiV^- centers (at 738 nm) superimposed on a broadband luminescence of other diamond defects clearly dominates in the three PL spectra. The PL intensity from the PhC structure is in the whole detected spectral range slightly higher than that of the homogeneous suspended diamond slab due to the concerted action of the PL collection efficiency and the Purcell factor. For a detailed explanation see Fig. S6 in the ESI.† In the PL spectrum of the PhC cavity, we observe a clear cavity mode at around 780 nm and an enhancement of the PL intensity at the emission wavelength of the SiV^- centers. This enhancement is localized around the center of the cavity as evidenced by a PL map of the photonic structure (Fig. 2a). The PL map was measured with a confocal microscope and the emission was focused on the avalanche photodiode *via* a filter transmitting in the range of 740 ± 13 nm. We would like to note that a point with increased intensity occurs also in the right bottom part of the photonic crystal. By closer analysis of the SEM image of the whole photonic crystal structure (see Fig. S2 in the ESI†) we assign this enhancement to the localized mode in a PhC cavity formed by one missing hole (L1-cavity), which was created unintentionally during the fabrication process. Furthermore, the border of the PhC structure has slightly increased PL intensity compared to both the inner part of the PhC and the homogeneous diamond slab due to the additional scattering on the interface of the latter two.

In order to examine the origin of the PL enhancement, we plot the enhancement factor, given as a ratio of the PL intensity measured at the PhC cavity and at the surrounding PhC, as a function of the emission wavelength in Fig. 2d. The obtained enhancement factor can be fitted with multiple Lorentzian functions representing the L3 PhC cavity modes. In order to justify the correctness of this fit, we have performed finite-difference time-domain (FDTD) simulation[49] to identify the spectral position of the cavity modes (Fig. 2d) based on the geometrical parameters from SEM images. Namely, in the fit we have fixed the hole diameter (185 nm) and the lattice constant (300 nm) and varied the diamond thickness in order to reach a spectral overlap between the measured and calculated fundamental mode (e1). The obtained thickness is 185 nm, which corresponds well with the thickness evaluated from reflectance measurements performed on the larger area (not shown) and from the angle-view SEM image of the sample (Fig. 1e). By this approach, also the calculated higher order modes are in very good spectral agreement with the Lorentzian functions fitted to the experimental data. Surface roughness of the polycrystalline layer and structural imperfections of the fabricated photonic structures are the reason for the small discrepancy between the measured and calculated positions of the higher order modes.

The PhC cavity modes can be divided into even (e) and odd (o) modes based on the symmetry of the E_y component of the electric field with respect to the axis going along the cavity. The TE-mode relevant components of the electric and magnetic fields calculated by the FDTD are displayed with their labels in Fig. 2c. We have verified the polarization of the modes by polarization-resolved PL measurements (Fig. S3 in the ESI†).

Table 1 summarizes the Q-factors extracted from the Lorentzian fits of the computed (Q_{theory}) and measured (Q_{exp}) cavity modes. For all the detected modes, the theoretical Q-factor is higher than that obtained by measurements. However, by including optical losses due to absorption (measured on the polycrystalline diamond layer by photothermal deflection spectroscopy[23]) to the theoretical values, we have obtained a very good agreement between the theory and experiment. This indicates that the quality factor of the PhC cavity structure is in our case limited mostly by the intrinsic absorption of the polycrystalline diamond and not by the structural imperfections (tilt of holes, varying diameter or surface roughness).

The spectral and Q-factor agreement between the calculated and measured cavity modes shows that the emission from the SiV^- centers couples to one of the higher-order photonic modes of the PhC cavity and it is subsequently enhanced by a factor of 2.5 (Fig. 3d), which we define as the ratio between the PL intensity measured at the cavity (I_{cav}) to that on the PhC structure (I_{PhC}), *i.e.* $\mathrm{Enh}_{\mathrm{exp}} = I_{\mathrm{cav}}/I_{\mathrm{PhC}}$. The enhancement factor is approximately 3.2 when the air-suspended homogeneous diamond slab is taken for comparison (see Fig. S8 in the ESI†). The difference in the enhancement factors arises mainly from the difference in the collection efficiency and the Purcell factor

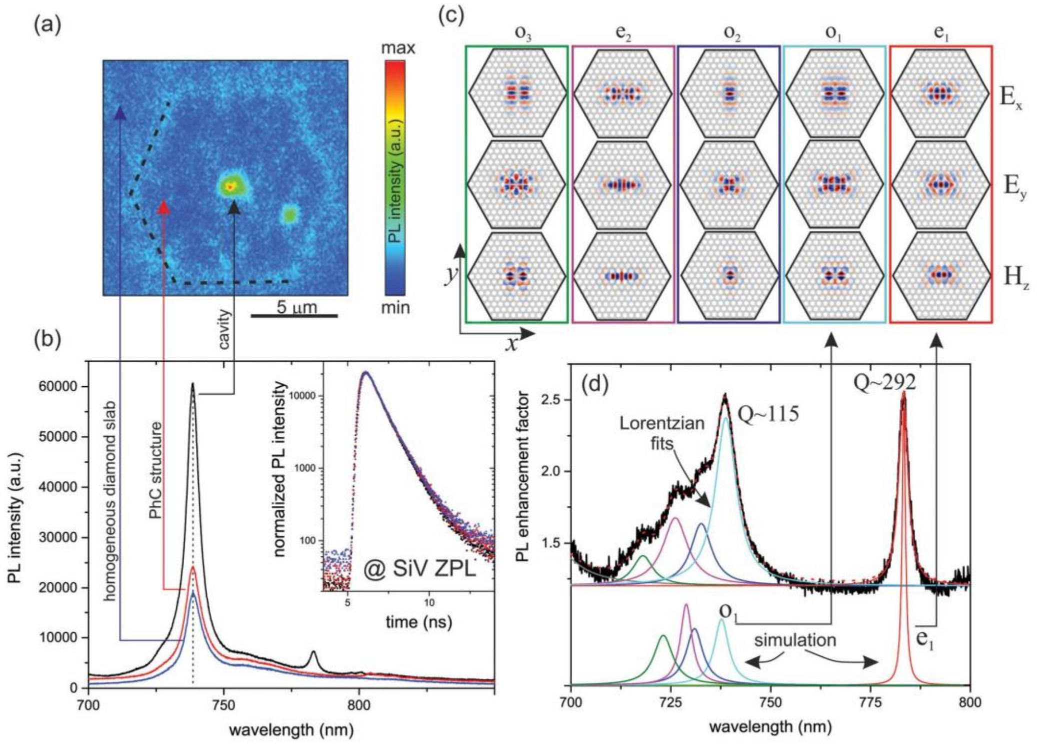

Fig. 2 Photoluminescence of the selected PhC cavity possessing the highest enhancement of the SiV$^-$ center PL emission with respect to the PL spectra of the adjacent periodically patterned PhC slab and with respect to the adjacent homogeneous diamond slab suspended in air. (a) Confocal microscope PL map of the photonic structure measured through a filter transmitting 740 ± 13 nm placed in front of the detector. The dashed line depicts the border of the PhC structure, *i.e.* the interface of the PhC and the homogeneous diamond slab. (b) Micro-PL spectra of the PhC cavity (black curve), the PhC structure (red), and the homogeneous diamond air-suspended slab. The most prominent peak at 738 nm is the emission from SiV$^-$ centers enhanced by the coupling to the higher order photonic crystal cavity modes. The peak at around 780 nm superimposed on the broad PL is a fundamental cavity mode. The inset shows PL decay at 738 nm of the PhC cavity, of the PhC structure, and of the homogeneous diamond slab. (c) In-plane electric field components (E_x, E_y) and vertical magnetic field component (H_z) of the L3 PhC cavity TE modes obtained by the FDTD simulation. (d) Experimental PL enhancement factor given by the ratio of the PL intensity measured at the cavity and at the PhC structure. The enhancement factor is fitted by Lorentzian peaks. Below the fits of the experimental data, cavity modes acquired from FDTD simulation of the PhC cavity are plotted as well.

Table 1 *Q*-Factors of even (e) and odd (o) modes of the PhC cavity. Calculated *Q*-factors for the ideal diamond material (Q_{theory}), *Q*-factors including the losses of 500 cm^{-1} ($Q_{\text{theory+abs}}$) due to absorption measured on the polycrystalline diamond layer (the scattering is not included), and the *Q*-factors exported from the measured spectra (Q_{exp})

Cavity modes	e1	o1	o2	e2	o3
Q_{theory}	759	171	145	219	126
$Q_{\text{theory+abs}}$	252	119	106	142	96
Q_{exp}	292	115	116	96	118

of the respective structures as discussed in the ESI.† The close spectral separation between the higher-order modes causes slight broadening of the SiV$^-$ center PL peak but, on the other hand, simplifies the spectral matching of the cavity mode and the zero-phonon emission line of the SiV$^-$ centers. The fact that the higher-order modes are spectrally close to each other increases the probability of successful coupling to one of these modes.

The theoretical Purcell enhancement factor for a single emitter in a cavity (placed in the maximum of the cavity mode) can be calculated from the measured *Q*-factor of the modes and their theoretical mode volume *V* using the equation

$$F_{\text{cav}} = \frac{3}{4\pi^2}\left(\frac{\lambda}{n}\right)^3\frac{Q}{V}, \tag{1}$$

where the refractive index for our sample is n = 2.33 (obtained from the photothermal deflection spectroscopy experiment[23]). For the mode in resonance with the maximum of the SiV$^-$ center emission (o_1) having the theoretical modal volume $V = 0.67(\lambda/n)^3$ and $Q_{\text{exp}} = 115$, the expected value of $F_{\text{cav}} = 13$. When considering $I_{\text{cav}} \sim F_{\text{cav}}\eta_{\text{cav}}$ ($\eta_{\text{cav}} \approx 0.42$ being the collection efficiency of the o_1 mode with the NA = 0.9 objective) and $I_{\text{PhC}} \sim$

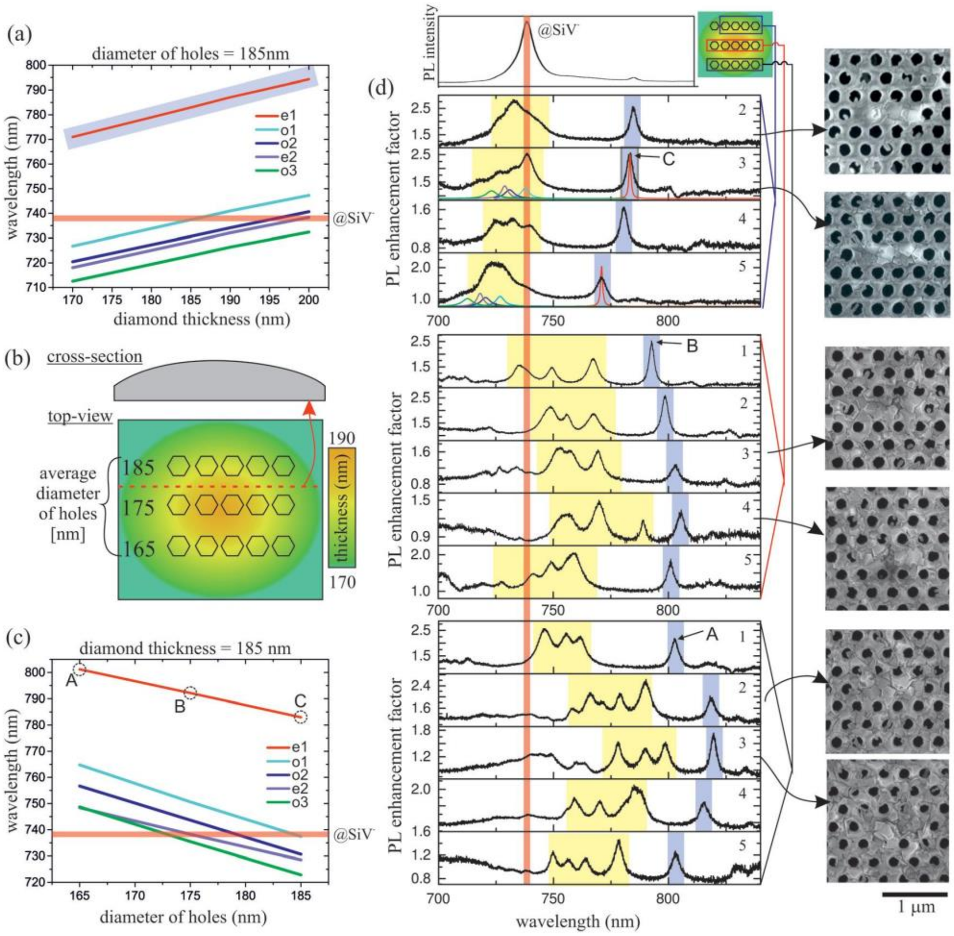

Fig. 3 Tuning of the PhC cavity modes to match the SiV⁻ zero-phonon line (depicted by the red rectangle throughout the image). (a and c) Simulated spectral position of the cavity modes as a function of the diamond thickness for a fixed hole diameter (185 nm) and as a function of the diameter of the holes for a fixed diamond thickness (185 nm), respectively. (b) Schematic cross-section and layout of the sample under study. Each row of PhC cavities is prepared with a different radius of holes. The varying thickness of the pristine diamond layer is color-coded. (d) PL enhancement factors obtained on PhC cavities fabricated on a polycrystalline diamond thin layer in a layout shown in (b). The blue shaded mode is a fundamental cavity mode. The yellow region depicts the higher-order modes and the red shaded area is at the spectral position of the SiV⁻ centers. At the very top of the image, we have also plotted a PL spectrum of the second cavity (cavity no. 2) placed in the first row. In the right part, SEM images of the selected PhC cavities are displayed.

$F_{\mathrm{PhC}}\eta_{\mathrm{PhC}}$ ($F_{\mathrm{PhC}} \approx 0.15$ being the Purcell factor of the PhC and $\eta_{\mathrm{PhC}} \approx 0.39$ being the collection efficiency of the emission from the PhC at the same wavelength), we obtain $\mathrm{Enh}_{\mathrm{theory}} = I_{\mathrm{cav}}/I_{\mathrm{PhC}} \approx 93$. Details on the determination of the F_{PhC} and the collection efficiency can be found in the ESI.† As the optical losses of the polycrystalline diamond (both absorption and scattering) are already included in the value of the experimental Q-factor, the main reason for the lower measured enhancement (2.5) compared to the ideal one (93) is the presence of an ensemble of the SiV⁻ emitters inside of the cavity because the relation for the Purcell factor applies to the emitter in perfect spatial and spectral overlap with the PhC cavity mode.

For the ensemble of emitters within the PhC cavity we define an ensemble-averaged PhC cavity Purcell factor $F_{\mathrm{cav}}^{\mathrm{ensemble}}$. By taking into account the measured enhancement factor of PL on the zero-phonon-line of the SiV⁻ centers, the ensemble-averaged Purcell factor of the fabricated PhC cavity $F_{\mathrm{cav}}^{\mathrm{ensemble}} \approx 0.24$ (see the ESI† for a detailed computation). The $F_{\mathrm{cav}}^{\mathrm{ensemble}}$ depends on the type of emitters within the excitation volume, on their spatial distribution with respect to the cavity mode and on the polarization of the emitted light. It is important to realize that the value of the ensemble-averaged Purcell factor reflects both the properties of the structure and experimental conditions of the measurement. For example, by decreasing the size of the excitation spot and changing its position, the value will change because the spatial overlap of the cavity mode and the excited ensemble will change. The ensemble-averaged PhC cavity Purcell factor being lower than unity was measured also by other groups using the ensemble of SiV^- centers coupled to PhC cavities.[50] In other words, if only a single emitter would be placed into the point of maximum local density of photonic states of the mode, then the ideal value should be reached. However, due to the averaging over the ensemble spatially distributed over the whole cavity, the enhancement is lower than the ideal value.

The inset of Fig. 2b shows that the PL decay of the SiV^- centers measured at the PhC cavity is within the detection error similar to the decay of the SiV^- centers in the PhC and the air-suspended homogeneous diamond slab. A similar effect has also been documented for the ensemble of emitters in monocrystalline diamond.[30] This may seem to be in contradiction with the measured PL intensity enhancement and with the changes in the Purcell factors, however, it has to be stressed that the Purcell factor affects only the radiative rate of the system[51] but the measurement contains the total decay rate including the non-radiative rate. The reported value of the quantum yield of SiV^- centers in polycrystalline diamond is ≈5%,[27] which means that the system decays to a large extent *via* non-radiative channels. As derived in detail in the ESI (section 6†), the 3.6% prolongation of the PL decay time on the PhC with respect to the homogeneous diamond slab is expected based on their Purcell factors. For the PhC cavity and the PhC, the expected shortening of the PL decay is below 1%. Both values are below the resolution of our detection system, which explains the recorded PL decay curves.

In order to put the performance of our photonic structure into perspective, diamond photonic cavities possessing ensembles of SiV^- must be taken into account. In principle a very similar type of structure with the ensemble of SiV^- centers, however, made on monocrystalline diamond using postprocessing is discussed in ref. 30. The measured enhancement factor of PL from the SiV^- centers ensemble provided by our polycrystalline diamond PhC cavity is almost similar (2.5) to the case of monocrystalline diamond (2.8).[30] However, when we take into consideration the collection efficiency and the Purcell factors of the PhC slabs surrounding the cavities in both cases, the cavity structure presented here performs worse by a factor of ≈2 compared to the PhC cavities on monocrystalline diamond presented in ref. 30. Nevertheless, this still presents a remarkable success realizing that the polycrystalline diamond possesses two-orders of magnitude higher optical losses. Furthermore, the lower efficiency is counterbalanced by cheaper and relatively easily up-scalable growth of polycrystalline diamond films. An alternative solution to all-diamond structures could be coupling the SiV^- centers into PhC cavities made from materials that are cheaper and easier to process than diamond.[50] At room-temperature, these hybrid structures possess an approximately three times higher ensemble-averaged Purcell-factor than the all-diamond PhC structures studied in this paper mainly thanks to the high optical quality of the cavity material.[50]

Spectral tuning of the photonic crystal cavity modes

In order to demonstrate our approach of obtaining spectral matching between the PhC cavity modes and the narrow emission line of the SiV^- centers, we have fabricated a series of PhC cavities on a polycrystalline diamond layer. The layout of the sample is shown in Fig. 3(b). Each row contains five L3-PhC cavities being 500 μm apart from each other. The thickness of the layer varies from approximately 170 to 190 nm which gives us a relatively large span for spectral tuning of the cavity modes. Fig. 3(a) shows the calculated dependence of the spectral position of the L3 PhC cavity modes on the thickness of the polycrystalline diamond layer for the first row having a diameter of the holes of ≈185 nm. The second and third rows have L3 PhC cavities with a smaller diameter of the holes, namely 175 and 165 nm, respectively. The motivation behind the fabrication of PhC cavities with a smaller hole diameter was to verify the correctness of the simplified calculations also for the rough-surface polycrystalline diamond, namely that the modes redshift with decreasing the diameter (Fig. 3c).

Fig. 3d shows the experimentally obtained PL enhancement factors on the three rows of PhC cavities. The first cavity in the first row was damaged and thus its spectrum is not plotted. The shift of the cavity modes with the thickness and the diameter can be most easily seen on the fundamental cavity mode (which we highlighted by blue color-filled rectangles in the figure). For the first row of the PhC cavities, it blueshifts from 785 to 770 nm with decreasing the thickness, which is in agreement with the simulation. For the second and third rows of the cavities, the fundamental mode first redshifts and then blueshifts due to slightly different thickness profiles among the rows. The thickness of the polycrystalline diamond layer decreased from the middle to the edges of the sample in the way that is schematically color-coded into the sketch in Fig. 3b. Simultaneously, also the higher order modes blueshift with decreasing the thickness of the layer which tune them into the resonance with the SiV^- zero-phonon line. The best match of the SiV^- center emission line with the cavity modes was obtained for the first row of the PhC cavities, where three out of five L3 PhC cavities provided from 1.2 to 2.5-fold enhancement of the PL intensity due to the Purcell effect.

The limiting factor of using polycrystalline diamond for producing PhC cavities is a certain randomness in the structural quality of the final PhC cavities. SEM images of the representative PhC cavities are shown in Fig. 3(d) and it is clear that some holes are not fully etched due to local inhomogeneities and/or surface roughness. This effect then causes a decrease of performance due to the decreased *Q*-factor of the cavity and modified mode volume. Furthermore, the ratio of the enhancement factors among the modes of the PhC cavity differs from cavity to cavity. This can be seen, for example, in Fig. 3(d): the measured PL enhancement factor at the fundamental mode (e1) is typically similar or even lower to that of the closest higher order mode (o1), even though its theoretical F_p is more than twice higher due to the higher *Q*-factor (see Table 1, the mode volumes are comparable). The local imperfections can even lead to the formation of other photonic modes localized in such defects (see the ESI†) which might be exploited, for example, for decoupling emission from the excited area. However, the spectral position of the fundamental and higher order cavity modes is only marginally affected by the presence of such a defect mode due to the fact that they are localized in the main L3 cavity. Nevertheless, by improving the surface roughness of the polycrystalline diamond layer, the above-discussed effects could be minimized. The strong side of using polycrystalline diamond for PhC cavities is that the properties of the starting material, the thickness of the layer and its surface roughness are reproducible with an error lower than few percent. In total more than 40 cavities were fabricated on 4 polycrystalline diamond samples and ≈20% of the fabricated cavities were in resonance with the zero-phonon-line of the SiV^- centers.

3 Conclusions

In conclusion, we have presented a simple yet efficient approach for reaching spectral overlap between the narrow zero-phonon emission line of the SiV^- centers and the photonic cavity modes. On photonic cavities prepared on polycrystalline diamond, we have obtained 2.5-fold enhancement of the intensity *via* coupling the emission from SiV^- centers into the cavity modes, which is comparable to that obtained on a monocrystalline diamond.[30] Furthermore, by improving the optical and structural quality of the final structures, it is expected that the enhancement can be further improved. We would also like to note that the fabricated PhC cavities are robust toward mechanical vibrations caused by the sample manipulation. Our approach which takes advantage of the non-homogeneous thickness of the polycrystalline diamond layer presents a much cheaper and faster alternative to post-processing techniques used for fine-tuning the photonic structures from monocrystalline diamond. In order to fully exploit this approach for practical applications in quantum photonics, a single-photon emission from polycrystalline diamond has to be demonstrated and also a protocol for matching the emission of multiple devices has to be found.

4 Experimental section

Sample fabrication

The schematic illustration of the PhC cavity fabrication process is shown in Fig. S1 (ESI†). Cleaned Si/SiO_2 substrates (1×1 cm^2) were first nucleated using ultrasonic seeding with diamond nanoparticles (NanoAmando Aqueous Colloid: Dispersed Bucky diamond with a median diamond grain size of 4.8 ± 0.6 nm). A continuous polycrystalline diamond film was grown in a focused microwave plasma enhanced chemical vapour deposition reactor (Aixtron P6). Process parameters used for the deposition process were as follows: 6 kPa, 1% CH_4 in H_2, 3 kW, 700 °C, 2 hours. The main source of Si was a piece of crystalline Si wafer placed near the substrate. After the growth process, the diamond film was treated in oxygen plasma (0.5 mbar, 12 W, 20 seconds) to achieve hydrophilic surface. Next, a thin continuous Al layer (80 nm) was sputtered on the top of the diamond film. The periodic PhC structure containing a cavity in the middle was fabricated employing electron beam lithography on the polycrystalline diamond film coated with an Al layer and a spin-coated (4500 rpm, 20 seconds) electron sensitive polymer layer (ARP 617.06, 200 nm). Through a periodic matrix prepared in the polymer, the Al layer was etched in $SiCl_4/Ar$ plasma (30 W, 5 minutes) using inductively coupled plasma reactive ion etching (Plasmalab System 100, Oxford Plasma Technology). Subsequently the polymer mask was removed in O_2/Ar plasma. The air holes in the diamond film were created through a structured Al mask using capacitively coupled plasma RIE (Phantom LT RIE System, Trion Technology) at 150 mTorr, 100 W, O_2/CF_4 = 45/2 sccm, 18 minutes. After that the Al mask was chemically wet-etched in 2.7% TMAH solution. Finally, the SiO_2 layer was wet-etched through the holes of the photonic structure in the BOE solution (7 : 1 volume ratio of 40% NH_4F in water to 40% HF in water, 15 minutes).

Micro PL measurements

The sample was excited with a HeCd cw laser (442 nm) and the spectrally resolved PL was detected with a silicon CCD camera. The photoluminescence was excited and measured in a direction perpendicular to the sample plane employing a 100× Leica objective with NA = 0.9. The excitation spot diameter was ≈600 nm.

Confocal imaging and decay measurements

We employed a MicroTime200 (PicoQuant) confocal time resolved microscope platform.[52] The sample was excited with 2 μW average power in the diffraction limited confocal observation spot by a 470 nm diode laser through 100× magnification air spaced objective (Olympus, NA = 0.8). The PL was collected in epifluorescence observation mode by the same objective, passed through a 75 μm wide pinhole and detected with a Si-avalanche photodiode (PerkinElmer SPCM-AQR-14) through an optical filter transmitting 740 ± 13 nm (Semrock). Pixel resolution was 533 nm.

Reflectance measurements

The thickness of the diamond layers was evaluated from the interference fringes of the reflectance spectra measured in the UV-VIS-NIR region using commercial software for modeling of the optical properties of thin films (FilmWizard).

Simulations

Photonic crystal cavity modes were analyzed with the MEEP package[49] using the harminv function. The collection efficiency was calculated by integrating the radiation collected by the objective with respect to the overall radiation.

Conflicts of interest

There are no conflicts to declare.

Acknowledgements

This work was supported by the grant GACR 19-14523S and the Operational Programme Research, Development and Education, financed by European Structural and Investment Funds and the Czech Ministry of Education, Youth and Sports (Project No. SOLID21-CZ.02.1.01/0.0/0.0/16_019/0000760). The support of Lumina Quaeruntur fellowship of the Czech Academy of Sciences is also acknowledged.

References

1 I. Aharonovich, D. Englund and M. Toth, *Nat. Photonics*, 2016, **10**, 631–641.
2 J. C. Loredo, N. A. Zakaria, N. Somaschi, C. Anton, L. de Santis, V. Giesz, T. Grange, M. A. Broome, O. Gazzano, G. Coppola, I. Sagnes, A. Lemaitre, A. Auffeves, P. Senellart, M. P. Almeida and A. G. White, *Optica*, 2016, **3**, 433–440.
3 P. Schnauber, A. Singh, J. Schall, S. I. Park, J. D. Song, S. Rodt, K. Srinivasan, S. Reitzenstein and M. Davanco, *Nano Lett.*, 2019, **19**, 7164–7172.
4 I. Aharonovich and E. Neu, *Adv. Opt. Mater.*, 2014, **2**, 911–928.
5 T. van der Sar, Z. H. Wang, M. S. Blok, H. Bernien, T. H. Taminiau, D. M. Toyli, D. A. Lidar, D. D. Awschalom, R. Hanson and V. V. Dobrovitski, *Nature*, 2012, **484**, 82–86.
6 M. Atatüre, D. Englund, N. Vamivakas, S.-Y. Lee and J. Wrachtrup, *Nat. Rev. Mater.*, 2018, **3**, 38–51.
7 D. D. Awschalom, R. Hanson, J. Wrachtrup and B. B. Zhou, *Nat. Photonics*, 2018, **12**, 516–527.
8 T. Schröder, S. L. Mouradian, J. Zheng, M. E. Trusheim, M. Walsh, E. H. Chen, L. Li, I. Bayn and D. Englund, *J. Opt. Soc. Am. B*, 2016, **33**, B65–B83.
9 S. Castelletto, L. Rosa, J. Blackledge, M. Z. A. Abri and A. Boretti, *Microsyst. Nanoeng.*, 2017, **3**, 1–16.
10 I. Aharonovich, A. D. Greentree and S. Prawer, *Nat. Photonics*, 2011, **5**, 397–405.
11 B. A. Fairchild, P. Olivero, S. Rubanov, A. D. Greentree, F. Waldermann, R. A. Taylor, I. Walmsley, J. M. Smith, S. Huntington, B. C. Gibson, D. N. Jamieson and S. Prawer, *Adv. Mater.*, 2008, **20**, 4793–4798.
12 M. P. Hiscocks, K. Ganesan, B. C. Gibson, S. T. Huntington, F. Ladouceur and S. Prawer, *Opt. Express*, 2008, **16**, 19512–19519.
13 B. J. M. Hausmann, B. Shields, Q. Quan, P. Maletinsky, M. McCutcheon, J. T. Choy, T. M. Babinec, A. Kubanek, A. Yacoby, M. D. Lukin and M. Lončar, *Nano Lett.*, 2012, **12**, 1578–1582.
14 B. J. M. Hausmann, B. J. Shields, Q. Quan, Y. Chu, N. P. de Leon, R. Evans, M. J. Burek, A. S. Zibrov, M. Markham, D. J. Twitchen, H. Park, M. D. Lukin and M. Loncar, *Nano Lett.*, 2013, **13**, 5791–5796.
15 M. J. Burek, Y. Chu, M. S. Z. Liddy, P. Patel, J. Rochman, S. Meesala, W. Hong, Q. Quan, M. D. Lukin and M. Lončar, *Nat. Commun.*, 2014, **5**, 5718.
16 S. Mouradian, N. H. Wan, T. Schröder and D. Englund, *Appl. Phys. Lett.*, 2017, **111**, 021103.
17 N. H. Wan, S. Mouradian and D. Englund, *Appl. Phys. Lett.*, 2018, **112**, 141102.
18 C. Dory, D. Vercruysse, K. Y. Yang, N. V. Sapra, A. E. Rugar, S. Sun, D. M. Lukin, A. Y. Piggott, J. L. Zhang, M. Radulaski, K. G. Lagoudakis, L. Su and J. Vučković, *Nat. Commun.*, 2019, **10**, 3309.
19 C. F. Wang, R. Hanson, D. D. Awschalom, E. L. Hu, T. Feygelson, J. Yang and J. E. Butler, *Appl. Phys. Lett.*, 2007, **91**, 201112.
20 X. Checoury, D. Neel, P. Boucaud, C. Gesset, H. Girard, S. Saada and P. Bergonzo, *Appl. Phys. Lett.*, 2012, **101**, 171115.
21 L. Ondič, M. Varga, K. Hruška, J. Fait and P. Kapusta, *ACS Nano*, 2017, **11**, 2972–2981.
22 N. Felgen, B. Naydenov, F. Jelezko, J. P. Reithmaier and C. Popov, *Phys. Status Solidi A*, 2018, **215**, 1800371.
23 J. Fait, M. Varga, K. Hruška, Z. Remeš, V. Jurka, A. Kromka, B. Rezek and L. Ondič, *Nanophotonics*, 2019, **8**, 1041.
24 E. M. Purcell, *Phys. Rev.*, 1946, **69**, 681.
25 J. P. Goss, R. Jones, S. J. Breuer, P. R. Briddon and S. Öberg, *Phys. Rev. Lett.*, 1996, **77**, 3041–3044.
26 L. Rogers, K. Jahnke, T. Teraji, L. Marseglia, C. Müller, B. Naydenov, H. Schauffert, C. Kranz, J. Isoya, L. McGuinness and F. Jelezko, *Nat. Commun.*, 2014, **5**, 4739.
27 A. V. Turukhin, C.-H. Liu, A. A. Gorokhovsky, R. R. Alfano and W. Phillips, *Phys. Rev. B: Condens. Matter Mater. Phys.*, 1996, **54**, 16448–16451.
28 E. Neu, M. Agio and C. Becher, *Opt. Express*, 2012, **20**, 19956–19971.
29 A. Sipahigil, K. Jahnke, L. Rogers, T. Teraji, J. Isoya, A. Zibrov, F. Jelezko and M. Lukin, *Phys. Rev. Lett.*, 2014, **113**, 113602.
30 J. Riedrich-Möller, L. Kipfstuhl, C. Hepp, E. Neu, C. Pauly, F. Mücklich, A. Baur, M. Wandt, S. Wolff, M. Fischer, S. Gsell, M. Schreck and C. Becher, *Nat. Nanotechnol.*, 2012, **7**, 69–74.
31 J. Riedrich-Möller, C. Arend, C. Pauly, F. Mücklich, M. Fischer, S. Gsell, M. Schreck and C. Becher, *Nano Lett.*, 2014, **14**, 5281–5287.
32 J. L. Zhang, S. Sun, M. J. Burek, C. Dory, Y.-K. Tzeng, K. A. Fischer, Y. Kelaita, K. G. Lagoudakis, M. Radulaski, Z.-X. Shen, N. A. Melosh, S. Chu, M. Lončar and J. Vučković, *Nano Lett.*, 2018, **18**, 1360–1365.
33 M. Schatzl, F. Hackl, M. Glaser, P. Rauter, M. Brehm, L. Spindlberger, A. Simbula, M. Galli, T. Fromherz and F. Schäffler, *ACS Photonics*, 2017, **4**, 665–673.
34 S. Kim, J. E. Fröch, J. Christian, M. Straw, J. Bishop, D. Totonjian, K. Watanabe, T. Taniguchi, M. Toth and I. Aharonovich, *Nat. Commun.*, 2018, **9**, 2623.

35 O. Williams, *Diamond Relat. Mater.*, 2011, **20**, 621–640.

36 A. F. Sartori, P. Belardinelli, R. J. Dolleman, P. G. Steeneken, M. K. Ghatkesar and J. G. Buijnsters, *Small*, 2019, **15**, 1803774.

37 J. Heupel, N. Felgen, R. Merz, M. Kopnarski, J. P. Reithmaier and C. Popov, *Phys. Status Solidi A*, 2019, 1900314.

38 J. Wolters, A. W. Schell, G. Kewes, N. Nüsse, M. Schoengen, H. Döscher, T. Hannappel, B. Löchel, M. Barth and O. Benson, *Appl. Phys. Lett.*, 2010, **97**, 141108.

39 D. Englund, B. Shields, K. Rivoire, F. Hatami, J. Vučković, H. Park and M. D. Lukin, *Nano Lett.*, 2010, **10**, 3922–3926.

40 K. G. Fehler, A. P. Ovvyan, N. Gruhler, W. H. P. Pernice and A. Kubanek, *ACS Nano*, 2019, **13**, 6891–6898.

41 A. W. Schell, G. Kewes, T. Hanke, A. Leitenstorfer, R. Bratschitsch, O. Benson and T. Aichele, *Opt. Express*, 2011, **19**, 7914–7920.

42 A. Huck, S. Kumar, A. Shakoor and U. L. Andersen, *Phys. Rev. Lett.*, 2011, **106**, 096801.

43 N. P. de Leon, B. J. Shields, C. L. Yu, D. E. Englund, A. V. Akimov, M. D. Lukin and H. Park, *Phys. Rev. Lett.*, 2012, **108**, 226803.

44 R. Kolesov, B. Grotz, G. Balasubramanian, R. J. Stöhr, A. A. L. Nicolet, P. R. Hemmer, F. Jelezko and J. Wrachtrup, *Nat. Phys.*, 2009, **5**, 470–474.

45 J. T. Choy, B. J. M. Hausmann, T. M. Babinec, I. Bulu, M. Khan, P. Maletinsky, A. Yacoby and M. Lončar, *Nat. Photonics*, 2011, **5**, 738–743.

46 H. Siampour, S. Kumar and S. I. Bozhevolnyi, *ACS Photonics*, 2017, **4**, 1879–1884.

47 H. Siampour, S. Kumar, V. A. Davydov, L. F. Kulikova, V. N. Agafonov and S. I. Bozhevolnyi, *Light: Sci. Appl.*, 2018, **7**, 1–9.

48 A. R. A. Chalcraft, S. Lam, D. O'Brien, T. F. Krauss, M. Sahin, D. Szymanski, D. Sanvitto, R. Oulton, M. S. Skolnick, A. M. Fox, D. M. Whittaker, H.-Y. Liu and M. Hopkinson, *Appl. Phys. Lett.*, 2007, **90**, 241117.

49 A. F. Oskooi, D. Roundy, M. Ibanescu, P. Bermel, J. D. Joannopoulos and S. G. Johnson, *Comput. Phys. Commun.*, 2010, **181**, 687–702.

50 K. G. Fehler, A. P. Ovvyan, L. Antoniuk, N. Lettner, N. Gruhler, V. A. Davydov, V. N. Agafonov, W. H. P. Pernice and A. Kubanek, 2019, *arXiv:1910.06114 [cond-mat, physics: quant-ph]*.

51 M. Pelton, *Nat. Photonics*, 2015, **9**, 427–435.

52 F. Koberling, M. Wahl, M. Patting, H.-J. Rahn, P. Kapusta and R. Erdmann, *Proc. of SPIE: Novel Optical Instrumentation for Biomedical Applications*, 2003, vol. 5143, pp. 181–192.

Memorandum
optica

High finesse telecom O-band microcavities

Jan Fait,[1,2,3,†] Stefan Putz,[1,†] Georg Wachter,[1] Johannes Schalko[4], Ulrich Schmid[4], Markus Arndt[1], and Michael Trupke[1,*]

[1]*Vienna Center for Quantum Science and Technology, Universität Wien, Boltzmanngasse 5, 1090 Vienna, Austria*
[2]*Institute of Physics, Academy of Sciences of the Czech Republic, Cukrovarnická 10, 162 00 Prague, Czech Republic*
[3]*Czech Technical University in Prague, Faculty of Electrical Engineering, Technická 2, 166 27 Prague, Czech Republic*
[4]*Institute of Sensor and Actuator Systems, TU Wien, Gußhausstr. 27-29, 1040 Vienna, Austria*
*†These authors contributed equally to this work *Correspondence should be sent to: michael.trupke@univie.ac.at*

Received XX Month XXXX; revised XX Month, XXXX; accepted XX Month XXXX; posted XX Month XXXX (Doc. ID XXXXX); published XX Month XXXX

We report on a scalable, open-access optical microcavity platform which significantly exceeds the highest optical enhancement factors achieved to date. These devices will boost the performance of light-matter interaction in quantum science and technology.
http://dx.doi.org/10.1364/optica.99.099999

The confinement of the electromagnetic field inside a small volume is key in building devices with high quantum efficiency, by enhancing the interaction strength between photons and qubits. For instance, cavities can increase the single-photon count rate from an emitter due to the Purcell effect [1]. More generally, such strong confinement enables interactions of light and atoms in cavity quantum electrodynamics (CQED) [2], or with dielectric particles in cavity quantum optomechanics [3].

There are many types of optical resonators, such as Fabry-Perot (FP), micro-sphere, micro-disc or photonic crystal cavities, that can be used to enhance light-matter interactions [4]. Regardless of the cavity type, the mode volume (V) is a significant design parameter. The advantage of FP cavities is their fast tuneability by changing the mirror spacing L, which can be achieved in a scalable manner [5]. However, the mode volume of FP resonators is usually larger when compared to micro-disc or photonic crystal cavities. We report on our progress on building a scalable architecture for open-access FP micro-cavities with high finesse and exceedingly small mode volumes. To the best of our knowledge, the reported $Q/(V/\lambda^3) \approx 1.8 \times 10^5$ value exceeds the performance of all open-access optical microcavities to date [6-8].

Our microcavity mirrors are coated for high performance in the telecom O-band (1.26 - 1.36 μm). We have chosen this band since several promising emitters exist which are optically active in this regime, among which are the vanadium (V) center in silicon carbide (SiC) [9,10] and the G center in Si [11,12]. SiC and Si are stable host environments and offer superb optical properties. They are therefore prime candidates for implementation in long range quantum communication networks.

Dissipation due to surface roughness, diffraction or absorption inside the cavity must be reduced to achieve high performance in any optical resonator. Two important figures of merit are the finesse $\mathcal{F} = FSR/\Delta\nu$ and the quality factor $Q = \nu_r/\Delta\nu$ with the resonance frequency ν_r, the FWHM linewidth $\Delta\nu$ and the free spectral range FSR of the cavity. The finesse is proportional to the number of roundtrips before a photon leaves the cavity or is lost via dissipation, while the Q factor is the average number of optical cycles before a photon is lost from the cavity.

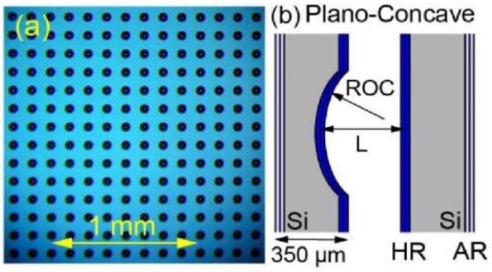

Figure 1. (a) Microscope image of the coated Si chip showing the micro mirrors on a 125 µm grid (b), Schematic of a PC microcavity.

In the paraxial approximation, the mirror spacing L and the radius of curvature R of the mirrors determine the mode properties of the resonator. The beam waist w_0 defines the mode volume V given by:

$$\boldsymbol{V = \frac{\pi}{4} w_0^2 L} \text{ with } \boldsymbol{w_0 = \sqrt{\frac{\lambda}{\pi\alpha}\sqrt{\alpha\, R\, L - L^2}}}, \qquad (1)$$

with the wavelength λ and $\alpha = \{1,2\}$ for plano-concave (PC) and concave-concave (CC) cavities, respectively [13]. With the Rayleigh range $z_r = \pi w_0^2/\lambda$, R is given by $R = z[1 + (z_r/z)^2]$. We collect several of these terms in the optical enhancement $\Upsilon = (Q/V)\,(\lambda/n)^3$, with n the refractive index of the medium. This term is a key quantity in the interaction of nanoparticles, atoms, or molecules with light. It is also central to the Purcell enhancement $P = 3\Upsilon\eta/4\pi^2$ where η is the branching ratio of the relevant two-level transition.

Short cavities with a small beam waist naturally require a small R, which is challenging to fabricate with high precision. Our micro-mirrors were fabricated from four-inch silicon wafer substrates by a two-step dry etching process (see Ref [8] for details). The structured substrate is diced into chips of $3 \times 3\ \mathrm{mm}^2$ which host hundreds of mirrors spaced on a 125 µm grid (see Figure 1). The Si chips are coated with a dielectric high-reflectivity Bragg multi-layer coating with $L_{\mathrm{in}} = L_{\mathrm{out}}$ =5 ppm transmissivity (at 1280 nm) giving a theoretical limit of $\mathcal{F} \leq 6.3 \times 10^5$. The backside of the Si chips is coated with a corresponding anti-reflection layer. To characterize the cavities, we used a tunable narrow bandwidth laser source (EXFO T100S-HP). The laser light is coupled into the cavities in free space and the reflected laser light was separated by a fiber circulator and detected by a high-bandwidth photodiode. The mirror shape was determined by a white light interferometer (Filmetrics Profilm 3D) to extract *R*.

The shortest cavities are assembled in a PC configuration by gluing two mirror chips together. The length of each cavity is fixed, but in order to vary the resonance frequency of the cavities across the array, a spacer with ≈ 16 µm thickness was inserted between the Si chips on one side, forming a narrow wedge with ≈ 0.3 degrees tilt. The curved mirrors have $R = (63 \pm 4)$ µm and the depth of the mirrors is ≈ 4.5 µm. The cavities are characterized by scanning the laser wavelength over a broad range and recording the position and spectral distance between fundamental and higher order modes. The *FSR* for such short cavities could not be observed directly as it exceeds the wavelength range of the laser. Instead, we determined the cavity length from the spectral position of fundamental and higher order modes (see Figure 2a), and from *R*. The radius of curvature is related to the cavity length *L* by:

$$\boldsymbol{L} = \boldsymbol{R}\left(\boldsymbol{1} - \left[\cos\left(\frac{\boldsymbol{1}}{\boldsymbol{p}+\boldsymbol{q}}\Delta\boldsymbol{\nu}_{\boldsymbol{p}+\boldsymbol{q}}\frac{\boldsymbol{2L\pi}}{\boldsymbol{c}}\right)\right]^{\boldsymbol{2}}\right), \qquad (2)$$

where (*p,q*) is the Hermite-Gaussian beam order, $\Delta\nu_{00\leftrightarrow p,q}$ is the frequency difference between $\mathrm{TEM}_{0,0}$ and $\mathrm{TEM}_{p,q}$ Gaussian mode, and *c* is the speed of light [8]. With Equation (2) the calculated length of the shortest cavity that supported a $\mathrm{TEM}_{0,0}$ mode at 1275.7 nm and a mode with $p + q = 1$ at 1263.5 nm was (7.4 ± 0.5) µm, which corresponds to $FSR = c/2L = (20.3 \pm 1.4)$ THz (see Figure 2a). Hence the mode volume is $V = (23 \pm 1.4)\ \lambda^3$. Note that the field mode also extends into the Bragg coating for $0.8\ \lambda \approx 1$ µm [14].

The cavity linewidth was measured by scanning the probe laser over the cavity resonance while a 200 MHz sideband modulation was applied, and the observed linewidth is compared with the known splitting of the sidebands (see Figure 2b). The highest observed cavity finesse for the shortest possible cavities was $\mathcal{F} \approx 350{,}000$ which corresponds to a roundtrip loss of 18 ppm. The excess dissipation of ≈ 8 ppm could arise due to slight distortions of the curved mirror shape, or from scattering losses due to surface roughness (see Table 1: "PC-f").

We also assembled cavities with variable mirror spacing L by mounting one of the mirrors on a piezoelectric actuator, enabling rapid tuning of the resonance frequency. For this setup we measured PC and CC cavity configurations with $L \geq 15$ µm. Longer cavities allowed to measure the $FSR = 9.3$ THz directly. We found good agreement between the *L* obtained via the FSR and the value computed using Eq. (3). For the actuated cavities we used mirrors with larger $R \approx 100$ µm with a mirror depth of 8.5 µm, giving a spacing between the mirror chips of 6 µm. This configuration reaches $\mathcal{F} = 490{,}000$ (see Table 1: PC-a and CC-a).

In conclusion, we have built small volume, high finesse optical Fabry-Perot cavities for the telecom O-band at 1280 nm wavelength. These cavities are suitable for enhancement of photon count rates from vanadium in silicon carbide or G centers in silicon. The extracted optical enhancement value reaches $\Upsilon = 1.8 \times 10^5$, almost three times larger than other types of open-access microcavities [7,8]. This improvement is highly desirable for spin-photon interfaces, cavity cooling of nanoparticles, and other applications requiring extreme enhancement of the interaction of light with matter.

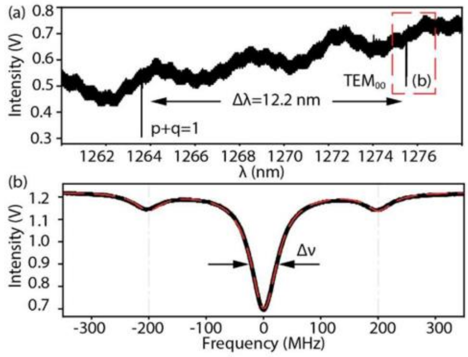

Figure 2. Spectra for "PC-f" (see Table 1) (a) fundamental TEM_{00} mode and one higher order mode. (b) resonance at $\lambda = 1276$ nm with sideband modulation of 200 MHz (black dots). FWHM linewidth of $\Delta\nu = (58 \pm 2)$ MHz is extracted by a Lorentzian fit (red dashed line).

Table 1. Comparison of selected cavity assemblies

type	λ (nm)	*R* (µm)	*L* (µm)	*V* (λ^3)	$\mathcal{F}$ (/10^3)
PC-f	1276	63±4	7.4±0.5	23±1.4	350±30
PC-a	1280	109±1	16.9±0.1	102±1.4	490±90
CC-a	1280	100±1	25.4±0.1	129±1.4	180±10

Funding. J.F.: GACR (19-14523S), OeAD-GmbH (Aktion Österreich-Tschechien program, ICM-2019-13725); S.P.: Marie Skłodowska-Curie Action through the Erwin Schrödinger Quantum Fellowship Program (No 801110). M. T.: FWF projects I 3167-N27 and P 27297-N27, EU FET-Open 862721QuanTELCO.

Disclosures. The authors declare no conflicts of interest.

REFERENCES

1. E. Purcell, Phys. Rev. **69**, 681 (1946)
2. R.J. Thompson, Phys. Rev. Lett. **68**, 1132 (1992)
3. U. Delic, Science **367** 892-895 (2020)
4. K. J. Vahala, Nature **424**, 839-846 (2003)
5. C. Derntl, Optics express 22 (18), 22111-22120 (2014)
6. K. M. Birnbaum et al. Nature **436**, 87–90 (2005)
7. D. Najer et al. Appl. Phys. Lett. **110**, 011101 (2017)
8. G. Wachter et al., Light Sci. Appl. **8** (2019)
9. L. Spindelberger et al., Phys. Rev. Appl. **12** (2019)
10. G. Wolfowicz Science Advances 6 (18), eaaz1192 (2020)
11. C. Beaufils et al., Phys. Rev. B **97** (2018)
12. C. Chartrand Phys. Rev. B **98**, 195201 (2018)
13. A. Muller et al., Opt.Lett. **35** (2010)
14. C. J. Hood et al., Phys. Rev. A **64** (2001)

Applied Surface Science 428 (2018) 1159–1165

Contents lists available at ScienceDirect

Applied Surface Science

journal homepage: www.elsevier.com/locate/apsusc

Full Length Article

Complex nano-patterning of structural, optical, electrical and electron emission properties of amorphous silicon thin films by scanning probe

Jan Fait[a,b,*], Jan Čermák[a], Jiří Stuchlík[a], Bohuslav Rezek[a,b]

[a] *Institute of Physics, The Czech Academy of Sciences, Cukrovarnická 10, 16200 Prague, Czech Republic*
[b] *Faculty of Electrical Engineering, Czech Technical University in Prague, Technická 27, 16627 Prague, Czech Republic*

ARTICLE INFO

Article history:
Received 25 May 2017
Received in revised form 1 September 2017
Accepted 26 September 2017
Available online 28 September 2017

Keywords:
Amorphous silicon
Nano-templates
Nanostructures
Electrical conductivity
Electron emission
Atomic force microscopy

ABSTRACT

Preparation of nanoscale templates represents an important step for synthesis and assembly of diverse nanostructures and nanoscale devices. We show that complex nano-structural templates in a thin (40 nm) layer of hydrogenated amorphous silicon (a-Si:H) can be prepared by using locally applied electric field in an atomic force microscope (AFM). Depth of the resulting structures (1–40 nm) can be controlled by the process parameters (magnitude of electric field, exposure time, or nano-sweeping of the tip). We demonstrate that complex patterns can be scribed into the a-Si:H layer in that way. The prepared patterns exhibit different structural, optical, electrical, and electron emission properties, compared to the surroundings as detected by Raman micro-spectroscopy, scanning electron microscopy (SEM), and conductive AFM. The silicon thin films with locally modified properties can be useful in themselves or can serve as templates for further nanoscale growth or assembly.

1. Introduction

Preparation of nanoscale templates represents an important step in many methods which use bottom-up approach for controlled synthesis of nanomaterials, formation of nanostructures, or guided assembly of whole nanoscale devices for prospective applications in electronics, plasmonics, photonics, energy sources as well as biosensors [1]. Such function can be predefined by natural substrate features (such as step-edges or dimer rows) or induced by substrate modification on a microscopic level. Diverse types of the substrate modification such as structural [2–5], chemical [6,7], electrostatic [8,9], or their combinations can be utilized as nano-templates.

There is a broad range of techniques and materials for creating the structural templates. The most established method is optical lithography using shadow masks or direct laser writing to modify photoresist properties. This method can be used also in an innovative way for direct modification or assembly. For instance, laser assisted corrosion of aluminum [10] can be used for preparation of various patterns in a thin aluminum layer [11]. Structured illumination can be used for modification of electrode conductivity and thereby for electrophoretic deposition of nano-particle patterns [12].

However, optical techniques working in the visible spectral range are not capable of creating structures significantly smaller than the wavelength of light. Using the radiation with shorter wavelengths (UV, XUV, X-ray) or electrons instead is possible but it makes the creation of nano-structures more complicated and expensive. Therefore, nanotechnology techniques have emerged that use self-organized template structures, e. g. nanosphere lithography [13,14] or porous alumina templates [15,16]. These techniques are inexpensive and capable of creating large area (square centimeters [17]) nano-templates. However, only limited types of pattern shapes [18,19] and dimensions (mostly with the hexagonal structure) can be prepared using the self-organization techniques.

Local anodic oxidation [20] represents another group of methods in which scanning probe microscopy is employed for localized microscopic modification of a substrate [21–23]. Oxidation of the substrate is achieved by applying voltage (negative polarity on the tip) on the scanning tip in form of a sharp needle or atomic force microscopy (AFM) probes. Oxidized features can then, for instance, act as insulating patterns around transistor structures in GaAs [24] or diamond [25,26], or they can control selective assembly of metal nano-dots on silicon due to differences in sticking coefficient and wettability [27]. Another AFM-based technique was introduced for

---

* Corresponding author at: Institute of Physics, The Czech Academy of Sciences, Cukrovarnická 10, 16200 Prague, Czech Republic.
E-mail address: fait@fzu.cz (J. Fait).

https://doi.org/10.1016/j.apsusc.2017.09.228
0169-4332/

producing nanostructures in a thin layer of hydrogenated amorphous silicon (a-Si:H) [5].

Thin layers of a-Si:H have been of particular interest in the recent decades. Due to the lack of long-range crystal periodicity, the band structure is modified compared to crystalline silicon. That leads to many applications in photoluminescence [28], photovoltaics [29,30], electronics, and others [31]. Amorphous silicon is usually prepared in the form of thin layers by chemical vapor deposition (CVD).

When a-Si:H temperature is heated over 600 °C, the material starts to crystallize. Presence of some metals (nickel, chrome, or palladium) can reduce the crystallization temperature [32,33]. Moreover, if an electric field is additionally applied the crystallization can occur even at room temperature by the so-called field-enhanced metal-induced solid phase crystallization (FE-MISPC) [34,35].

By using a similar process to FE-MISPC, nano- or micro-pits can be prepared in the thin film of a-Si:H [36]. Preparation of pits in a-Si:H layers with thickness above 170 nm was investigated by using specialized electronic circuitry [37]. Conductive (crystallized silicon) or non-conductive pits were formed in such layers depending on the parameters used. Both types of pits were further used as templates for growth of localized silicon nano-crystals [5]. Such direct structuring of a-Si:H films thus avoided multistep lithography process including typically the use of resist layers, shadow masks, and wet or dry etching.

In this work, we build upon this phenomenon further and present a way for preparation of complex, large area nano-patterned templates in a thin layer of amorphous silicon by using a simple single-step technology utilizing AFM. We identify several crucial factors for achieving reliable and well reproducible process: i) thin enough layer of amorphous silicon (40 nm), ii) nano-sweeping of the tip (local modulation of the tip position) during the process, iii) parameter window of electrical current amplitude and exposure time. Furthermore, by using optical microscopy, Raman micro-spectroscopy, scanning electron microscopy (SEM), and conductive AFM, we show that the process gives rise to local modification of not only structural but also optical (Raman scattering) and electronic (electron emission and conductivity) properties of the exposed places while not changing the amorphous character of the thin film.

2. Experimental

Glass (Corning 7059) or monocrystalline silicon wafers were used as substrates. Nickel film (thickness 40 nm) with titanium adhesion layer (10 nm) was deposited on the substrates using vacuum thermal evaporation. Subsequently, thin layers of a-Si:H (thickness 40 nm ± 5 nm) were deposited on the Ni-coated substrates by plasma-enhanced CVD. High hydrogen content in the layers (20–45 at.%) was achieved by using 0.02 % of SiH_4 (1 sccm) diluted in helium (5000 sccm), and low temperature (50 °C) of the CVD process. Some samples were made with Pt electrode (40 nm again) instead of Ni in order to find out whether the role of nickel is crucial for the pit formation.

The fabrication of nano-structures was done by atomic force microscope (AFM; Veeco DI3100 IV) in contact mode equipped with metal coated silicon tips (ContE-G, BudgetSensors, force constant 0.2 N/m). Constant electrical current (0.5–15 nA) was locally applied to the sample using the Ni film (negative polarity) and the AFM tip as electrodes (see Fig. 1). External unit (Keithley K237) was used as a current source as well as a voltage monitor. Using the constant current regime is preferable due to better control over the process [36].

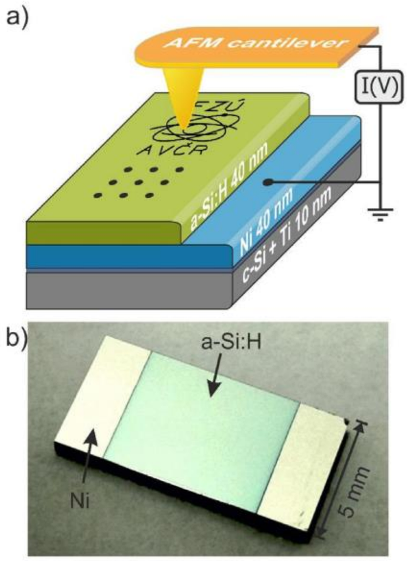

Fig. 1. (a) Schematic drawing of the experimental setup. (b) Photography of the sample.

In the first employed method, nano-pits were created by the AFM tip which was not moving during the exposition. Exposure time was in the range of 10–30 s. In the second method, the tip was sweeping across the sample during the process, i.e. its position was laterally modulated. The amplitude of the sweeping was in the range of 0 nm (corresponding to static regime) to 300 nm and the frequency in the range of 0 Hz (corresponding to static regime) to 0.5 Hz. Tip velocity may be calculated from these parameters. In the third method, complex movements of the tip across the surface of sample were employed to draw line art patterns. The parameters were chosen based on prior optimization measurements. Larger current (at least 8 nA) was needed for continuous drawings. In addition, depth and width of the structures depended on the tip velocity. Note that scanning the tip in a raster (bitmap) pattern turned out to be less precise and more time consuming. Thus it was not further investigated.

The morphology of nano-structures was characterized using AFM in contact mode with the same tip which had been used for their preparation before. Conductive AFM (with a new metal coated tip) was used to measure local conductivity map of the samples when biased by a constant voltage. Furthermore, some nano-structures were re-measured with different tip in tapping mode to improve image clarity. The dependence of the size of the pits on different parameters during the process (especially the current magnitude and the exposure time as well as tip wear and sample-tip force) were investigated.

Material and chemical composition of the exposed places was determined by Raman micro-spectroscopy (Horiba XploRA, excitation wavelength 532 nm, objective 100x, Raman resolution <1 μm). Changes of optical properties were characterized in reflected light by bright field optical microscope images using 100 x objective and Xe lamp illumination. Scanning electron microscopy (SEM, Tescan Maia3) was used to measure morphology complementary to AFM and also to characterize changes of secondary electron emission using an in-beam detector.

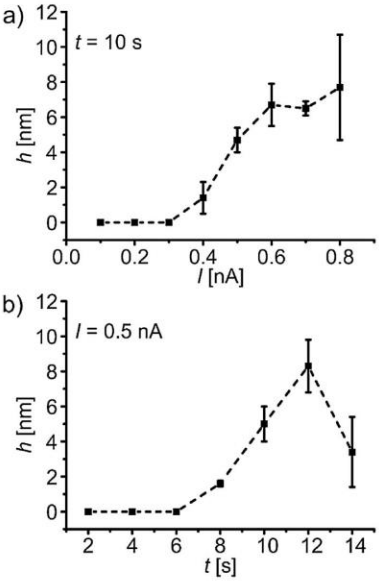

Fig. 2. Depth of the structure (pit) h as a function of: (a) the electric current magnitude I (at the fixed 10 s exposure); (b) the exposure time t (at the fixed current of 0.5 nA) for static method. Each data point was evaluated as an average value of three single pits – error bars show standard deviation of arithmetic mean. The connecting lines are guide for eye.

3. Results

Fig. 2 shows the typical resulting depth of the structure (pit) created by the static method, where the tip was not moving during the exposition, as a function of exposure time and current. As a function of the current (at the fixed 10 s exposure), the depth of the pits remained zero until a threshold current of about 0.4 nA was reached. Then the pit depth quickly increased and saturated above 0.6 nA. As function of the exposure time (at the fixed current of 0.5 nA), the depth of the pits remained zero until a threshold time of about 8 s was reached. Then the pit depth quickly increased up to 12 s and dropped for longer times.

The maximum depth of the pits achieved by the static method was around 10 nm. Lateral diameter of the pits was in the range of few hundreds of nanometers. The depth and diameter of the pits did not depend on a force between tip and sample (at least in the range of 20–60 nN). The force during the process was adjusted by the deflection setpoint of AFM.

Note that voltage, supplied to keep the constant current, increased gradually during the pit creation. Then for lower currents the voltage saturated (~15 V for 0.3 nA; ~50 V for 0.5 nA). On the other hand, for larger currents (>0.8 nA) the voltage dropped to zero if certain value (usually between 80 V–120 V) was reached. The process was not fully controllable in such case and large craters with diameter >1 μm were created. Similar behavior was observed before [36] and it was attributed to current surges due to discharging parallel capacitance when voltage becomes lower as conductive path is formed.

When sweeping was utilized during the process, deeper pits were created. Fig. 3(a–c) shows dependence of the depth of pits on current magnitude and exposure time. In Fig. 3(a) the pits with lower current were prepared first and in Fig. 3(b) the other way round. The sweeping amplitude was fixed at 100 nm and the sweeping frequency at 0.3 Hz. These parameters were chosen by exploring dependence of the pit depth on the sweep amplitude and frequency. The data are shown in the Supplementary information (see Fig. S-1 in the Supporting information).

For the sweeping tip, currents lower than typically 0.5 nA did not create pits at all. Thus the threshold is somewhat higher than for the static method above. The depth of the pits tends to increase within the range 0.5–1.5 nA. Currents >4 nA led again to creation of

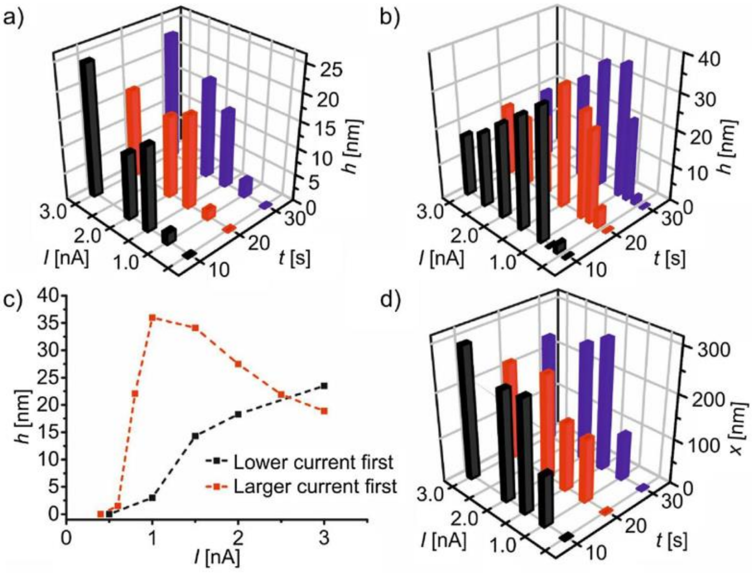

Fig. 3. Dependence of pit depth h on the electric current magnitude I and the exposure time t for sweeping tip (amplitude 100 nm and frequency 0.3 Hz): (a) The pits with lower current were prepared first; (b) The pits with larger current were prepared first. New tip was used for this data set. (c) Comparison of dependences for exposure time 30 s (the connecting lines are guides for eye.). (d) Dependence of pit lateral diameter x (in the direction of sweeping). Same pits as in (a). Each data point was evaluated as an average value of three single pits.

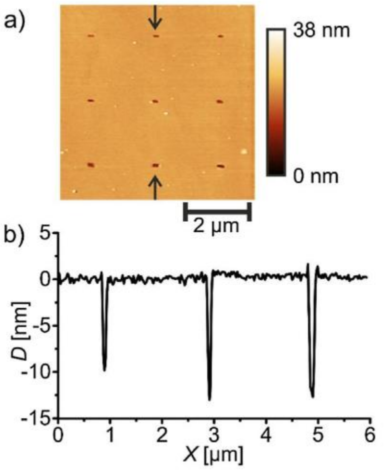

Fig. 4. (a) AFM topography image of nanostructured part of the sample with a matrix of pits. (b) Height cross-section along the line indicated by the arrows in the image.

large craters with diameter of few micrometers and tip modification or destruction. The values of maximum current and threshold slightly vary (20%) even for tips of the same type. Nevertheless, the trends are similar with all tips. Actual pit depth depends on whether the process starts from higher or lower currents, as summarized in Fig. 3(c). It affects also the overall trend. It is monotonously increasing when starting from lower currents but exhibits a maximum when going from high to low currents. It may be related to the observation that new tips create shallower pits. Thus certain forming of the tip seems to be advantageous for the process.

The maximum depth of the pits achieved by the sweeping method was around 40 nm, thus significantly deeper than depth obtained by the static method. Lateral dimensions of the pits were again in the range of few hundreds of nanometers (Fig. 3(d)).

Fig. 4 shows that the process can be used to create a well-defined ensemble of many pits precisely placed at given coordinates. The pits are stretched in horizontal direction because of the sweeping (100 nm amplitude). Experiments with more pits can be found in the Supplementary material (Fig. S-2 in the Supporting information). The number of pits that can be created by one tip is 80–120. Afterwards, the tip is too worn to create pits with controlled sizes. Nevertheless, more durable tips such as diamond ones [38] could be employed.

Based on the fact that the sweeping of the tip was favorable for the process, application of more complex movements across the sample was also investigated. Fig. 5 shows the picture of the logo of the Institute of Physics of the Czech Academy of Sciences that was scribed into a-Si:H film by this technique. The logo is made of line art many micrometers long within the area 6×8 µm^2 with the depth between 20 and 40 nm.

The tip was moving along a trajectory defined as a vector image. The velocity of the tip was 50 nm/s along the line art segments. Faster movement (10 µm/s) was used between the individual segments. Those lines are also faintly visible in Fig. 5 (electric current was not switched off in these segments for simplicity). The depth of lines can be obviously controlled by adjusting the tip velocity. Nevertheless, it is also possible to develop methods in which the current is switched off (or the tip retracted) and such joining lines are not made. It took approximately 20 min to scribe the logo. Another logo is shown in Fig. S-3 in the Supporting information. That logo was made using the same parameters but a new tip (same type). The lines are shallower (few nanometers) and thinner (~100 nm).

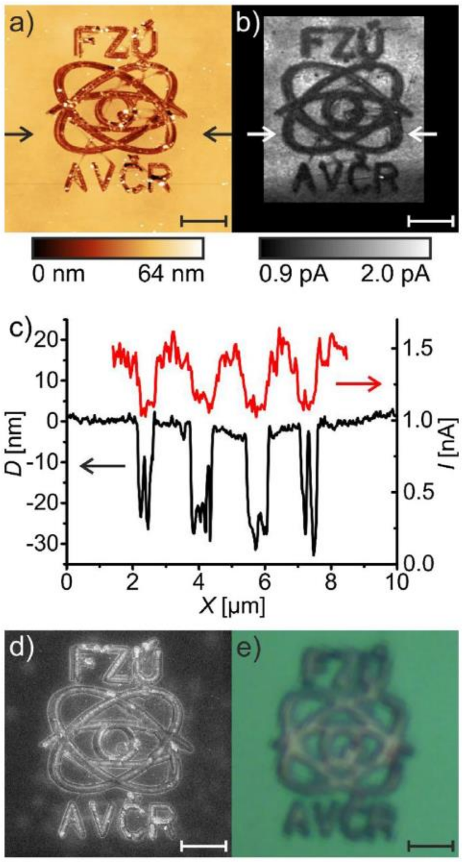

Fig. 5. (a) AFM topography image of nanostructured part of the sample with the logo of the Institute of Physics of the Czech Academy of Sciences; (b) map of local electric current (measured with bias voltage 3.5 V); (c) height cross-section and current cross-section along the lines indicated by the arrows in the images; (d) SEM image of secondary electron emission; (e) bright field optical microscope image in reflected light. Scale bars 2 µm.

Constant electric current of 13 nA was used to create the logo, which is approximately four times more than maximum current used for the pit fabrication. Larger currents led again to formation of large craters. The currents <8 nA did not make continuous lines, but isolated holes or short segments instead. The voltage was oscillating between 14 – 20 V during the scribing.

Fig. 5(b) shows the current map (bias voltage 3.5 V) of the sample with logo. Exposed places feature lower conductivity than the surrounding area. Also electron emission is different (increased) along the exposed lines, which can be seen in the SEM image (Fig. 5(d)).

The Raman spectra of the same area are shown in Fig. 6. The sharp peak of crystalline silicon at 520 cm^{-1} is missing in Raman spectra. Only broad amorphous band is present instead. The shape of Raman spectra on the exposed places and on the surrounding area differs for wavenumbers <1800 cm^{-1} just minutely. However, the overall intensity of Raman signal changes throughout the exposed area. Map of the integrated Raman intensity (300–1800 cm^{-1}) is shown in Fig. 6 (inset). Raman intensity detected on the lines is lower than on the unexposed area (same parameters of acquisition). On the other hand, the Raman intensity alongside these lines is higher than intensity on the unexposed area.

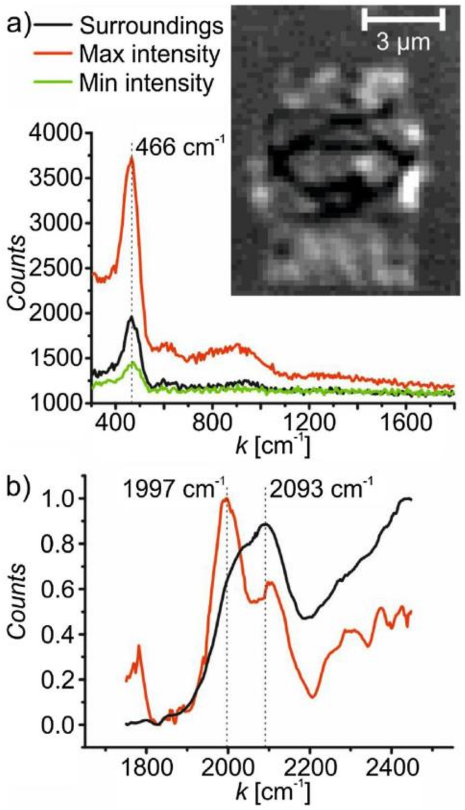

Fig. 6. (a) Raman spectra on the exposed area (place with maximal signal and place with minimal signal) and in the surrounding unexposed area. The noise is the consequence of short acquisition time (0.5 s) as the spectra were measured during the acquisition of the Raman map. Inset: Map of the Raman intensity on the logo. The spectra in each point were integrated and converted to grey scale. White places correspond to the largest signal. (b) Normalized Raman spectra of unexposed (black) and exposed (red) places. (For interpretation of the references to colour in this figure legend, the reader is referred to the web version of this article.)

The change of Raman signal between exposed places and surrounding area was observed around 2000 cm^{-1} (Fig. 6(b)), where the Si—H and Si—H$_2$ bonds are evidenced. A peak with maximum at 2093 cm^{-1}, which corresponds to Si—H$_2$ bonds [39–41], was observed on the as deposited layer. A shoulder at lower wavenumbers (2030 cm^{-1}) was observed. After the nanofabrication process, a peak at 1997 cm^{-1}, which corresponds to Si-H bonds, became dominant while the peak at 2093 cm^{-1} decreased. This is probably caused by the overall decrease of hydrogen concentration inside the a-Si:H film.

4. Discussion

The process which leads to the creation of pits has not been sufficiently described yet. The pits are most probably created by the change of the density of the layer (as discussed before in [42]). The a-Si:H layers with high hydrogen concentration typically contain voids, which decrease the overall density of the layer [43]. Energy supplied by the electric current which is flowing through the layer increase the mobility of hydrogen atoms. Subsequently, hydrogen atoms leave a-Si:H and the layer shrinks. This assumption is supported by the changes which we observed in Raman spectra in the region of Si—H bonds around 2000 cm^{-1}.

Smets et al. [43] have shown that films with hydrogen concentration below 14 ± 2 at.% are dominated by di-vacancies, which contain hydrogen, and low stretching mode (1980–2030 cm^{-1}) is dominant in IR absorption spectroscopy. On the other hand, films with hydrogen concentration over 14 ± 2 at.% of hydrogen are dominated by voids and high stretching mode (2060–2160 cm^{-1}) is dominant in IR absorption spectroscopy. Moreover, density of the layer is significantly reduced in films with voids. These measurements are in accordance with our observations of topographical and Raman spectra changes, and also with the fact that the deposition parameters were chosen to achieve high hydrogen content (>20 at.%) in the a-Si:H layer. Therefore, we propose that locally applied electric field promotes the escape of hydrogen, which leads to shrinking of the layer.

The contribution of silicide forming metals (both nickel and platinum) must be also taken into consideration. Those metals significantly contribute to the FE-MISPC process [34]. Even though the crystallization was not observed in our case, silicide forming metals could facilitate the hydrogen escape. Also the mechanical force induced by the tip could influence the constriction of the layer. However, the tip does not make any observable changes in a-Si:H layer when the current is switched off or lower than the threshold. Moreover, slight changes of the force magnitude between tip and sample did not measurably affect the process of pit creation. Hence the influence of the tip-surface mechanical interaction can be neglected.

During a process of pit creation, the depth of pits grows with the exposition time as expected, because more hydrogen leaves the a-Si:H layer. Nevertheless, after certain time (~12 s) the depth starts to decrease again. It was observed repeatedly when the static regime was used. Hence we assume that there is some mechanism behind.

There is obviously no other possibility than that some material fills the pit. We propose that it is oxide from the AFM tip. When the tip is static the oxide grows on the positively biased tip during the pit formation process. After some time the tip is covered by oxide, which increases electrical resistance of the tip-surface contact. Thus in order to maintain the current the voltage increases up to the discharge through the oxide layer, which may blow away some of the oxide from the tip, a well-known process used for improving conductivity measurements in AFM [44]. This effect is reproducible, albeit with some variations in the outcome as reflected by increased error bar in Fig. 2. When the topography of pits was measured after the process, artefacts were observed in some cases. This might be caused by the modified tip.

The same mechanism can also explain why the pit depth is larger for sweeping tip. The thickness of oxide layer is reduced for tips moving faster [45]. In our case, smaller oxide thickness is evidenced by lower voltage which is required to maintain the current constant for sweeping tip (fluctuating between 14 and 20 V). Thus oxide growth on the tip is inhibited and the voltage is not enough to blow away the oxide and fill the pits. The sweeping also reduces the possibility of electrical discharge as the conducting channel is spatially spread during the exposure. Analogous effect was observed for electric discharges in gas when discharge “cooling” was generated by acoustic field in the gas [46]. At the same time, the current flow is not inhibited and the modification of a-Si:H layer may proceed further. Moreover, larger currents and longer exposition times may be used for sweeping tip because the voltage does not increase over the discharge threshold. Yet when the current is set too high (>4 nA), the voltage increases and leads to the discharge. The optimal velocity for sweeping is about 60 nm/s. The achievable depth becomes again smaller for faster sweeping. Electrical current driving the reaction is most likely too dissipated.

Significant changes of the tip properties occur during the first few (usually three) expositions. This process is denoted as tip forming [37] and has mostly positive effect on the process. The ability to control the pit depth is reduced by gradual tip wear in later stages. Various mechanisms could be responsible for the tip wear including decrease of metal coating thickness, material accumulation on the tip, increasing radius of the tip or aforementioned anodic oxidation of the tip [38]. Opposite polarity reducing the anodic oxidation of the tip is not convenient for pit creation though [36]. Moreover, the opposite polarity could lead to oxidation of silicon surface. Tip wear can be reduced when more durable tips are used [38]. Using for instance diamond-based tips may increase the number of pits and also improve the control over their size.

Compared to previous studies [36,42], thinner a-Si:H layers were used now (40 nm vs. >170 nm). Much thinner layers have lower overall resistance, which has several important consequences. Firstly, the current magnitude required for pit creation (>0.5 nA) is higher than 0.2 nA, which was typically used before [47]. Secondly, the a-Si:H layer does not crystallize as is evidenced by Raman spectroscopy and conductive AFM measurement (exposed places exhibit lower electrical conductivity). Before, regulation of current magnitude (by external circuitry with MOSFET) had to be used to avoid crystallization [5]. Thirdly, the external voltage, which keeps the current constant, is generally lower. That significantly suppresses the current surges from parallel capacitance after the pit formation. Again external circuitry was used before to avoid current surges. Thin layer of a-Si:H (40 nm) provides therefore better reproducibility and better control over the pit depth.

As mentioned above, the created features exhibit generally lower electrical conductivity than the surroundings even though the thickness of the layer is lower there. The conductivity of material would have to decrease by a factor of ~4 in order to explain the decrease shown in Fig. 5(b). The decreased conductivity is not due to larger tip contact area inside the pits, which would lead rather to increased currents [48]. More likely it is influenced by the change of hydrogen content. It was shown before that conductivity of a-Si:H films varies by few orders of magnitude if illuminated by visible light or thermally annealed [49,50]. This change was attributed to the displacement of hydrogen atoms. Hydrogen terminates the dangling bonds of silicon atoms in a-Si:H layer and affects its density of gap states. In our case, hydrogen content is greatly reduced and the dominant type of bonding (SiH or SiH_2) is significantly changed on processed places. Decrease in hydrogen content increases the number of unsatisfied silicon dangling bonds, which leads to the observed increased electrical resistance of the created pits or pattern.

Besides electrical conductivity, the Raman intensity was also modified on the exposed area. Raman intensity coming from the lines in the middle of the logo (Fig. 6) is lower in comparison with the unexposed area. We assume that the drop is the consequence of the lower thickness of a-Si:H layer on the exposed places. Surprisingly, the Raman intensity alongside these lines is higher. This could be caused by accumulation of material along the exposed places. However, such accumulation was not observed with AFM. We therefore suggest that this enhancement may be caused by diffraction of Raman signal on roughened surface, which leads to its more efficient collection. Such optical effects could be useful in various photonics applications [51].

5. Conclusion

Nano-patterns of various complex shapes and sizes were reproducibly created in a thin (40 nm) layer of hydrogenated amorphous silicon by local application of electrical current, via conductive AFM tip. Sweeping of the AFM tip during the process led to deeper and better defined features. It was possible to control the feature depth by adjusting the electric current magnitude and the sweeping amplitude and frequency. By using AFM, the features were localized with high accuracy and precision into matrices. Moreover, complex line art patterns were scribed into the a-Si:H film by moving the tip across the surface during exposition. It was possible to control the depth and width of the lines by changing the velocity of the tip or by adjusting the current magnitude.

The a-Si:H film did not crystallize during exposition as evidenced by conductivity measurements and Raman microspectroscopy. Properties of exposed places still differed from their surroundings. In addition to morphological (pit or trench formation), electrical conductivity of the features dropped while electron emission and light interaction was enhanced. This may be useful for various applications of a-Si:H itself. The modified properties of the patterns may also become useful as universal templates for further growth or assembly of nano-materials and nanostructures by geometrical, physical, chemical, or optical processes. Some possibility of such use has already been demonstrated [5,52].

Acknowledgements

This work has been supported by the projects 15-01809S (GACR), SGS17/179/OHK4/3T/13 (SGS CVUT), and the European Regional Development Fund project CZ.02.1.01/0.0/0.0/15_003/000046. It occurred in the frame of LNSM infrastructure. Technical support by P. Bauerová is kindly acknowledged.

Appendix A. Supplementary data

Supplementary data associated with this article can be found, in the online version, at https://doi.org/10.1016/j.apsusc.2017.09.228.

References

[1] D. Whang, S. Jin, Y. Wu, C.M. Lieber, Large-Scale Hierarchical Organization of Nanowire Arrays for Integrated Nanosystems, Nano Lett. 3 (2003) 1255–1259, http://dx.doi.org/10.1021/nl0345062.

[2] J.P. Hoogenboom, C. Rétif, E. de Bres, M. van de Boer, A.K. van Langen-Suurling, J. Romijn, A. van Blaaderen, Template-induced growth of close-packed and non-close-packed colloidal crystals during solvent evaporation, Nano Lett. 4 (2004) 205–208, http://dx.doi.org/10.1021/nl034867h.

[3] Y. Cui, M.T. Björk, J.A. Liddle, C. Sönnichsen, B. Boussert, A.P. Alivisatos, Integration of colloidal nanocrystals into lithographically patterned devices, Nano Lett. 4 (2004) 1093–1098, http://dx.doi.org/10.1021/nl049488i.

[4] J.G. Son, W.K. Bae, H. Kang, P.F. Nealey, K. Char, Placement control of nanomaterial arrays on the surface-reconstructed block copolymer thin films, ACS Nano 3 (2009) 3927–3934, http://dx.doi.org/10.1021/nn900914q.

[5] E. Verveniotis, E. Šípek, J. Stuchlík, J. Kočka, B. Rezek, Generating ordered Si nanocrystals via atomic force microscopy, J. Non-Cryst. Solids 358 (2012) 2118–2121, http://dx.doi.org/10.1016/j.jnoncrysol.2011.12.018.

[6] J.-M. Liu, S.C. Yang, Novel colloidal polyaniline fibrils made by template guided chemical polymerization, J. Chem. Soc. Chem. Commun. (1991) 1529–1531, http://dx.doi.org/10.1039/c39910001529.

[7] G.P. Lopinski, D.D.M. Wayner, R.A. Wolkow, Self-directed growth of molecular nanostructures on silicon, Nature 406 (2000) 48–51, http://dx.doi.org/10.1038/35017519.

[8] H.O. Jacobs, S.A. Campbell, M.G. Steward, Approaching nanoxerography the use of electrostatic forces to position nanoparticles with 100 nm scale resolution, Adv. Mater. 14 (2002) 1553–1557, http://dx.doi.org/10.1002/1521-4095(20021104)14:21<1553:AID-ADMA1553>3.0.CO;2-9.

[9] E. Verveniotis, A. Kromka, M. Ledinský, J. Čermák, B. Rezek, Guided assembly of nanoparticles on electrostatically charged nanocrystalline diamond thin films, Nanoscale Res. Lett. 6 (2011) 144, http://dx.doi.org/10.1186/1556-276X-6-144.

[10] D. Haefliger, A. Stemmer, Structuring of aluminum films by laser-induced local oxidation in water, Appl. Phys. Mater. Sci. Process 74 (2002) 115.

[11] D. Haefliger, B.P. Cahill, A. Stemmer, Rapid prototyping of micro-electrodes on glass and polymers by laser-assisted corrosion of aluminum films in water, Microelectron. Eng. 67–68 (2003) 473–478, http://dx.doi.org/10.1016/S0167-9317(03)00103-5.

[12] R.C. Hayward, D.A. Saville, I.A. Aksay, Electrophoretic assembly of colloidal crystals with optically tunable micropatterns, Nature 404 (2000) 56–59, http://dx.doi.org/10.1038/35003530.
[13] J.C. Hulteen, D.A. Treichel, M.T. Smith, M.L. Duval, T.R. Jensen, R.P. Van Duyne, Nanosphere lithography: size-tunable silver nanoparticle and surface cluster arrays, J. Phys. Chem. B 103 (1999) 3854–3863, http://dx.doi.org/10.1021/jp9904771.
[14] C.L. Haynes, R.P. Van Duyne, Nanosphere lithography: a versatile nanofabrication tool for studies of size-dependent nanoparticle optics, J. Phys. Chem. B 105 (2001) 5599–5611, http://dx.doi.org/10.1021/jp010657m.
[15] H. Masuda, M. Satoh, Fabrication of gold nanodot array using anodic porous alumina as an evaporation mask, Jpn. J. Appl. Phys. 35 (1996) 126–129, http://dx.doi.org/10.1143/JJAP.35.L126.
[16] K. Nielsch, J. Choi, K. Schwirn, R.B. Wehrspohn, U. Gösele, Self-ordering regimes of porous alumina: the 10 porosity rule, Nano Lett. 2 (2002) 677–680, http://dx.doi.org/10.1021/nl025537k.
[17] W. Li, J. Zhou, X. Zhang, J. Xu, L. Xu, W. Zhao, P. Sun, F. Song, J. Wan, Kunji Chen, Field emission from a periodic amorphous silicon pillar array fabricated by modified nanosphere lithography, Nanotechnology 19 (2008) 135308, http://dx.doi.org/10.1088/0957-4484/19/13/135308.
[18] A. Kosiorek, W. Kandulski, P. Chudzinski, K. Kempa, M. Giersig, Shadow nanosphere lithography: simulation and experiment, Nano Lett. 4 (2004) 1359–1363, http://dx.doi.org/10.1021/nl049361t.
[19] C.L. Haynes, A.D. McFarland, M.T. Smith, J.C. Hulteen, R.P. Van Duyne, Angle-resolved nanosphere lithography: manipulation of nanoparticle size, shape, and interparticle spacing, J. Phys. Chem. B 106 (2002) 1898–1902, http://dx.doi.org/10.1021/jp013570+.
[20] R. Held, T. Heinzel, P. Studerus, K. Ensslin, Nanolithography by local anodic oxidation of metal films using an atomic force microscope, Phys. E Low-Dimens. Syst. Nanostruct. 2 (1998) 748–752, http://dx.doi.org/10.1016/S1386-9477(98)00153-2.
[21] R.M. Nyffenegger, R.M. Penner, Nanometer-Scale surface modification using the scanning probe Microscope: progress since 1991, Chem. Rev. 97 (1997) 1195–1230, http://dx.doi.org/10.1021/cr960069i.
[22] F. Forouzan, A.J. Bard, Evidence for faradaic processes in scanning probe microscopy on mica in humid air, J. Phys. Chem. B 101 (1997) 10876–10879, http://dx.doi.org/10.1021/jp972728g.
[23] Y. Li, B.W. Maynor, J. Liu, Electrochemical AFM. dip-pen nanolithography, J. Am. Chem. Soc. 123 (2001) 2105–2106.
[24] M. Sigrist, A. Fuhrer, T. Ihn, K. Ensslin, D.C. Driscoll, A.C. Gossard, Multiple layer local oxidation for fabricating semiconductor nanostructures, Appl. Phys. Lett. 85 (2004) 3558–3560, http://dx.doi.org/10.1063/1.1809273.
[25] T. Banno, M. Tachiki, H. Seo, H. Umezawa, H. Kawarada, Fabrication of diamond single-hole transistors using AFM anodization process, Diam. Relat. Mater. 11 (2002) 387–391, http://dx.doi.org/10.1016/S0925-9635(01)00655-0.
[26] M. Tachiki, H. Seo, T. Banno, Y. Sumikawa, H. Umezawa, H. Kawarada, Fabrication of single-hole transistors on hydrogenated diamond surface using atomic force microscope, Appl. Phys. Lett. 81 (2002) 2854–2856, http://dx.doi.org/10.1063/1.1513656.
[27] M. Bartošík, M. Kolíbal, J. Čechal, J. Mach, T. Šikola, Selective growth of metallic nanostructures on surfaces patterned by AFM local anodic oxidation, J. Nanosci. Nanotechnol. 9 (2009) 5887–5890, http://dx.doi.org/10.1166/jnn.2009.1251.
[28] D.J. Dunstan, Photoluminescence in hydrogenated amorphous silicon, Phys. Rev. B 30 (1984) 5945–5957, http://dx.doi.org/10.1103/PhysRevB.30.5945.
[29] D.E. Carlson, C.R. Wronski, Amorphous silicon solar cell, Appl. Phys. Lett. 28 (1976) 671–673, http://dx.doi.org/10.1063/1.88617.
[30] M. Schaper, J. Schmidt, H. Plagwitz, R. Brendel, 20.1%-efficient crystalline silicon solar cell with amorphous silicon rear-surface passivation, Prog. Photovolt. Res. Appl. 13 (2005) 381–386, http://dx.doi.org/10.1002/pip.641.
[31] R.A. Street, Hydrogenated Amorphous Silicon, Cambridge University Press, 2005.
[32] P. Fojtík, K. Dohnalová, T. Mates, J. Stuchlík, I. Gregora, J. Chval, A. Fejfar, J. Kočka, I. Pelant, Rapid crystallization of amorphous silicon at room temperature, Philos. Mag. Part B 82 (2002) 1785–1793, http://dx.doi.org/10.1080/13642810208222940.
[33] L.K. Lam, S. Chen, D.G. Ast, Kinetics of nickel-induced lateral crystallization of amorphous silicon thin-film transistors by rapid thermal and furnace anneals, Appl. Phys. Lett. 74 (1999) 1866–1868, http://dx.doi.org/10.1063/1.123695.
[34] I. Pelant, P. Fojtík, K. Luterová, J. Kočka, K. Knížek, J. Štěpánek, Room temperature electric field induced crystallization of wide band gap hydrogenated amorphous silicon, Thin Solid Films 383 (2001) 101–103, http://dx.doi.org/10.1016/S0040-6090(00)01633-3.
[35] I. Pelant, P. Fojtík, K. Luterová, J. Kočka, A. Poruba, J. Štěpánek, Electric-field-enhanced metal-induced crystallization of hydrogenated amorphous silicon at room temperature, Appl. Phys. A 74 (2002) 557–560, http://dx.doi.org/10.1007/s003390100913.
[36] B. Rezek, E. Šípek, M. Ledinský, P. Krejza, J. Stuchlík, A. Fejfar, J. Kočka, Spatially localized current-induced crystallization of amorphous silicon films, J. Non-Cryst. Solids 354 (2008) 2305–2309, http://dx.doi.org/10.1016/j.jnoncrysol.2007.10.045.
[37] E. Verveniotis, B. Rezek, E. Šípek, J. Stuchlík, M. Ledinský, J. Kočka, Impact of AFM-induced nano-pits in a-Si:H films on silicon crystal growth, Nanoscale Res. Lett. 6 (2011) 145, http://dx.doi.org/10.1186/1556-276X-6-145.
[38] E. Verveniotis, B. Rezek, E. Šípek, J. Stuchlík, J. Kočka, Role of current profiles and atomic force microscope tips on local electric crystallization of amorphous silicon, Thin Solid Films 518 (2010) 5965–5970, http://dx.doi.org/10.1016/j.tsf.2010.05.107.
[39] G. Lucovsky, R.J. Nemanich, J.C. Knights, Structural interpretation of the vibrational spectra of a-Si: H alloys, Phys. Rev. B 19 (1979) 2064–2073, http://dx.doi.org/10.1103/PhysRevB.19.2064.
[40] A.A. Langford, M.L. Fleet, B.P. Nelson, W.A. Lanford, N. Maley, Infrared absorption strength and hydrogen content of hydrogenated amorphous silicon, Phys. Rev. B 45 (1992) 13367–13377, http://dx.doi.org/10.1103/PhysRevB.45.13367.
[41] V.A. Volodin, D.I. Koshelev, Quantitative analysis of hydrogen in amorphous silicon using Raman scattering spectroscopy, J. Raman Spectrosc. 44 (2013) 1760–1764, http://dx.doi.org/10.1002/jrs.4408.
[42] B. Rezek, E. Šípek, M. Ledinský, J. Stuchlík, A. Vetushka, J. Kocka, Creating nanocrystals in amorphous silicon using a conductive tip, Nanotechnology 20 (2009) 045302, http://dx.doi.org/10.1088/0957-4484/20/4/045302.
[43] A.H.M. Smets, W.M.M. Kessels, M.C.M. van de Sanden, Vacancies and voids in hydrogenated amorphous silicon, Appl. Phys. Lett. 82 (2003) 1547–1549, http://dx.doi.org/10.1063/1.1559657.
[44] B. Rezek, J. Stuchlıík, A. Fejfar, J. Kočka, Microcrystalline silicon thin films studied by atomic force microscopy with electrical current detection, J. Appl. Phys. 92 (2002) 587–593, http://dx.doi.org/10.1063/1.1486032.
[45] M. Bartošík, D. Škoda, O. Tomanec, R. Kalousek, P. Jánský, J. Zlámal, J. Spousta, P. Dub, T. Šikola, Role of humidity in local anodic oxidation: a study of water condensation and electric field distribution, Phys. Rev. B 79 (2009) 195406, http://dx.doi.org/10.1103/PhysRevB.79.195406.
[46] R. Bálek, M. Červenka, S. Pekárek, Acoustic field effects on a negative corona discharge, Plasma Sources Sci. Technol. 23 (2014) 035005, http://dx.doi.org/10.1088/0963-0252/23/3/035005.
[47] B. Rezek, E. Šípek, M. Ledinský, J. Stuchlík, A. Vetushka, J. Kočka, Creating nanocrystals in amorphous silicon using a conductive tip, Nanotechnology 20 (2009) 045302, http://dx.doi.org/10.1088/0957-4484/20/4/045302.
[48] B. Rezek, J. Stuchlik, A. Fejfar, J. Kocka, Microcrystalline silicon thin films studied by atomic force microscopy with electrical current detection, J. Appl. Phys. 92 (2002) 587–593, http://dx.doi.org/10.1063/1.1486032.
[49] I. Solomon, T. Dietl, D. Kaplan, Influence of interface charges on transport measurements in amorphous silicon films, J. Phys. 39 (1978) 1241–1246, http://dx.doi.org/10.1051/jphys:0197800390110124100.
[50] D.L. Staebler, C.R. Wronski, Optically induced conductivity changes in discharge-produced hydrogenated amorphous silicon, J. Appl. Phys. 51 (1980) 3262–3268, http://dx.doi.org/10.1063/1.328084.
[51] L. Ondič, K. Dohnalová, M. Ledinský, A. Kromka, O. Babchenko, B. Rezek, Effective extraction of photoluminescence from a diamond layer with a photonic crystal, ACS Nano 5 (2011) 346–350, http://dx.doi.org/10.1021/nn1021555.
[52] A.J. Page, R.P. Sear, Heterogeneous Nucleation in and out of Pores, Phys. Rev. Lett. 97 (2006) 065701, http://dx.doi.org/10.1103/PhysRevLett.97.065701.

Applied Surface Science 480 (2019) 1008–1013

Contents lists available at ScienceDirect

Applied Surface Science

journal homepage: www.elsevier.com/locate/apsusc

Full length article

Nucleation of diamond micro-patterns with photoluminescent SiV centers controlled by amorphous silicon thin films

Jan Fait[a,b,*], Štěpán Potocký[a], Štěpán Stehlík[a], Jiří Stuchlík[a], Anna Artemenko[a], Alexander Kromka[a], Bohuslav Rezek[b]

[a] *Institute of Physics, CAS, Cukrovarnická 10, 16200 Prague, Czech Republic*
[b] *Faculty of Electrical Engineering, Czech Technical University in Prague, Technická 27, 16627 Prague, Czech Republic*

ARTICLE INFO

Keywords:
Spontaneous nucleation
Diamond
Hydrogenated amorphous silicon
Selective growth
Focused microwave CVD

ABSTRACT

Selective deposition of diamond allows bottom-up growth of diamond nanostructures and nanoscale devices. However, it remains challenging to reduce the size of the patterns and to suppress parasitic spontaneous nucleation. We show here that thin layers of hydrtogenated amorphous silicon (down to 40 nm) efficiently suppress spontaneous nucleation of diamond. The suppression of diamond nucleation does not depend on the substrate materials below hydrogenated amorphous silicon (Si, SiO_2, Pt, Ni). We attribute the suppressed diamond nucleation to surface disorder on atomic scale. By using a structured layer of hydrogenated amorphous silicon, highly selective growth of diamond micro-patterns with optically active SiV centers by low-temperature microwave plasma chemical vapor deposition is achieved.

1. Introduction

Diamond has many outstanding properties – optical, thermal, electrochemical, chemical, electronic [1] – which are very promising for many potential applications. One of the most interesting and intensively studied features are diamond colour centers [2,3]. They are investigated for many reasons such as detection of very weak magnetic fields [4,5] and quantum computing [6] by nitrogen-vacancy (NV) centers, and biomarkers and (bio-)sensing by silicon-vacancy (SiV) centers [7]. Many of these applications require, or may benefit from, precise placement of luminescent diamonds on a substrate.

When chemical vapor deposition (CVD) of diamond is carried out on a non-diamond substrate, stable clusters of carbon atoms with a diamond structure (called nuclei) must first be created. In order to become stable, clusters must overcome the energetic barrier (i.e. to achieve a critical size). This process is called spontaneous nucleation [8,9]. The height of the energetic (or nucleation) barrier is determined by the deposition conditions – the deposition system, the gas mixture, pressure or temperature [10]. The spontaneous nucleation rate is usually characterized by the nucleation density – the number of spontaneously created diamond grains per unit surface area. Spontaneous nucleation depends not only on the deposition conditions, but also on the properties of the substrate material. CVD diamonds usually start to grow after the formation of a carbide buffer layer on the substrate (e.g. SiC on Si substrates). Moreover, the same material can lead to different nucleation densities if defects are present on the surface. For example, spontaneous nucleation is markedly enhanced near the scratches on an otherwise smooth surface [11].

The substrate is often seeded with diamond nanoparticles before deposition (e.g. in an ultrasonic bath), because the spontaneous nucleation process is typically slow and the nucleation density is relatively low and insufficient for growing thin, continuous films. Subsequently, the diamond grows directly on diamond grains. Lateral structuring of the seeding layer can be used for selective growth of diamond devices [12]. However, it is challenging to reduce the size of the patterns in the seeding layer to nanoscale, to control the position of the seeding particles in order to prepare small clusters of diamond crystals, as well as to reduce unwanted growth outside the defined areas [13].

A mask made of material that suppresses diamond nucleation can be used instead of lateral structuring of the seeding layer in order to achieve selective growth. There are several requirements on the material of the mask. 1. It must suppress spontaneous nucleation in order to achieve growth only within predefined areas. 2. It must be compatible with the conditions that are used for the diamond growth. 3. The material should be easily deposited, structured on nanoscale and, preferably, easily removable.

In this respect, hydrogenated amorphous silicon (a-Si:H) thin films are appealing. A layer of a-Si:H can easily be deposited by chemical

---

[*] Corresponding author at: Institute of Physics ASCR, Cukrovarnická 10, 16200 Prague, Czech Republic.
E-mail address: fait@fzu.cz (J. Fait).

https://doi.org/10.1016/j.apsusc.2019.03.064
Received 5 December 2018; Received in revised form 20 February 2019; Accepted 7 March 2019

vapor deposition, can easily be etched chemically, and can be locally structured by photolithography or even by a conductive atomic force microscope (AFM) [14–16].

In this study, we first investigate the effect of a-Si:H thin film coating on the spontaneous nucleation of diamond on various substrate materials. In order to quantify the effect, the nucleation density on a-Si:H is compared with the nucleation density on a bare Si wafer, as a reference. Low temperature diamond growth [17,18] was used for deposition in order to avoid thermally-induced changes in a-Si:H layers. We show that spontaneous nucleation of diamond is completely suppressed on amorphous silicon in contrast to monocrystalline silicon, where high spontaneous nucleation density can be achieved. In this sense, the a-Si:H film can work as a mask for selective diamond deposition, as demonstrated. Moreover, we show that the chemical purity of the diamond is high enough for optically active SiV centers to be observed. The method presented here can thus be highly beneficial for bottom-up growth of diamond photonic [19] or electronic devices [12].

2. Experimental

Spontaneous nucleation was investigated on the following substrates: standard polished monocrystalline p-type Si (100) wafers, or Si wafers with additional interlayer made of Ni (40 nm by evaporation), of Pt (40 nm by sputtering) or of SiO_2 (900 nm). All of these substrates were covered by a thin layer (40 nm–230 nm) of a-Si:H. The a-Si:H layers were deposited by chemical vapor deposition (CVD), using 0.02% of SiH_4 (1 sccm) diluted in helium (5000 sccm), and a low substrate temperature (50 °C). This process leads to a high hydrogen content in the a-Si:H layers (20–45 at. %). The thickness of the a-Si:H layer was controlled by the CVD deposition time, with a linear increase in thickness with deposition time, and was determined by atomic force microscopy (AFM). A bare monocrystalline silicon wafer (placed side-by-side with the a-Si:H covered samples) was used as a reference during subsequent diamond deposition, and the nucleation density on a-Si:H was compared with the nucleation density on this reference sample.

The diamond deposition was carried out in a focused microwave plasma CVD (MP-CVD) reactor (*Aixtron P6*) using an ellipsoidal cavity resonator. For the setup scheme of the reactor, see Fig. S1 in Supplementary Information. The plasma is located close (1–2 mm) to the substrate surface [8]. This proximity of the plasma limits the lowest substrate temperature that can be achieved during CVD deposition. The substrate temperature was kept low (approximately 430 °C; monitored by a *Williamson, PRO 92-20-C-23* type IR pyrometer) in order to reduce possible thermally-induced changes to the a-Si:H. In some cases, a higher surface temperature (approximately 560 °C) was used while keeping the deposition conditions unchanged. This was achieved by using a hollow substrate holder with lower thermal conductivity.

The deposition conditions were adjusted so that the nucleation density on the reference polished monocrystalline silicon substrates was higher than $10^6\,cm^{-2}$, which is the maximum that we could achieve while keeping the substrate temperature low. The reference substrates were cleaned using O_2 plasma treatment before depositions. The parameters used for diamond deposition were as follows: deposition time $t = 3$ h–12 h, total gas pressure $p = 4$ kPa, gas flow of hydrogen H_2 equal to 300 sccm, gas flow of methane CH_4 equal to 3 sccm (or 15 sccm), power of the MW source $P = 4$ kW. Three different deposition scenarios were used. In the first scenario (labeled as *long*), the deposition time was 12 h. All parameters were kept constant during the deposition. In the second scenario (labeled as *methane*), the deposition was shortened to 4 h. In order to enhance and accelerate spontaneous nucleation, the methane concentration was increased to 5% during the first hour. In the third scenario (labeled as *interrupted*), the deposition was interrupted after 0.5 h. Deposition was restarted after 0.25 h, and lasted a further period 3 h.

Scanning electron microscopy (SEM; *Tescan Maia3*) was used to determine the nucleation density of the diamond grains and the morphology of the samples after deposition. The particles on randomly selected regions (each 1500 μm^2 in area) over the surface of the sample were manually counted. Subsequently, the number of particles was divided by the total area of these regions.

The material and chemical composition of grains was characterized by Raman micro-spectroscopy (*Renishaw inVia Reflex*, excitation wavelength 442 nm, objective 100×; *Horiba XploRA*, excitation wavelength 325 nm, objective 100×). The micro-photoluminescence of the structures was also measured in the same setup (*Renishaw inVia Reflex*). The chemical composition of some samples was analyzed by X-ray photoelectron spectroscopy (XPS; *AXIS Supra*, *Kratos* spectrometer with a hemispheric analyzer and a monochromatic Al Kα X-ray source, 1486.6 eV; high resolution spectra pass energy 20 eV). The XPS spectra were acquired from an area of 700 × 300 μm^2 with a 90° take-off angle 90°.

The selective growth of diamond was demonstrated on samples consisting of a Si wafer covered by 40 nm of Pt. We used FDP (Fumed Diamond Powder, 3.1 ± 0.6 nm; NanoCarbon Research Institute) detonation nanodiamonds, which were dispersed in DI water by means of ultrasonication (200 W, 1 h; Hielscher UP200S) for seeding. The samples to be seeded were immersed in a colloidal solution (1 mg/ml) of FDP diamond nanoparticles for 30 min, were rinsed in DI water, blown by nitrogen and covered with a layer of a-Si:H (230 nm). Part of this layer was removed using a standard photolithographic process (positive photoresist, 6 s exposition with UV light, 40 s in the developer) and dry etching in SF_6 plasma. SF_6 plasma, which is not harmful for the diamond seeding layer, was used to selectively remove a-Si:H in places where the resist was removed in the photolithographic process, revealing the diamond seeding layer. The rest of the photoresist was removed in an acetone bath. The final samples consisted of a Pt layer (on a Si wafer) seeded with diamond nanocrystals and partially covered with a-Si:H layer.

Subsequently, diamond deposition was carried out in the focused MP-CVD reactor. The deposition parameters were: power 4 kW, pressure 4 kPa, concentration of methane in hydrogen 1%, and deposition time 3.5 h. The samples were characterized using SEM, Raman micro-spectroscopy and micro-photoluminescence measurements.

3. Results

3.1. Spontaneous nucleation on monocrystalline silicon

We detected clusters of nanocrystalline diamond (NCD) spontaneously nucleated on the surface of monocrystalline Si (Fig. 1). The size of the clusters differed according to the deposition scheme. The largest clusters (up to 2 μm) were observed on the sample with long deposition. The surface of this sample was also covered by a thin layer of non-diamond carbon particles. The larger clusters were composed of smaller diamond grains 50 nm–100 nm in size. Solitary grains were also observed on the samples.

The nucleation density on the reference sample (monocrystalline silicon) achieved by three different growth scenarios was determined from SEM images. The deposition scenarios are described in detail in the Experimental section. The diamond nucleation density is roughly the same ($4 \times 10^6\,cm^{-2}$) for all three scenarios (Table 1). The uncertainty of the spontaneous nucleation was estimated on the basis of the slightly different number of particles in several SEM images taken in various places over the sample.

The chemical composition of the nucleated particles was determined by Raman micro-spectroscopy. The diamond peak is clearly visible in the spectra of the particles, confirming their diamond composition. Raman spectroscopy also revealed different ratios of the sp^3 to sp^2 bonds for the three scenarios. The highest concentration of sp^2 bonds was detected on the sample with interrupted deposition (relatively, in comparison with the other two depositions). The absolute height of the diamond peak cannot be compared, as the Raman spectra

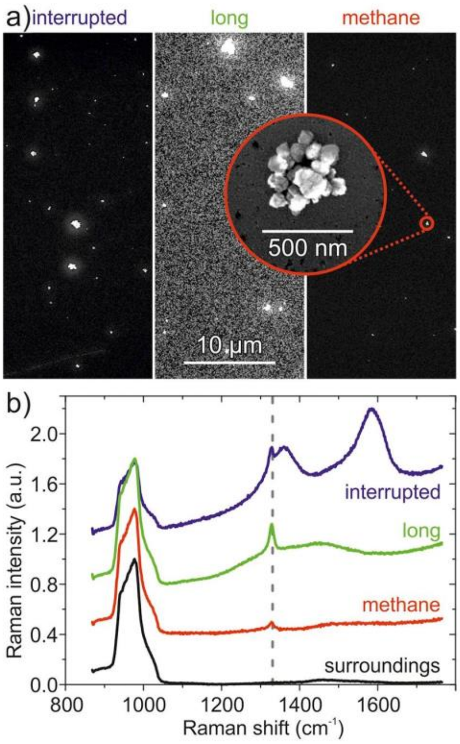

Fig. 1. Monocrystalline silicon samples with spontaneously nucleated diamond clusters (three different deposition scenarios): (a) SEM images, (b) Raman spectra of clusters; the grey dashed line denotes the position of the diamond peak.

Table 1
Nucleation density on monocrystalline silicon for three different deposition scenarios. The estimated uncertainty is $1 \times 10^6\ \mathrm{cm}^{-2}$.

Temperature	approx. 430 °C
Interrupted	5×10^6
Long	4×10^6
Methane	5×10^6

were measured on clusters of different sizes.

The diamond nature of the nucleated particles was also confirmed indirectly by the micro-photoluminescence measurements [20]. The photoluminescence spectra show that optically active SiV centers were created in diamond crystals formed on monocrystalline silicon (Fig. 2). The zero phonon line (ZPL) is centered at approximately 738 nm. The characteristic phonon band (wavelength > 750 nm) is also present. The luminescence of the SiV centers was detected for all deposition scenarios. However, the luminescence intensity varied in different scenarios. This is most probably due to the different sizes of the particles. The highest intensity was detected for the long deposition scenario with the biggest clusters, which supports this assumption. However, the role of different chemical composition (e.g. a different ratio of the sp^2 bonds) cannot be excluded.

Some carbon deposits were detected even in the surroundings of diamond grains on the sample with the long deposition scenario. However, these carbon deposits are not composed of diamond, as evidenced by both Raman and PL spectra (Fig. 1(b) and 2). Note that even very small diamonds may contain optically active SiV centers [20,21] and the PL spectra can thus confirm the presence/absence of diamond nanoparticles.

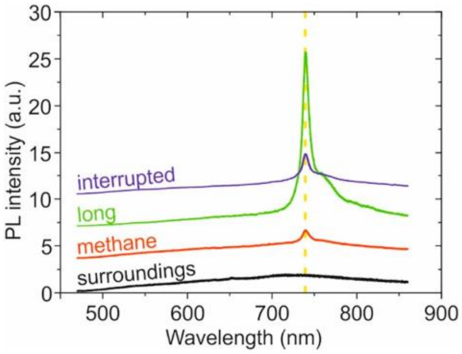

Fig. 2. Photoluminescence of spontaneously nucleated diamond clusters (various scenarios). The yellow dashed line denotes the position of SiV centers ZPL (738 nm).

3.2. Spontaneous nucleation on a-Si:H

SEM images of a-Si:H coated samples with various thicknesses and interlayers after diamond deposition (interrupted deposition) are shown in Fig. 3. The results of other deposition scenarios were similar. The first four samples were placed side-by-side inside the reactor chamber. Deposition on the other two samples was carried out separately, using the same deposition conditions.

The nucleation density was determined from SEM images (the number of all particles in a given area). The nucleation density on samples with microcrystalline silicon (a 40 nm layer of a-Si:H which crystallized during diamond deposition due to the metal-induced crystallization process [22]) is at least one order of magnitude lower than on monocrystalline silicon (Table 2). A few particles can be seen on the SEM image (Fig. 3(c), bottom right corner). However, not all the particles were composed of diamond, as was revealed by Raman spectroscopy. Detailed pictures of some particles can be found in Fig. S2, in Supplementary Information. Some of the particles may be diamonds. However, the diamond sp^3 peak was observed only in a few cases in the Raman spectra of the particles. The absence of a diamond peak in other cases is not caused by the small size of the particles, since different Raman peaks (e. g. crystalline Si, carbon G-band, examples given in Figs. S3 – S5, in Supplementary Information) were observed on the particles.

No presence of spontaneously nucleated diamond particles was observed on the samples with a thicker (150–230 nm) a-Si:H layer, which remained amorphous during diamond deposition, as detected by Raman micro-spectroscopy. Nevertheless, the layer was wrinkled in some cases (Ni interlayer) due to the elevated temperature during deposition (Fig. 3(d)).

Fig. 4 shows the Raman spectra of the samples presented above. These spectra were taken on parts of the samples that did not contain any particles (observable in the optical microscope). The spectrum of a diamond particle nucleated on monocrystalline silicon is plotted at the top for comparison. There is no sign of carbon in the spectra of the other samples, with the exception of the sample with a 40 nm a-Si:H layer on a Ni interlayer, which is covered with a continuous carbon film. Moreover, a layer of carbon nanostructures composed of diamond-like carbon (see Supplementary Information for details) was repeatedly observed by SEM on this sample at high magnification. Luminescence of the SiV centers was not detected on either of the samples with an amorphous/microcrystalline silicon layer.

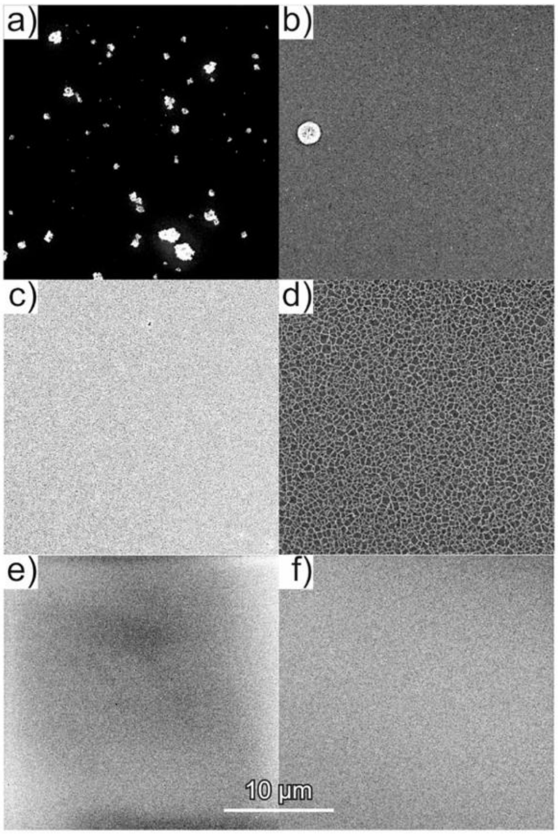

Fig. 3. SEM images of samples on different substrates after diamond deposition (interrupted deposition): (a) Monocrystalline silicon (reference and carrier substrate); (b) Si/Ni/a-Si:H (40 nm); (c) Si/Pt/a-Si:H (40 nm); (d) Si/Ni/a-Si:H (230 nm); (e) Si/SiO$_2$/a-Si:H (150 nm); (f) Si/a-Si:H (150 nm). Note that the contrast on the samples was intentionally increased in order to show details on the surface of the sample.

Table 2
Diamond nucleation density (N$_D$) on six different samples after diamond deposition (interrupted deposition). Based on data from SEM. * denotes that the a-Si:H layer crystallized during diamond deposition due to elevated temperature.

Substrate	N_D (cm^{-2})
Reference	$5 \times 10^6 \pm 1 \times 10^6$
Si + Ni + a-Si:H* (40 nm)	Non-diamond carbon particles (see Supplementary material)
Si + Pt + a-Si:H* (40 nm)	$< 2 \times 10^5$
Si + Ni + a-Si:H (230 nm)	No diamond particles
Si + SiO$_2$ + a-Si:H (150 nm)	No diamond particles
Si + a-Si:H (150 nm)	No diamond particles

3.3. Selective growth of diamond

Based on knowledge of suppressed diamond nucleation on a-Si:H, the application of an a-Si:H layer as a mask for diamond deposition was tested. Fig. 5 shows the sample, which was seeded by diamond nanocrystals and was selectively covered by an a-Si:H layer (approx. 230 nm in thickness) during diamond deposition. The SEM image and the Raman spectra clearly show that the diamond is growing only on areas that are not covered by an a-Si:H layer. The detailed SEM image shows that the deposited layer has the form of nanocrystalline diamond with grain size between 20 and 50 nm. Moreover, the diamond contains optically active SiV centers that are clearly evidenced by the microphotoluminescence measurement. No diamond crystals were detected on the a-Si:H part of the sample.

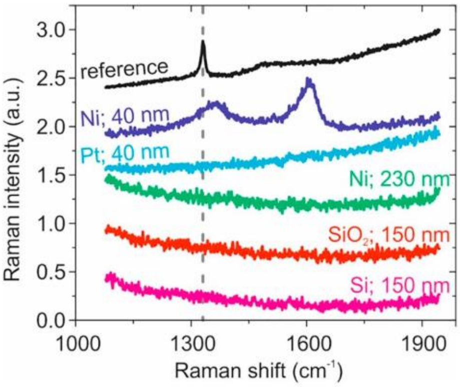

Fig. 4. Raman spectra of the surface of the sample after diamond deposition (interrupted deposition, temperature approx. 430 °C). From the top: Monocrystalline silicon (reference - diamond particle); Ni/a-Si:H (40 nm); Pt/a-Si:H (40 nm); Ni/a-Si:H (230 nm); SiO$_2$/a-Si:H (150 nm); Si/a-Si:H (150 nm).

When a thinner layer of a-Si:H (40 nm) was deposited on the sample, we observed some growth of nanocrystalline diamond even on the masked areas of the sample. This is most likely because the thickness of the a-Si:H layer tends to decrease during diamond CVD growth, due to an escape of hydrogen or due to crystallization. The diamond nanoparticles in the seeding layer can thus be partially uncovered, and diamond grows directly on them without the spontaneous nucleation process.

4. Discussion

The nature of the a-Si:H films remained amorphous during diamond deposition if the layer was sufficiently thick (150 nm–230 nm). Thicker a-Si:H layers on the Ni interlayer were wrinkled (Fig. 3(d)), which is very likely caused by the different coefficient of thermal expansion of Ni and a-Si:H. The situation was different for thinner layers of a-Si:H (40 nm). These layers crystallized during diamond deposition (temperature approx. 430 °C). The crystallization was probably caused by the presence of metals (Ni, Pt), both of which significantly reduce the temperature at which amorphous silicon crystallizes [22]. In addition, the high concentration of hydrogen reduces the crystallization temperature [23]. However, both the metal interlayer and a high hydrogen content are essential for templating a-Si:H layers with AFM [14].

We propose the following explanation of the observed phenomenon of suppressed or reduced spontaneous nucleation on amorphous Si layer and on a microcrystalline Si layer, in comparison with a monocrystalline Si wafer. On monocrystalline Si, diamond nuclei are created on preferential sites on its surface, such as defects or nano-scratches, where the concentration of carbon atoms is increased. Between these sites, carbon atoms can migrate relatively freely over the surface. However, the nucleation in the immediate neighborhood (10 nm) of nucleation sites is suppressed, because they act as sinks for the diffusing adatoms [24].

In contrast to crystalline Si, there are many more surface defects on amorphous/microcrystalline Si that may act as potential preferential sites [25]. However, all preferential sites also act as sinks for diffusing adatoms and prevent nucleation in their neighborhood. The high surface density of the preferential sites results in high competition between them, and in the slow growth of carbon clusters. The slow growth rate causes the diamond nuclei to be dissolved or destroyed by the

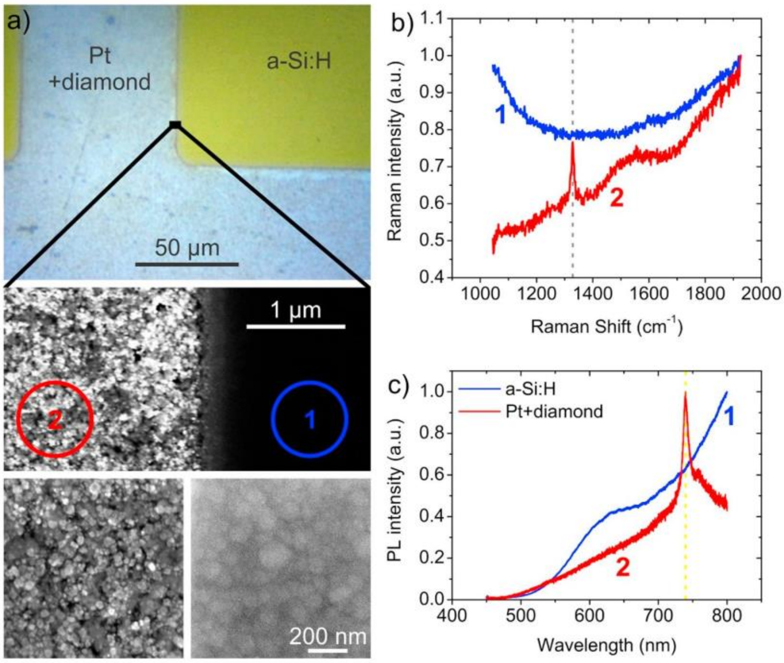

Fig. 5. (a) Optical microscope image (top) and SEM morphology (middle) of the sample with an a-Si:H layer patterned by photolithography after diamond growth. The pictures at the bottom shows SEM details of the NCD structure (left) and the a-Si:H morphology (right). (b) Raman spectra taken on the a-Si:H and on the NCD part of the sample; the grey dashed line denotes the position of the diamond peak. (c) PL intensity taken on the a-Si:H and on the NCD part of the sample; the yellow dashed line denotes the spectral position of the SiV peak.

bombarding energetic species [26] before they reach the diamond nucleation critical size. The low temperature of the substrate may play an important role in this process, because it further reduces the diffusion rate of adatoms or of clusters of adatoms over the surface.

The role of surface termination and the surface energy difference between monocrystalline Si and a-Si:H was also considered. The surfaces of both materials were covered by a native oxide layer prior to deposition. The thickness of the oxide layer on a-Si:H was roughly the same as on monocrystalline Si [27], taking into account that there were several days between the deposition of a-Si:H and the diamond deposition. The surface energy is about 50 mJ/m^2 both for microcrystalline Si [28] and for a-Si:H [29] covered with native oxide, which is significantly lower than the surface energy of diamond [30]. Thus, there is no significant difference in surface termination or in surface energy. Note that it cannot be only the amorphous structure of the surface that suppresses the spontaneous nucleation of diamond, because low nucleation density was also observed on microcrystalline Si (a thin layer of a-Si:H that crystallized during deposition). However, the number of surface defects is still significantly higher on microcrystalline Si than on the monocrystalline reference. This can again lead to limited diffusion of carbon atoms over the surface.

Some carbon nanostructures were observed only on Ni samples with a thin (40 nm) layer of a-Si:H. The carbon layer is probably composed of diamond-like carbon (DLC), as evaluated by Raman micro-spectroscopy and XPS analysis (see Supplementary Information for details). At the same time, there was no such nucleation of carbon on other types of samples (a different material below a-Si:H, or a thicker a-Si:H layer). The nucleation is, therefore, caused by the presence of Ni in the vicinity of the surface. Similar structures were observed on Fe substrates in [31]. We suppose that the a-Si:H layer (40 nm) shrinks and crystallizes during deposition, due to the elevated temperature. Layer shrinkage was observed after local application of an electric field in [16], and was assigned to an escape of hydrogen atoms from the layer. Increased temperature (400 °C) also leads to the effusion of hydrogen atoms from hydrogen-rich layers [32]. The crystallization was evidenced by Raman micro-spectroscopy. Subsequently, Ni atoms can diffuse through the crystallized Si layer towards the surface. The Ni diffusion rate is significantly higher for crystalline Si than for amorphous Si [33], which explains why we observed the effect of Ni only for the case of the thin layer that crystallized during diamond deposition. This observation shows that the a-Si:H layer must be thick enough in order to prevent nucleation of carbon nanoparticles. If the layer is too thin, it crystallizes during diamond deposition and the substrate material may affect the deposition process and catalyze the growth of carbon species.

Similarly, a thicker layer (> 150 nm) must also be deposited for the use of a-Si:H as an efficient mask over the diamond seeding layer. We have demonstrated that thick layers block the growth of diamond and at the same time reduce unwanted spontaneous nucleation. When very thin layers (20 nm) of amorphous Si were used, they crystallized during diamond deposition, and diamond growth was observed [34]. This is in accordance with our observation here. This fact limits the maximal deposition temperature (approx. 500 °C) that can be used during diamond deposition. On the other hand, it means that an a-Si:H layer does not have to be completely removed in order to achieve diamond deposition on selected areas. This could be very important for the use of AFM for a-Si:H lithography [16], where the a-Si:H is structurally modified but is not completely removed. The process is therefore also not so sensitive to the accuracy of dry etching in conventional patterning by photolithography or electron beam lithography.

5. Conclusion

Coating various substrates (Si, SiO$_2$, Pt, Ni) with a thin (150–230 nm) a-Si:H films leads to complete suppression of the spontaneous nucleation of diamond at deposition conditions when diamond spontaneously nucleates and grows on monocrystalline Si. Reduced nucleation density was also detected on microcrystalline silicon thin films. The suppression of spontaneous nucleation was explained by the amorphous nature and, therefore, the large number of surface defects, which greatly hinder the surface diffusion of C atoms. The suppression of spontaneous nucleation by a-Si:H films opens a new way for highly selective deposition of diamond nanostructures. By patterning the a-

Si:H layer with the use of photolithography, highly selective growth of nanocrystalline diamond with optically active SiV centers was achieved even at relatively low substrate temperatures. This method can be further miniaturized to nanoscale by using conductive AFM for creating patterns in a-Si:H thin films. The results presented here thus open prospects for various applications in photonics and in sensor systems.

Acknowledgements

The work has been supported by GACR project 17-19968S, by CTU project SGS18/179/OHK4/3T/13, and by European projects CZ.02.1.01/0.0/0.0/15 003/0000464 and CZ.02.1.01/0.0/0.0/16 019/0000760. The work has been carried out within the frame of the LNSM infrastructure. Technical support from P. Bauerová (SEM images and photolithography) and Ondřej Rezek (diamond deposition) is gratefully acknowledged. We thank Oleksandr Romanyuk for his kind help in interpreting the XPS spectra.

Appendix A. Supplementary data

Supplementary data to this article can be found online at https://doi.org/10.1016/j.apsusc.2019.03.064.

References

[1] R.S. Balmer, J.R. Brandon, S.L. Clewes, H.K. Dhillon, J.M. Dodson, I. Friel, P.N. Inglis, T.D. Madgwick, M.L. Markham, T.P. Mollart, N. Perkins, G.A. Scarsbrook, D.J. Twitchen, A.J. Whitehead, J.J. Wilman, S.M. Woollard, Chemical vapour deposition synthetic diamond: materials, technology and applications, J. Phys. Condens. Matter 21 (2009) 364221, , https://doi.org/10.1088/0953-8984/21/36/364221.

[2] E. Neu, D. Steinmetz, J. Riedrich-Möller, S. Gsell, M. Fischer, Matthias Schreck, C. Becher, Single photon emission from silicon-vacancy colour centres in chemical vapour deposition nano-diamonds on iridium, New J. Phys. 13 (2011) 025012, , https://doi.org/10.1088/1367-2630/13/2/025012.

[3] I. Aharonovich, S. Castelletto, D.A. Simpson, C.-H. Su, A.D. Greentree, S. Prawer, Diamond-based single-photon emitters, Rep. Prog. Phys. 74 (2011) 076501, , https://doi.org/10.1088/0034-4885/74/7/076501.

[4] A. Gruber, A. Dräbenstedt, C. Tietz, L. Fleury, J. Wrachtrup, C. von Borczyskowski, Scanning confocal optical microscopy and magnetic resonance on single defect centers, Science. 276 (1997) 2012–2014, https://doi.org/10.1126/science.276.5321.2012.

[5] D.A. Redman, S. Brown, R.H. Sands, S.C. Rand, Spin dynamics and electronic states of N-V centers in diamond by EPR and four-wave-mixing spectroscopy, Phys. Rev. Lett. 67 (1991) 3420–3423, https://doi.org/10.1103/PhysRevLett.67.3420.

[6] M.D. Eisaman, J. Fan, A. Migdall, S.V. Polyakov, Invited review article: single-photon sources and detectors, Rev. Sci. Instrum. 82 (2011) 071101, , https://doi.org/10.1063/1.3610677.

[7] V. Sedov, V. Ralchenko, A.A. Khomich, I. Vlasov, A. Vul, S. Savin, A. Goryachev, V. Konov, Si-doped nano- and microcrystalline diamond films with controlled bright photoluminescence of silicon-vacancy color centers, Diam. Relat. Mater. 56 (2015) 23–28, https://doi.org/10.1016/j.diamond.2015.04.003.

[8] A. Kromka, O. Babchenko, Š. Potocký, B. Rezek, Sveshnikov, Diamond nucleation and seeding techniques for tissue regeneration, in: Diam.-Based Mater. Biomed. Appl., Elsevier, 2013.

[9] R.P. Sear, Nucleation: theory and applications to protein solutions and colloidal suspensions, J. Phys. Condens. Matter 19 (2007) 033101, , https://doi.org/10.1088/0953-8984/19/3/033101.

[10] T. Izak, A. Sveshnikov, P. Demo, A. Kromka, Enhanced spontaneous nucleation of diamond nuclei in hot and cold microwave plasma systems, Phys. Status Solidi B 250 (2013) 2753–2758, https://doi.org/10.1002/pssb.201300117.

[11] H. Liu, D.S. Dandy, Studies on nucleation process in diamond CVD: an overview of recent developments, Diam. Relat. Mater. 4 (1995) 1173–1188, https://doi.org/10.1016/0925-9635(96)00297-2.

[12] H. Kozak, A. Kromka, O. Babchenko, B. Rezek, Directly grown nanocrystalline diamond field-effect transistor microstructures, Sens. Lett. 8 (2010) 482–487, https://doi.org/10.1166/sl.2010.1298.

[13] O. Babchenko, T. Izak, E. Ukraintsev, K. Hruska, B. Rezek, A. Kromka, Toward surface-friendly treatment of seeding layer and selected-area diamond growth, Phys. Status Solidi B 247 (2010) 3026–3029, https://doi.org/10.1002/pssb.201000124.

[14] B. Rezek, E. Šípek, M. Ledinský, P. Krejza, J. Stuchlík, A. Fejfar, J. Kočka, Spatially localized current-induced crystallization of amorphous silicon films, J. Non-Cryst. Solids 354 (2008) 2305–2309, https://doi.org/10.1016/j.jnoncrysol.2007.10.045.

[15] E. Verveniotis, E. Šípek, J. Stuchlík, J. Kočka, B. Rezek, Generating ordered Si nanocrystals via atomic force microscopy, J. Non-Cryst. Solids 358 (2012) 2118–2121, https://doi.org/10.1016/j.jnoncrysol.2011.12.018.

[16] J. Fait, J. Čermák, J. Stuchlík, B. Rezek, Complex nano-patterning of structural, optical, electrical and electron emission properties of amorphous silicon thin films by scanning probe, Appl. Surf. Sci. (2018), https://doi.org/10.1016/j.apsusc.2017.09.228.

[17] F. Piazza, G. Morell, Synthesis of diamond at sub 300 °C substrate temperature, Diam. Relat. Mater. 16 (2007) 1950–1957, https://doi.org/10.1016/j.diamond.2007.08.038.

[18] K. Tsugawa, M. Ishihara, J. Kim, Y. Koga, M. Hasegawa, Nanocrystalline diamond film growth on plastic substrates at temperatures below 100°C from low-temperature plasma, Phys. Rev. B 82 (2010) 125460, , https://doi.org/10.1103/PhysRevB.82.125460.

[19] L. Ondič, M. Varga, K. Hruška, J. Fait, P. Kapusta, Enhanced extraction of silicon-vacancy centers light emission using bottom-up engineered polycrystalline diamond photonic crystal slabs, ACS Nano (2017), https://doi.org/10.1021/acsnano.6b08412.

[20] S. Stehlik, M. Varga, P. Stenclova, L. Ondic, M. Ledinsky, J. Pangrac, O. Vanek, J. Lipov, A. Kromka, B. Rezek, Ultrathin Nanocrystalline diamond films with silicon vacancy color centers via seeding by 2 nm detonation nanodiamonds, ACS Appl. Mater. Interfaces 9 (2017) 38842–38853, https://doi.org/10.1021/acsami.7b14436.

[21] I.I. Vlasov, A.A. Shiryaev, T. Rendler, S. Steinert, S.-Y. Lee, D. Antonov, M. Vörös, F. Jelezko, A.V. Fisenko, L.F. Semjonova, J. Biskupek, U. Kaiser, O.I. Lebedev, I. Sildos, P.R. Hemmer, V.I. Konov, A. Gali, J. Wrachtrup, Molecular-sized fluorescent nanodiamonds, Nat. Nanotechnol. 9 (2014) 54–58, https://doi.org/10.1038/nnano.2013.255.

[22] S.Y. Yoon, S.J. Park, K.H. Kim, J. Jang, Metal-induced crystallization of amorphous silicon, Thin Solid Films 383 (2001) 34–38, https://doi.org/10.1016/S0040-6090(00)01790-9.

[23] P. Fojtík, K. Dohnalová, T. Mates, J. Stuchlík, I. Gregora, J. Chval, A. Fejfar, J. Kočka, I. Pelant, Rapid crystallization of amorphous silicon at room temperature, Philos. Mag. B 82 (2002) 1785–1793, https://doi.org/10.1080/13642810208222940.

[24] X. Jiang, K. Schiffmann, C.-P. Klages, Nucleation and initial growth phase of diamond thin films on (100) silicon, Phys. Rev. B 50 (1994) 8402–8410, https://doi.org/10.1103/PhysRevB.50.8402.

[25] D.M. Tanenbaum, A.L. Laracuente, A. Gallagher, Surface roughening during plasma-enhanced chemical-vapor deposition of hydrogenated amorphous silicon on crystal silicon substrates, Phys. Rev. B 56 (1997) 4243–4250, https://doi.org/10.1103/PhysRevB.56.4243.

[26] Y. Lifshitz, T. Köhler, T. Frauenheim, I. Guzmann, A. Hoffman, R.Q. Zhang, X.T. Zhou, S.T. Lee, The mechanism of diamond nucleation from energetic species, Science. 297 (2002) 1531–1533, https://doi.org/10.1126/science.1074551.

[27] R.A. Street, Hydrogenated Amorphous Silicon, Cambridge University Press, 2005.

[28] S.R. Narayan, J.M. Day, H.L. Thinakaran, N. Herbots, M.E. Bertram, C.E. Cornejo, T.C. Diaz, K.L. Kavanagh, R.J. Culbertson, F.J. Ark, S. Ram, M.W. Mangus, R. Islam, Comparative study of surface energies of native oxides of Si(100) and Si(111) via three liquid contact angle analysis, MRS Adv. 3 (2018) 3379–3390, https://doi.org/10.1557/adv.2018.473.

[29] F. Mussano, T. Genova, M. Laurenti, L. Munaron, C.F. Pirri, P. Rivolo, S. Carossa, P. Mandracci, Hydrogenated amorphous silicon coatings may modulate gingival cell response, Appl. Surf. Sci. 436 (2018) 603–612, https://doi.org/10.1016/j.apsusc.2017.11.283.

[30] J.-M. Zhang, F. Ma, K.-W. Xu, X.-T. Xin, Anisotropy analysis of the surface energy of diamond cubic crystals, Surf. Interface Anal. 35 (2003) 805–809, https://doi.org/10.1002/sia.1605.

[31] N.M. Hwang, J.H. Hahn, D.Y. Yoon, Charged cluster model in the low pressure synthesis of diamond, J. Cryst. Growth 162 (1996) 55–68, https://doi.org/10.1016/0022-0248(95)00943-4.

[32] W. Beyer, Diffusion and evolution of hydrogen in hydrogenated amorphous and microcrystalline silicon, Sol. Energy Mater. Sol. Cells 78 (2003) 235–267, https://doi.org/10.1016/S0927-0248(02)00438-5.

[33] A.Y. Kuznetsov, B.G. Svensson, Nickel atomic diffusion in amorphous silicon, Appl. Phys. Lett. 66 (1995) 2229–2231, https://doi.org/10.1063/1.113175.

[34] Š. Potocký, J. Holovský, Z. Remeš, M. Müller, J. Kočka, A. Kromka, Si-related color centers in nanocrystalline diamond thin films, Phys. Status Solidi B 251 (2014) 2603–2606, https://doi.org/10.1002/pssb.201451177.